COMPARATIVE STUDIES OF JET QUENCHING IN RELATIVISTIC HEAVY ION COLLISIONS

ROUZBEH MODARRESI YAZDI

Department of Physics
McGill University, Montréal

A thesis submitted to McGill University
in partial fulfillment of the requirements of the degree of
Doctor of Philosophy

CONTENTS

LIST OF FIGURES

LIST OF TABLES

ACRONYMS

ALICE A Large Ion Collider Experiment, experimental collaboration, located in Geneva, Switzerland

AMY Arnold–Moore–Yaffe

ATLAS A Toroidal LHC Apparatus, experimental collaboration, located in, Geneva, Switzerland

CMS Compact Muon Solenoid, experimental collaboration located in Geneva, Switzerland

CUJET Columbia University Jet

DGLAP Dokshitzer–Gribov–Lipatov–Altarelli–Parisi

DGLV Djordjevic–Gyulassy-–Levai–Vitev

GLV Gyulassy–Levai–Vitev

INCNLO Inclusive Next-to-Leading Order

JETSCAPE Jet Energy-loss Tomography with a Statistically and Computationally Advanced Program Envelope

LBT Linear Boltzmann Transport

LHC Large Hadron Collider

LO Leading Order

LPM Landau-Pomeranchuk-Migdal

MARTINI Modular Algorithm for Relativistic Treatment of heavy IoN Interactions

MATTER Modular All Twist Transverse-scattering Elastic- drag and Radiation

MUSIC MUScl for Ion Collisions

NLO Next-to-Leading Order

NP Non-Perturbative

PHENIX Pioneering High Energy Nuclear Interaction eXperiment, experimental collaboration, located in Brookhaven, NY, USA

pQCD perturbative Quantum Chromodynamics

QGP Quark-Gluon Plasma

RHIC Relativistic Heavy Ion Collider

STAR Solenoidal Tracker at RHIC, experimental collaboration, located in Brookhaven, NY, USA

UrQMD Ultra relativistic Quantum Molecular Dynamics

VISHNU Viscous Israel-Stewart Hydrodynamic Simulator 'N UrQMD

ABSTRACT

Heavy ion collisions (HIC) performed at major experimental facilities such as the Large Hadron Collider (LHC, Switzerland) or the Relativistic Heavy Ion Collider (RHIC, USA) produce a novel state of matter known as the Quark-Gluon Plasma (QGP). An important signal of the creation of the QGP is the observation of jet energy loss or jet quenching in these collisions.

This thesis studies jet energy loss via two parallel and independent comparative analyses. The first study uses MARTINI in the first, single-stage energy loss simulation to analyze the effect of changing the collision kernel which encodes information about the interactions of the jet with the QGP medium and is a crucial ingredient of energy loss rates. Recent efforts have resulted in this kernel's next-to-leading order (NLO) and non-perturbative (NP) evaluations. New inelastic rates are generated with the higher-order kernels and used in MARTINI simulations of energy loss. The simulations are then compared against those using the leading-order (LO) kernel. Systematic differences are shown between the three rate-sets, which can be absorbed into a re-scaled strong coupling constant within a single-stage energy loss model. Simulation results also demonstrate the need to go beyond a single-stage simulation and the physical necessity of a delayed parton shower or a multi-stage simulation.

The second study concerns the first comparative analysis of two important models of jet-medium interactions, MARTINI and CUJET, which employ the AMY-McGill and the DGLV energy loss frameworks, respectively. Two multi-stage models are constructed using JETSCAPE, incorporating MARTINI and CUJET as components in their workflow. The models are then applied to multiple HIC systems to calculate nuclear modification factors of charged hadrons, jets and jet substructure observables such as jet fragmentation function ratio. The simulations also contain photons via jet-medium interactions for the first time. We show systematic differences between the models in jet and jet-medium photon observables. The relation of the observed differences to the inelastic rates of the models is shown and points of improvement are discussed.

ABSTRAIT

Les collisions d'ions lourds (HIC) réalisées dans les grandes installations expérimentales telles que le Grand collisionneur de hadrons (LHC, Suisse) ou le collisionneur d'ions lourds relativistes (RHIC, États-Unis) produisent un nouvel état de la matière connu sous le nom de Plasma de Quarks et de Gluons (QGP). Ces collisions produisent initialment des ensembles de particules relativistes: des "jets". L'observation de la perte d'énergie des jets ou de l'extinction des jets dans ces collisions constitue un signal important de la création du QGP.

Cette thèse étudie la perte d'énergie des jets par le biais de deux analyses comparatives parallèles et indépendantes. La première étude utilise MARTINI dans la première simulation de perte d'énergie en une étape, en vue d'analyser l'effet du changement du noyau de collision qui encode des informations sur les interactions du jet avec le milieu QGP. Des efforts récents ont abouti à des évaluations nonperturbatives (NP) et au prochain ordre dominant (NLO) de ce noyau. De nouveaux taux inélastiques sont générés avec les noyaux d'ordre supérieur et utilisés dans des simulations de perte d'énergie. Les simulations sont ensuite comparées à celles utilisant le noyau d'ordre dominant (LO). Des différences systématiques apparaissent entre les trois ensembles de taux, qui peuvent être absorbées dans une constante de couplage rééchelonnée dans un modèle de perte d'énergie en une seule étape. Les résultats des simulations démontrent également la nécessité d'aller au-delà d'une simulation à une étape et la nécessité physique d'une pluie de partons realiste.

La seconde étude concerne la première analyse comparative de deux modèles importants d'interactions jet-milieu, MARTINI et CUJET qui utilisent respectivement les systèmes de perte d'énergie AMY-McGill et DGLV. Deux modèles à plusieurs étapes sont construits à l'aide de JETSCAPE, incorporant MARTINI et CUJET en tant que composants dans leur flux opérationnel. Les modèles sont ensuite appliqués à plusieurs systèmes HIC pour calculer les facteurs de modification nucléaire des hadrons chargés, des jets et des observables de la sous-structure des jets tels que le rapport de la fonc-

tion de fragmentation des jets. Pour la première fois, les simulations contiennent également des photons via des interactions jet-milieu. Nous trouvont des différences systématiques entre les modèles dans les observables de photons de jet et de jet-medium. La relation entre les différences observées et les taux inélastiques des modèles est montrée et les points d'amélioration sont discutés.

PUBLICATIONS

Some of the contents of Chapter 5 and Chapter 6 have resulted in the following publications:

[1] Rouzbeh Modarresi Yazdi, Shuzhe Shi, Charles Gale, and Sangyong Jeon. "Leading order, next-to-leading order, and nonperturbative parton collision kernels: Effects in static and evolving media." In: *Phys. Rev. C* 106.6 (2022), p. 064902. DOI: 10.1103/PhysRevC.106.064902. arXiv: 2206.05855 [hep-ph].

[2] Shuzhe Shi, Rouzbeh Modarresi Yazdi, Charles Gale, and Sangyong Jeon. "Comparing the martini and cujet models for jet quenching: Medium modification of jets and jet substructure." In: *Phys. Rev. C* 107.3 (2023), p. 034908. DOI: 10.1103/PhysRevC.107.034908. arXiv: 2212.05944 [hep-ph].

[3] Rouzbeh Modarresi Yazdi, Shuzhe Shi, Charles Gale, and Sangyong Jeon. "Jet-medium Photons as a Probe of Parton Dynamics." In: *Acta Phys. Polon. Supp.* 16.1 (2023), p. 129. DOI: 10.5506/APhysPolBSupp.16.1-A129. arXiv: 2207.12513 [hep-ph].

[4] Rouzbeh Modarresi Yazdi, Shuzhe Shi, Charles Gale, and Sangyong Jeon. "Comparative multi-probe study of jet energy-loss in QGP." In: *11th International Conference on Hard and Electromagnetic Probes of High-Energy Nuclear Collisions: Hard Probes 2023*. July 2023. arXiv: 2307.07890 [hep-ph].

ACKNOWLEDGEMENTS

I would like to gratefully acknowledge the support from McGill University via the Tomlinson Doctoral Fellowship (2017-2020). I am also grateful to the good people at the Digital Research Alliance of Canada for the computing clusters and facilities used throughout my research time at McGill.

I thank my supervisor, Prof. Charles Gale, for his unlimited support, mentorship and guidance throughout my Ph.D. studies. His incredible patience, encouragement and the atmosphere of collaboration he fostered made this research possible. I would also like to thank Prof. Sangyong Jeon for his insightful and probing questions during our group meetings, which led me to better understand the topic. I also extend my gratitude to Dr. Shuzhe Shi for the opportunity to closely collaborate with him and for all I learned from him. Every meeting with him has been a joy.

I would also like to thank my dear friends and colleagues, Matthew Ramin Hamedani Heffernan, Nicolas Fortier, Scott McDonald, Chanwook Park, Dylan Linthorne, Taylor Howarth, Jessica Churchill and Amit Kumar. Thanks to them, my graduate life became far more exciting and enriching. I learned much from our conversations about physics and other unrelated topics.

To my old friends, Iman Anvari, Farhang Khajenasiri, Sina Derhami, Ardavan Arfaei, Reza Sefidgar and Ahmad Mardoukhi, with whom I am guaranteed a close and deep connection no matter how far apart. In particular, I extend my deepest and most heartfelt appreciation to Ahmad, whose intervention at a crucial time made all the difference.

Finally, I dedicate this work to my parents, Shahabeddin and Malektaj, my brother Ramin and my partner Sharada. Their love and unending support made even the most challenging times bearable, and to whom I owe a debt of gratitude, I can never repay.

STATEMENT OF ORIGINALITY

Chapter 1-4 — provide introductory information on heavy ion collisions, jet production and energy loss modelling, and the different approaches to modelling the soft and hard sectors.

Chapter 5 — presents the first study of the effect of using higher order collision kernels in single-stage MARTINI simulations of jet energy loss. Energy loss rates were computed and implemented in MARTINI by Dr. Shuzhe Shi. I performed the full test and validation of the implementation, generated all the results and simulations presented here and performed the first fit of the model parameters using Gaussian Process Regression. This is the first systematic study of the parameter space of MARTINI. I also present original work on jet-medium photons in single-stage MARTINI simulation, and the study of the effect of a delayed parton shower, demonstrating the need for multi-stage modelling of jet energy loss. The simulations of this chapter use hydrodynamic histories generated using (2+1)D IP-GLASMA simulations of the initial state coupled with (3+1)D MUSIC hydrodynamics. The hydrodynamic background files used in this chapter were generated by Dr. Scott McDonald and Dr. Mayank Singh. This is the current state-of-the-art approach in the field.

Chapter 6 — showcases the first multi-probe study and analysis of CUJET and MARTINI when used in a multi-stage jet evolution model. The model parameters for CUJET and MARTINI were fitted by Dr. Shuzhe Shi and Dr. Chanwook Park, respectively. I contributed to the final implementation of the two models in the JETSCAPE, performed comprehensive tests and validations, and generated all the simulation results and analyses. Among the novel work here is the usage of a modified CUJET in Monte Carlo simulations. I present original work on the first-ever fully-reconstructed jet calculations and jet-medium photon spectra from CUJET. Other novel and original aspects of the work are jet-medium photons from MARTINI in a multi-stage simulation of an evolving QGP and the usage of direct photons and their scaling in studying parton energy loss mechanisms. Figure 6.19 in this chapter was generated by Dr.

Shuzhe Shi and has been properly attributed. The hydrodynamic histories used here were generated by me, using the parameters and the T-V approach's workflow as described in Chapter 3 with the exception of `Pb-Pb` collisions at 2.76 ATeV, $0-5\%$, $20-30\%$ and $30-40\%$ centrality histories which were generated by the JETSCAPE Collaboration and provided along side the publicly-available JETSCAPE framework.

Chapter 7 — presents the conclusions of the above studies and the discussion of what can be done going forward.

Part I

OVERVIEW OF HEAVY ION COLLISIONS AND JET PRODUCTION

1

INTRODUCTION

You cannot learn about the insides of a watch
by colliding two watches together.

— A famous theorist [1]

The *Standard Model of Particle Physics* (SM) is the current reigning theory that explains much of what we can observe in the universe[1]. The three fundamental forces in the SM are electromagnetic, weak and strong nuclear forces. Here, we are interested in the dynamics of quarks and gluons, the strongly interacting particle content of the Standard Model. The quantum field theory that governs the strong nuclear force and, therefore, the interactions of quarks and gluons (collectively called *partons*) is QCD or Quantum Chromodynamics. The naming of the theory stems from the labels assigned to the charges that quarks and anti-quarks carry: r, b, g for red, blue and green, respectively. Gluons are the mediators of the force, similar to the role played by the photon in electromagnetism. However, unlike photons, gluons also carry colour charge. The Lagrangian density of QCD is given by

$$\mathcal{L}_{QCD} = \bar{\psi}_{q,a}\left(i\partial\!\!\!/\delta_{ab} - g t^{C}_{a,b} A\!\!\!/^{C} - m_q \delta_{ab}\right)\psi_{q,b} - \frac{1}{4}F^{\mu\nu}_{A}F^{A}_{\mu\nu} \tag{1.1}$$

where repeated indices are summed over. The index q denotes the flavour of the fermion, one of the standard model's six quarks (or their equivalent anti-quarks), summarized in Table 1.1. The lower cases a, b signify the colour charge index of the fermion, while the upper case superscripts A, B and C are the colour indices of the gluon. $F^{A}_{\mu\nu}$ is the gluon field strength tensor and is given in terms of the gluon field, A^{A}_{μ}

$$F^{A}_{\mu\nu} = \partial_\mu A^{A}_{\nu} - \partial_\nu A^{A}_{\mu} - g f_{ABC} A^{B}_{\mu} A^{C}_{\nu}. \tag{1.2}$$

1 In this thesis, we are not concerned with physics beyond the Standard Model. This pronouncement includes gravity.

PARTICLE	Electric Charge	Mass (multiple of m_u)
u	$+\frac{1}{3}e$	2.16 MeV
d	$-\frac{2}{3}e$	2 m_u
s	$-\frac{2}{3}e$	43 m_u
c	$+\frac{1}{3}e$	588 m_u
b	$-\frac{2}{3}e$	1935 m_u
t	$+\frac{1}{3}e$	79949 m_u
g	0	0

Table 1.1: Particle content of QCD. Masses are shown as multiples of the up quark mass, and the charges as multiples of the electron charge. Data from the Particle Data Group [2].

f_{ABC} in the above are the structure constants, and t^C_{ab} are the Gell-Mann matrices, the generators of the symmetry group of QCD, $SU(3)$. The structure constants are defined via the commutation relation

$$[t^A, t^B] = if_{ABC}t^C. \tag{1.3}$$

1.1 RUNNING COUPLING AND ASYMPTOTIC FREEDOM

While the discussion above is on quarks and gluons, neither has been observed as free, isolated particles in nature. Instead, we observe them as constituents of hadrons in their *dressed* or *bound* form. This fact indicates that QCD has to be a *confining* theory for long distances where the strength of the interaction increases as the particles separate. The confining behaviour tells us something about the nature of the running coupling in QCD. We can assume that the coupling constant $g \equiv 4\pi\alpha_s^2$ is small at very high energies. We can then divide the Lagrangian density into free and interacting terms

$$S = \exp\left(\int d^4x[\mathcal{L}_{\text{free}} + \mathcal{L}_{\text{int.}}]\right) \tag{1.4}$$

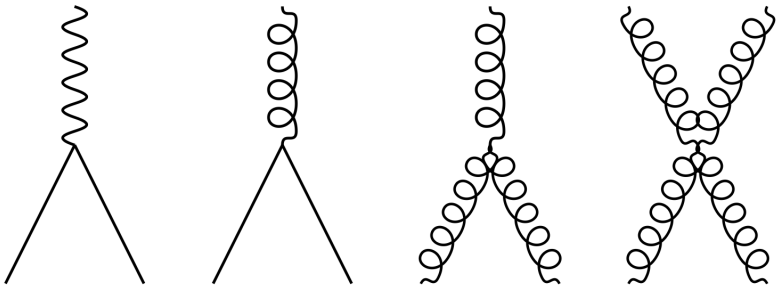

Figure 1.1: Allowed vertices in QED (leftmost) and QCD (rest). Solid lines represent fermions, wavey line represents the photon and the curly lines stand in for gluons. Every diagram describing an interaction in either quantum field theory is made of repeated combinations of these diagrams. Notice that unlike in QED, the gauge boson of QCD can self-interact.

and expand the interaction term in powers of g. The renormalization group equation for QCD is given by

$$\mu^2 \frac{\partial \alpha_s}{\partial \mu^2} = \beta(\alpha_s) \tag{1.5}$$

where μ is the scale at which α_s is to be evaluated and $\beta(\alpha_s)$ is the QCD beta function whose value at LO in the perturbative expansion is given by

$$\beta(\alpha_s) = -\frac{33 - 2N_f}{12\pi}\alpha_s^2. \tag{1.6}$$

where N_f is the number of active quark flavours. Solving for α_s, we get

$$\alpha_s(\mu^2) = \frac{12\pi}{(33 - 2N_f)\ln(\frac{\mu^2}{\Lambda^2_{QCD}})} \tag{1.7}$$

where $\Lambda_{QCD} = 200$ MeV is the QCD scale parameter, the scale at which the perturbative expansion breaks down and α_s becomes large. Finally, $N_f = 6$ in QCD[2]. Thus we see that as the scale μ is increased, α_s is reduced while as μ approaches Λ_{QCD}, α_s grows and eventually becomes undefined. The reason for this behaviour is the gluon self interaction (see Figure 1.1) [3]. In Quantum Electrodynamics, where we also have a series of spin-1/2 fermions interacting via exchanges of a spin-1 boson (the photon), the gauge boson does not have a self-interaction term as the equivalents

2 While in general there are six quarks in QCD, we include only the number of *active* flavours, due to the wide spread in the masses of the quarks as evidenced by Table 1.1, depending on the scales and the nature of the problem.

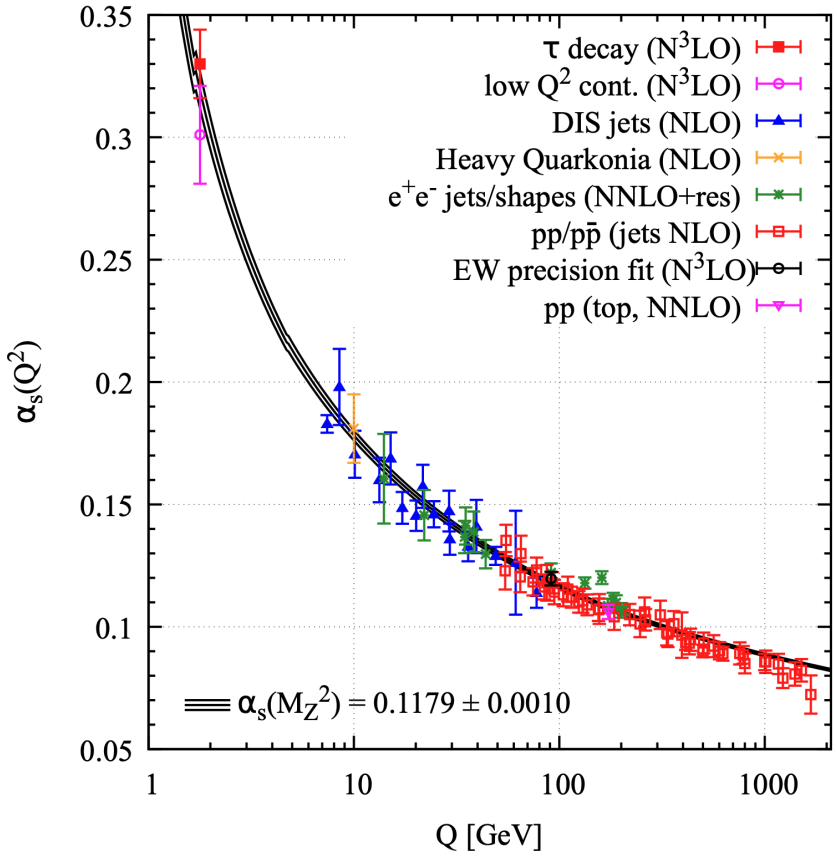

Figure 1.2: The running coupling of QCD, measured at different scales. Figure adapted from Ref. [2].

of the structure constants, f_{ABC}, for the $U(1)$ symmetry group are zero. Thus in the QED-equivalent of Equation 1.2, the third term is zero, and the photon does not couple directly to itself[3]. The β function of QED (for one fermion flavour) is, to leading order,

$$\beta_{QED}(\alpha) = \frac{1}{3\pi}\alpha^2 + \cdots \tag{1.8}$$

which, in stark contrast to Equation 1.6, is positive. Figure 1.2 shows the measurements of the running coupling at different scales. Asymptotic freedom of α_s, as demonstrated in Figure 1.2, then requires different techniques to be applied at different scales. Far above the Λ_{QCD} scale, one can safely use pQCD techniques. As the scale μ in Equation 1.7 approaches the scale of hadronic physics, $\mu \approx 1$ GeV, more and more terms must be included in the perturbative expansion. Below this scale, the

3 One can have photon-photon collisions in QED, but these go through higher-order diagrams, such as the famous box diagrams.

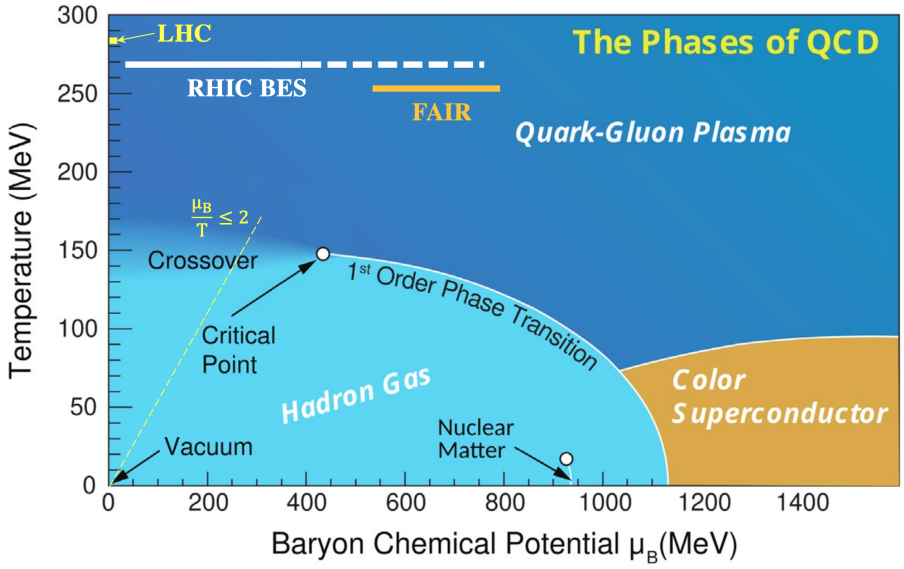

Figure 1.3: Sketch of the QCD Phase diagram, with the conjectured first order phase transition and critical end point. Figure adapted from Ref. [5].

coupling is too large and non-perturbative techniques, like Lattice QCD (LQCD) are used [4].

1.2 QCD PHASE DIAGRAM

Figure 1.3 shows a sketch of the QCD phase diagram. This work's region of interest is the high-temperature and zero baryon chemical potential. Lattice calculations of the Equation of State (EOS) of QCD in this region suggest that at high temperatures, the relevant degrees of freedom are quarks and gluons in a deconfined medium, while at lower temperatures, they are constrained to hadrons. The transition is shown in Figure 1.4 for EOS as calculated by the HotQCD [6] Collaboration. At low temperatures, the lattice results fall neatly on top of model calculations of hadron resonance gas (HRG), while at high temperatures, they approach the limit of an ideal gas. The lattice results diverge from the HRC calculations at around the cross-over temperature, T_c. No quantity (or their derivative) is discontinuous in this transition. Calculations of the hadron resonance gas model at high baryon chemical potential suggest that the hadron resonance gas undergoes a first-order phase transition to a plasma of quarks and gluons [7]. This fact, coupled with the lattice calculations of a cross-over at zero baryon chemical potential, suggests the existence of a critical point, the search for

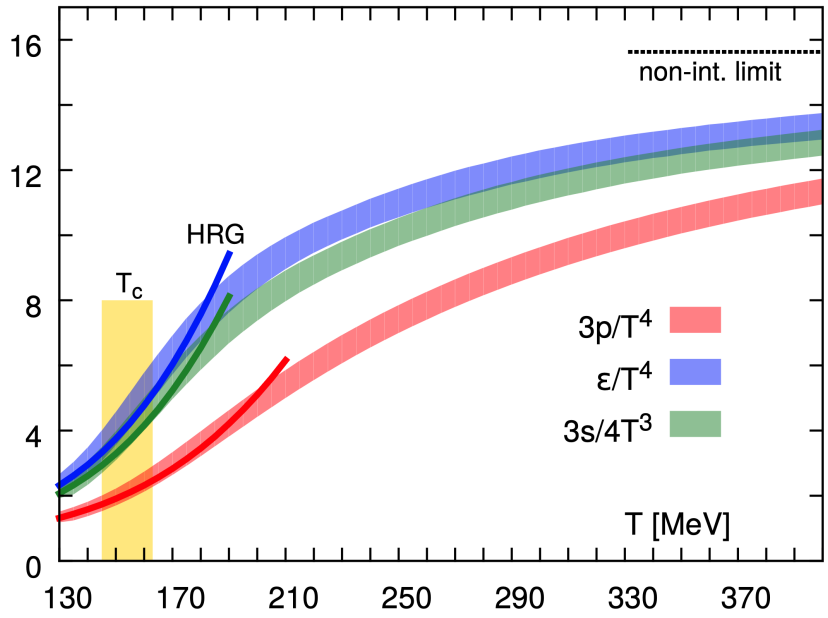

Figure 1.4: Equation of state calculated by Lattice QCD. Light colour bands are the Lattice QCD results, while the dark lines at low temperatures are the EOS of a hadron resonance gas model. A yellow box marks the cross-over temperature. The quantities shown are pressure (p), energy density (ϵ) and entropy density (s). Figure from Ref. [6].

which is a major goal of experiments. Recent lattice calculations place this critical point beyond $\mu_B/T = 2$ [8, 9].

1.3 HEAVY ION COLLISIONS AND THE QUARK-GLUON PLASMA

The laboratories for studying the quark-gluon plasma (QGP), the deconfined phase in the QCD phase diagram, are the major experimental facilities involved in colliding heavy ions at high energies. The Large Hadron Collider (LHC) at CERN, Switzerland and the Relativistic Heavy-Ion Collider (RHIC) at the Brookhaven National Laboratory in NY, USA, collide heavy ions at ultra-relativistic energies. The collisions have resulted in the creation of droplets of QGP with life-time less than ≈ 20 fm/c[4]. Even in this short time, however, the produced matter undergoes several stages of evolution. Figure 1.5 shows a cartoon of the space-time evolution of plasma. The stage immediately after the collision is labelled the *pre-equilibrium* phase, where the created

4 This translates to approximately 7×10^{-23} seconds.

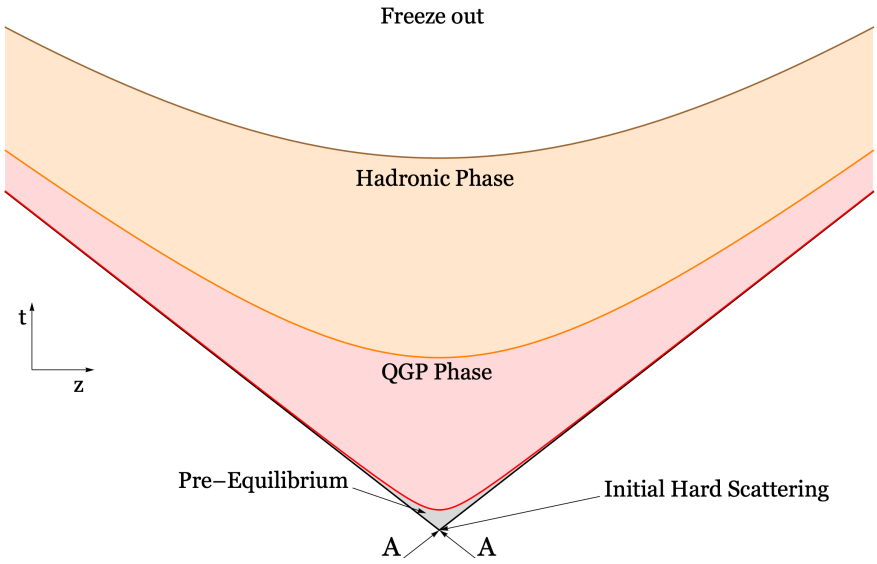

Figure 1.5: Sketch of the evolution history of the QGP produced in heavy ion collisions in $t - z$ coordinate system.

medium is highly out of equilibrium. As the medium expands and cools down, it approaches equilibrium where one can use relativistic hydrodynamics to model the evolution of the medium. The hydrodynamic medium expands further and cools until the local temperature reaches the cross-over. As discussed in the previous section, the degrees of freedom change from quarks and gluons to hadrons. The evolution then continues as the hot, hadron gas expands. Eventually, the mean free path becomes large, the gas dilutes, and hadrons fly toward the detectors.

The spectra and distributions of final state particles (mostly hadrons) then encode within them information about the various stages of the evolution. The coordinate system in which these quantities are described is the traditional coordinate system of colliders where the momenta of the final state partons are decomposed to its transverse components[5], $p_T = \sqrt{p_x^2 + p_y^2}$, the azimuthal angle $\phi = \arctan(p_y/p_x)$ and the rapidity variable

$$y = \frac{1}{2} \ln\left(\frac{E + p_z}{E - p_z}\right) \tag{1.9}$$

5 *Transverse* here means transverse to the beamline in a collision event.

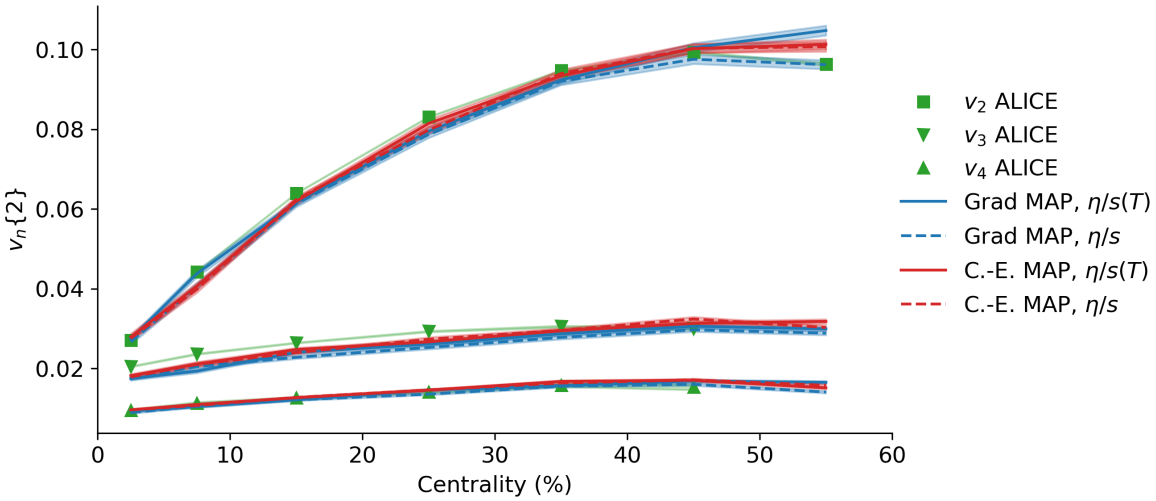

Figure 1.6: Comparison of flow coefficients as measured by the ALICE Collaboration [10] versus theoretical calculations generated using (2+1)-dimension IPG-M composite model. Figure is adapted from Ref. [11].

where E is the energy of the particle, $E = \sqrt{\mathbf{p}^2 + m^2}$. In this thesis, *pseudorapidity* variable is used,

$$\begin{aligned}\eta =& \frac{1}{2} \ln \tan(\theta/2) \\ =& \frac{1}{2} \ln \frac{|\mathbf{p}| + p_z}{|\mathbf{p}| - p_z}\end{aligned} \tag{1.10}$$

which is favoured by experiments since the rapidity variable requires the measurement of the energy of the particle as well as its longitudinal momentum, while the pseudorapidity variable requires the measurement of the particle's momentum and its angle relative to the beam axis, θ.

One of the most important signatures of collective behaviour is the observation of non-zero flow coefficients. These are Fourier coefficients of the invariant differential yield

$$\frac{dN}{p_T \, d\phi \, dp_T \, d\eta} = \frac{dN}{2\pi \, p_T \, dp_T \, d\eta} \left(1 + \sum_{n=0}^{\infty} 2 v_n(p_T) \cos\left(n\phi - n\Psi_n(p_T)\right) \right) \tag{1.11}$$

where v_n are the Fourier coefficients (also called *flow* harmonics), ϕ is the azimuthal angle and Ψ_n are the event-plane angles. Without a medium or collective flow, the particles flying out of the collision point are doing so isotropically, and all flow coefficients are zero. A non-zero measurement of these coefficients is strong evidence for

the existence of collective behaviour [12]. A comparison of the measurements of these flow coefficients versus theoretical calculations employing relativistic hydrodynamics is shown in Figure 1.6.

1.3.1 *Hard and soft probes of QGP*

The flow coefficients described above exemplify a *soft* observable[6]. These observables or measurements are dominant at relatively lower values of transverse momenta. Typically, the soft observables are those whose dominant contribution occurs at $p_T < 4$ GeV [7]. There are other classes of observables, including measurements of hadrons but those at much higher transverse momenta. These are high p_T hadrons and jets produced at the moment of initial scattering. The mechanism of generating such probes is via large momentum transfer reactions, allowing for a perturbative treatment. Another piece of evidence for the creation of QGP has been the observation of the softening of the hard particle and jet spectra relative to an (appropriately scaled) proton-proton collision at the same energy. The cause of this softening of the spectrum is jet energy loss via gluon bremsstrahlung due to the hard parton's interactions with the thermal medium.

A primary focus of this thesis is the study of jet energy loss and high-p_T hadrons and jets. This is done using models of jet-medium interactions and pQCD-inspired analyses for simulations of jet energy loss. Many models, with different assumptions on the nature of the process and the QGP medium, have been proposed to explain jet energy loss and reproduce experimental observations. An important question, as well as the current focus of the field, is to determine the extent to which these models can explain the data, in what regions do they agree with each other, and whether we can use such comparative studies to guide further theoretical development.

Throughout the discussion above, the focus has been on gluon radiation. In such processes, the radiated gluon can further interact with the medium. These interactions can then modify the gluon spectra and wash away some of the information

6 Soft as compared to the scales set by jets.

7 This is approximately four times the proton's mass ($4m_p$). It also works out to around four times the average energy of a particle at a temperature of $T = 0.6$ GeV, an achievable temperature in the initial steps of the medium evolution.

about the local conditions of the gluon radiation. Photons generated during the evolution of quarks or anti-quarks through the medium, on the other hand, have large mean-free-paths compared to the size of the medium. As such, measurements of the photon spectra allow for more direct access to information about the medium. The photon spectrum also includes photons not generated from hard scattering processes or jet evolution. The pre-equilibrium and hydrodynamic stages can also emit photons. Indeed the low p_T part of the measurements of the photon spectrum can be used to infer an *effective* temperature for the QGP fireball. Thus one can ask about the relative contribution of jet-medium photons to the total direct photon spectrum and the possibility of experimental measurements or detection of these photons. Composition of the direct photon spectrum is an open question and an active area of research, one that we will contribute to here.

1.4 THESIS PURPOSE AND ORGANIZATION

This work presents the results of two novel, parallel and state-of-the-art studies of jet energy loss in heavy ion collisions. The first of these is the first study which uses the higher-order collision kernels in the energy loss simulations of hard parton evolution through an evolving QGP. Scattering kernels encode information about the elastic scatterings of hard partons with the medium constituents and are, therefore, a crucial element in determinations of radiative energy loss. For the study presented in this work, we use what is known as a *single-stage* energy loss simulation. This is when the energy loss is assumed to be dominated by a single stage of the evolution, for instance energy loss of partons when at low virtuality. In the case of this study, MARTINI, which implements the AMY framework, is used to model the evolution of the hard partons through the QGP medium. The new kernels are used to generate associated rates within the AMY framework. These rates are then compared and contrasted against each other in static as well as evolving QGP simulations. A series of hadronic, jet and electromagnetic probes are employed, in a first multi-messenger study of MARTINI, to analyze the effect of the higher-order kernels. The limitations of single-stage modelling of jet energy loss are studied where Gaussian Process Regression is used, for the first time, to probe the parameter space of MARTINI. The importance of multi-

stage (as compared to single-stage) evolution of partons is clearly demonstrated and the presented results show the importance of the high-virtuality stage of jet evolution. The hydrodynamic evolution of this study is also seeded by the state-of-the-art model of initial conditions, IP-GLASMA.

As mentioned before, there are many approaches to modelling the jet-medium interactions, each with a different view of the nature of the underlying medium. They also differ in their assumptions of the radiative process itself. The jet energy loss community is now focused on comparative studies of these energy loss models in anticipation of entering the precision studies era of heavy ion collisions. The second independent and complementary study of this work aims to contribute to this effort by presenting a novel analysis of two important models of jet energy loss, CUJET and MARTINI. For the first time, these two models are compared against each other in the context of a multi-stage, multi-probe analysis with a realistically evolving hydrodynamic background. In order to have tight control over all aspects of the simulation and to have a fair comparative study, we use the JETSCAPE framework as our model factory and use charged hadrons, jets, jet substructure and jet-medium photons to probe the differences between the models. The aim is to further illuminate the nature of jet-medium interactions and to probe the assumptions of the two models via a comparative study of them against the data and each other. The jet, jet substructure and jet-medium photon results presented here are the first calculations of such observables for CUJET and the CUJET framework itself had to be modified explicitly from a deterministic approach to a Monte Carlo generator for our purposes here.

The document, then, is organized as follows. Chapter 2 describes hard parton generation in proton-proton collisions. Chapter 3 briefly describes the modelling of the soft sector, which provides the QGP temperature and flow velocity evolution profiles as a function of time. A theoretical overview of the jet energy loss models used in this thesis is given in Chapter 4. The study of the new collision kernels is presented in Chapter 5 using the single-stage study of MARTINI. Chapter 6 then shows the results of the first multi-stage study of MARTINI and CUJET. The findings of this study and the discussion of what is to be done next are presented in Chapter 7.

NOTATIONS

This thesis uses natural units where $\hbar = c = k_B = 1$. The bold font $\mathbf{x}$ denotes three-vectors whose magnitude is $|\mathbf{x}| = x$. Four vectors are written with lower case p or p^μ, and context should help distinguish between a four-vector and the magnitude of a three-vector. In some parts of the thesis, light cone coordinates will be used. These are defined for a given four-vector p^μ,

$$\begin{aligned} p^+ &= \frac{p^0 + p^z}{\sqrt{2}} \\ p^- &= \frac{p^0 - p^z}{\sqrt{2}}. \end{aligned} \tag{1.12}$$

Finally, the mostly negative metric tensor, $g^{\mu\nu} = (1, -1, -1, -1)$ is used. Throughout the text we refer to Mandelstam variables, s, t and u. For a reaction $p_1 + p_2 \to p_3 + p_4$, where p_i are momentum four-vectors, these are defined as

$$s = (p_1 + p_2)^2,\ t = (p_1 - p_3)^2,\ u = (p_1 - p_4)^2. \tag{1.13}$$

Thus s is the total energy in the collision and t and u measure the momentum transfers between different particles during the collision.

2

JET PRODUCTION IN PROTON-PROTON COLLISIONS

Hard-parton generating processes[1] in hadron-hadron collisions are of particular interest to theorists and experimentalists alike. These processes interest theorists as they allow for a perturbative expansion and are studied by experimentalists since with large momentum transfers come large transverse momentum particles. In a collider experiment, this translates to energetic partons in the final state travelling perpendicularly to the beamline, a (somewhat) clean signal to measure. Calculations of these processes, their modelling and measurements are now at such a state of maturity that we can use them as probes of other systems, such as heavy ion collisions and QGP formation.

At a fundamental level, we are interested in the scatterings of partons. However, due to confinement, we do not have access to free quarks and gluons and instead have to deal with hadrons. Using high-energy collisions of hadrons, we can probe their internal structure and then study the resulting spray of particles that exit the interaction point. Typically, this is done by grouping hadrons to form *jets*, the hadronic analogues of an energetic parton. Figure 2.1 shows a schematic diagram of the scattering of two hadrons, A and B, resulting in h_1 and h_2, the outgoing hadrons. The differential cross section for this process is, after suppressing all scale dependencies, given by

$$d\sigma_{A+B\to C+D} = \sum_{a,b,c,d} \int_{x_a,x_b,z_c,z_d} f_{a/A}(x_a)\, f_{a/B}(x_b)\, d\hat{\sigma}\, D_{h_1/c}(z_c)\, D_{h_2/d}(z_D). \quad (2.1)$$

where the momentum fractions x and z are defined by

$$x_a = \frac{p_a}{p_A},\ x_b = \frac{p_b}{p_B},\ z_c = \frac{p_{h_1}}{p_c},\ z_d = \frac{p_{h_2}}{p_d}. \quad (2.2)$$

1 *Hard*, in QCD, typically means energies involved are larger than the QCD scale $\Lambda_{QCD} = 200$ MeV. In proton-proton collisions and simulations, hard is taken to mean transverse momenta or energies above 10 GeV, where perturbative techniques can be comfortably applied. In this work, we use *hard* to be pQCD events resulting in the generation of a parton with $p_T \geqslant 4$ GeV.

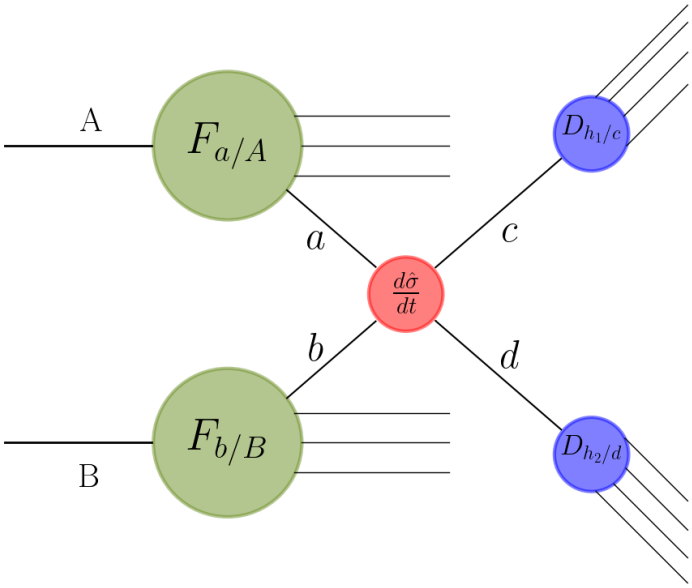

Figure 2.1: Schematic diagram showing the scattering of two hadrons, A and B, resulting in the production of two hadrons h_1 and h_2 in the final state along with other debris. The parton level scattering is shown as a red circle in the middle.

We can now go through Equation 2.1 term by term. $f_{a/A}(x_a)$ and $f_{b/B}(x_b)$ are the parton distribution functions (PDFs) of hadrons A and B. At leading order, they can be thought of as the probability of finding partons a and b in their respective hadrons with the given momentum fractions x_a and x_b. $d\hat{\sigma}$ is the differential cross-section of the process at a partonic level, where partons a and b scatter to a final state of c and d. Finally, the functions $D_{h_1/c}(z_c)$ and $D_{h2/d}(x_d)$ are the fragmentation functions and represent the probability of parton c(d) fragmenting into hadron $h_1(h_2)$ which then carries $z_c(z_d)$ fraction of the original parton. The PDFs and the fragmentation functions depend on the scales –*factorization* and *fragmentation*, respectively– at which they are evaluated.

Both PDFs and fragmentation functions are non-perturbative objects. Their values or functional forms are unknown and need to be extracted from data. Once determined, however, they are process independent, and their scale evolution is described by the famous DGLAP evolution equation. For PDFs, this is given by

$$\mu_F^2 \frac{\partial f_{i/A}(x,\mu_F^2)}{\partial \mu_F^2} = \sum_j \frac{\alpha_s(\mu_F^2)}{2\pi} \int_x^1 \frac{dz}{z} P_{i\leftarrow j}(z) f_{j/A}(\frac{x}{z},\mu_F^2) \tag{2.3}$$

PROCESS	SPLITTING FUNCTION
$q \to q + g$	$P_{q\to q} = \frac{4}{3}\left[\frac{1+z^2}{(1-z)_+} + \frac{3}{2}\delta(1-z)\right]$
$q \to g + q$	$P_{q\to g} = \frac{1}{2}\left[z^2 + (1-z)^2\right]$
$q \to q + \gamma$	$P_{q\to\gamma} = \frac{1+(1-z)^2}{z}$
$g \to q + \bar{q}$	$P_{g\to q} = \frac{4}{3}\left[\frac{1+(1-z)^2}{z}\right]$
$g \to g + g$	$P_{g\to g} = 6[\frac{z}{(1-z)_+} + \frac{1-z}{z} + z(1-z) + \left(\frac{11}{12} - \frac{N_f}{18}\delta(1-z)\right)$

Table 2.1: DGLAP splitting functions for each QCD and QED process of quarks using the shortened notation.

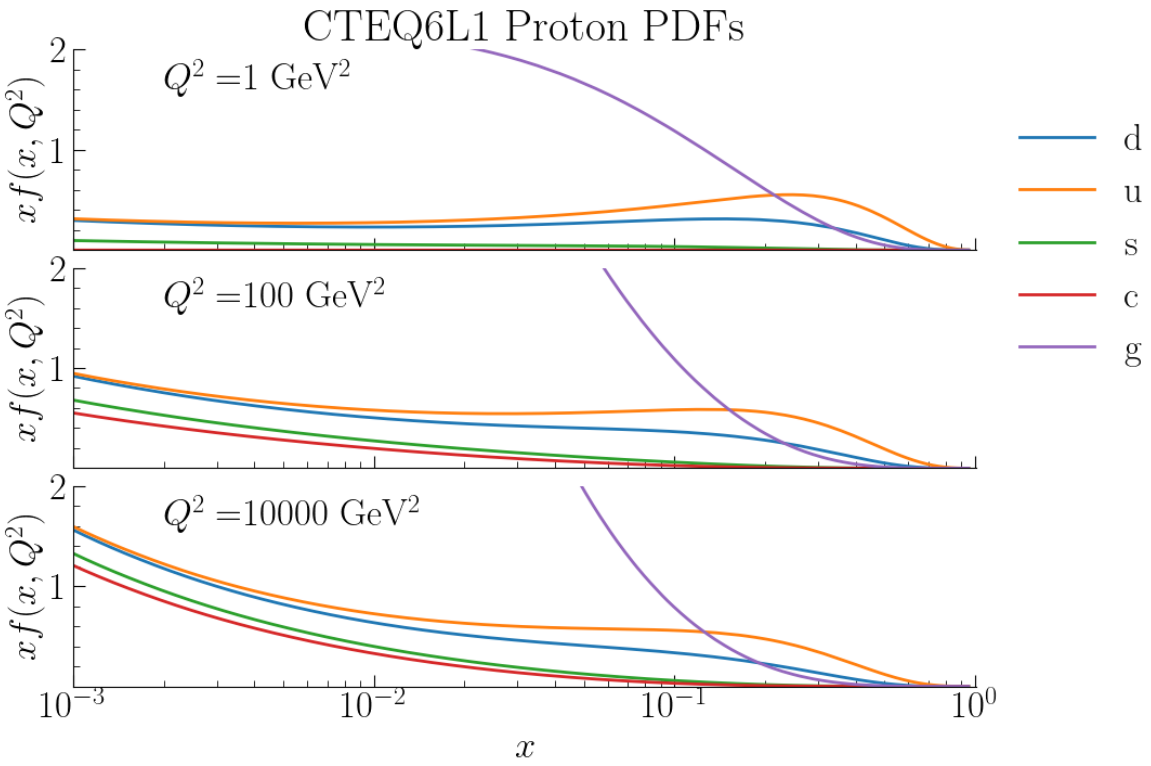

Figure 2.2: Example of the free proton parton distribution function using for CTEQ6L1 [13] proton PDFs, evaluated at three different scales. PDFs were generated using LHAPDF6 [14] PDF Library code.

where μ_F is the factorization scale and the function $P_{i\leftarrow j}(z)$ is the DGLAP splitting function[2] given in Table 2.1. The + (plus) description is defined as

$$\int_0^1 dz \frac{f(z)}{(1-z)_+} = \int_0^1 \frac{f(z) - f(1)}{1-z} \tag{2.4}$$

Figure 2.2 shows the parton distribution functions for u, d, s, c quarks and gluons in a free proton, evaluated at three scales. The dominance of gluons for small momentum fractions and lower scales is visible in the figure.

Evaluation of Equation 2.1 can be done in three ways. One way is to perform a fixed-order pQCD calculation. Such schemes require knowledge of the matrix elements at the given order. They are typically referred to as *inclusive* or *semi-inclusive* calculations since most of the information of the final state is integrated over. The benefit of such techniques is that they have very few free parameters, usually only the three scale parameters: renormalization, factorization and fragmentation. The downside is the inclusive nature of the calculation: one has to calculate the observable of interest directly, and any new observable would then require a new calculation.

Another technique is to utilize a Monte Carlo generator. In this scheme, the process of interest is simulated (typically at LO). Then a parton shower is constructed based on some shower parameter that defines the ordering, with typical choices being the virtuality or the relative angle of the parent and the daughter parton [15]. Showers are split into two parts: initial state radiation (ISR), which happens before, and final state radiation (FSR), which occurs after the hard scattering. The probability of a branching, for a parton a to branch to partons b and c is given by [16]

$$d\mathcal{P}_a(z,t) = \frac{dt}{t}\frac{\alpha_s(t)}{2\pi}\sum_{b,c} P_{a\to bc}(z)dz \tag{2.5}$$

where t is the scale used to order the emissions and z is the momentum fraction of parton b, and $1-z$ is the fraction taken by c. The above expression gives the differential probability of branching in a $dz\ dt$ step. Integrating over the kinematically allowed region of z gives the differential probability of branching in a dt step

$$d\mathcal{P}_a(t) = \frac{dt}{t}\frac{\alpha_s(t)}{2\pi}\sum_{b,c}\int_{z_{min}(t)}^{z_{max}(t)} P_{a\to bc}(z)\ dz. \tag{2.6}$$

2 The full notation for these functions is $P_{a\to b+c}$ but c is always uniquely defined in accordance to various conservations laws and the allowed interactions terms from the Lagrangian. Thus it can be dropped from the notation.

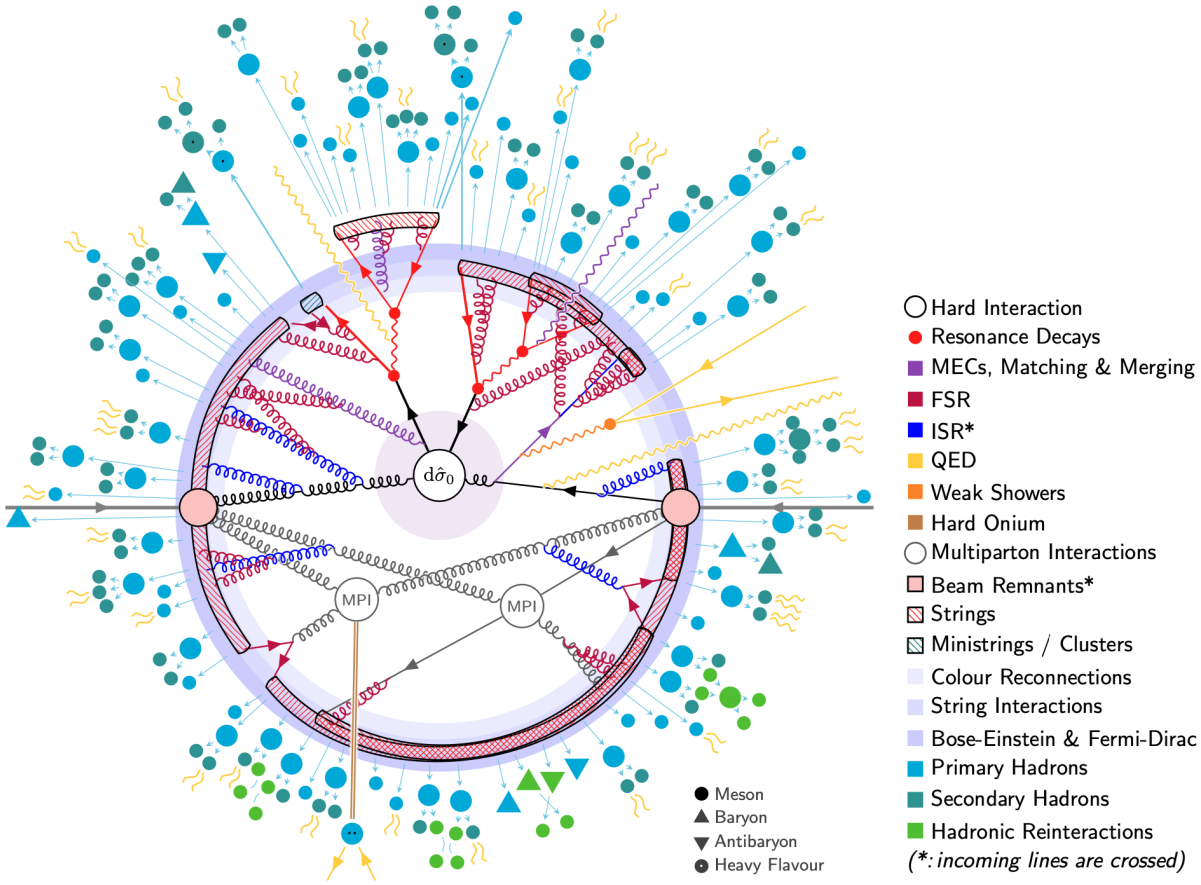

Figure 2.3: Example of a proton-proton collision event generated via PYTHIA where the underlying partonic process is $pp \to t\bar{t}$. Figure taken from Ref. [16].

The probability to not branch is $1 - d\mathcal{P}_a(t)$. We can define the Sudakov form factor [16],

$$S_a(t_0, t_1) = \exp\left(-\int_{t_0}^{t_1} d\mathcal{P}_a(t)\right) \tag{2.7}$$

which results from the repeated application of the *no-branching* probability. It has the physical interpretation of the probability of parton a experiencing no branchings between t_0 and t_1. The full shower is then generated recursively via repeated application of the Sudakov form factor. The fully simulated parton shower is then hadronized using a hadronization model. The final state of an MC generator workflow looks very similar to a realistic collider event: a list of hadrons, photons, leptons and so on with their associated momenta. An example of such an event is given in Figure 2.3. The downside of an MC generator approach is the relatively larger number of free parameters that need to be fitted to the data.

Finally, one could mix the two approaches by generating the process of interest using a higher order matrix element and then couple the calculation to a parton shower. This way, one benefits from a higher-order pQCD calculation while obtaining a realistic final state. Of course, this has a downside: the technical difficulty of matching the parton shower to the hard scattering generation.

In this work we use the Monte Carlo method and utilize PYTHIA in generating the hard scattering events in `p-p` and `A-A` collisions.

3

THE SOFT SECTOR

The modelling of the soft sector of heavy ion collisions has been an active and very fertile area of research for several decades. The prevalent view of the soft sector, a *standard model of heavy ion collisions and QGP evolution*, is that of a multi-stage evolution expected to represent the plasma's true or physical spacetime evolution. The stages of the evolution, as previously shown in Figure 1.5, are enumerated as

1. *Initial conditions* where an energy or entropy density profile is generated immediately after the collision,
2. *Pre-equilibrium evolution* where a highly out of equilibrium system evolves toward equilibrium,
3. *viscous, relativistic hydrodynamic expansion* where the system is taken to be close to local thermal equilibrium with viscous corrections and is then evolved (typically) as a (2+1)-dimensional medium
4. *Particlization* at some switching temperature, T_{sw}, the macroscopic model of hydrodynamics is abandoned in favour of a microscopic transport model,
5. *Transport* below the switching temperature, the hadron gas is evolved, hadrons are allowed to rescatter, and resonances are allowed to decay. This stage ends when all hadrons are kinetically frozen out.

The focus of this work is not on the details of modelling the soft sector. As such, only the relevant details and descriptions for each model used in the composite, multi-stage modelling of the soft sector are provided. The interested reader is referred to the original references for the technical specifications.

The evolution of the QGP is modelled in a multi-stage and multi-scale simulation. This perspective on jet evolution and simulation results from decades of very successful model building and analysis, and it rests on the assumption that the fast, energetic

modes, as represented by jets, are perturbations on the evolution of QGP and do not fundamentally alter the fireball. The soft sector is simulated and stored, and the jets are propagated through the history files generated from that simulation. There are new studies indicating the need for more connection and cross-talk between the hard and soft sectors [17–20] and the potentially significant modification affected by jet, and in particular mini-jet, propagation in a QGP medium. However, this branch of QGP studies is still in its infancy and more studies are needed.

3.1 COMPOSITE MODELS

Simulations of the soft sector are grouped into two *composite* models or approaches, and resulting simulations provide the evolution histories that are then used as the background for the medium evolution of the hard partons. These are[1]

A. T-V approach: TRENTO+free-streaming+VISHNU+FRZOUT+URQMD

B. IPG-M approach: IP-GLASMA+MUSIC+ISS+URQMD.

There are several parameters whose values need to be tuned to use the two workflows introduced here. These will be presented and discussed in their appropriate sections. The T-V model's parameters were tuned to data in the Bayesian study of Ref. [22]. The free parameters of the IPG-M model were fixed phenomenologically, with values that provided a good visual fit to heavy ion collision data. A recent, state-of-the-art Bayesian analysis of the soft sector [23] used a modified[2] version of the IPG-M model and found very similar values for the parameters shown here.

All initial state models used here are evolved or computed in (2+1)-dimensions. Most of the hydrodynamic profiles – with the exception of the `Pb-Pb` hydrodynamic histories of Chapter 5– also have the same spacetime dimensions. The choice of using a (2+1)D initial condition or later for hydrodynamic simulation is motivated by the observation of a plateau in charged hadron density $dN_{ch}/d\eta$. Given the focus of

1 The T-V uses a customized version of ISS [21] available at https://github.com/Duke-QCD/frzout.

2 the modifications involved were strict usage of the (2+1)-dimensional MUSIC and different particlization and hadronic-afterburner packages for the last stage of evolution. The parameterization of the specific shear and bulk viscosities were also different. However, the extracted profiles are not materially different from what is presented in Section 3.4.

experiments on midrapidity observables and the approximate boost-invariance observed in charged hadron density, a boost invariant evolution is a good, reasonable and successful approximation. The midrapidity region is also the region of interest in this thesis.

In terms of performance against the data, we use the terminology introduced in Ref. [11] of *first generation* and *next generation* of observables. The first generation observables are those which capture the large-scale features of the QGP evolution and are typically observables introduced in the earlier studies of QGP. These incldue charged hadron multiplicity, mean transverse energy and so on. Next generation observables are those which are far more sensitive to the momentum correlations, geometric fluctuations and non-linear response of the medium. It is the latter class of observables that can distinguish between the modelling approachs enumerated in the above. For our purposes and given the focus on high energy probes of the medium, the two approaches are equivalent and the choice to use one over the other, in each study presented in Chapter 5 and Chapter 6 is purely based on computational and logistical considerations.

3.2 INITIAL STAGE

The initial stage of evolution begins with the collision of the two nuclei and extends until the onset of hydrodynamics. This stage of evolution is the least well-understood part of the overall modelling of the QGP and is an active area of research. Models of the initial state can be broadly classified as

A. parametric models such as Glauber [24] and TRENTO [25],

B. transport models such as AMPT [26],

C. saturation-based models such as IP-GLASMA [27] and EKRT [28].

Here, we discuss the models used in the multi-stage simulations used in the thesis.

NUCLEUS	a (fm)	R (fm)
^{197}Au	6.38	0.535
^{208}Pb	6.62	0.546

Table 3.1: Woods-Saxon distribution parameters used in this thesis. The values are taken from Refs. [29, 30].

3.2.1 *Optical Glauber*

One of the earliest models of the initial state is the Optical Glauber model [31, 32]. In this model, the Woods-Saxon distribution [33][3] which has been used to model the charge distribution in nuclei, is taken to be a good parametrization of the density of nucleons in the nucleus

$$\rho(r) = \rho_0 \frac{1}{1 + \exp\frac{r-R}{a}} \tag{3.1}$$

where R is the charge radius of the nucleus, a is the nuclear skin parameter, and ρ_0 is the density at the center of the nucleus which can be treated as a normalization parameter. The values of R and a can be measured in elastic electron scatterings off target nuclei [35, 36]. The measurements associated with the two nuclei used in this thesis, Au and Pb, are presented in Table 3.1. The ρ_0 parameter can then be fixed via the normalization condition [37]

$$\int \rho(r)\, d^3r = 1. \tag{3.2}$$

In high-energy collisions, the nuclei experience severe Lorentz contraction. The Lorentz factor can be worked out to

$$\begin{aligned} \gamma &= \frac{E}{m} \\ &= \frac{\sqrt{s}}{2m} \end{aligned} \tag{3.3}$$

3 This parametrization of Woods-Saxon is for *underformed* nuclei. The equivalent form for deformed nuclei includes an additional term in the numerator to account for the deformation. In this thesis, only the high-energy collisions of gold (Au) and lead (Pb) ions are considered, which are generally assumed to be spherical. This is an assumption that is coming under scrutiny (see Ref. [34]), but the discussion of which is beyond the scope of this work.

which for Pb-Pb (^{208}Pb) collisions at 2.76 ATeV, becomes approximately 1490. For a lead ion with a radius of approximately 7 fm and colliding at this energy, we have a Lorentz contracted thickness

$$\begin{aligned} d_{\text{cont.}} =& \frac{2R_{\text{Pb}}}{\gamma} \\ =& 0.009 \text{ fm}. \end{aligned} \tag{3.4}$$

Thus this is an extremely contracted object, even more so for higher energy collisions like $\sqrt{s} = 5.02$ ATeV, and is said to resemble a pancake[4]. To model the initial conditions, the optical Glauber model assumes straight path trajectories for the nucleons in each nucleus[5]. With this approximation and the significantly Lorentz-contracted nucleus, we can then think of the colliding nuclei as two thin overlapping pancakes and define the *nuclear thickness function*

$$T_{A(B)}(\mathbf{s}) = \int_{-\infty}^{\infty} \rho_{A(B)}(\mathbf{s}, z_{A(B)})\ dz_{A(B)} \tag{3.5}$$

which is normalized to unity

$$\int T_{A(B)}(\mathbf{s})\ d^2s = 1. \tag{3.6}$$

The nuclear thickness function is the probability of finding a baryon in the transverse plane at location $\mathbf{s}$. The subscripts A and B denote the projectile and the target nucleus, respectively. Using the nuclear thickness function, we can write down the overlap function of two colliding nuclei

$$T_{AB}(\mathbf{b}) = \int T_A(\mathbf{s} - \mathbf{b}/2) T_B(\mathbf{s} + \mathbf{b}/2)\ d^2s \tag{3.7}$$

where $\mathbf{b}$ is the impact parameter of the collision. The integrand of this quantity is the joint probability per unit area of two nucleons overlapping. The main input to the Optical Glauber model, is the inelastic nucleon-nucleon cross section or $\sigma_{\text{Inel.}}^{\text{NN}}$ which together with the nuclear overlap function $T_{AB}(\mathbf{b})\sigma_{\text{Inel.}}^{\text{NN}}$, gives the probability of an

4 This is the terminology that is typically used in the literature to describe the shape of the colliding ions. Given the amount of contraction, I find *crêpe* to be a better analogy.

5 This is the eikonal approximation, true when the velocities of the nucleons are very high. In such a limit, most interactions are small deflections, too small to change the direction of travel. This is sensible given that soft QCD interactions (momentum exchanges less than 1 GeV) are much more likely to happen than hard collisions which result in significant deflections of the nucleons.

interaction occuring. Using this information, the Optical Glauber model can compute various quantities of interest for heavy ion collisions. However, it is a *smooth* model with no fluctuations. While it has been able to adequately explain some experimental observables when coupled to a realistic hydrodynamic simulation, it is not capable of capturing fluctuation-driven observables, such as triangular flow (v_3, see Equation 1.11).

3.2.2 *Monte Carlo Glauber*

Monte Carlo Glauber (MCGlauber) model is a natural improvement on the Optical Glauber model. It introduces fluctuations via sampling the Woods-Saxon distribution of Equation 3.1 for nucleon positions rather than using it as a smooth distribution. Two nucleons then are taken to have experienced a collision if their distance, d, satisfies

$$d \leqslant \sqrt{\frac{\sigma_{\text{Inel.}}^{\text{NN}}}{\pi}}. \tag{3.8}$$

The nucleons that have experienced at least one collision are called *participants* while the rest are *spectators*. Another parameter in MCGlauber is the radius associated with the proton. The proton shape is taken as an exponential $\exp(r/R)$ where R can be the root-mean-squared charge radius of the proton ($R = 0.88$ fm) or the gluon radius of proton ($R = 0.4$ fm). Both Optical Glauber and MCGlauber can be used to directly initialize the hydrodynamic stage by calculating the initial entropy density profile s_0[6] [38]

$$\begin{aligned} s_0(\mathbf{r}_\perp) \equiv & \frac{dS}{\tau_0 d^2 r_\perp d\eta}|_{\eta=0} \\ = & \frac{C}{\tau_0}\left(\frac{1-\alpha}{2}\, n_{\text{part.}}(\mathbf{r}_\perp) + \alpha\, n_{\text{bin.}}(\mathbf{r}_\perp)\right) \end{aligned} \tag{3.9}$$

where S is entropy and τ_0 is the start time of the hydrodynamic evolution with $n_{\text{part.}}$ and $n_{\text{bin.}}$ being the number density of participants and number density of binary collisions. α is the relative weight, a phenomenological parameter, and C is the overall

6 Energy density can also be used to initialize the hydro stage, and it is related to the entropy density via the EOS.

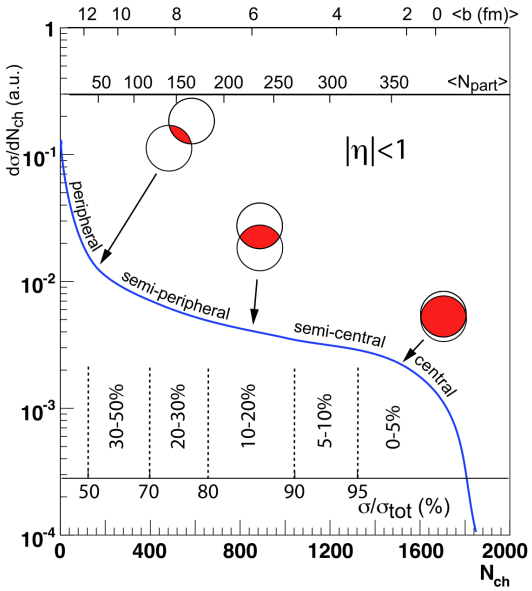

(a) Sketch of the relation between centrality and N_{ch}

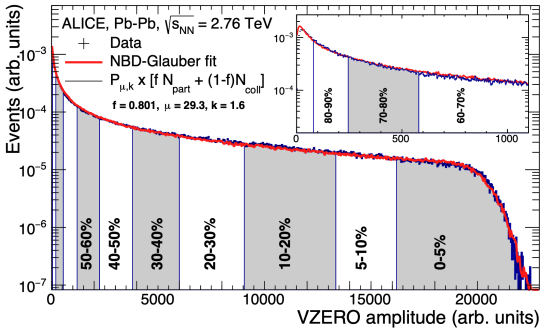

(b) Example of centrality determination by the ALICE Collaboration

Figure 3.1: (a) Sketch of the relationship between impact parameter, centrality and charged particle multiplicity. Figure is taken from Ref. [24]. (b) ALICE Collaboration's centrality determination of method in `Pb-Pb` collisions at 2.76 ATeV using the VZERO detector. Figure is taken from Ref. [39].

constant that can be tuned to charged hadron multiplicity at midrapidity to reproduce the data.

The MCGlauber model then incorporates fluctuations into the Glauber model and expands the range and number of observables it can accommodate. However, it is a purely geometry-based model and currently, the main application is centrality class determination. Centrality is a measure of how *head on* the heavy ion collision was (see Figure 3.1). Centrality determination in experiments is done by correlating the measurement of energy deposition or number of particles in a given detector to the size of the QGP created in the HIC [24]. One way is to measure the charged particle multiplicity (N_{ch}) at midrapidity for all events in a given run and order them in increasing order of N_{ch}. This is shown in Figure 3.1a. The centrality classes are then determined by binning the distribution into fractions of its total integral [24, 38]. For

example, for the 20-30% centrality class, we need the boundaries c_{20} and c_{30} which are determined using

$$\frac{\int_{\infty}^{n_{c_{20}}} \frac{dN_{evt.}}{dN_{ch}} dN_{ch}}{\int_{\infty}^{0} \frac{dN_{evt.}}{dN_{ch}} dN_{ch}} = 0.20, \quad \frac{\int_{\infty}^{n_{c_{30}}} \frac{dN_{evt.}}{dN_{ch}} dN_{ch}}{\int_{\infty}^{0} \frac{dN_{evt.}}{dN_{ch}} dN_{ch}} = 0.30. \tag{3.10}$$

The experimental example for the ALICE Collaboration using their VZERO detector is provided in Figure 3.1b[7].

3.2.3 IP-GLASMA *initial state model*

The (2+1)-dimensional, boost-invariant IP-GLASMA model [27, 41, 42] is a state-of-the-art, QCD-inspired initial state model within the Colour-Glass-Condensate (CGC) framework. The CGC framework is an effective field theory based on the idea that the hadronic structure depends on the scales probed by the external observer [43]. It argues for a separation of scales for a nucleon travelling with a high velocity: the valence quarks (partons with large x) of our nucleon are highly time-dilated and act as colour-charge sources for the soft (or small x) gluons. Virtual radiations or fluctuations of these valence quarks are also occurring at much larger time scales due to the Lorentz time dilation. A valence quark, then, can radiate a gluon that will go on to radiate another gluon and so on, forming a gluon cascade. Thus going to low-x seems like a mistake: the gluon density is going to explode the lower we go in x[8]. This is where the idea of *gluon saturation* comes in. Gluon recombination processes also become more likely as the number density of gluons increases. The scale at which the two balance each other is the *Saturation Scale* or Q_s. While gluon-saturation has not been directly observed, saturation-based models have been very successful in simulations of HIC. Further studies of gluon saturation are a part of the physics program of the Electron-Ion Collider [44].

The discussion of IP-GLASMA here follows Refs. [42, 45, 46][9] and references therein.

7 The VZERO detector at ALICE is a scintillator array, placed asymmetrically at both ends of the interaction point [40].

8 Refer back to Figure 2.2 where for lower values of the parton momentum fraction x, the gluon is by far the dominant constituent of the proton.

9 In Ref. [46] a (3+1)-dimensional implementation of IP-GLASMA is presented. In this work, the simulated hydrodynamic backgrounds that are used were seeded by a (2+1)-dimensional simulation. This

The initial state of the collision, using IP-GLASMA is simulated first by determining the position of the nucleons via sampling the Woods-Saxon distribution of Equation 3.1. The impact parameter of the collision, b, is also sampled from

$$P(b)db = \frac{2b\ db}{b_{max}^2 - b_{min}^2} \tag{3.11}$$

after which the two nuclei are shifted by $\pm b/2$ in opposite directions. The nuclear thickness functions are computed by summing over the contributions of individual nucleons

$$T_{A_j}(\mathbf{x}) = \sum_{i=1}^{A_j} \frac{1}{2\pi\ B_G} \exp \frac{(\mathbf{x} - \mathbf{x}_i)^2}{2B_G} \tag{3.12}$$

where A_j is the mass number of nucleus A and $B_G = 4\ GeV^{-2}$ is the size of the nucleonic hotspot extracted from deep-inelastic scattering (DIS) data. Once the nuclear thickness function is determined, using the IP-SAT model [47], we can compute the saturation scale at midrapidity

$$Q_s^2 = \frac{\pi^2}{N_c} \alpha_s(\mu^2(r^2))x\ G(x, \mu^2(r^2))T(b) \tag{3.13}$$

where μ is the energy scale, G is the gluon PDF and x its momentum fraction. Finally, $N_c = 3$ is the number of colours. The colour charge density is then sampled across the transverse plane from a Gaussian whose width is proportional to Q_s^2. From the colour charge distribution, gauge fields for each nucleus are computed and evolved using the classical Yang-Mills (CYM) equations

$$[D_\mu, F^{\mu\nu}] = 0 \tag{3.14}$$

where $D_\mu = \partial_\mu + igA_\mu^a t^a$ is the covariant derivative and $F^{\mu\nu}$ the field strength tenosr. The gauges fields are evolved until the start time of the hydrodynamic phase, τ_0. At this point, the energy-momentum tensor is constructed [45]

$$T^{\mu\nu} = -g^{\mu\alpha}g^{\nu\beta}g^{\gamma\delta}F_{\alpha\gamma}F_{\beta\delta} + \frac{1}{4}g^{\mu\nu}g^{\alpha\gamma}g^{\beta\delta}F_{\alpha\beta}F_{\gamma\delta} \tag{3.15}$$

is because while the 3D IP-GLASMA is more physical, it is also significantly more computationally intensive. As such, the tuning and validation of the runs are, at this point, computationally prohibitive. Furthermore, as stated before, a boost invariant approximation is valid in heavy ion collision and has been very successful.

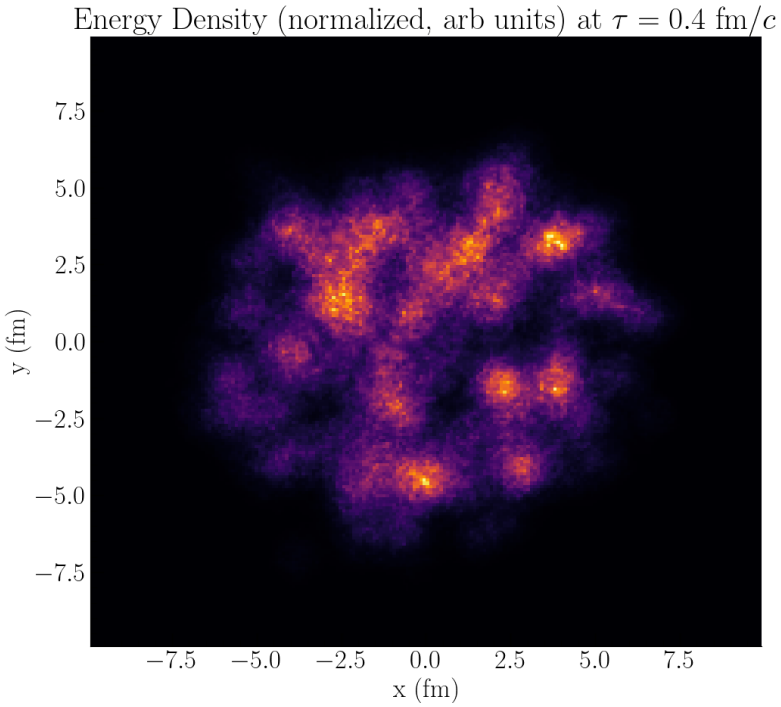

Figure 3.2: Example of an initial energy density profile generated using IP-GLASMA for a head-on Pb-Pb collision at 2.76 ATeV.

and diagonalized

$$T^{\mu\nu}u^{\nu} = \epsilon u^{\nu} \tag{3.16}$$

where u^{μ} is the local flow velocity and ϵ the local energy density. Finally, $T^{\mu\nu}$ is separated into ideal and viscous components and used to initialize the hydrodynamic evolution. This process is called *Landau Matching*. An example of an initial profile from IP-GLASMA is shown in Figure 3.2. This energy density profile is evolved to $\tau = 0.4$ fm/c, the start time of the hydrodynamic evolution in the IPG-M model.

3.2.4 TRENTO *initial state model*

The Thickness (Reduced) Event-by-event Nuclear Topology or TRENTO [25] is a parametric initial state model. The model uses a smoothly varying parameter, p, in computing the reduced thickness function

$$T_R(p; T_A, T_B) = \left(\frac{\hat{T}_A^p + \hat{T}_B^p}{2} \right)^{1/p} \tag{3.17}$$

where $\hat{T}_A$ and $\hat{T}_B$ are the *participant* thickness functions of the nuclei involved in the collision, A and B. These are given by [25]

$$\hat{T}_{A,B} = \int dz \rho^{\text{part.}}_{A,B}(x, y, z) \tag{3.18}$$

with $\rho^{\text{part.}}_{A,B}$ being the density of the nucleus that participates in inelastic collisions. The idea is that the reduced thickness function, T_R, is the deposited energy in the collision and is some function of the respective thickness functions of the colliding nuclei. By having the smoothly varying parameter p, then, one can probe different models of initial state models and how they deposit the energy[10]. TRENTO constructs the thickness function of each nucleus via

$$\hat{T}_{A,B}(x, y) = \sum_{i}^{N_{\text{part.}}} u_i T_p(x - x_i, y - y_i) \tag{3.19}$$

where x_i and y_i are the transverse plane positions of the nucleon, sampled from the Woods-Saxon distribution of Equation 3.1 and u_i are fluctuation factors, included to account for the large fluctuations that are observed in p-p collisions [21]. The values for the u_i are sampled from a Gamma distribution

$$P_k(u) = \frac{k^k}{\Gamma(k)} u^{k-1} e^{-k\,u} \tag{3.20}$$

where k is the shape parameter, related to the standard deviation of nucleon multiplicity fluctuations [21]. The participant thickness function, T_p, is given by a Gaussian characterized by nucleon width w

$$T_p(x, y) = \frac{1}{2\pi\, w^2} \exp -(\frac{x^2 + y^2}{2w^2}). \tag{3.21}$$

There are also other parameters in the TRENTO model, such as the minimum distance of the nucleons when sampling the Woods-Saxon distribution or the overall normalization factor for energy (or entropy) deposition. Through all of this, the TRENTO model aims to provide an initial state model that is agnostic on the exact physical mechanisms of entropy production, thermalization or pre-equilibrium dynamics. The simplicity and the parametric nature of the model have made it a (nearly) universal choice for generating initial states for hydrodynamic simulations, with particular application in Bayesian studies of the QGP [21, 22, 48–51]. Here, TRENTO is used within a JETSCAPE workflow and only for event-averaged simulations. An example for such initial profiles in event-averaged mode is given in Figure 3.3.

10 See Chapter 4 of Ref. [11] for a thorough discussion on the caveats of using TRENTO.

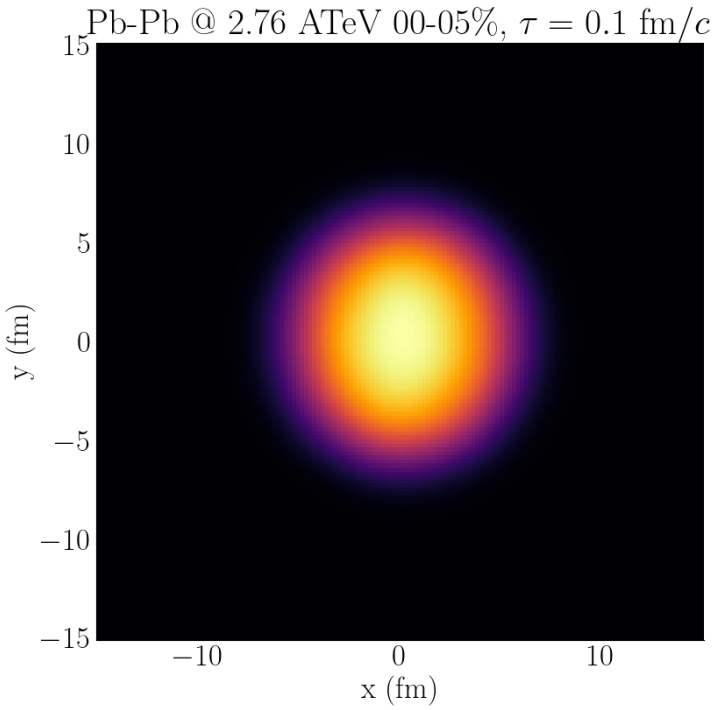

Figure 3.3: Example of the initial energy density profile generated by the TRENTO model for `Pb-Pb` collisions at 2.76 ATeV at 0-5% centrality class. For this figure, 500 profiles were generated and averaged to produce the profile.

3.3 PRE-EQUILIBRIUM STAGE

Once the initial conditions are generated, they have to be evolved through the pre-equilibrium stage until the onset of hydrodynamics. Examples of models designed connect the initial state to the hydrodynamic stage are KøMPøST [52] and free-streaming [53, 54]. KøMPøST seeks to smoothly connect the microscopic description of the initial state to the macroscopic description of later evolution governed by hydrodynamics. An alternative approach is to use free-streaming and evolve the initial conditions, without interactions, up to the start time of the hydrodynamics.

Free-streaming is used in the T-V model for the soft-sector event backgrounds used here. KøMPøST, is not used as a part of soft-sector modelling. The contribution of KøMPøST is its input to the photon spectra that are calculated from the pre-equilibrium stage. As discussed in Chapter 1, the evolving QGP can be a source of photons, both in the hydrodynamic and pre-equilibrium stages. In Chapter 5 and

Chapter 6, the contribution of jet-medium photons to the direct photon spectra is analyzed. Therefore it is necessary to include pre-equilibrium and thermal photon spectra for completeness. The spectra are taken from Ref. [55], and were generated using a KøMPøST background.

3.3.1 *Free-streaming*

Free-streaming is an approach which mimics the pre-equilibrium state, based on the idea that the initial state is an infinitely weakly coupled system [56]. It assumes the coupling to be zero and the system to be a collection of noninteracting, massless partons [21, 53, 54]. Free-streaming takes the output of TRENTO and interprets it as the density of partons in the transverse plane. The partons are then assumed to travel at the speed of light, without further interactions and are evolved for some time, τ_{FS}. This is the only parameter of the model whose value can (and indeed has been) learned from data to be close to 1 fm/c [21]. At the end of the free streaming process, the stress-energy tensor is matched to the hydrodynamic one using the same Landau matching condition described for IP-GLASMA.

3.3.2 KøMPøST

In contrast to free-streaming, KøMPøST [52, 57] is designed to smoothly match the initial condition to the hydrodynamic stage within a weakly-coupled kinetic theory approach. It uses non-equilibrium linear response theory [58] to evolve the energy-momentum tensor from its non-equilibrium form up to the onset of hydrodynamics. The stress-energy tensor for a given spacetime point $(\tau, \mathbf{x})$ is decomposed into a segment that is averaged over the causally connected part and perturbations [55]

$$T^{\mu\nu}(\tau, \mathbf{x}) = \bar{T}^{\mu\nu}(\tau, \mathbf{x}) + \delta T^{\mu\nu}(\tau, \mathbf{x}) \tag{3.22}$$

The two components are then evolved using response functions, computed within a purely gluonic QCD.

As explained previously, the only input of the KøMPøST pre-equilibrium model into this work is the pre-equilibrium photons calculated in Ref. [55]. The calculation is

done with the same steps as photon calculations from the hydrodynamic stage. The stress-energy tensor is decomposed into energy density, flow velocity and viscous components. An *effective* temperature is calculated from the energy density using the QCD equation of state, and the equilibrium photon emission rates are then folded with this information.

Photon production requires a quark population since gluons are not charged under QED and do not couple directly to photons. A purely gluonic QCD can dynamically generate quarks via gluon scatterings as the system evolves towards equilibrium. To model this behaviour, Ref. [55] uses the equilibrium quark distribution (Fermi-Dirac distribution) multiplied by a time-dependent suppression factor characterized by a chemical equilibration time, τ_{chem} with chemical equilibrium defined as the time at which this suppression factor reaches 0.9 [59]. This accounts for low quark population density at the early times and their rising population as we approach the hydrodynamic stage. The pre-equilibrium photon spectra used in this work are the $\tau_{\text{chem.}} = 1$ fm/c spectra of Ref. [55]. The relevant physical scale of the pre-equilibrium matter is the effective temperature which in the very early stages of the simulation is less than 1 GeV and falls rapidly. Thus the contribution of these photons is most significant for lower values of transverse momenta, and they are not a significant source of high-p_T photons.

3.4 RELATIVISTIC HYDRODYNAMICS

We have arrived at the hydrodynamic stage. Relativistic hydrodynamics is the model used for the collective expansion of the QGP. It is a macroscopic theory which deals with average thermodynamic quantities. Here only a summary of the basic equations used in the simulations is provided. The discussion of this section closely follows Refs.[21, 60].

All hydrodynamic simulations aim to solve

$$\partial_\nu T^{\mu\nu} = 0 \tag{3.23}$$

which is simply a conservation equation for the energy and momentum of the system. When at local thermal equilibrium, we can write the stress-energy tensor as

$$T^{\mu\nu} = T^{\mu\nu}_{\text{ideal}} = (\epsilon + P)u^{\mu}u^{\nu} - Pg^{\mu\nu} \tag{3.24}$$

where as before, u^{μ} is the local flow velocity with $u^{\mu}u_{\nu} = 1$, ϵ the local energy density and P the pressure. There are four equations in Equation 3.23 while there are five unknowns to solve for: three in the flow velocity and two for energy density and pressure. The system of equations and unknowns is closed using the equation of state (EOS) to connect the pressure to energy density.

When out of local thermal equilibrium, the stress-energy tensor is modified to account for the energy dissipation,

$$\begin{aligned} T^{\mu\nu} &= T^{\mu\nu}_{\text{ideal}} + T^{\mu\nu}_{\text{viscous}} \\ T^{\mu\nu}_{\text{viscous}} &= \pi^{\mu\nu} + \Delta^{\mu\nu}\Pi \end{aligned} \tag{3.25}$$

where $\pi^{\mu\nu}$ is the (traceless) shear viscous tensor and Π the bulk pressure. The projection tensor is also defined as $\Delta^{\mu\nu} = g^{\mu\nu} - u^{\mu}u^{\nu}$. These introduce 16 new components and unknowns, which must be solved for 15 from $\pi^{\mu\nu}$ and one for the bulk viscous pressure. Given the freedom in choosing the definition of u^{μ}, we can choose the Landau frame where u^{μ} is defined as the velocity of energy transport

$$u_{\mu}T^{\mu\nu} = \epsilon u^{\nu}. \tag{3.26}$$

which leads to the relation $u_{\mu}\pi^{\mu\nu} = 0$. These relations, coupled with the requirement that shear viscous tensor is traceless and symmetric, leaves only six additional degrees of freedom, five from $\pi^{\mu\nu}$ and one from the bulk viscous pressure. We can now take the first order in deviation from local thermal equilibrium, which leads to the Navier-Stokes theory [61]

$$\begin{aligned} \pi^{\mu\nu} &= 2\eta\sigma^{\mu\nu} \\ \Pi &= -\zeta\theta \end{aligned} \tag{3.27}$$

where η and ζ are shear and bulk viscosities, $\theta = \partial_{\mu}u^{\mu}$ is the expansion rate and $\sigma^{\mu\nu} = \partial^{<\mu}u^{\nu>}$ is the Navier-Stokes tensor. The angular brackets denote the traceless part of the symmetrized tensor. The Navier-Stokes tensor, in expanded form, is written as

$$\partial^{<\mu}u^{\nu>} = \frac{1}{2}(\partial^{\mu}u^{\mu} + \partial^{\nu}u^{\mu} - \frac{2}{3}\Delta^{\mu\nu}\partial^{\alpha}u_{\alpha}). \tag{3.28}$$

In the above equations, the instantaneous connection between the fluid flow and viscous pressures leads to superluminal flow and acausality [62]. This issue was resolved[11] by the introduction of the first relativistic viscous hydrodynamics by Müller, Israel and Stewart. By including terms up to the second order in the gradient expansion [64, 65] they introduced relaxation-time type equations for the viscous corrections,

$$\begin{aligned}\tau_\pi \dot{\pi}^{<\mu\nu>} + \pi^{\mu\nu} =& 2\eta\sigma^{\mu\nu} - \frac{4}{3}\pi^{\mu\nu}\theta \\ \tau_\Pi \dot{\Pi} =& -\zeta\theta - \frac{2}{3}\tau_\Pi \Pi\theta\end{aligned} \tag{3.29}$$

where τ_π and τ_Π are the relaxation times of the shear and bulk viscosities, respectively. The dot above a variable denotes the proper time derivative ($\dot{\pi} = u^\mu \partial_\mu \pi$). The variant of the Müller-Israel-Stewart used by the hydrodynamic models used here is the kinetic-theory-based formulation of by Denicol, Niemi, Molnar, and Rischke called DNMR hydrodynamics [66–68]. The DNMR equations read

$$\begin{aligned}\tau_\pi \dot{\pi}^{<\mu\nu>} + \pi^{\mu\nu} &= 2\eta\sigma^{\mu\nu} - \frac{4}{3}\tau_\pi \pi^{\mu\nu}\theta + \frac{9}{70P}\pi_\alpha^{<\mu}\pi^{\nu>\alpha} - \frac{10}{7}\tau_\pi \pi_\alpha^{<\mu}\sigma^{\nu>\alpha} + \frac{6}{5}\tau_\pi \Pi\sigma^{\mu\nu} \\ \tau_\Pi \dot{\Pi} + \Pi &= -\zeta\theta - \frac{2}{3}\tau_\Pi \Pi\theta + \frac{8}{5}\left(\frac{1}{3} - c_s^2\right)\tau_\Pi \pi^{\mu\nu}\sigma_{\mu\nu}.\end{aligned} \tag{3.30}$$

The relaxation times, τ_π and τ_Π provide a time scale over which the dissipative modes decay and their values are derived as [68]

$$\begin{aligned}\tau_\pi =& \frac{5\eta}{\epsilon + P} \\ \tau_\Pi =& \frac{\zeta}{(\epsilon + P)} \frac{1}{14.55(1/3 - c_s^2)}\end{aligned} \tag{3.31}$$

where c_s is the speed of sound in the medium. When these relaxation times are zero, we recover the Navier-Stokes hydrodynamics. All transport coefficients have been written in terms of known quantities and η and ζ, the two transport coefficients of interest. In this work, the medium temperature evolution profiles are generated by two main hydrodynamic models: MUSIC [69], VISHNU [48, 61, 70]. Both models are numerical solutions to equations discussed above and differ only in their numerical

11 There are still some acausality issues in hydrodynamic simulations and it is an active area of research, see for example [63].

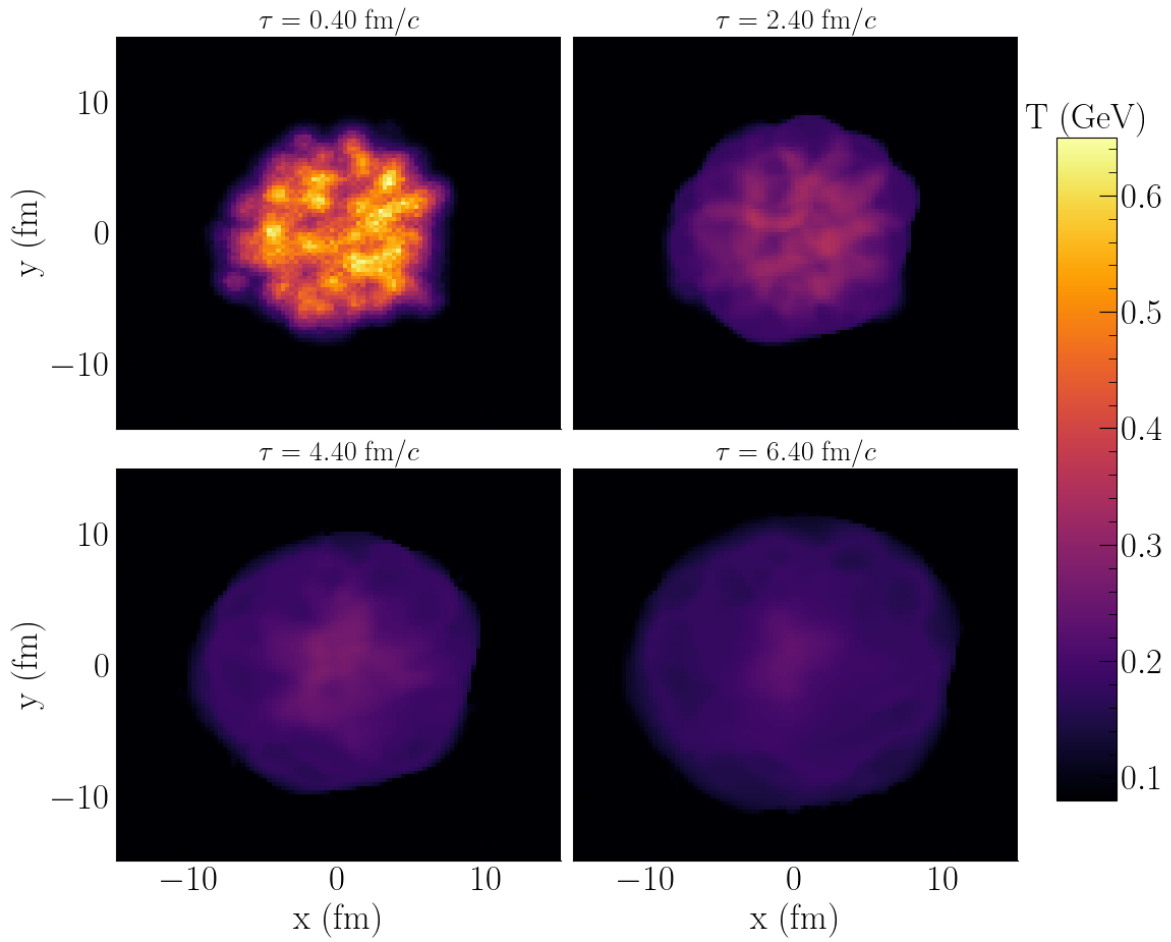

Figure 3.4: Example of a (3+1)-dimensional MUSIC simulation of Pb-Pb collisions at 2.76 ATeV, for a highly central event belonging to the 0-5% centrality class. The plotted profiles are of the midrapidity slice $\eta = 0$ at four different times.

implementation. On the physics side, the only difference is the choice of the implementation of viscous corrections and their functional forms (see Figure 3.5). MUSIC chooses a fixed value for the shear viscosity to entropy density ratio [12], $\eta/s = 0.13$, which is motivated by phenomenological studies [69, 71, 72]. The bulk viscosity to entropy density used by MUSIC was parametrized in Ref. [73] and is given by

$$\zeta/s(x) = \begin{cases} A_1 x^2 + A_2 x - A_3 & (0.995T_c \leqslant T \leqslant 1.05T_c) \\ \lambda_1 e^{\frac{1-x}{\sigma_1}} + \lambda_2 e^{\frac{1-x}{\sigma_2}} + 0.001 & T > 1.05T_c \\ \lambda_3 e^{\frac{x-1}{\sigma_3}} + \lambda_4 e^{\frac{x-1}{\sigma_4}} + 0.03 & T < 0.995T_c \end{cases} \tag{3.32}$$

12 The values and the functional form of the viscosities implemented in either hydrodynamic model, MUSIC or VISHNU, is purely a choice. The models can be used with any parameterization or value for the viscous corrections.

where $x \equiv T/T_c$. The parameters are fitted to data from lattice QCD [74] and hadron resonance gas [75] and are given by

$$\begin{aligned} &A_1 = -13.77,\ A_2 = 27.55,\ A_3 = 13.45 \\ &\lambda_1 = \lambda_3 = 0.9,\ \lambda_2 = 0.25,\ \lambda_4 = 0.22 \\ &\sigma_1 = 0.025,\ \sigma_2 = 0.13,\ \sigma_3 = 0.0025,\ \sigma_4 = 0.022 \end{aligned} \tag{3.33}$$

The critical temperature, T_c is taken to be 180 MeV in MUSIC simulations used in this work. While the parameters presented here are the results of phenomenological studies, the Bayesian analysis of Ref. [23], which sought to extract the various parameters of an IP-GLASMA(2+1)D coupled to a MUSIC(2+1)D simulation from HIC data has found similar values for viscous corrections. The parameters of the current implementation of viscous corrections in VISHNU were tuned in the Bayesian analysis of Ref. [22].

The parametrization on the shear viscosity to entropy density is given by

$$\begin{aligned} \eta/s(T) =& (\eta/s)_{\text{min}} + (\eta/s)_{\text{slope}}(T - T_c)(T/T_c)^{(\eta/s)_{\text{crv}}} \\ \zeta/s(T) =& \frac{(\zeta/s)_{\text{max}}}{1 + (\frac{T-(\zeta/s)_{T_0}}{(\zeta/s)_{\text{width}}})^2} \end{aligned} \tag{3.34}$$

where the maximum a posteriori values for the parameters introduced were found to be

$$\begin{aligned} &(\eta/s)_{\text{min}} = 0.081,\ (\eta/s)_{\text{slope}} = 1.11\ \text{GeV}^{-1},\ (\eta/s)_{\text{crv}} = -0.48 \\ &(\zeta/s)_{\text{max}} = 0.052\ (\zeta/s)_{T_0} = 183\ \text{MeV},\ (\zeta/s)_{\text{width}} = 0.022\ \text{GeV}. \end{aligned} \tag{3.35}$$

The events used in this thesis for jet energy loss simulations are generated using both hydrodynamic models. While VISHNU is in (2+1)-dimensions only, MUSIC can generate (2+1)D and (3+1)D simulations. An example of the hydro temperature profile at midrapidity for Pb-Pb collisions at 2.76 ATeV is given in Figure 3.4 for simulations performed using MUSIC. The temperature dependence of the specific shear and bulk viscosities discussed above is provided in Figure 3.5. The significant difference observed in the viscosities are largely functions of the modelling choices made during their extractions [11]. Finally, the thermal photon spectra emitted from the hadronic gas and the QGP were computed in Ref. [55], using an IPG-M model, and it is this thermal photon spectrum that is used throughout the thesis when the total direct photon yield is presented.

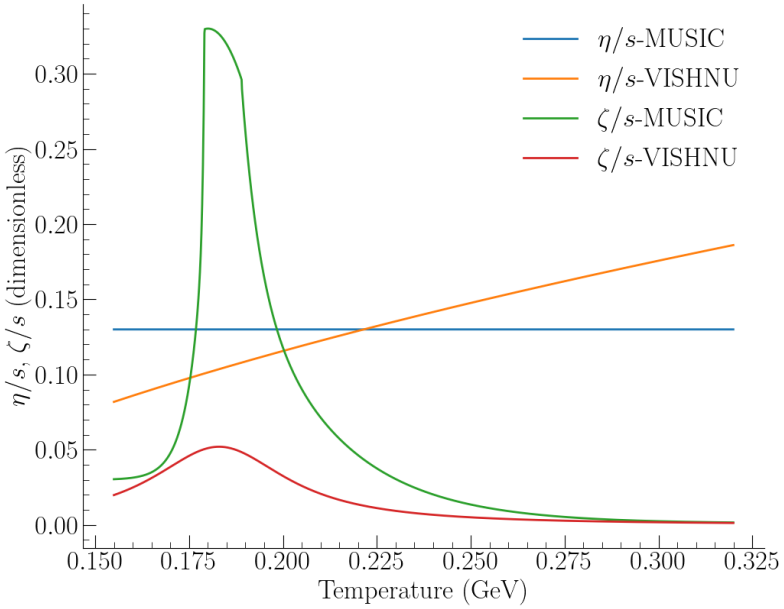

Figure 3.5: Temperature dependence of the specific shear (η/s) and bulk (ζ/s) viscosities implemented in IPG-M model (MUSIC) and T-V model (VISHNU).

3.5 PARTICLIZATION AND TRANSPORT

The hydrodynamic evolution continues until the mean free path is large enough that both hydrodynamics and transport become reasonable ways of modelling the medium. This is also around the time that confinement causes the relevant degrees of freedom of the system to transition from quarks and gluons to hadrons. The transition is modelled to occur at a switching temperature, T_{sw}. Above this temperature, $T > T_{sw}$, hydrodynamics is taken to be the model of the evolution of the system while $T < T_{sw}$ is seen as a microscopic system whose evolution is governed by transport. The process of converting the hydrodynamic prescription and preparing the medium for transport is *particlization*. A general overview of the process is provided in what follows, loosely following the discussion of Refs. [11, 21, 60].

The current standard in particlization is the Cooper-Frye prescription [70, 76]. The idea is to construct isothermal hypersurfaces and describe the differential particle yield from a hypersurface as

$$E\frac{dN}{d^3p} = \frac{\mathcal{N}}{(2\pi)^3}\int_\sigma f(x,p)p_\mu d\Sigma^\mu \tag{3.36}$$

where $\mathcal{N}$ is the particle degeneracy and $f(x,p)$ the phase-space distribution. The integral is over the hypersurface σ, and $d\Sigma^\mu$ is the differential surface four-vector. At

equilibrium, the Bose-Einstein or Fermi-Dirac gives the phase-space distribution, as appropriate for the hadron. Out of equilibrium, the distribution function is broken up into its equilibrium and viscous components [60]

$$f = f_{\text{equilibrium}} + \delta f_{\text{shear}} + \delta f_{\text{bulk}}. \tag{3.37}$$

The viscous corrections can be evaluated in different ways. Two methods of doing so are the Relaxtion Time Approximation [77] or the Grad's 14 moment [78] approach.

After the particlization process, a Boltzmann transport model is used to further evolve the sampled hadrons, including their rescatterings and decays until the system is kinetically frozen out. The most popular implementation is that of UrQMD [79, 80]. It solves the relativistic Boltzmann equation

$$p^{\mu}\partial_{\mu}f_i(x,p) = \mathcal{C}[f_i] \tag{3.38}$$

where $f_i(x,p)$ is the phase space distribution of the hadron type i and $\mathcal{C}$ is the collision kernel, encoding the elastic and inelastic scatterings. It is via the collision kernel that the phase space distributions of the different hadrons become coupled to each other. UrQMD then propagates the hadrons along classical trajectories and allows for collisions. It also accounts for resonance formation and decay. The evolution ends once the hadron density is so low that collisions can no longer occur, and the hadrons have undergone kinetic freezeout.

Part II

JET QUENCHING IN HEAVY ION COLLISIONS

4

JET-QUENCHING: AN OVERVIEW

Jets produced from hard scatterings of constituent hadrons in heavy ion collisions encounter a QGP medium as they leave the interaction point. The hard partons then lose energy via their interactions with the thermal medium. The modelling of jet quenching requires an understanding of the physics of very different scales:

A. hard parton generation via high p_T collisions

B. time evolution of the QGP

C. jet-medium interactions of partons traversing the QGP

D. transition at temperature T_c where jets decouple from the medium and hadronize.

Our current understanding of jet energy-loss indicates two dominant channels available to a high-p_T parton: collisional and radiative energy loss. The first work on the quenching of jets in a QGP medium was done by Bjorken [81] with a focus on collisional energy loss, and the effect was found to be significant for intermediate transverse momentum ($p_T \leqslant 30$GeV, approximately) partons. Further work on this topic was done in Refs. [82–89]. It is now accepted that while radiation is the dominant mode of energy loss for light quarks and the gluon, elastic scatterings modify the evolving parton spectrum in a non-trivial way [89] and affect final observables such as jet-shape and charged hadron fragmentation functions within jets.

Radiative energy loss via gluon bremsstrahlung is the dominant mode of energy loss for an energetic parton. A number of different radiative energy loss approaches have been proposed [90–96] to model this process with different sets of assumptions. There have been previous attempts at systematic comparisons of these models [97] in a QGP brick: the idealized QGP environment which is static and at a fixed temperature, and allows for comparative studies of the rates of emission and for understanding the average path length dependence. Moving from an idealized brick to an evolving QGP, however, has been more challenging. This is due to the practical

approximations and assumptions that had to go into how the formalisms were implemented. These assumptions include the initial jet profile that would be fed into the calculation, the hydrodynamic background that the jets would travel through[1], the hadronization scheme to be applied and finally, the jet-clustering algorithm to be used. The JETSCAPE collaboration sought to create a modular approach to jet simulation in heavy ion collisions and thus to enable a direct and faithful comparison between various jet-quenching models. The modularity of JETSCAPE then allows for the creation of multi-stage models, where different regimes of a hard parton's evolution through the medium can be modelled separately and with significant control over the details of the evolution. As it will be shown in the following two chapters, particularly in Chapter 5, multi-stage modelling is essential in the successful and simultaneous description of different hard probes.

Here JETSCAPE is used for two tasks

A. the first comparative analysis of two jet quenching models: MARTINI and CUJET in the context of Monte Carlo simulation

B. the study of the effects of single vs. multi-stage modelling of jet energy loss in realistic simulations.

The structure of the rest of the thesis, then, would be as follows: this chapter will deal with the theory behind CUJET and MARTINI. Chapter 5 is dedicated to the new phenomenological study of the higher order collision kernels in MARTINI and their effect on hadronic observables and jet-medium photon spectra. Chapter 6 presents the novel and state-of-the-art multi-probe, multi-system comparative analysis of CUJET and MARTINI in a JETSCAPE workflow.

It should be noted that recent works on jet energy-loss in the pre-equilibrium stage indicate the possibility of significant quenching of high-p_T jets [98]. Energy loss of jets in the initial stages is not considered in this work beyond what is done via MATTER, and only in Chapter 6.

1 This includes the modelling of the initial, pre-equilibrium state as well.

4.1 COLLISIONAL ENERGY LOSS

In collisional energy loss (or elastic scattering) reactions, the identity of the hard parton[2] is conserved while its momentum receives minor modifications. These are t-channel-dominated processes where the energetic parton exchanges a space-like gluon. One can also have processes where a space-like quark (or anti-quark, depending on the identity of the partons involved) is exchanged. However, the fermion-mediated processes are not identity-preserving and will be discussed in Section 4.3.

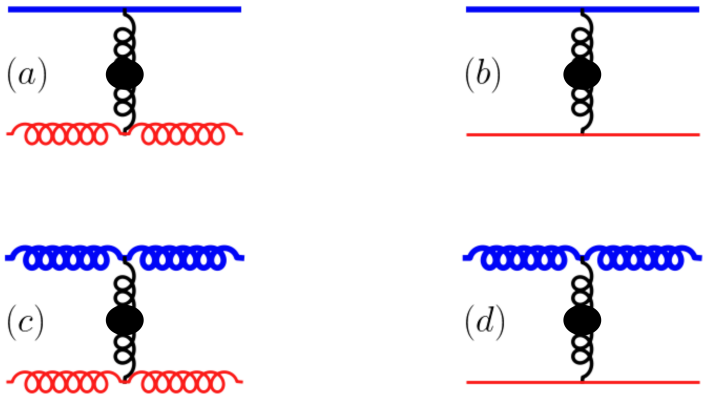

Figure 4.1: Elastic scattering channels for quarks, anti-quarks and gluons. The blue line denotes the hard parton, while the red is reserved for soft particles. The black lines with a circle are the internal, *dressed* propagators. Solid lines denote quarks or anti-quarks, and curly lines are the gluons. See text for details.

Figure 4.1 shows the $2 \to 2$ elastic scattering channels open to QCD fermions and bosons in the QGP where figures (a) and (b) show the possible scattering channels of a quark or anti-quark while (c) and (d) are the channels available to gluons. The solid lines can be either quark or anti-quark. To calculate the cross-section of these processes, we need to regulate the infrared divergence of the internal propagator for small momentum exchanges. At finite temperatures, gauge fields acquire a *thermal* mass $m_g \approx gT$ [99]. When the momentum of the internal propagator is of this same order, then all effects of $\mathcal{O}(T)$ need to be re-summed to get a *dressed* propagator [100]. This procedure is known as the *Hard Thermal Loops* (HTL) resummation and was

2 *Hard* partons are distinguished from the soft, medium background by some cut on their momentum $p > p_{cut}$. Typically this cut is related to the local temperature, T.

performed by Braaten and Pisarski in Refs. [101–103], Frenkel and Taylor in Refs. [104, 105] and Taylor and Wong in Ref. [106] to dress the propagators inside a medium.

4.1.1 *Collisional Energy Loss in* MARTINI

MARTINI uses the elastic scattering channels of Figure 4.1 and regulates the divergence by taking the re-summed HTL gluon propagator when computing the matrix elements. The implementation of elastic energy loss in MARTINI follows the original work in Ref. [89]. More recently, Ref. [107] added the ability to promote a medium particle to a hard parton (called *recoil* partons) in case of large momentum transfers. Presented here is the approach of Ref. [89] in calculating transition rates from elastic scattering[3]. In the massless (or ultra-relativistic) limit, the general expression for the transition rate of a $2 \to 2$ process is given by

$$\frac{d\Gamma_{\text{elas.}}}{d\omega} = d_2 \int \frac{d^3p_2}{(2\pi)^3}\frac{d^3p_4}{(2\pi)^3}\frac{2\pi}{16p_1p_2p_3p_4}\delta(p_1 - p_3 - \omega)\,\delta(p_4 - p_2 - \omega) \times |\mathcal{M}|^2 f_2(p_2, T)\,(1 \pm f_4(p_4, T)) \tag{4.1}$$

where the lower case p_i is the magnitude of the three-momenta of particle i and f_i is the distribution function, Bose-Einstein or Fermi-Dirac, depending on the particle species. The plus or minus sign $(\pm)$ accounts for Bose-enhancement $(+)$ or Pauli-blocking $(-)$. d_2 is the spin, colour and flavour degeneracy factor of the thermal particle. The integration is performed using the technique proposed by Ref. [108, 109], where the p_2 integral is replaced by an integral over the exchanged three momentum, $\mathbf{q} = \mathbf{p}_1 - \mathbf{p}_3$. Allowing $\mathbf{q}$ to define the z-axis, restricting the incoming parton to the x-z plane and taking the ultra-relativistic limit for the incoming parton ($p_1 \to \infty$) enables us to write

$$\frac{d\Gamma_{\text{elas.}}}{d\omega}(p, \omega, T) = \frac{d_2}{(2\pi)^3}\frac{1}{16p^2}\int_0^p dq \int_{\frac{q-\omega}{2}}^{\infty} dp_2\,\Theta(q - |\omega|) \times \int_0^{2\pi}\frac{d\phi_{p_2q|pq}}{2\pi}|\mathcal{M}|^2 f_2(p_2, T)(1 \pm f_4(p_2 + \omega, T)) \tag{4.2}$$

where p was re-defined $p \equiv p_1$. The angle $\phi_{p_2q|pq}$ is the angle between the planes defined by $\mathbf{p}_2 \times \mathbf{q}$ and $\mathbf{p} \times \mathbf{q}$. The Heaviside step function (Θ) ensures that the mo-

3 Specifically it is *Method B* of Ref. [89] that is discussed here and implemented in MARTINI.

mentum transfer is space-like. Ref. [89], which is the basis for elastic rates implemented in MARTINI performed the calculation in two ways, demonstrating that they are equivalent

A. break the integration domain with $q^* \approx \mathcal{O}(T)$

- use bare propagator for hard momentum transfers $q > q^*$
- used HTL re-summed gluon propagator for soft momentum transfers $0 < q < q^*$

then carefully match the two computations.

B. use the HTL re-summed propagator of the gluon throughout.

MARTINI implements the second method where the HTL re-summed gluon propagator is used to compute the matrix element. The Coulomb gauge propagator is given by [101, 102]

$$D^{\mu\nu}(Q^\alpha) = \delta^{\mu 0}\delta^{\nu 0}\Delta_L(\omega, q) + P_T^{\mu\nu}\Delta_T(\omega, q) \tag{4.3}$$

where $P_T^{\mu\nu}$ is the transverse projector operator with components

$$P_T^{00} = 0, \quad P_T^{ij} = \delta^{ij} - \hat{q}^i\hat{q}^j. \tag{4.4}$$

The four-vector $Q^\alpha = (\omega, \mathbf{q})$ is the momentum flowing through the gluon. Finally, Δ_L and Δ_T are, respectively, the longitudinal and transverse propagators of the gluon

$$\Delta_T(\omega, q) = \frac{1}{F_T - Q^2}, \quad \Delta_L(\omega, q) = \frac{1}{F_L - Q^2}\frac{Q^2}{q^2}. \tag{4.5}$$

The expressions for F_L and F_T are

$$\begin{aligned} F_L &= 2m_D^2(1-x^2)(1 - xQ_0(x)) \\ F_T &= m_D^2 - \frac{1}{2}F_L \end{aligned} \tag{4.6}$$

with $x \equiv \omega/q$. m_D is the gluon Debye mass

$$m_D^2 = \frac{1}{6}\left(N_c + \frac{N_f}{2}\right)g^2T^2 \tag{4.7}$$

where N_c and N_f are the numbers of colours and flavours in the theory, respectively. $Q_0(x) = \frac{1}{2}\log\left(\frac{1+x}{1-x}\right)$ is the Legendre function. The propagator of Equation 4.3 is then

used in calculating the matrix element squared of Equation 4.2. The matrix element is taken to the soft momentum transfer limit $q \sim gT$. Elastic channels present in MARTINI are presented in Figure 4.1. The rates for each channel are then computed using the HTL re-summed gluon propagator, tabulated and read into MARTINI at run time.

As the hard parton travels through the medium and interacts via elastic scatterings, it deposits energy into the medium. This jet-induced flow is correlated with the hard parton and travels alongside the jet. Its effect is enhanced production of soft hadrons along the main jet axis. MARTINI uses the kinetic theory approach where the jet is scattering off of and transferring energy/momentum to a thermal particle from the medium [107]. The distinction between a hard, jet parton and a soft, medium particle is made using a momentum cut, p_{cut}. Partons with energies larger than this value are considered hard, while those below are taken to be indistinguishable from the medium. The value of this cut is then a parameter that can be varied and can be seen as either fixed ($p_{cut} = 2$ GeV, for instance) or as a multiple of local temperature, $p_{cut} = n\,T$ where n is some number[4]. A medium particle that receives enough energy as a scattering partner of a jet parton and passes the momentum cut will then be treated as another jet and evolved accordingly. To conserve energy and momentum, the *hole* that is left in the medium is allowed to free-stream, hadronize and then be subtracted at the analysis stage.

Figure 4.2 shows the elastic scattering rate for the four channels implemented in MARTINI for a fixed temperature ($T = 300$ MeV, left) and a fixed jet momentum ($p = 20$ GeV, right). The dotted lines in the figure are the elastic rates evaluated for a fixed $\alpha_s = 0.3$ while the solid lines are with a running coupling[5]. The shaded region on the left side is momenta that are below p_{cut}, which for this plot is chosen to be 2 GeV. In the figures, we can see that the relative position and general behaviour of the total elastic rates are as expected:

1. parton travelling through a high-temperature plasma would experience more elastic scattering than plasma at a lower temperature,

4 For the MARTINI vs. CUJET comparison work, $p_{cut} = 2$ GeV is used for both models. In simulations comparing the effect of collision kernels, $p_{cut} = 4T$ was used.

5 See Section 4.4 for the discussion on running coupling of MARTINI and Section 4.2.1 for CUJET.

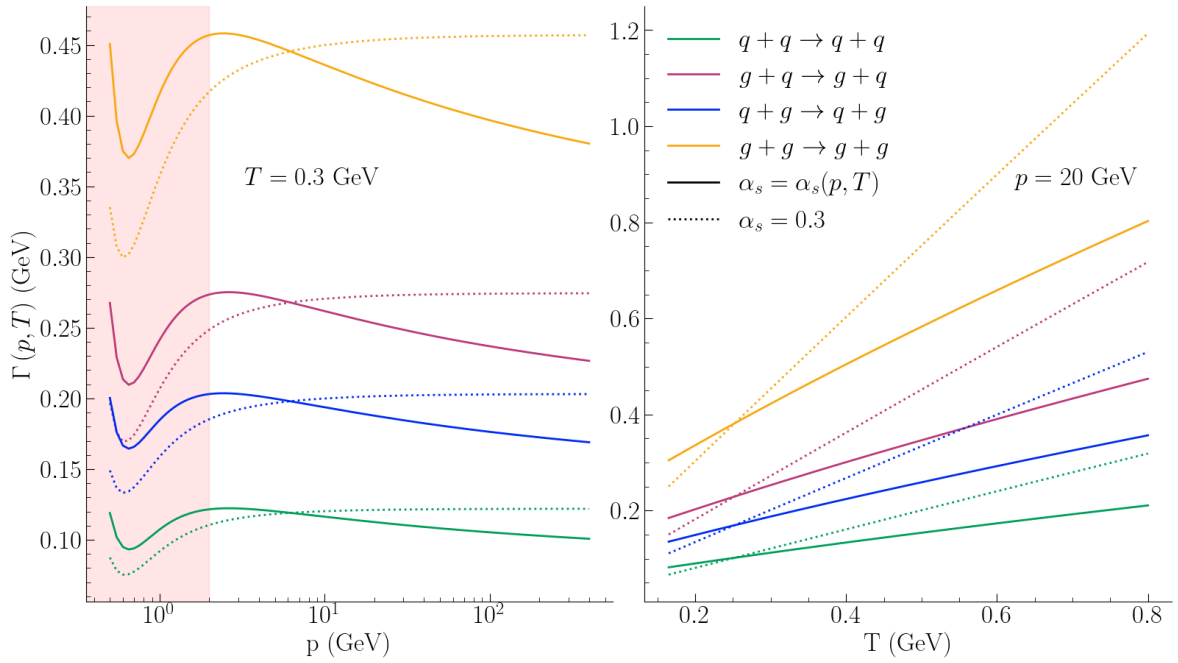

Figure 4.2: Elastic scattering rates implemented in MARTINI for temperature fixed to $T = 0.3$ GeV (left) and momentum fixed to $p = 20$ GeV (right). The solid lines are elastic rates, including the effect of the running coupling, while the dotted lines are for a fixed α_s. The shaded red region denotes momenta $p < p_{cut}$ where in this plot, it is set to $p_{cut} = 2$ GeV. For the solid lines, the elastic running coefficient is set to $\kappa_e = 4.5$ (see Equation 4.39 for the definition).

2. owing to their much larger Casimir factors, hard gluons experience more energy loss than quarks.

4.1.2 *Collisional energy-loss in* CUJET

CUJET employs the Thoma-Gyulassy model [82]. Unlike MARTINI where a dressed gluon propagator is used to regulate the divergences for all values of the momentum exchange, CUJET uses the vacuum gluon propagator and approximates the thermal effects by using the gluon Debye mass as the regulator. The differential scattering cross-section is given by

$$\frac{d\sigma_{i,j}}{dt} = \frac{2\pi\alpha_s^2}{(t+m_D^2)^2} c_{i,j} \tag{4.8}$$

where subscripts i and j denote the identities of the jet parton and the medium particle, respectively. The momentum exchange variable, the Mandelstam t, is the same

Table 4.1: Colour factors used in CUJET modelling of elastic scatterings. Subscripts i and j are used to denote the hard and soft parton, respectively.

Scattering Partons	$c_{i,j}$
q, q	$4/9$
q, g	1
g, g	$9/4$

as before, and m_D^2 is the square of the gluon Debye mass, given by Equation 4.7. The numerical constants $c_{i,j}$ are the colour factors, presented in Table 4.1. The total elastic scattering rate is given by a convolution of the differential cross-section and the thermal distribution function of the medium particle

$$\Gamma_{\text{elas.}}(p, T) = \sum d_j \int \frac{d^3\mathbf{p_2}}{(2\pi)^3} f_2(p_2, T) \int dt \frac{d\sigma_{i,j}}{dt} \tag{4.9}$$

where d_j is the degeneracy factor of the thermal parton. There are two significant dif-

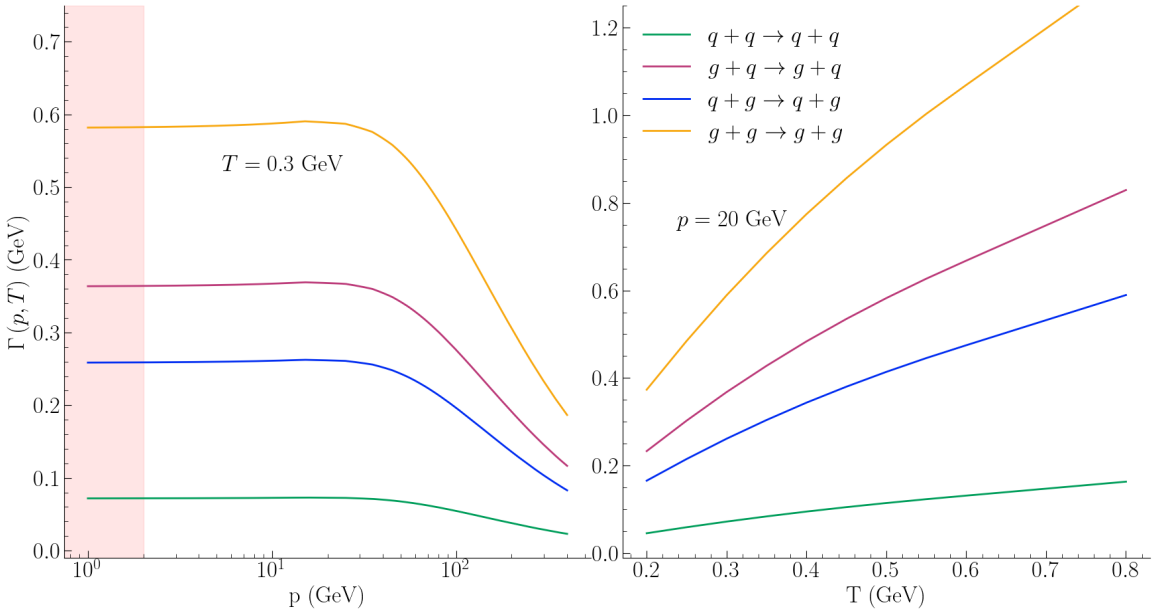

Figure 4.3: Elastic rates implemented in CUJET for fixed temperature ($T = 0.3$ GeV, left) and fixed momentum ($p = 20$ GeV, right). The shaded red area is $p < p_{cut}$ where the momentum cut is set to $p_{cut} = 2$ GeV. Compare with Figure 4.2.

ferences between the models of the elastic energy loss channels in CUJET and MARTINI. First is the simplistic inclusion of thermal medium effects in the gluon propagator in

CUJET via a simple gluon Debye mass versus the full HTL gluon propagator in MARTINI. Second is the accounting for quantum statistics: MARTINI uses Fermi-Dirac and Bose-Einstein statistics for both the initial and final state of the interaction while CUJET uses Boltzmann statistics for the initial state and ignores the final state. The more major of the two differences is the treatment of the matrix element. While at the differential cross-section level, for large momentum transfers, the two models would look very similar to each other, they will give different total scattering rates due to their very different treatments of the small-t region. This can be readily seen by considering Figure 4.3, which presents the elastic scattering rate for a representative temperature, $T = 300$ MeV (left figure) and a fixed jet momentum $p = 20$ GeV (right figure). One can contrast this figure with Figure 4.2, where we can observe the differences in shapes and overall scale of the elastic scattering rates of CUJET and MARTINI. Though the shapes are different, the two models of collisional energy loss result in rates that are of the same order.

This discussion and comparison are somewhat complicated by the effect of the running coupling, $\alpha_s(p, T)$, and how the two models have chosen to implement it. While both models take the LO pQCD formula of running coupling, they chose to implement different scale dependencies. In particular, MARTINI allows for a different scale dependence for its radiative and elastic channels while CUJET implements the same functional form and applies the same parameters for both. More details on the CUJET running coupling, can be found in Section 4.2.2. The MARTINI implementation of the running coupling is discussed in Section 4.4.

4.2 RADIATIVE ENERGY LOSS

The main and most important difference between CUJET and MARTINI frameworks is their implementation of radiative energy loss of hard partons in a QGP medium. This is the dominant energy loss mechanism for energetic, light partons and has significant implications for the observables we consider in this thesis.

The discussion here will begin with CUJET which implements DGLV radiative rates. This is followed by a discussion of MARTINI's inelastic rates, which are computed in the AMY framework. Here these models are referred to as *low-virtuality* energy models

as they do not assume the hard parton to be far off-shell[6]. This will prepare us for a comparative, multi-probe study of CUJET and MARTINI when embedded in realistic simulations of heavy ion collisions using JETSCAPE.

As a matter of notation, unless explicitly stated otherwise, the coordinate system is defined by the hard parton. For example, the transverse momentum of a radiated gluon, k_T, is the transverse momentum of that gluon *relative* to the incoming parton.

4.2.1 CUJET *and* DGLV *rates: gluon emission*

CUJET models the radiative energy loss of hard partons via the LO-DGLV opacity expansion. In this model, the radiated gluon spectrum is expanded in powers of the opacity, L/λ_{mfp}, where L is the size of the QGP medium. Thus, the fundamental assumption in CUJET is its view of the medium: one that has a size comparable with the mean free path of hard partons. In other words, it is a *thin* medium, and as such, one can calculate the spectrum of the radiated gluons from jets that have experienced a single soft scattering. If we assume the medium is at very high temperature T with static, well-separated colour sources [110], we can write the effective qg scattering cross-section

$$\sigma \sim 2\pi\alpha_s^2/m_D^2,\ m_D \propto gT,\ \sigma \sim g^2/(8\pi T^2).$$

Taking a Stefan-Boltzmann parton density $\rho \sim (T^3)$ [7], we see that the mean free path is approximately $\lambda_{mfp} \sim (g^2T)^{-1}$. Comparing this to the length scale set by the Debye mass ($m_D^{-1} \sim (gT)^{-1}$), it is evident that if the strong coupling $g \ll 1$, the assumption that the plasma is made of a series of well-separated, static scattering centers is a valid one.

The first attempt at the opacity expansion is the GLV (Gyulassy–Wang–Vitev) model [111–114], the direct precursor to DGLV. There, the bremsstrahlung gluon spectrum was calculated for a hot QGP medium with static sources. The model continued with the high-temperature assumption and the static-source approximation and used them to

6 MARTINI specifically assumes the parton to be on-shell. CUJET makes no such assumption, but in practical applications, it is only applied as a low-virtuality energy-loss model.

7 In this chapter, ρ is the density of the scattering centers in the QGP medium, and should not be confused with the $\rho(\mathbf{x})$ in Chapter 1 where it was nucleon density in a nucleus.

simplify further the physical picture of gluon radiation. Due to high temperature and small coupling assumptions, GLV neglects the average energy loss ($q_0 \sim q_z \sim g^2T$) when compared to the average transverse momentum transfer ($q_\perp \sim m_D \sim gT$) [110]. The model also takes an eikonal view of the jet propagation in the medium by assuming that the energies of the hard parton and the emitted gluon are so much larger than the magnitude of the transferred transverse momentum, $(E, k) \gg q_\perp$, that the direction of the hard parton is not modified as a result of its travel through the plasma. The calculation is simplified further by assuming that the radiated gluon takes away only a fraction of the incoming parton's energy[8]. The final piece of the GLV model focuses on radiated gluons with small k_T, which can be thought of as collinear or nearly-collinear with the incoming parton.

The DGLV model, builds on GLV by including an effective gluon mass [116] and heavy quark masses [117]. Finally, dynamical scattering centers were added in Ref. [118, 119]. It should be emphasized that both GLV and DGLV are general frameworks within which one can calculate the radiated gluon spectrum to arbitrary order in the opacity expansion. The diagrams used for calculating gluon radiation from an energetic parton at LO in the opacity expansion are shown in Figure 4.4. The $\mathcal{M}_i$ denotes the family of diagrams contributing at i-th order in the opacity expansion. The labelling of individual diagrams, $\mathcal{M}_{n,m,l}$, was introduced in Ref. [111], and translates to a diagram of n number of scattering centres where l gluons are radiated in the final state with the gluon emitted in the m-th time interval. The first order opacity expansion result for the double differential, single inclusive radiated gluon distribution is given by [117]

$$d^3N_g^{(1)} d^3N_J = \left(\frac{1}{d_T} \mathrm{Tr} \langle |M_1|^2 \rangle + \frac{2}{d_T} \mathrm{ReTr} \langle M_0^* M_2 \rangle \right) \frac{d^3p}{2p^0 (2\pi)^3} \frac{d^3k}{2\omega(2\pi)^3} \tag{4.10}$$

where d_T is the dimension of $SU(3)$ representation of the target (8 for gluons, 3 for quarks). DGLV assumes that the scattering centres are distributed with the same density [117]

$$\rho(\mathbf{x}) = \frac{N}{A_\perp} \bar{\rho}(z), \quad \int \bar{\rho}(z) dz = 1. \tag{4.11}$$

8 This approximation, also known as the soft-gluon approximation was recently tested in Ref. [115] where it was relaxed for gluon radiation from gluons and found to be valid. I emphasize that the *soft* in soft-gluon approximation means the gluon is soft relative to the incomig parton. This gluon is still hard compared to the temperature scale.

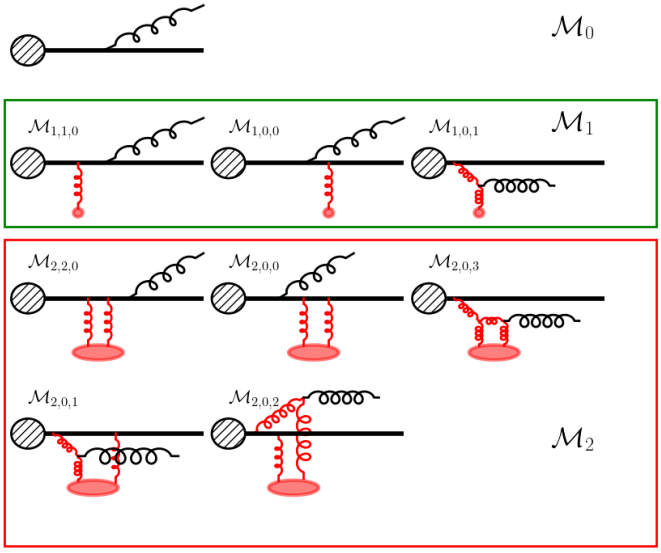

Figure 4.4: Diagrams included in DGLV calculation of gluon radiation at LO in the opacity expansion. The diagrams inside the green rectangle are gluon emission diagrams involving a single soft scattering with the medium, while those in the red rectangle include two soft scatterings with the medium. The red oval indicates that $\mathcal{M}_2$ diagrams are evaluated in the contact limit. The hard parton, denoted by the straight black line, can be a quark, anti-quark or gluon.

where $A_\perp$ is a large (relative to the interaction area, m_D^{-2}) transverse area. The angle brackets are ensemble averages over the scattering centre locations [117]. The notation $(p^0, \mathbf{p})$ is used for the four-momentum of the outgoing hard parton (post-radiation) and $(\omega, \mathbf{k})$ for the four-momentum of the radiated gluon. N_J is the distribution of the hard partons, defined by [117]

$$d^3N_J = d_T |J(p)|^2 \frac{d^3p}{2p^0 (2\pi)^3} \tag{4.12}$$

where J is the source current of the hard partons, assumed to vary slowly as a function of momentum: $J(p+k-q) \approx J(p+k) \approx J(p)$ and d_T is the dimension of the representation of the hard parton, same as before. Finally, M_i in Equation 4.10 denote the sum of the $\mathcal{M}_i$ family of diagrams in Figure 4.4. These are

$$\begin{aligned} M_1 &= \mathcal{M}_{1,1,0} + \mathcal{M}_{1,0,0} + \mathcal{M}_{1,0,1} \\ M_2 &= \mathcal{M}_{2,2,0} + \mathcal{M}_{2,0,3} + \frac{1}{2}(\mathcal{M}_{2,0,1} + \mathcal{M}_{2,0,2}) \end{aligned} \tag{4.13}$$

where the factor of 1/2 multiplies the two topologically indistinct diagrams $\mathcal{M}_{2,0,1}$ and $\mathcal{M}_{2,0,2}$, to avoid double counting. Defining the four momenta involved in the process, with parentheses and square brackets denoting Minkowski and light-cone momenta, respectively

$$\begin{aligned} p =& (E, E, 0) = [2E, 0, 0_\perp] \\ k =& (x_E E, \sqrt{(x_E E)^2 - \mathbf{k}^2}, \mathbf{k}_\perp) = [x_+ E^+, \frac{\mathbf{k}^2}{2x_+ E^+}, \mathbf{k}_\perp] \\ q =& (q_0, q_z, \mathbf{q}_\perp) \end{aligned} \tag{4.14}$$

where p, k and q are the four-momenta of the jet parton, emitted gluon and the exchanged gluon, respectively. x_E is the energy fraction of the gluon to the jet parton ω/E in Minkowski space, with x_+ its light-cone counterpart. The two are related via

$$x_+(x_E) = \frac{1}{2}\left(1 + \sqrt{1 - (\frac{k_\perp}{x_E E})^2}\right). \tag{4.15}$$

Thus the LO-DGLV expression for the double-differential gluon multiplicity distribution at LO of the opacity expansion with dynamic sources, is given by [120]

$$\begin{aligned} \frac{d\Gamma^{DGLV}_{i\to gi}}{dx}(p, x, \tau) =& \frac{18C_i^R}{\pi^2}\frac{4+N_f}{16+9N_f}\rho(T)\int d^2\mathbf{k}_\perp \left\{\frac{1}{x_+}\left|\frac{dx_+}{dx}\right|\alpha_s\left(\frac{\mathbf{k}_\perp^2}{x_+ - x_+^2}\right)\right. \\ &\times \int \frac{d^2\mathbf{q}_\perp}{\mathbf{q}_\perp^2}\left[\frac{\alpha_s^2(\mathbf{q}_\perp^2)}{\mathbf{q}_\perp^2 + m_D^2}\frac{-2}{(\mathbf{k}_\perp - \mathbf{q}_\perp)^2 + \chi^2}\left(\frac{\mathbf{k}_\perp\cdot(\mathbf{k}_\perp - \mathbf{q}_\perp)}{\mathbf{k}_\perp^2 + \chi^2} - \frac{(\mathbf{k}_\perp - \mathbf{q}_\perp)^2}{(\mathbf{k}_\perp - \mathbf{q}_\perp)^2 + \chi^2}\right)\right. \\ &\left.\left.\times\left(1 - \cos\left(\frac{(\mathbf{k}_\perp - \mathbf{q}_\perp)^2 + \chi^2}{2x_+ p}\tau\right)\right)\right]\right\} \end{aligned} \tag{4.16}$$

where C_R is the quadratic Casimir factor of the jet parton (4/3 for quarks, 3 for gluons) and χ^2 contains the quark and gluon effective mass factors and regulates the soft and collinear divergences

$$\chi^2 = M^2 x_+^2 + m_g^2(1 - x_+) \tag{4.17}$$

where M is the mass of the quark[9] and the m_g is the thermal gluon mass: $m_g^2 = m_D^2/2$. Finally, τ is the distance between the production vertex (black blob in Figure 4.4) and

9 The M notation used in DGLV was included from work done on massive quarks. In this work, massive quarks –charm and bottom– are not considered and light quarks are taken to be massless. M is kept so as to be consistent with the existing DGLV published works. To summarize, in gluon bremsstrahlung processes here, gluons have a thermal mass and quarks are massless.

the scattering vertex or equivalently, the time since the creation of the hard parton. The existence of the cosine term is the manifestation of the LPM effect [121–123], where the radiation rate gets suppressed because of the destructive interference of successive collisions of the jet with the medium. In DGLV this effect manifests itself in the interference of M_0 and M_2 diagram classes. The integration limits of the momentum integrals are $\mathbf{q}_\perp \leqslant q_{max} = \sqrt{6pT}$ and $\mathbf{k} \leqslant xp$. The factor $\rho(T)$ is the number density of the scattering centers and a function of local temperature. The value of $\rho\left(T\left(\tau, \mathbf{z}\right)\right)$ can be estimated by connection to the QCD equation of state for which we use the *s95p-PCE* [124] EOS via $\rho = s/4$ where s is the entropy density.

As previously mentioned, the strong coupling in CUJET is allowed to run, and in the equation above, there are three powers of the coupling. Two powers stem from the momentum exchange during the soft scattering process, and thus their scale is chosen to be $\mathbf{q}_\perp^2$, the exchanged momentum. The remaining power is the gluon radiation vertex, where the chosen scale is the virtuality of the quark propagator post scattering, $Q^2 = \frac{\mathbf{k}_\perp^2}{x_+ - x_+^2}$. There is also the evaluation of the Debye mass, which we solve for at any given temperature using the self-consistent equation

$$m_D^2\left(T\right) = 4\pi\alpha_s(m_D^2\left(T\right))T^2(1 + N_f/6). \tag{4.18}$$

The form of the running coupling implemented in CUJET is given by the LO pQCD equation for α_s, with one free parameter, $\alpha_{s,max}$, to be determined by fits to the data

$$\alpha_s(Q^2) = \begin{cases} \frac{4\pi}{9\ln(Q^2/\Lambda_{QCD}^2)}, & Q > \Lambda_{QCD}\, e^{\frac{2\pi}{9\alpha_{max}}}, \\ \alpha_{max}, & Q \leqslant \Lambda_{QCD}\, e^{\frac{2\pi}{9\alpha_{max}}}. \end{cases} \tag{4.19}$$

where $\Lambda_{QCD} = 200$ MeV is the QCD scale parameter. All α_s running in CUJET for elastic and radiative processes, is implemented using Equation 4.19 except for the jet-medium photon conversion channel. The last note on Equation 4.16 is the interpretation of τ. The standalone CUJET is a deterministic calculation of jet energy loss. In this work, we converted the standard CUJET model from a deterministic to a Monte Carlo implementation for the first time. Among the changes made is the interpretation of τ: while in standalone CUJET it was the time from the production of the hard parton and the scattering vertex, in the Monte Carlo implementation (used in Chapter 6), it is taken to be the *time since last radiation*. This will have consequences for the

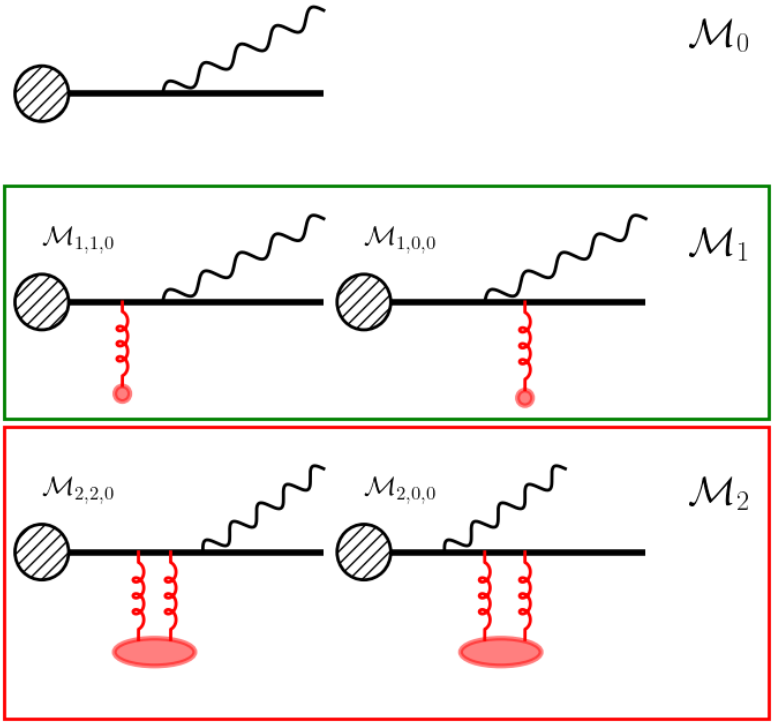

Figure 4.5: Feynman diagrams involved in the LO opacity calculation of photon bremsstrahlung within the DGLV framework. Contrast with the diagrams of Figure 4.4.

fitted value of $\alpha_{s,max}$, which we will discuss when considering CUJET in the context of realistic simulations. From here on, CUJET, LO-DGLV and DGLV are used interchangeably. It should be clear that the standalone CUJET will not be referred to at any point in the remainder of this work.

4.2.2 CUJET *and* DGLV *rates: photon emission*

The first calculation of photon bremsstrahlung within DGLV was performed in Ref. [125] for a static medium. Beyond the static medium approximation, another assumption was using a Gaussian profile ansatz for the number density of the particles in the medium to simply the integrals. Figure 4.5 shows the Feynman diagrams involved in the calculation, which can be contrasted with the Figure 4.4. The photon emission process, at leading order in the fine structure constant α and α_s, does not include pro-

cesses where the emitted particle experiences further scattering with the medium[10]. We modified the photon bremsstrahlung rates to go beyond the static sources and used the same density for the medium scattering centers as the gluon bremsstrahlung rate. The photon radiation rate is then given by

$$\begin{aligned}\frac{d\Gamma^{DGLV}_{q\to q\gamma}}{dx}(p,x,\tau) = \frac{e_f^2\alpha_{em}}{\pi^2}\frac{32+8N_f}{16+9N_f}\rho(T)\int d^2\mathbf{k}_\perp \frac{(1-x_+)^2}{x_+}\left|\frac{dx_+}{dx}\right| \\ \times\int\frac{d^2\mathbf{q}_\perp}{\mathbf{q}_\perp^2}\frac{\alpha_s^2(\mathbf{q}_\perp^2)}{\mathbf{q}_\perp^2+m_D^2}\left[\left(\frac{\mathbf{k}_\perp-x_+\mathbf{q}_\perp}{(\mathbf{k}-x_+\mathbf{q})^2+\chi^2}-\frac{\mathbf{k}_\perp}{\mathbf{k}^2+\chi^2}\right)^2\right. \\ \left.+2\left(\frac{\mathbf{k}_\perp\cdot(\mathbf{k}_\perp-x_+\mathbf{q}_\perp)}{((\mathbf{k}_\perp-x_+\mathbf{q}_\perp)^2+\chi^2)(\mathbf{k}_\perp^2+\chi^2)}-\frac{\mathbf{k}_\perp^2}{(\mathbf{k}_\perp^2+\chi^2)^2}\right)\cos\left(\frac{\mathbf{k}_\perp^2+\chi^2}{2x_+p_\perp}\tau\right)\right]\end{aligned} \tag{4.20}$$

where e_f is the charge of the quark or anti-quark involved in the process and the kinematic factors x and x_+, are defined using Equation 4.14 and Equation 4.15. The regulator for soft, collinear divergences is now given by

$$\chi^2 = M^2x_+^2 \tag{4.21}$$

where M is the quark thermal mass and given by

$$M^2 = \frac{4\pi}{6}\alpha_s T^2. \tag{4.22}$$

When used in evaluating the rate in Equation 4.20, the thermal quark mass is solved for using the self-consistent equation

$$M^2 = 4\pi\alpha_s(M(T)^2)\frac{T^2}{6}. \tag{4.23}$$

All other variables are defined analogously to the gluon radiation case of Equation 4.16. The differences in the momentum structure of the photon and gluon radiative processes are due to the former missing 4 diagram classes (those with where the emitted particle rescatters with the medium) and all the interference terms that those would have provided. The final difference is the coupling constant of the radiation vertex. Unlike the gluon emission case, the coupling strength of the electromagnetic vertex is fixed to the fine structure constant, $\alpha_{em} = 137^{-1}$. The integration limits here are $|\mathbf{q}|_\perp \leqslant \sqrt{6\,p\,T}$ for the integral over the exchanged transverse momentum during the soft process and $m_D \leqslant |\mathbf{k}|_\perp \leqslant x\,p$ for the photon transverse momentum.

10 As it will be mentioned throughout this thesis, photons can, in principle interact with the QGP medium. However, their mean free path is much larger than the size of the medium, and thus such an interaction is extremely unlikely.

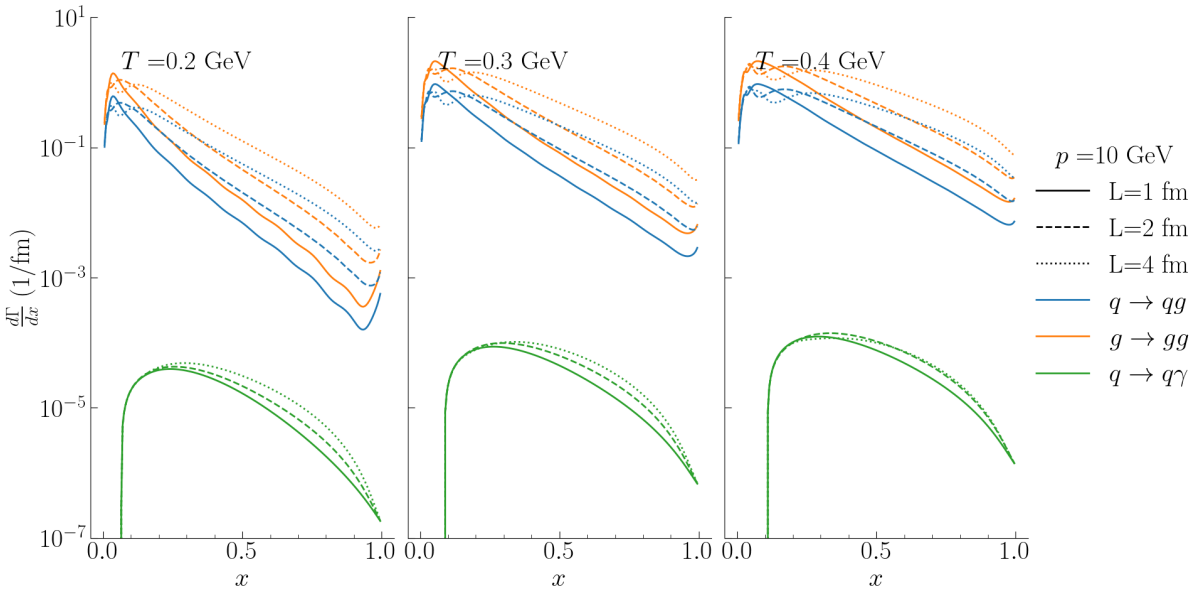

Figure 4.6: Example of differential radiative rates for gluon emission from a quark (blue), gluon emission from a gluon (orange) and photon emission from a quark (green). The rates are provided for a quark of momentum 10 GeV in a static QGP of three representative temperatures (columns) and for path lengths of 1 fm (solid), 2 fm (dashed) and 4 fm (dotted). Generated using $\alpha_{s,max} = 0.68$.

Figure 4.6 gives an example of the shape and behaviour of the differential radiative rates in DGLV as a function of the fractional energy. The temperatures chosen are typical of heavy ion collisions. The apparent threshold effect in the photon bremsstrahlung rates is due to the lower bound on **k** integral.

4.2.3 MARTINI *and* AMY *rates*

MARTINI [126] simulates energy-loss of hard partons within the AMY framework [127–130] of Arnold–Moore–Yaffe, a kinetic theory approach based on the techniques of finite-temperature field theory. In the AMY framework, the medium is viewed as an equilibrated, stationary, infinite slab of QGP at asymptotically high temperatures. As such, the medium is *weakly-coupled* with the strong coupling taken to be $g \ll 1$.

The genesis of the framework is in the realization that for calculations of hard thermal photon production at LO, the diagrams of Figure 4.7a are incomplete. It was found [131] that the bremsstrahlung or inelastic pair annihilation processes, given by Figure 4.7b, also contribute at leading order, despite being $2 \to 3$ processes. This is

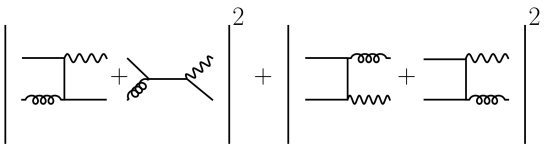

(a) QCD Compton scattering and $q\bar{q}$ annihilation

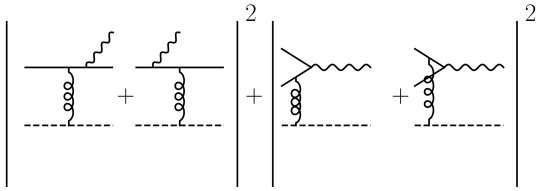

(b) Bremsstrahlung and inelastic pair annihilation

Figure 4.7: (a) Diagrams of LO thermal production of photons in QGP. The diagrams on the left are the t and s channels of QCD Compton scattering, while those on the left are the u and t channel diagrams of $q/\bar{q}$ annihilation, respectively. (b) diagrams of bremsstrahlung (left) and inelastic pair annihilation (right). The dotted line can be a quark, anti-quark or gluon from the thermal medium.

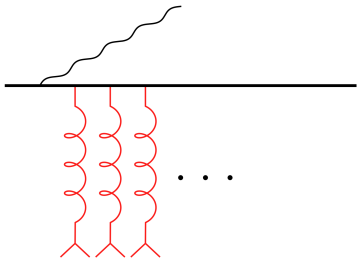

Figure 4.8: Example of a photon emission diagram where the radiator experiences multiple elastic scatterings while undergoing radiation. The black line is a parton of $\mathcal{O}(T)$ momentum, and the red curly lines are soft gluons with momenta of $\mathcal{O}(gT)$.

based on the fact that if the momentum scale of the internal propagators is hard (of $\mathcal{O}(T)$), then the diagrams contribute at next-to-leading order or $\mathcal{O}\left(\alpha\alpha_s^2\right)$. However, when the internal momenta are of order $\mathcal{O}(gT)$, then the enhancement in the propagator, $(gT)^{-1}$ cancels the extra power of g in the numerator resulting in the diagram contributing at $\mathcal{O}(\alpha\alpha_s)$, same as the $2 \to 2$ channels.

The initial application of the discussion above was in thermal photon radiation from a QGP plasma. However, the discussion is generalizable to photon or gluon emission from a hard jet traversing a plasma, and this is how it will be applied in this work. We can now go back to Section 4.2.1 and Section 4.2.2, where the LO results of the DGLV framework were discussed. Since the medium is assumed to be infinite in the AMY framework, we must more carefully consider the interplay of the radiation formation time and the mean free path of the incoming particle. The time taken for

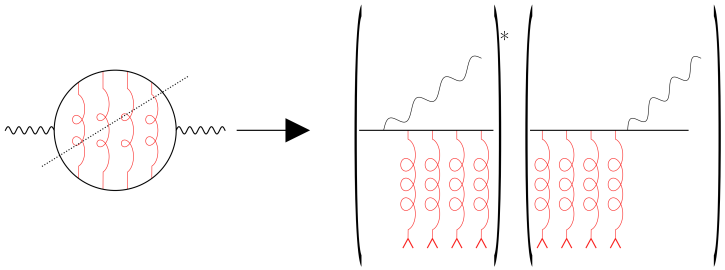

Figure 4.9: Example of a photon self-energy diagram with four soft gluon exchanges. The cut of this diagram results in the interference term between the photon radiation before and after four elastic collisions with the medium.

each soft scattering to occur can be estimated as $\tau_{\text{el.}} \propto m_D^{-1} \propto (gT)^{-1}$. The formation time of the radiation is estimated via uncertainty principle-type arguments, as [132]

$$\tau_{\text{form.}} = \frac{2E\, x(1-x)}{k_\perp^2} \tag{4.24}$$

where E is the energy of the incoming parton, $k_\perp$ is the transverse momentum component of one of the outgoing particles relative to the incoming and $x = k/p$ the momentum fraction of the radiated parton to the parent. Thus, the formation time is of order $\left(g^2T\right)^{-1}$. This is larger, given our assumption of $g \ll 1$, than the typical time of elastic scatterings.

The diagrams of Figure 4.7b, then, are not sufficient, and we have to consider diagrams with an arbitrary number of elastic scatterings, of which Figure 4.8 is an example. Diagrams such as this must be re-summed to arrive at the photon or gluon radiation rate at leading order. The production rate of photons or gluons is related to the imaginary part of their self-energy [133]. Cuts in the self-energy ladder diagrams, similar to the one in Figure 4.9, result in diagrams contributing to bremsstrahlung or inelastic annihilation at LO with the LPM effect due to the interference between different diagrams. The resummation of the infinite set of ladder diagrams, each with

a different number of gluon legs, yields a linear integral equation [127–129] for the transverse dynamics of the emission process. This is given by

$$\begin{aligned} 2\mathbf{h}_\perp = i\delta E(x,p,\mathbf{h}_\perp)\mathbf{g}_{(x,p)}(\mathbf{h}_\perp) + \int \frac{d^2\mathbf{q}_\perp}{(2\pi)^2}\,\bar{C}(q_\perp) \\ \times \Big\{ C_1[\mathbf{g}_{(x,p)}(\mathbf{h}_\perp) - \mathbf{g}_{(x,p)}(\mathbf{h}_\perp - \mathbf{q}_\perp)] \\ + C_x[\mathbf{g}_{(x,p)}(\mathbf{h}_\perp) - \mathbf{g}_{(x,p)}(\mathbf{h}_\perp - x\mathbf{q}_\perp)] \\ + C_{1-x}[\mathbf{g}_{(x,p)}(\mathbf{h}_\perp) - \mathbf{g}_{(x,p)}(\mathbf{h}_\perp - (1-x)\mathbf{q}_\perp)] \Big\} \end{aligned} \tag{4.25}$$

where x is the momentum fraction of the radiated parton given by

$$x \equiv \frac{k}{p} \tag{4.26}$$

and used throughout the rest of this chapter. The factors $C_{1,x,1-x}$ are functions of Casimir operators of the incoming and outgoing particles. These are explicitly given by

$$\begin{aligned} C_1 &= \frac{1}{2}\Big(-C_1^R + C_x^R + C_{1-x}^R \Big)\,, \\ C_x &= \frac{1}{2}\Big(C_1^R - C_x^R + C_{1-x}^R \Big)\,, \\ C_{1-x} &= \frac{1}{2}\Big(C_1^R + C_x^R - C_{1-x}^R \Big)\,, \end{aligned} \tag{4.27}$$

where $C^R_{(1,x,1-x)}$ are the colour Casimir of the parton with the specified momentum fraction with $C^R = C_F$ for quarks and $C^R = C_A$ for gluons. The integral equation solves for $\mathbf{g}_{(x,p)}(\mathbf{h}_\perp)$, the function that contains information on the transverse dynamics of the process. $\mathbf{h}_\perp$, the argument of the function, measures the collinearity of the outgoing parton, $\mathbf{h} \equiv (\mathbf{k}\times\mathbf{p})\times e_\parallel$. Parametrically, the magnitude of this vector is of order $\mathcal{O}\left(gT^2\right)$. In the first term in Equation 4.25, δE is the energy difference between the initial and final states of the radiation process. It is given by

$$\delta E(x,p,\mathbf{h}_\perp) = \frac{\mathbf{h}_\perp^2}{2p\,x(1-x)} + \frac{m^2_{\infty,(x)}}{2xp} + \frac{m^2_{\infty,(1-x)}}{2(1-x)p} - \frac{m^2_{\infty,(1)}}{2p} \tag{4.28}$$

where $m^2_{\infty,(1,x,(1-x))}$ is the asymptotic mass of the particle which carries the specified momentum fraction. Its possible values are $m^2_{\infty,g} = m_D^2/2$ and $m^2_{\infty,q} = 2M^2$ where m_D and M is the gluon Deybe mass and quark thermal mass, specified previously in Equation 4.7 and Equation 4.22. Finally, $\bar{C}(q_\perp)$ is the LO (in α_s) collision kernel, also

known as the *transverse momentum broadening kernel* with the colour factors removed and it is given by [134]

$$\bar{C}_{LO}(\mathbf{q}_\perp) = \frac{g^2T^3}{q_\perp^2\left(q_\perp^2+m_D^2\right)}\int\frac{d^3p}{(2\pi)^3}\frac{p-p_z}{p}\times \\ [2C_A n_B(p)(1+n_B(p'))+4N_f T_f n_F(p)(1-n_F(p'))] \tag{4.29}$$

where p and $p' = p + \frac{q_\perp^2+2\mathbf{q}_\perp\cdot\mathbf{p}}{2(p-p_z)}$ are the momentum of the thermal particle before and after the elastic scattering, respectively. $\bar{C}_{LO}(\mathbf{q}_\perp)$ is then the differnetial rate of exchaning transverse momentum $\mathbf{q}_\perp$ with the jet parton. Once the function $\mathbf{g}_{(x,p)}(\mathbf{h})$ is solved for, it is used as input in the AMY splitting rate

$$\frac{d\Gamma^{AMY}_{i\to jk}}{dx}(p,x) = \frac{\alpha_s P_{i\to jk}(x)}{[2p\,x(1-x)]^2}\bar{f}_j(x\,p)\,\bar{f}_k((1-x)p)\int\frac{d^2\mathbf{h}_\perp}{(2\pi)^2}\,\mathrm{Re}\left[2\mathbf{h}_\perp\cdot\mathbf{g}_{(x,p)}(\mathbf{h}_\perp)\right]\,, \tag{4.30}$$

where $\bar{f}_{j,k} \equiv (1 \pm f_{j,k})$ are the distribution functions of particles j and k, which depending on the particle species, are Bose-Einstein or Fermi-Dirac and include the appropriate enhancement or suppression, respectively. $P_{i\to jk}$ are the usual DGLAP splitting functions

$$P_{g\to gg}(z) = 2C_A\frac{[1-z(1-z)]^2}{z(1-z)},\; P_{q\to qg}(z) = C_F\frac{1+(1-z)^2}{z}\,, \\ P_{g\to q\bar{q}}(z) = \frac{1}{2}\left(z^2+(1-z)^2\right),\; P_{q\to q\gamma}(z) = \frac{1+(1-z)^2}{z}. \tag{4.31}$$

Figure 4.10 shows the radiative AMY rates of Equation 4.30 for a energetic quark of 10 GeV in a plasma of three different tempratures.

4.3 JET-MEDIUM CONVERSION PROCESSES

The last remaining set of energy loss processes is jet-medium conversions. Similar to collisional energy loss channels of Section 4.1, these are $2 \to 2$ channels and contribute at leading order in the strong coupling. Unlike the elastic processes, however, these do not conserve the identity of the incoming parton. In the discussion that follows, the focus is on jet-medium conversion photons but the discussion is general and can be equally applied to quark to gluon or gluon to quark conversion.

Interest in jet-conversion processes began with work done in Ref. [135], where it was hinted that this source of photons could potentially be an important if not dom-

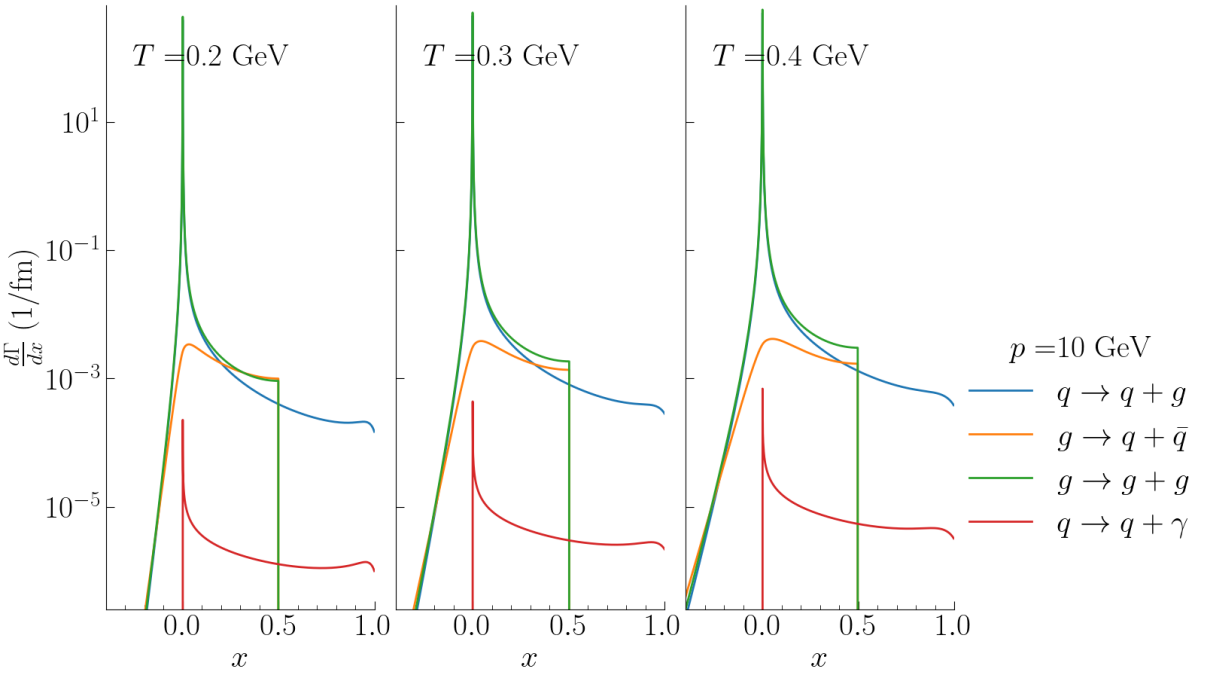

Figure 4.10: Example of the inelastic differential rates implemented in MARTINI (AMY rates) for a parton of $p = 10$ GeV at three representative temperatures as a function of the momentum fraction of the radiated parton. The rate of the two gluon splitting channels is zero for $x > 1/2$ due to symmetry. The coupling is allowed to run in this figure, with parameters $(\kappa_r, \kappa_e, \alpha_{s,0}) = (1.5, 4.5, 0.3)$. See Section 4.4 for details.

inant source of photons in the intermediate p_T region. The derivation of the rate of conversion is discussed below, following in the spirit of Ref. [135] but using the more complete rate calculation of AMY in Ref.[128].

The diagrams at play in $q(\bar{q})$ to photon conversion are the same as those in Figure 4.7a. The rate per unit spacetime volume of these processes, within kinetic theory, is given by [133]

$$\frac{dN^c}{d^3x\,dt} = \mathcal{N}_c \int_{p_1,p_2,p_\gamma,p_4} |\mathcal{M}_c|^2 f_1(p_1)\, f_2(p_2)\, \bar{f}_4(p_4)\, (2\pi)^4\, \delta^{(4)}\Big(\sum_i p_i^\mu\Big) \tag{4.32}$$

where c denotes the channel, either QCD Compton scattering or $q\bar{q}$ annihilation. The symbols $\mathcal{N}_c$ and $\mathcal{M}_c$ denote the degeneracy factor and the matrix element of the channel under study, respectively. The particle labels, 1, 2 and 4, correspond to the jet parton, the incoming thermal parton and the outgoing recoil parton. The distribution functions are associated with this labelling, and the same bar notation as in Section 4.2.3 is used where $\bar{f}_i \equiv (1 \pm f_i)$, with the plus and minus sign corresponding

to Bose enhancement or Pauli blocking. Finally, the integral sign is short-hand for Lorentz invariant integration

$$\int_{p_i} \cdots \to \int \frac{d^3\mathbf{p}_i}{2E_i\,(2\pi)^3}$$

The typical approximation used in the literature when evaluating Equation 4.32 is to use vacuum propagators when evaluating the matrix element $\mathcal{M}_c$ and to ignore modifications to external legs from thermal effects or masses [128]. Much like the discussion of elastic scattering channels, so long as the exchanged momenta are hard, this approximation will hold. However, if the exchanged momenta are soft, one has to perform a resummation on the fermion propagator and use a dressed propagator instead. The calculation of the rate of these processes was previously done by AMY [128], building on previous work by Baier et al. [136] and Kapusta et al. [137]. The main difference between the AMY calculation and the other two is how the large momentum transfer region is treated. Unlike AMY, Refs. [136, 137] assumed that the energy of the emitted photon is hard relative to the local temperature, i. e. $k \ll T$. This assumption allows for an analytical solution to the integral. The rate, then is calculated [11] by introducing a cutoff scale on the exchanged momenta, q^*, which separates the integral to hard ($q > q^*$) and soft ($q < q^*$) contributions. The integral over the large momentum transfers use the vacuum matrix elements and is numerically integrated, while the one over the soft momentum exchanges uses the HTL re-summed quark propagator. The final result for the total rate of photon emission via QCD Compton scattering and $q\bar{q}$ annihilation is given by [128]

$$(2\pi)^3 \frac{dR}{d^3k} = \frac{2\pi\, C_F\, \alpha\alpha_s}{k} T^2 n_{FD}(k) \left[d_F \sum_f (e_f)^2 \right] \left[\frac{1}{2} \ln \frac{2kT}{m_{\infty,q}^2} + C_{2\to2}\,(k/T) \right] \tag{4.33}$$

where n_{FD} is the Fermi-Dirac distribution, which is assumed to be only a function of the magnitude of the three momenta. The factor e_f is the fractional charge of each quark, and $d_F = N_c$ is the dimension of the quark representation. Finally, $C_{2\to2}(k/T)$ is fitted to the numerical calculation and is given by

$$C_{2\to2}(k/T) = 0.041\,\frac{T}{k} - 0.3615 + 1.01\,e^{-1.35\,k/T}. \tag{4.34}$$

Much like the elastic energy loss processes, the conversion process is t-channel dominated. As such, the conversion processes are implemented in the *collinear* or *loss-less*

11 For more details see Section V of Ref. [128].

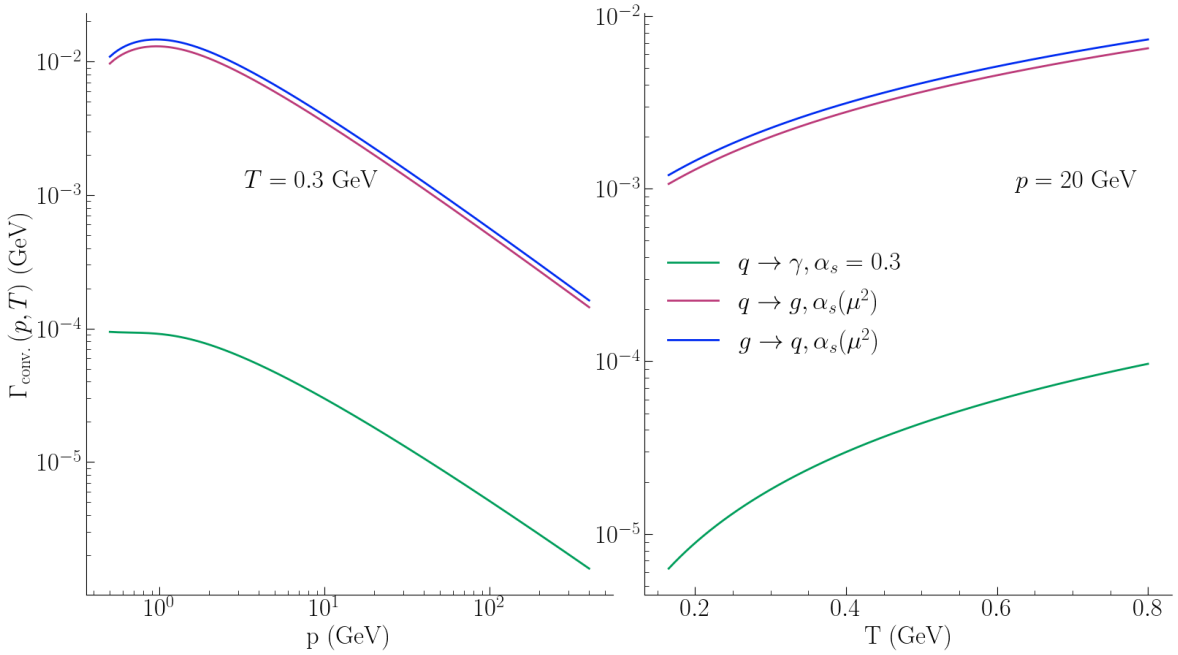

Figure 4.11: Conversion rate of an up quark to photon and gluon as well as gluon conversion rate to an up quark. The coupling constant for the conversion photon channel is fixed to $\alpha_s = 0.3$ while the other two channels have a running coupling.

conversion limit, i. e. no energy-loss during the process. This is done by first rewriting the rate formula above into a conversion rate [138] which can then be used in jet energy loss calculations

$$k\frac{dR}{d^3k} = \int \frac{d^3p}{(2\pi)^3}(2\pi)^3 \frac{dN^{q/\bar{q}}}{d^3x\, d^3p} k\frac{d\Gamma^{q(\bar{q})\to\gamma}}{d^3k} \int \frac{d^3p}{(2\pi)^3} f_{q,\bar{q}}(p)\, k\frac{d\Gamma^{q,\bar{q}\to\gamma}}{d^3k} \tag{4.35}$$

where $\mathbf{p}$ and $\mathbf{k}$ are the three momenta of the fermion and the photon. The function $f_{q/\bar{q}} \equiv (2\pi)^3 \frac{dN^{q,\bar{q}}}{d^3x\, d^3p}$ is interpreted as the phase space distribution of quarks and anti-quarks. By comparing Equation 4.35 and Equation 4.33, and replacing $n_{FD} \to f_{q/\bar{q}}$ we can write the conversion rate in the collinear conversion approximation for a single quark or anti-quark

$$\frac{d\Gamma^{q(\bar{q})\to\gamma}}{d^3k} = e_f^2 \frac{2\pi\,\alpha\,\alpha_s}{k} T^2 C_F \left[\frac{1}{2}\ln\frac{2kT}{m_{\infty,q}^2} + C_{2\to2}(k/T)\right] \delta^{(3)}(\mathbf{p}-\mathbf{k})\,. \tag{4.36}$$

In a Monte Carlo simulation, evolving the jet distribution through the plasma and applying Equation 4.36 to the hard quark or anti-quarks would result in the total conversion photon yield, in the collinear approximation. Equivalent rates for $q(\bar{q}) \to$

g and $g \to q(\bar{q})$ can be calculated by simply correcting for the different colour factors, the fine structure(α) constant and fractional charges [126]

$$\begin{aligned}\frac{d\Gamma^{q(\bar{q})\to g}}{d^3k} &= \frac{1}{e_f^2}\frac{\alpha_s}{\alpha}\frac{d\Gamma^{q(\bar{q})\to\gamma}}{d^3k}\\ \frac{d\Gamma^{g\to q(\bar{q})}}{d^3k} &= \frac{1}{e_f^2}N_f\frac{\alpha_s}{\alpha}\frac{N_c}{N_c^2-1}\frac{d\Gamma^{q(\bar{q})\to\gamma}}{d^3k}.\end{aligned} \tag{4.37}$$

Finally, MARTINI implements all conversion channels above while CUJET contains only the $q(\bar{q}) \to \gamma$ channel. Figure 4.11 shows the conversion rate of a quark (up quark) to a photon and a gluon as well as the gluon conversion rate to a quark.

4.4 α_s RUNNING IN MARTINI

MARTINI implements a running coupling, $\alpha_s\left(\mu^2\right)$ for both elastic and radiative energy loss channels. The addition of running coupling to MARTINI was done in Ref. [139]. Here a brief description of the implementation is provided for two reasons. First, for completeness as it includes the two most important parameters of MARTINI and second, since in Chapter 5 these parameters are re-fitted for AMY radiative rates that are generated using higher order collision kernels.

In MARTINI the expression for the strong coupling as a function of the running scale, much like CUJET is the LO pQCD result and is given by

$$\alpha_s(\mu^2) = \frac{4\pi}{(11-\frac{2}{3}N_f)\log\left(\mu^2/\Lambda^2_{QCD}\right)}. \tag{4.38}$$

However, unlike CUJET, where the only parameter of the running coupling is the value of its plateau, $\alpha_{s,max}$, MARTINI introduces two multiplicative constants for the scale at which the α_s of each process, is evaluated. The rationale behind this choice is that while it is known that the strong coupling has a scale dependence (see discussion of Section 1.1), there is freedom in the choice of what it should be. MARTINI takes the running scale, μ, to be the average momentum transfer [139] which can be calculated as

$$\mu = \sqrt{\langle p_T^2\rangle} = \begin{cases}\kappa_e\sqrt{\hat{q}\lambda_{mfp}} & \text{Elastic}\\ \kappa_r\left(\hat{q}p\right)^{1/4} & \text{Radiative}\end{cases} \tag{4.39}$$

where κ_r and κ_e are the scale factors. Furthermore, $\Lambda_{QCD} = 200$ MeV is the QCD scale parameter, and the running coupling is set to its maximum of 0.42 for $\mu = \Lambda_{QCD}$. The average momentum transfer per mean free path, $\hat{q}$ is the second moment of the HTL re-summed elastic collision rate [97]

$$\frac{d\Gamma_{elas.}}{d^2\mathbf{q}_\perp} = \frac{C_R}{(2\pi)^2}\frac{g^2 m_D^2 T}{\mathbf{q}_\perp^2\left(\mathbf{q}_\perp^2 + m_D^2\right)} \tag{4.40}$$

where m_D^2 is the squared of the Debye mass from Equation 4.7, C_R the Casimir operator of the jet parton and g the strong couling that is related to α_s via $\alpha_s = 4\pi g^2$. Using the elastic scattering rate then, $\hat{q}$ can be calculated as

$$\begin{aligned}\hat{q} =& \int^{q_{max}} d^2\mathbf{q}_\perp \mathbf{q}_\perp^2 \frac{d\Gamma_{elas.}}{d^2\mathbf{q}_\perp} \\ =& C_R \alpha_{s,0} m_D^2 \log\left(1 + \frac{q_{max}^2}{m_D^2}\right)\end{aligned} \tag{4.41}$$

where the upper bound of the integral is $q_{max} = \sqrt{6pT}$. For the elastic scattering renormalization scale, the mean free path is also computed using the elastic scattering rate

$$\begin{aligned}(\lambda_{mfp})^{-1} =& \Gamma_{elas.} = \int_{q_{min}}^{q_{max}} d^2\mathbf{q}_\perp \frac{d\Gamma_{elas.}}{d^2\mathbf{q}_\perp} \\ &= C_R\, \alpha_{s,0}\, T\left(\ln\left(1 + \frac{m_D^2}{q_{max}^2}\right) - \ln\left(1 + \frac{m_D^2}{q_{min}^2}\right)\right)\end{aligned} \tag{4.42}$$

where $q_{min} = 0.05T$, the lowest momentum exchange value used in generating the elastic scattering rate tables in MARTINI. The main parameters controlling the running coupling of MARTINI are $\alpha_{s,0}$, κ_r and κ_e, which are fixed by fits to experimental data. For all MARTINI results shown in this chapter and Chapter 6 the values used for these parameters are $(\kappa_r, \kappa_e, \alpha_{s,0}) = (1.5, 4.5, 0.3)$[139].

4.5 MATTER: A PARTON SHOWER GENERATOR

The *Modular All Twist Transverse-scattering Elastic-drag and Radiation* or MATTER [140–142] is the default model in JETSCAPE for final state showers of high virtuality partons both in `p-p` and `A-A` simulations. MATTER was introduced in order to incorporate spacetime information into the final state parton shower after a hard scattering event. The typical view of Monte Carlo simulations of jet energy loss before MATTER was

to have PYTHIA perform a full vacuum shower and then pass the parton list to the energy loss model of choice for further evolution. This assumes that allowing for a finite formation time for a parton shower is not necessary and that highly virtual, energetic partons generated in the hard scattering lose all their virtuality before they ever enter the medium. MATTER is a model that seeks to address this assumption.

Given the usage of MATTER in the multi-stage simulations of jet energy loss in HIC presented in Chapter 6, the section below is intended to present a brief introduction to MATTER and the physics included therein and in a very utilitarian manner. Specifically, the discussion here follows what is presented in Refs. [143, 144]. The interested reader is directed to the original references [140–142] for more information.

4.5.1 MATTER *in vacuum*

After PYTHIA generates the hard scattering process and the initial state radiation, it passes the active partons with four momenta $(E_i, \mathbf{p}_i)$ to MATTER. Initial virtuality is assigned to each parton by sampling the Sudakov form factor[143]

$$S(\nu_{max}, \nu) = \exp\left(-\int_{\nu}^{\nu_{max}} \frac{d\nu'}{\nu'} \alpha_s(\nu') \int_{y_{min}}^{y_{max}} dy\, P(y)\right) \tag{4.43}$$

where ν_{max} is set to $p_T/2$ with p_T being the transverse momentum of the particle for the very first branching. The function $P(y)$ is the DGLAP splitting function for a parton of light cone momentum p^+ to split to two partons with light cone momenta yp^+ and $(1-y)p^+$ and the limits of the integral are $y_{min} = Q_0/\nu'$ and $y_{max} = 1 - y_{min}$ where Q_0 is the minimum allowed virtuality set to 1 GeV for `p-p` simulations. The positive light cone momentum of the outgoing partons and their virtualities are then determined by sampling the splitting function and the Sudakov form factor, respectively. MATTER keeps track of the position information of the partons in the shower and the process is iterated until all partons have virtuality at or below Q_0.

4.5.2 MATTER *in medium*

The medium effects are included in MATTER via the medium-modified DGLAP splitting kernel

$$\begin{aligned} P^a(y,Q^2) &= P^a_{\text{vac.}}(y) + P^a_{\text{med.}}(y,Q^2) \\ &= P^a_{\text{vac.}}(y)\left[1+\int_{\xi_0^+}^{\xi_0^++\tau^+} d\xi^+ K^a(\xi^+,\xi_0^+,y,p^+,Q^2)\right] \end{aligned} \tag{4.44}$$

and therefore if a parton is within the medium and with virtuality above the cutoff scale, medium modifications to the DGLAP splitting functions are considered via the second term in Equation 4.44. Otherwise, only the vaccumm DGLAP functions are used. In the above, a denotes the particle species ($q,\bar{q},g$), $\tau^+ = 2p^+/Q^2$ the formation time of the radiated gluon. $K^a(\xi^+,\xi_0^+,y,p^+,Q^2)$ is the leading twist contribution [140] to the single-emission-single-scattering kernel [145–147][12]

$$K^a(\xi^+,\xi_0^+,y,p^+,Q^2) = \frac{C^a\hat{q}_a}{y(1-y)Q^2(1+\chi_a)^2}\left[2-2\cos\left(\frac{\xi^+-\xi_0^+}{\tau^+}\right)\right] \tag{4.45}$$

and is integrated from location ξ_0^+, the production position of the jet to $\xi_0^+ + \tau^+$, one splitting formation time later. The factor C^a is given by

$$C^a = \left[1-\frac{y}{2}\left(\delta_{a,q}+\delta_{a,\bar{q}}\right)\right] - \chi_a\left[1-\left(1-\frac{y}{2}\right)\chi_a\right]. \tag{4.46}$$

In the above, $\delta_{a,q(\bar{q})}$ are Kronecker delta functions and χ_a is given by

$$\chi_a = \frac{\left(\delta_{a,q}+\delta_{a,\bar{q}}\right)y^2m_a^2}{y(1-y)Q^2-y^2m_a^2} \tag{4.47}$$

where m_a is the mass of the parent parton, a. If the jet transport coefficient encoding the average momentum transfer per unit length, $\hat{q}$, is zero, then the medium-modified DGLAP splitting kernel is reduced to the vacuum equivalent. A non-zero $\hat{q}$ then introduces medium effects to the Sudakov factor. MATTER uses the HTL expression for $\hat{q}$ as calculated in Ref. [148] for single scattering with the medium and in the

$$\begin{aligned} \hat{q} = C_A\frac{42\zeta(3)}{\pi}\alpha_s^2T_{\text{local}}^3\Bigg[&\ln\left(\frac{5.7ET_{\text{local}}}{4m_D^2}\right)\Theta(E-2\pi T_{\text{local}})+ \\ &\ln\left(\frac{5.7\times 2\pi T_{\text{local}}^2}{4m_D^2}\right)\Theta(2\pi T_{\text{local}}-E)\Bigg] \end{aligned} \tag{4.48}$$

12 Original formulation includes drag ($\hat{e}$) and diffusion ($\hat{e}^2$) transport coefficients. Since these are not used in this work, they have been dropped from the equation for clarity.

where $\Theta(x)$ is the Heaviside function, T_{local} is the local temperature, m_D^2 the squared Debye mass given by Equation 4.7 and $\zeta(3)$ is the Apéry constant ($\zeta(3) = 1.20205$). The number 5.7 results from an analytical approximation of $\hat{q}$ as done in Ref. [148] where the small angle approximation was made on $2 \to 2$ elastic scattering cross-section,

$$\frac{d\sigma_{i,j}}{dq_\perp^2} \approx c_{i,j} \frac{2\pi\alpha_s^2}{q_\perp^4} \tag{4.49}$$

where $q_\perp$ is the magnitude of the exchanged transverse momentum and $c_{i,j}$ are the colour factors of jet parton i scattering off of the medium parton j, provided in Table 4.1. The equation for $\hat{q}$ resulting from the small angle approximation (first term of Equation 4.48) is then fitted for quarks and gluon separately for the constant factor in the logarithm term, and the average value is 5.7 which is then applied universally.

5

EXPLORATION OF HIGHER ORDER COLLISION KERNELS IN THE AMY FRAMEWORK

Chapter 4 presented the AMY formalism for radiative energy loss rates. A crucial ingredient in these rates is the collision kernel $C(\mathbf{q}_\perp)$, also known as the transverse momentum broadening kernel. It gives the rate at which the hard parton exchanges transverse momentum $\mathbf{q}_\perp$ with the particles of the medium and its expression at LO was given in Equation 4.29. Recently, this kernel has been evaluated to NLO [149] and there has also been a non-perturbative (NP) evaluation [150] of it on the lattice. This chapter presents the study of these new kernels, via their radiative rates, in static and evolving QGP.

The process of going beyond the LO evaluation of the collision kernels starts with Ref. [149]. The idea was inspired by previous work on perturbative corrections to thermodynamic pressure [151] where a three dimensional, Euclidean theory of QCD was introduced. By introducing a scale separation $gT \ll 2\pi T$ and integrating out the hard scale, one can arrive at a purely bosonic theory where the only remaing field, is the bosonic zero mode (Matsubara o-mode). All other bosonic and fermionic modes are *hard* and therefore integrated out, with their effects absorbed into effective parameters of the new, effective theory. This three-dimensional effective theory is called *Electrostatic QCD* or *EQCD* [152]. EQCD can then be used as an effective IR theory of QCD, where one computes higher order contributions to the collision kernel. A nice feature is the ability to relatively easily apply lattice techniques to the EQCD theory in order to have non-perturbative input in the calculation.

It was found in Ref. [153] that one could write the collision kernel in terms of certain light-like Wilson loops. Ref. [149] showed that these Wilson loops can be modified, at very high temperatures, and recast by going to EQCD [150]. The ability to use Euclidean techniques for EQCD then allows one to avoid the infrared problems [154] of finite temperature pQCD. In this way, the IR part of the QCD collision kernel can be

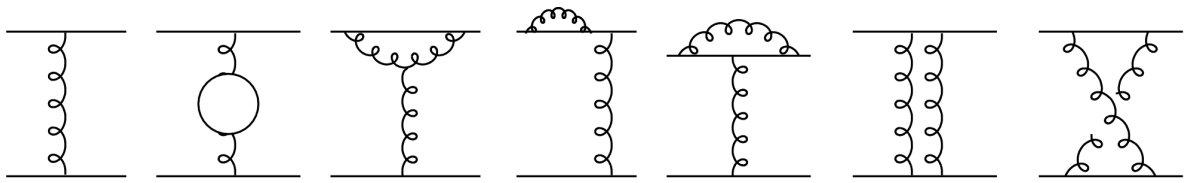

Figure 5.1: Feynman diagrams involved in the NLO kernel. The left most digaram shows the LO contribution while the rest are the one loop corrections. Figure adapted from Ref. [149].

evaluated in the effective theory to higher-order, either in a perturbative calculation or via lattice techniques. One can bring in non-perturbative input into jet-queching. However, while EQCD is an effective field theory for the IR region of QCD at high temperatures, it does not have the correct UV behaviour for QCD. As such, the collision kernel should be constructed by a careful matching procedure. Furthermore, this should be done at a scale where the unphysical UV and IR behaviour of EQCD and QCD, respectively, are in coincidence and the resulting kernel would have the physical UV properties of QCD and the physical IR contribution of EQCD.

The NLO kernel was computed in Ref. [149] and used in Ref. [155] in a calculation aimed at thermal photon emission rates at NLO as well as in Ref. [156] for jet energy-loss within the AMY formalism[1]. The IR region is calculated using perturbative results from EQCD and then matched to the LO collision kernel of Equation 4.29. The matching conditions reads [158]

$$C^{\text{NLO}}_{\text{QCD}}(q_\perp) = \left[C^{\text{LO}}_{\text{EQCD}}(q_\perp) + C^{\text{NLO}}_{\text{EQCD}}(q_\perp)\right] + \left[C^{\text{pert}}_{\text{QCD}}(q_\perp) - C^{\text{pert}}_{\text{subtr.}}(q_\perp)\right] \tag{5.1}$$

1 Ref. [156] does not have phenomenological jet energy loss calculations. Instead, what is attempted there is a very clever and novel look at recasting the energy loss channels in a way that would allow for Monte Carlo generators, like MARTINI to more naturally incorporate higher-order effects in energy loss. An application of this work was implemented in Ref. [157] for LO results as a proof of concept in the context of a brick test.

where the LO and NLO EQCD collision kernels are given by

$$
\begin{aligned}
C^{\text{LO}}_{\text{EQCD}}(q_\perp) =& C_R g^2 T \frac{m_D^2}{q_\perp^2(q_\perp^2+m_D^2)} \\
\frac{C^{\text{NLO}}_{\text{EQCD}}(q_\perp)}{g^4T^2C_sC_A} =& \frac{7}{32q_\perp^3} + \frac{-m_D - 2\frac{q_\perp^2-m_D^2}{q_\perp}\arctan\left(\frac{q_\perp}{m_D}\right)}{4\pi(q_\perp^2+m_D^2)^2} \\
&+ \frac{m_D - \frac{q_\perp^2+4m_D^2}{2q_\perp}\arctan\left(\frac{q_\perp}{2m_D}\right)}{8\pi q_\perp^4} - \frac{\arctan\left(\frac{q_\perp}{m_D}\right)}{2\pi q_\perp(q_\perp^2+m_D^2)} + \frac{\arctan\left(\frac{q_\perp}{2m_D}\right)}{2\pi q_\perp^3} \\
&+ \frac{m_D}{4\pi(q_\perp^2+m_D^2)}\left[\frac{3}{q_\perp^2+4m_D^2} - \frac{2}{q_\perp^2+m_D^2} - \frac{1}{q_\perp^2}\right]
\end{aligned}
\tag{5.2}
$$

and Figure 5.1 shows the Feynman diagrams of the LO and NLO kernels. The first term in brackets in Equation 5.1 provides the appropriate IR contribution to the Equation 4.29, with the unphysical UV part of the EQCD calculation subtracted by $C^{\text{pert}}_{\text{subtr.}}$. This term is given by [158]

$$
C^{\text{pert}}_{\text{subtr.}}(q_\perp) = \frac{C_R g^2 T m_D^2}{q_\perp^4} - \frac{C_R C_A g^4 T^2}{16 q_\perp^3} \tag{5.3}
$$

which is the $q_\perp \gg m_D$ limit of the $C^{\text{pert}}_{\text{EQCD}} = C^{\text{LO}}_{\text{EQCD}} + C^{\text{NLO}}_{\text{EQCD}}$. C_R and C_A are, respectively, the Casimir operator of the hard parton and the gluon.

The non-perturbative contribution to the collision kernel is computed [159–161], using lattice techniques, for this dimensionally reduced, effective theory. The matching calculation for the non-perturbative kernel, analogously to Equation 5.1, was done by Moore et al. in Ref. [158]

$$
C_{\text{QCD}}(b_\perp) \approx (C^{\text{pert.}}_{\text{QCD}}(b_\perp) - C^{\text{pert}}_{\text{EQCD}}(b_\perp)) - C^{\text{lattice}}_{\text{EQCD}}(b_\perp) \tag{5.4}
$$

where $b_\perp$ is the impact parameter, the Fourier transform of $q_\perp$. The matching calculation is done for the quantity in the parenthesis. In the above, $C^{\text{pert.}}_{\text{QCD}}$ is given by the Fourier transfrom of Equation 4.29 (in the large $q_\perp$ limit) and $C^{\text{pert.}}_{\text{EQCD}}$ is given by Equation 5.3. The lattice evaluation of $C^{\text{lattice}}_{\text{EQCD}}$ was done in Ref. [150].

Using the matching process described above, the cosntructed kernels at NLO and NP order were used to compute splitting rates within the AMY formalism for an infite [150] and finite [162] medium. In both cases, significant differences were observed between the computed rates from these kernels.

This chapter presents the consequences of using the new collision kernels via their implementation in the AMY framework. The study is done both in a static QGP brick

and a single-stage jet energy loss simulation with both fixed and running coupling constant. The medium evolution simulations used in this chapter are provided by the IPG-M approach as described in Chapter 3 and they are the current state-of-the-art in the modelling of the soft sector.

5.1 STUDY OF NEW RATES IN A STATIC MEDIUM

The collision kernels were placed in the AMY rate equation of Equation 4.30 and the resulting rates were implemented as alternatives to the LO rates[2]. As a matter of notation, the rates will be referred to by the collision kernel used to compute them. The rates calculated using the non-perturbative collision kernel will be referred to as the *NP rates*, and ditto for NLO and LO rates. As a first step to studying these new rates, we can consider their moments via

$$\langle x^n \rangle \equiv \frac{1}{g^4 T} \left(\int_{0^+}^{1} |x|^n \frac{d\Gamma}{dx} dx - \int_{-\infty}^{0^-} |x|^n \frac{d\Gamma}{dx} dx \right) \tag{5.5}$$

where $x \equiv k/p$ is the momentum fraction of the radiated parton k over the incoming parton p. For a given time interval, Δt, the zeroth moment $\langle x^0 \rangle \, g^4 T \, \Delta t$ gives the difference between the number of emissions and absorptions. The first moment, $\langle x^1 \rangle \, g^4 T \, \Delta t$, is the net energy loss fraction within that time interval, and finally, the second moment is related to the variance of the energy loss ratio per event via

$$\sigma^2 = \frac{\langle x^2 \rangle}{\langle x^0 \rangle} - \left(\frac{\langle x^1 \rangle}{\langle x^0 \rangle} \right)^2 .$$

Figure 5.2 shows the three moments discussed above. Arbitrary factors scale the three inelastic channels, so the scale on the y-axis is similar. The figure's general feature is that the NP rates sit between the NLO and LO results. The values of the new rates can be as much as 100% the LO rate, indicating their potentially significant power in jet quenching.

The new collision kernels are designed to match the LO collision kernel in the large momentum transfer limit. As such, the moments of the rates derived from these kernels also seem similar in the UV limit. We can rescale the NLO and NP curves to match the tails of their distributions to the LO rate to see better the differences in the

2 The implementation was done by Dr. Shuzhe Shi.

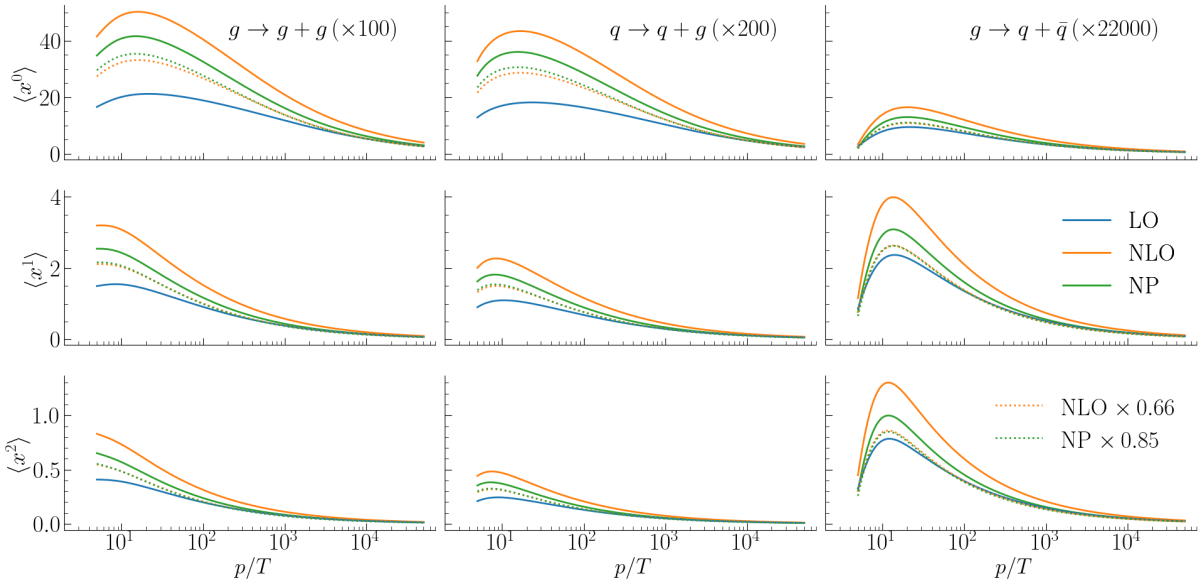

Figure 5.2: Moments of the total rates (Equation 5.5) computed within the AMY framework using the new collision kernels plotted against the temperature-scaled momentum (p/T). The solid lines are the direct output of the AMY rate equation after the collision kernels are put in. The dotted lines are the NLO and NP rates, scaled to match the high p/T limit of the LO rate. Each channel is scaled by a number (in parentheses) so that they can all be plotted on the same scale.

region of small p/T. The rescaled results are shown in Figure 5.2, denoted by dotted lines. The scaling factors are

$$\frac{\text{LO}}{\text{NLO}} \approx 0.66, \quad \frac{\text{LO}}{\text{NP}} \approx 0.85 \, . \tag{5.6}$$

This brings the new rates to a broad agreement with each other, particularly for their first and second moments. The scaling also flips the order of the curves, with the NLO curve now placed between the LO and NP across the plotted range of p/T. Finally, after the scaling, we can see that for $p/T \approx 10$, the new rates are the least similar to the LO rates.

We can now go beyond looking at the rates and study their effects on the evolving hard parton distribution. This is done by employing a static QGP brick held at a fixed temperature where a parton gun (quark or gluon) of fixed momentum p, with $p_z = 0$, is shot through the medium and evolved for some time. After each timestep Δt, the evolving partons (primary parton and those generated via its branchings) are collected and analyzed. In such a run, there is also the option for elastic scatterings. As such, we can construct four different sets of simulations using the combinations

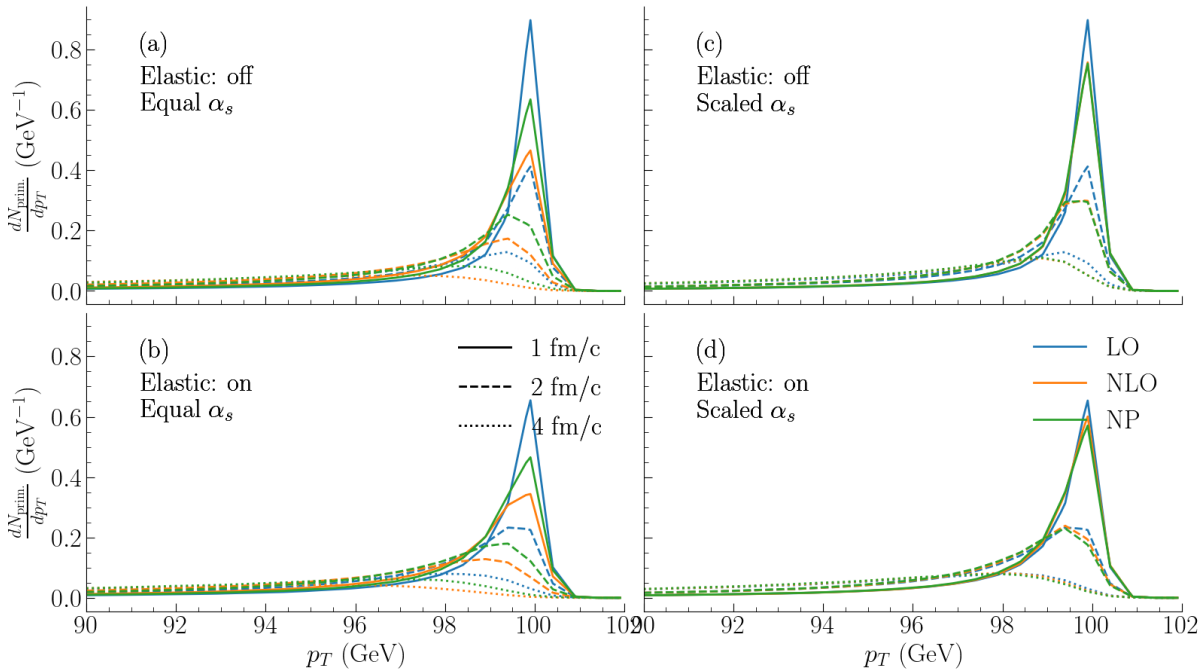

Figure 5.3: Distribution of primary parton – up quark – initially at p = 100 GeV, after travelling through a medium held at 0.2 GeV in temperature. The solid, dashed and dotted lines denote the travel time for 1, 2 and 4 fm, respectively. The top row does not include elastic collisions, while the bottom row has them enabled. Similarly, the medium evolution is performed in the left column with the three rate sets using the same $\alpha_s = 0.3$. The right column has $\alpha_{s,LO} = 0.3$ with the coupling of the other two rates scaled according to Equation 5.7. When turned on, the coupling of the elastic channels is the same as the radiative rate sets.

of elastic channels (*on* vs. *off*) and coupling constant (0.3 vs *scaled*) that can be made. The *scaled* runs refer to the scaling of the coupling, done according to

$$\alpha_{s,NLO} = \sqrt{0.66} \times \alpha_{s,LO}, \quad \alpha_{s,NP} = \sqrt{0.85} \times \alpha_{s,LO} \, . \tag{5.7}$$

Figure 5.3 shows static medium test results of a quark of $p_{init} = 100$ GeV[3] in a brick of $T = 0.2$ GeV. The runs are made using both for an $\alpha_s = 0.3$, a typical value in phenomenological studies of jet quenching that is used for all three rates and the case where the NLO and NP rates are scaled to this value. In each case, two calculations are made with elastic scatterings on and off (left and right column figures in Figure 5.3). The distributions shown in the figure are the primary parton gun after travelling 1, 2 and 4 fm in the QGP brick. Going from left to right, which goes for the rates

3 Visually, the initial distribution at $\tau = 0$ fm/c then is a δ-function centered at p = 100 GeV.

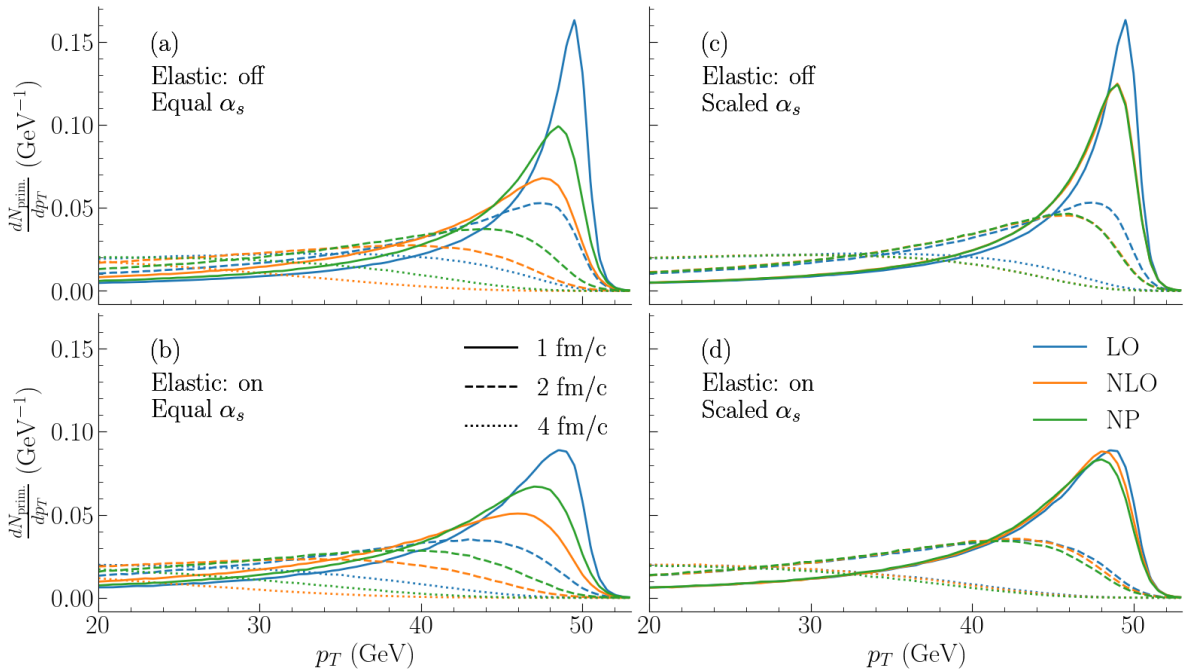

Figure 5.4: Same as Figure 5.3 but for $(p_{init}, T) = (50, 0.5)$ GeV system.

evaluated with the same α_s to rates evaluated with appropriately scaled α_s brings them close together. In the case of no elastic scatterings, the scaling of the coupling makes the NLO and NP-governed distributions nearly identical, while both are more quenched than the LO-governed result. When elastic scatterings are present, this clear grouping is minimized, where some – very small – visual difference remain between the NLO and NP curves. The inclusion of elastic scatterings breaks the degeneracy induced by the scaled α_s. The system studied in Figure 5.3 has $p/T = 500$, which is in a region where even before the scaling, the rates are converging towards each other (see Figure 5.2) and the NLO/NP rates are nearly indistinguishable. Furthermore, the figure is focused on the initial value of the parton momentum. Figure 5.4 shows the equivalent calculation for a $p/T = 100$ system. This value is the beginning of the range where the moments of the rates are becoming more clearly separated from each other. Compared to Figure 5.3, we can see that while the same general trend

A. scaling the coupling creates a degenerate result for NLO and NP,

B. including elastic scatterings breaks degeneracy by a small amount,

for a travel time of 2 fm/c with scaled coupling and elastic scattering, the ordering of the results is more visible than in the case where $p/T = 500$. Figure 5.5 reduced

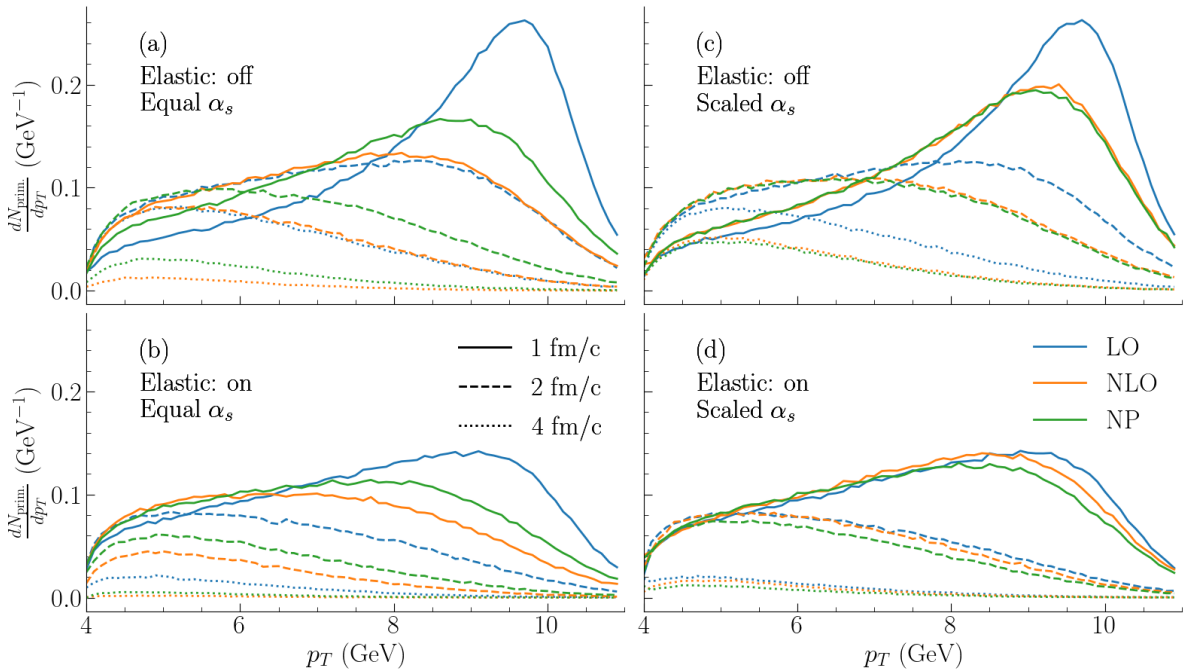

Figure 5.5: Same as Figure 5.3 but for the $(p_{init}, T) = (10, 0.5)$ GeV system.

the temperature-scaled momentum to $p/T = 20$, well inside the region where the rates were most different. In this case, the ordering of the curves before including elastic scattering is apparent. While the inclusion of the elastic scattering pushes them towards each other, the differences are not as small as the $p/T = 100$ or $p/T = 500$ case. This hints at the ability of the intermediate transverse momentum observables in HIC to probe the effects of the inclusion of higher-order kernels in a realistic simulation.

We can further probe the quenching ability of the radiative rates by computing the fractional energy loss

$$\frac{p_{init} - \langle p_T \rangle}{p_{init}} = \frac{1}{p_{init}} \left(p_{init} - \int_{p_{cut}} p_T \frac{dN_{primary}}{dp_T} \, dp_T \right) \tag{5.8}$$

where the $p_{cut} = 4$ GeV is the value of the momentum cut used in the brick simulation[4]. Figure 5.6 shows the fractional energy loss calculated for $p_i \in [20, 50, 100]$ GeV and $T \in [0.2, 0.3, 0.5]$ GeV, with a p/T ranging from 40 to 500. For each system of (p, T), as the parton evolves in the medium more and more energy is radiated out of

4 This is a somewhat large momentum cut to use. The brick tests above were all generated using this cut. The results in the realistic simulations use $p_{cut} = 4T$. So long as we are focused on the primary and high p_T partons, the brick results here are perfectly valid. A reminder that the p_{cut} means that radiated partons with energy less than this value are not taken into the event record. However, the energy loss due to their emission is still registered for the incoming parton.

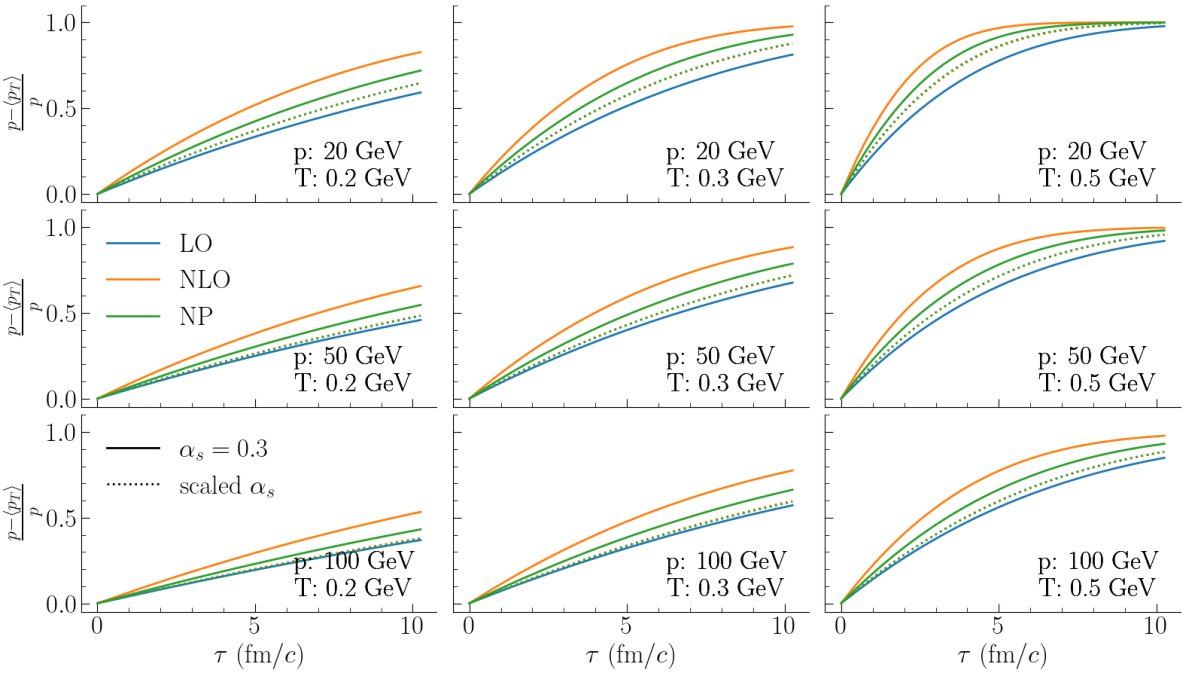

Figure 5.6: Fractional energy loss calculated for an up quark with three initial momenta (20, 50 and 100 GeV) in a static QGP brick held at three temperatures (0.2, 0.3 and 0.5 GeV). Elastic scatterings are turned off in this figure.

the transverse plane[5]. The effect of the scaling is to match the NLO and NP fractional energy loss to each other. The two are visibly different and more effective at quenching the energetic parton than the LO curve. Turning on the elastic channels for the fractional energy loss calculation results in Figure 5.7. Including collisional energy loss visually breaks the degeneracy of the NLO and NP results while reducing the separation between them and the LO simulation.

The conclusion here is that for an equal value of the coupling, the three rate sets predict a hierarchy of energy loss: $\Delta E_{NLO} > \Delta E_{NP} > \Delta E_{LO}$. However, rescaling the strong coupling for each rate set alters this ordering to $\Delta E_{NP} > \Delta E_{NLO} > \Delta E_{LO}$, bringing the rates with higher order kernels closer to the LO rate.

5 A caveat in the analysis is the value of p_{cut} that is used in the evaluation of the integral of Equation 5.8. With a high p_{cut}, while the leading parton is radiating away energy, new particles are not being added to the event. Therefore energy is not conserved at the event level.

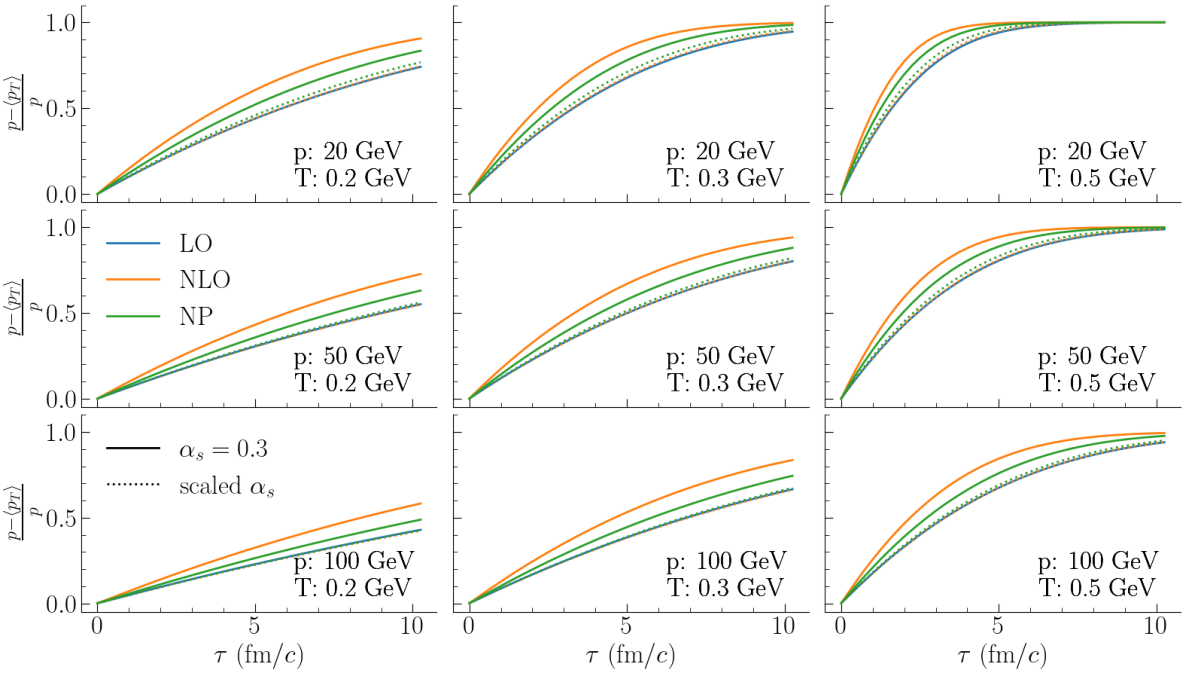

Figure 5.7: Same as Figure 5.6, including elastic scattering channels.

5.2 EVOLVING PLASMA AND FIXED COUPLING

A known fact about the LO-AMY calculations is how flat the computed charged hadron nuclear modification factor is relative to the data, particularly when the simulation is made using a fixed α_s [139]. The charged hadron nuclear modification factor is defined as

$$R_{AA}^{h^\pm}(p_T) = \frac{E\, d\sigma_{A\text{-}A}^{h^\pm}/dp^3}{N_{bin.}\, E\, d\sigma_{p\text{-}p}^{h^\pm}/dp^3} \tag{5.9}$$

where N_{bin} is the number of binary collisions that occur in a A-A and depends on the centrality of the collision. Deviations of this quantity from 1 can indicate energy loss of the hard partons[6] to the QGP medium. Another reason for taking such a ratio beyond its ability to clearly show the amount of the softening of the spectrum, is the assumption that systematic uncertainties (either in measurements or theoretical calculations) would cancel. Thus, in this chapter and throughout this work, all nuclear modification factors are computed with the same exact workflow, with and without medium effects for the numerator and the denominator, respectively.

6 The experimentally reported charged hadron R_{AA} is not specific to the hard sector and lower momentum regions are also measured. However, here the focus is specifically on hard parton energy loss and simulation.

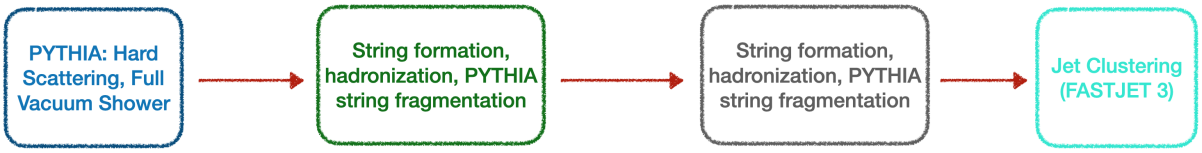

(a) `p-p` simulation workflow for single-stage calculations

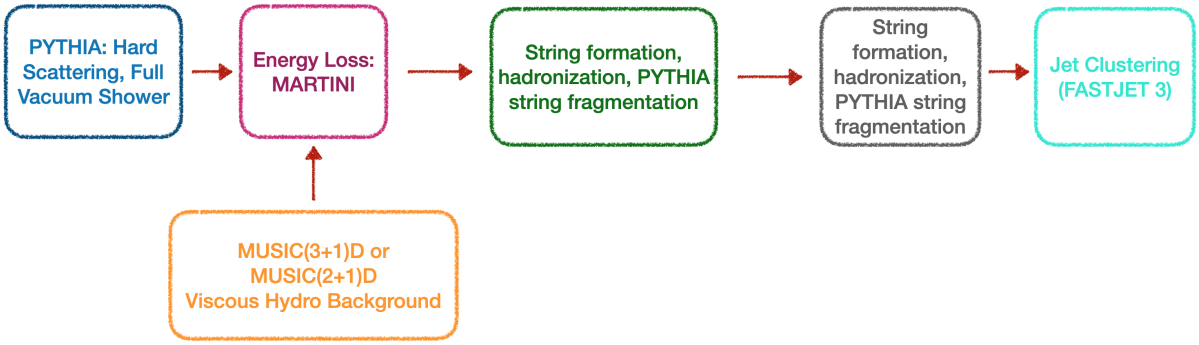

(b) `A-A` simulation workflow with single-stage MARTINI energy loss

Figure 5.8: (a) Workflow for simulation of proton-proton collisions (b) Single-stage workflow for simulation of jet energy loss in heavy ion collisions.

In this section, the new rates with higher-order collision kernels are used in simulations of jet energy loss in a realistic hydrodynamic background. Doing so requires a fit of the strong coupling. As mentioned before, typically, the main parameter of an energy loss model is either the value of the coupling (if one is considering a simulation with a fixed coupling) or the parameter(s) controlling its running.

5.2.1 *Event generation*

Figure 5.8 shows the workflow for `p-p` and `A-A` simulations. In this chapter, we employ a *single-stage* jet energy loss simulation[7] where a full vacuum shower is developed before MARTINI is used to model the interactions of the hard partons with the thermal medium.

7 The hard sector simulation is performed using PYTHIA+MARTINI but PYTHIA does not include any energy loss beyond the regular parton branching in vacuum. Thus the jet energy loss is a single-stage simulation.

$\sqrt{s}$ (GeV)	$\sigma_{\text{Inel.}}^{\text{NN}}$ (mb)-Theo.	$\sigma_{\text{Inel.}}^{\text{NN}}$ (mb)-Expt.
200	42	$43.82 \pm 0.21(\text{stat.})^{+1.37}_{-1.44}(\text{syst.})$[165]
2760	62	$62.8^{+2.4}_{-4.0}(\text{model}) \pm 1.2(\text{lumi.})$[166]
5020	68	-

Table 5.1: The inelastic proton-proton cross sections used in this thesis to convert differential cross sections to differential yields, presented with the current experimental measurements from the STAR [165] and ALICE [166] Collaborations.

For efficient simulation, the phase space is divided into sub-intervals in the transverse momentum of outgoing, hard partons, $\hat{p}_T$

$$\hat{\sigma} = N_{\text{evt}}^{-1} \sum_i \hat{\sigma}_i \tag{5.10}$$

where index i runs over the subintervals $[\hat{p}_{T,i}, \hat{p}_{T,i+1})$ and $\hat{\sigma}_i$ is the estimated cross section in that subinterval. The $\hat{p}_T$ intervals, in effect, control what range of exchanged momenta we wish to study, and the lowest and highest values are limited, respectively, by considerations for the validity of pQCD and maximum allowed momentum exchange in a $2 \to 2$ process ($< \sqrt{s}/2$). This subdivision of the phase space is necessary as the differential cross-section of most hard QCD processes falls off rapidly with transverse momentum. To effectively simulate high-p_T processes, it is necessary to artificially boost these regions of phase space. After the event simulation, the particle spectra from each $\hat{p}_T$ bin are added with the appropriate weight to construct the total cross-section, as shown in Equation 5.10. If the observable of interest is a yield, then the resulting spectrum from the simulation is divided by the total inelastic cross-section. The values used for this quantity in this thesis are provided in Table 5.1. These are computed within PYTHIA using the Regge Theory-based model of Refs. [163, 164].

Events in p-p hard collisions are generated using PYTHIA (version 8.209), including a full vacuum shower. The end of the parton shower signals the onset of the non-perturbative effects of hadronization. As there is currently no first-principles way of hadronizing a parton, Monte Carlo simulations rely on models of hadronization to convert the final state of a parton shower to a collection of hadrons which can then

be further processed. The default hadronization mechanism in this workflow is the famous Lund String Model, as implemented in PYTHIA [16, 167]. PYTHIA is also tasked with decaying unstable hadrons, defined as any hadron with a mean lifetime less than or equal to $\tau = 10$ mm/c [8].

The last stage of the simulation involves the clustering of the final particle list into jets. Jet reconstruction is a way of partially bypassing the non-perturbative physics by treating the composite jet object as a stand-in for the outgoing partons of the hard scattering. The most popular jet clustering algorithm, due to its infrared and collinear safety properties and computational viability, is the anti-k_T algorithm [168] as implemented in the FASJET3 package [169, 170]. The anti-k_T algorithm clusters the final hadrons into jets via the calculation and minimization of two distances,

$$\begin{aligned} d_{ij} &= \min\left(p_{T,i}^{-2}, p_{T,j}^{-2}\right)\frac{\Delta R_{i,j}^2}{R^2} \\ d_{iB} &= p_T^{-2} \end{aligned} \tag{5.11}$$

where d_{ij} is the distance between two particles i and j and d_{iB} is the distance between particle i and the beam. ΔR is the distance in the $\phi - \eta$ plane as given by

$$\Delta R_{i,j} = \sqrt{\Delta\eta_{i,j}^2 + \Delta\phi_{i,j}^2} \tag{5.12}$$

where $\Delta\eta$ and $\Delta\phi$ are the differences in the pseudorapidities and the azimuthal angles of the two particles, respectively. Finally, R is the algorithm's free parameter, controlling the cone size of the reconstructed jet. A limitation of anti-k_T algorithm is that it loses touch with QCD structure of parton branching and thus is unsuitable for jet substructure studies [171]. As such, more recent studies of jet quenching (see Ref. [172], for example), which are interested in the detailed structure of QCD emissions from a jet, first use the anti-k_T technique to find jets and then re-cluster the constituents of the jets using the Cambridge-Aachen algorithm, where the power of the transverse momentum factors in Equation 5.11 is set to zero. Therefore it clusters the jet based purely on pairwise geometrical distance. In this thesis, the anti-k_T algorithm is the only jet clustering algorithm used, with the same cone size radii and kinematic cuts as those of experiments whenever compared to measurements of jets.

8 This is a standard definition for the stability of a particle for experimental collaborations. The same definition is used when comparing simulation results to measurements. It is used universally throughout this thesis.

The jet-clustering stage in A-A collisions requires an extra step at the analysis level, corresponding to medium-response to the passage of the energetic partons. In elastic scattering events of the jet parton with the medium, the momentum transfer between the jet and the medium particle can occasionally be large enough to promote the latter to a jet ($p > p_{cut}$). In such a case, the medium particle is taken into the event record as a hard parton and called a *recoil* parton while the *hole* left in the medium as a result of this interaction is also taken in but only allowed to free-stream, to ensure energy-momentum conservation. At the end of evolution, jet particles, including recoils, are hadronized together, while holes are hadronized separately. The hadrons resulting from these negative energy partons are then subtracted from reconstructed jets. For jets reconstructed with a cone radius R, this subtraction is done via

$$p^{\mu}_{\text{jet,subtracted}} = p^{\mu}_{\text{jet,raw}} - \sum_{\text{holes},\Delta r_i \leqslant R} p^{\mu}_i , \tag{5.13}$$

where the criteria for subtraction from jets is if a hadron resulting from hole partons falls within the jet cone

$$\Delta R = \sqrt{\Delta\eta^2 + \Delta\phi^2} \leqslant R \tag{5.14}$$

with $\Delta\eta$ and $\Delta\phi$ being the difference of pseudorapidity and azimuthal angle between the jet and the hole hadron. The subtraction for the charged hadron spectrum is given by

$$E\frac{d\sigma}{dp^3}_{\text{subtracted}}(p_T) = E\frac{d\sigma}{dp^3}_{\text{raw}}(p_T) - E\frac{d\sigma}{dp^3}_{\text{holes}}(p_T) . \tag{5.15}$$

Including medium response via recoils and subtraction of holes has been shown to be an important effect in computing jet spectra and jet-substructure observables [107].

The information flow in the simulations of single-stage jet energy loss in heavy ion collisions is presented in Figure 5.8b. For jet calculations in HIC, the major difference between a heavy ion event and a p-p event, beyond nuclear PDFs, is the existence of the thermal medium and the addition of the low virtuality energy loss as described by MARTINI. The finalized parton shower from PYTHIA is passed to MARTINI for evolution in the hydrodynamic medium. The evolution starts at $\tau_0 = 0.4$ fm/c and ends, on a parton-by-parton basis, when the local temperature falls below the critical temperature, $T_c = 160$ MeV or if the parton's momentum falls below the momentum cut,

STAGE	PARAMETER	VALUE	NOTE
PYTHIA	Tune No.	15	CMS underlying event tune
	PDF	CTEQ6L.1	Free proton PDF
	nPDF	EPS09LO	Nuclear mods. to the PDFs
MARTINI	N_f	3	Number of flavours
	$\alpha_{s,0}$	0.3	Fixed coupling
	$E_{Loss,cut}$	4T	Energy loss cut
	p_{cut}	4T	Cut on radiated p
	$p_{recoil,cut}$	4T	Cut on recoil parton p
	T_c	160 MeV	Decoupling temperature

Table 5.2: Parameter list used in the fixed coupling workflow.

$p_{cut} = 4T$, where T is the local temperature of the fluid. Once all partons are frozen out of evolution, they are passed to PYTHIA for hadronization. The hadronization and jet clustering steps are done precisely like the proton-proton simulations which form the baseline. Table 5.2 summarizes the parameters.

5.2.2 *Simulation results*

The study of jet-medium interactions is through the construction of *nuclear modification factors*, an example of which was presented in Equation 5.9. These are defined as the ratio of an observable in `A-A` collisions over the value of that observable in the equivalent `p-p` collision, appropriately scaled. The `p-p` baseline forming the baseline of the nuclear modification factors used here is calculated using the simulation workflow of Figure 5.8a and shown in Section A.2. The events are simulated with PYTHIA Tune No. 15 [173], which uses the CTEQ6L.1 [13] parton distribution functions. The heavy ion simulations use the same tune and free proton PDFs and include nuclear modification factors from the EPOS09 [174] nuclear PDFs. The hydrodynamic background used throughout this chapter is the event-by-event simulations done using

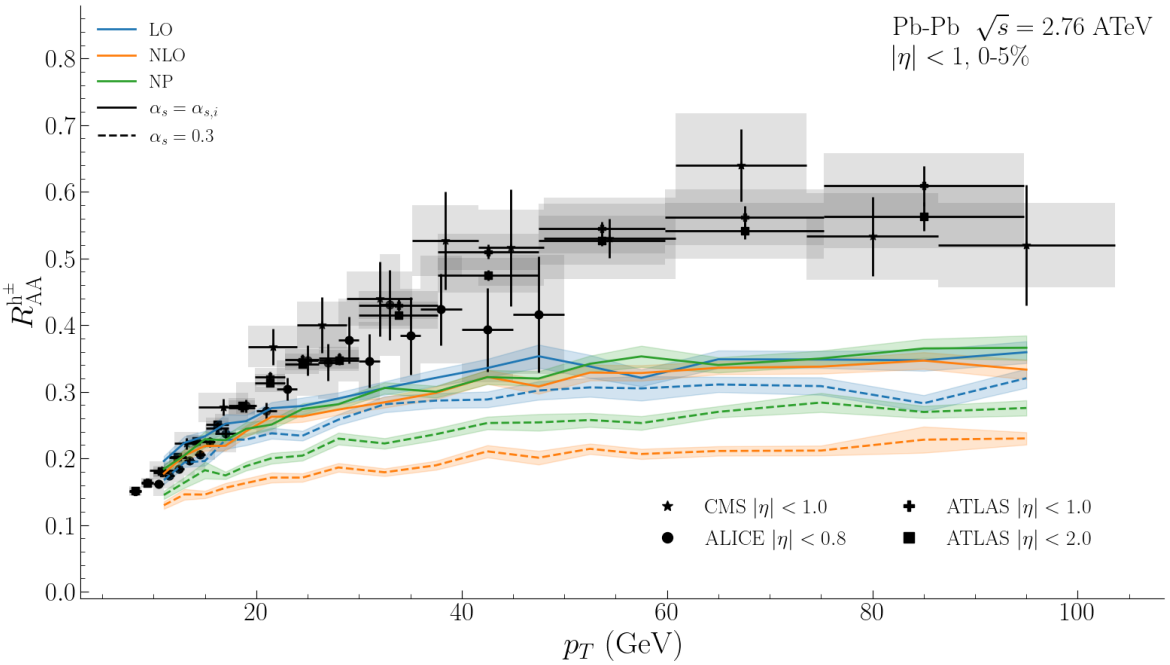

Figure 5.9: Charged hadron R_{AA} using the new rates, compared to experimental data. Solid and dashed lines denote the *fixed* and *fitted* setups, respectively (see text). The collision system is `Pb-Pb` at $\sqrt{s} = 2.76$ ATeV and the 0-5% centrality class. The spectra are constructed for midrapidity ($|\eta| < 1.0$). Experimental data is taken from ALICE [175], ATLAS [176] and CMS [177] Collaborations.

the IPG-M approach, described in Chapter 3. The dashed lines Figure 5.9 show the result of the simulation when $\alpha_{s,0} = 0.3$ is used for all three rate sets (and both energy loss channels). The ordering of the lines conforms to our expectation given the discussion of Section 5.1. The rate set affecting the most energy loss is the NLO, while NP and LO results are less quenched. The NLO curve is nearly 35% below the NP-calculated R_{AA} and 50% below the LO one. For further analysis, we fit the strong coupling constant of each rate set independently by minimizing the χ^2 function

$$\chi^2/\text{d.o.f} = \frac{1}{\sum_i 1} \sum_i \frac{\left(y_{\text{exp.},i} - y_{\text{theo.},i}\right)^2}{\sum_s \sigma_{s,i}^2} \tag{5.16}$$

on charged hadron R_{AA} data of `Pb-Pb` collisions at 2.76 ATeV and 0-5% centrality. In the equation above, i sums over the experimental data points with $p_T > 10$ GeV, and

RATE SET	α_s
LO	0.280
NLO	0.242
NP	0.260

Table 5.3: Fitted values of α_s from the χ^2 fit.

sum over the sum over s adds the uncertainties. The solid lines in Figure 5.9 show the results of this fit[9]. The labelling of the lines follows

A. *fixed*: $\alpha_{s,0} = 0.3$ for the three rate sets

B. *fitted*: each rate set uses the associated fitted value of α_s.

As before, the value of α_s is the same for the elastic and radiative channels in each run. The fitted curves collapse on top of each other, particularly for larger transverse momenta. At lower p_T, the LO results are visibly above those of the higher order corrections. However, given the size of the uncertainties, one cannot make a more categorical statement. The slope also, is mostly the same. Thus, in a fixed coupling simulation, the inclusion of the higher-order collision kernels does not change the curvature of the charged hadron R_{AA}. We can also look at the scaling of the fitted values of α_s from Table 5.3

$$\frac{\alpha_{s,NLO}}{\alpha_{s,LO}} \approx \sqrt{0.74} \quad \frac{\alpha_{s,NP}}{\alpha_{s,LO}} \approx \sqrt{0.86}. \tag{5.17}$$

The ratios are remarkably close to the values that were found in Equation 5.7, where the scaling was applied to the radiative rates directly. The deviations are due to the effects of including elastic scatterings. This once again confirms that in a realistic simulation, the differences between the rate sets as a result of using the new collision kernels can be absorbed in a rescaled value of the strong coupling.

9 The fit was performed with simulations where $p_{cut} = 4$ GeV. The p_{cut} of the results shown here are 4T, which is approximately equivalent to a $p_{cut} = 2$ GeV cutoff. As such the solid lines may not look like a good fit, but the fundamental conclusion of the discussion is the same.

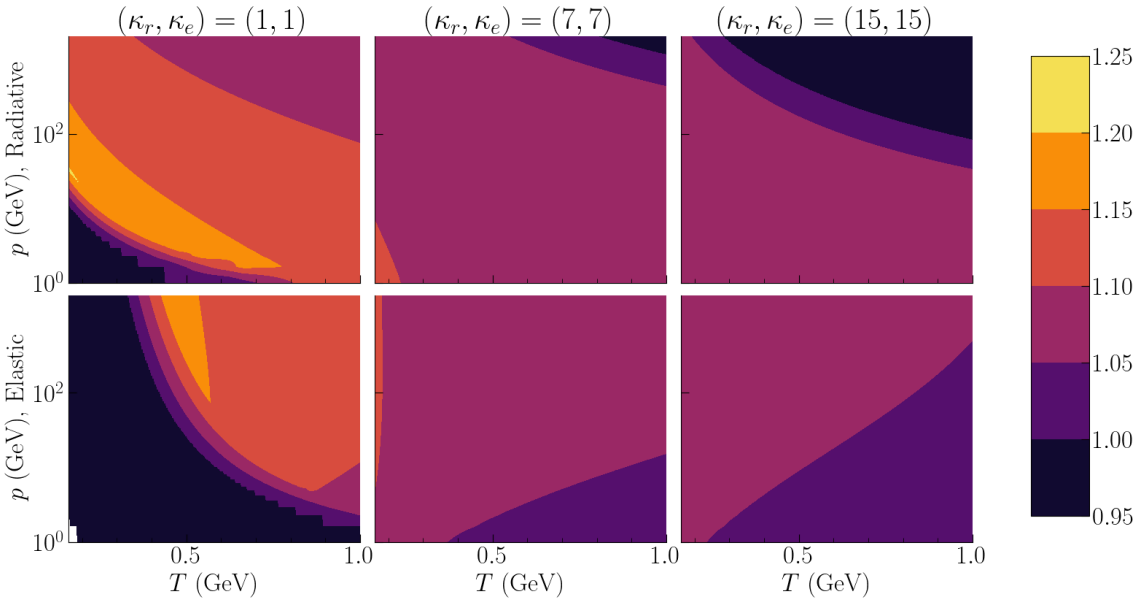

Figure 5.10: Ratio of the running radiative and elastic couplings for $\alpha_{s,0} = 0.2$ to $\alpha_{s,0} = 0.4$ for three choices for (κ_r, κ_e). The top row is the ratio of the radiative coupling, while the bottom panel shows the ratio of the elastic coupling.

5.3 EVOLVING PLASMA AND RUNNING COUPLING

The study in the previous section was done with a fixed and equal α_s for both energy loss channels. While such a study is instructive, it is an approximation. To better analyze the effect of the new collision kernels, we need to go beyond the fixed coupling and allow for the running and scale dependence of α_s. This is done by first fitting the running coupling parameters used in MARTINI, $(\kappa_r, \kappa_e, \alpha_{s,0})$ (see Section 4.4) for all three rate sets, before moving into a multi-probe study. The fit presented here is the first systematic fit and analysis of the parameters of the MARTINI energy loss framework.

5.3.1 *Fit of α_s: parameters and initial discussion*

In such a simulation, all parameters connected to the MARTINI model should be included in a fit. However, our aim is not a complete fine-tuning of MARTINI but rather to study the effect of the collision kernels on high-p_T observables. As such, only the parameters that are specific to the running coupling are considered for the fitting

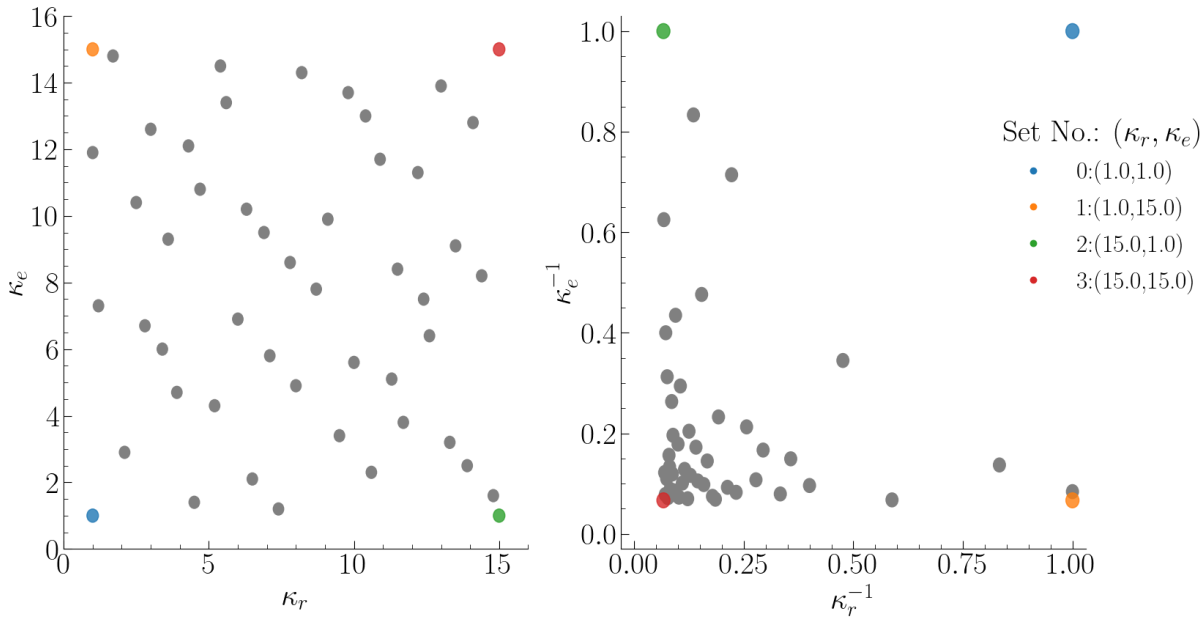

Figure 5.11: Parameter space in the (κ_r, κ_e) plane, sampled using the Sobol sequence. Fifty points are chosen on the plane for $\kappa_{r,e} \in [1, 15]$. The figure on the left shows the space while the figure on the right plots the points on the $(\kappa_r^{-1}, \kappa_e^{-1})$ plane. The latter is used in the fitting procedure. Highlighted points are the edges of the space.

procedure, and all others are fixed to physically motivated values. These include the momentum cut parameters $(p_{cut}, E_{loss,cut}, p_{recoil,cut})$, which are, respectively, the momentum cut controlling whether a radiated parton is taken into the event record, the energy cut below which the parton is no longer evolved and finally the momentum cut on recoil partons in elastic scattering events. These cuts are all a measure of whether a given parton is considered *hard* and thus evolved like a jet or *soft*, where MARTINI is unsuited for its evolution. The values of these cuts are set to $4T$, four times the local temperature. The average energy of a thermal particle is $\frac{3}{2}T$. Thus $4T$ is a reasonable cut to separate the soft and hard scales in the simulations. The other major parameter is the jet-decoupling temperature which we keep as $T_c = 160$ MeV. This value should be above the switching temperature of the QGP to hadronic gas (≈ 155 MeV). In principle, the momentum cuts and the decoupling temperature should be included in a tuning effort of MARTINI. However, such an exercise is not our intent. Moreover, based on preliminary studies, the dependence of the simulation results in moderate changes in these parameters is relatively weak.

The remaining parameters are those governing the running of the strong coupling. Figure 5.10 shows the sensitivity of the running coupling to a change in $\alpha_{s,0}$ for three different values of (κ_r, κ_e). The figure is the ratio $\alpha_{s,(rad/elas)}(\alpha_{s,0} = 0.2)$ to $\alpha_{s,(rad/elas)}(\alpha_{s,0} = 0.4)$. Doubling this parameter results in at most 20% difference in the running coupling. As such, for this fit, the value of $\alpha_{s,0}$ is set to 0.3 and eliminated from the parameter list.

The fit space is, then, the (κ_r, κ_e) plane. We sample the parameter space using Sobol sampling [178–180], a sampling method that gives even coverage of the space. The benefit of using the Sobol sequence is the ability to add new points to the parameter space if it is decided that more resolution is needed. The sampled points are presented in Figure 5.11. Figure 5.12 shows the charged hadron R_{AA} simulations results for each member of the parameter space shown in Figure 5.11. The R_{AA} curves from the boundary points are in shown colour. There are four main takeaways from the figure

A. different rate sets with the same $\kappa_{r,e}$ observe the $\Delta E_{LO} < \Delta E_{NLO} < \Delta E_{NP}$ pattern as the previous section

B. there is significant degeneracy where very different sets of $\kappa_{r,e}$ values, for example $(1, 15)$ and $(15, 1)$, give very similar results for $R_{AA}^{h^\pm}$. This is particularly true for LO and NP rates

C. the sample simulations provide a good coverage of the experimental data, thus there is reasonable expectation of recovering an optimal fit,

D. even for very large values of $\kappa_{r,e}$, i.e. $(15, 15)$, significant quenching can be observed.

The first observation is not surprising and is a good check on the running mechanism as the same parameters, applied in the same system, give the same running coupling, and therefore the rates would be evaluated with the same α_s. The issue of degeneracy can be handled by including an observable that breaks it. Jet nuclear modification factors for different jet cone radii are useful in this respect as due to their exclusive and three-dimensional nature. These are defined as

$$R_{AA}^{jet}(p_T; R) = \frac{d\sigma_{A\text{-}A}^{jet}/dp_T d\eta|_R}{N_{bin.}\, d\sigma_{p\text{-}p}^{jet}/dp_T d\eta|_R}. \tag{5.18}$$

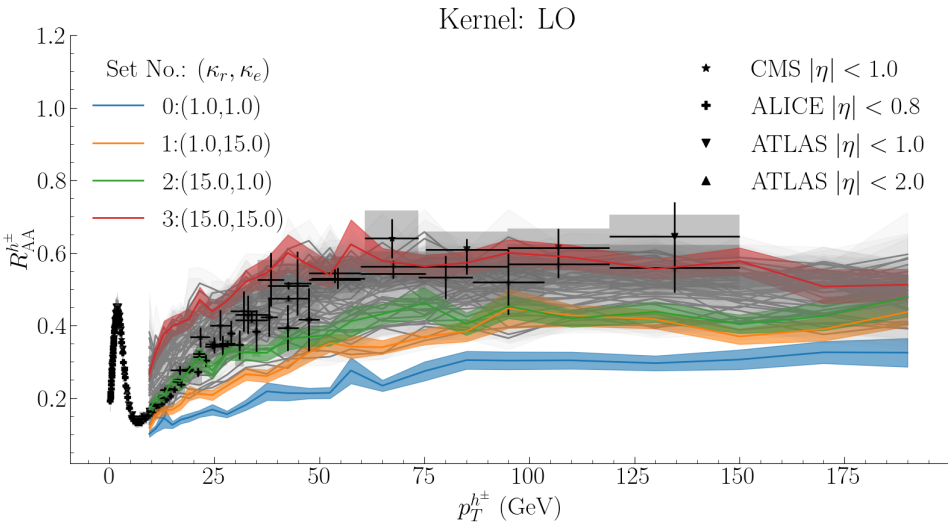

(a) $R_{AA}^{h^\pm}$ initial runs, LO set

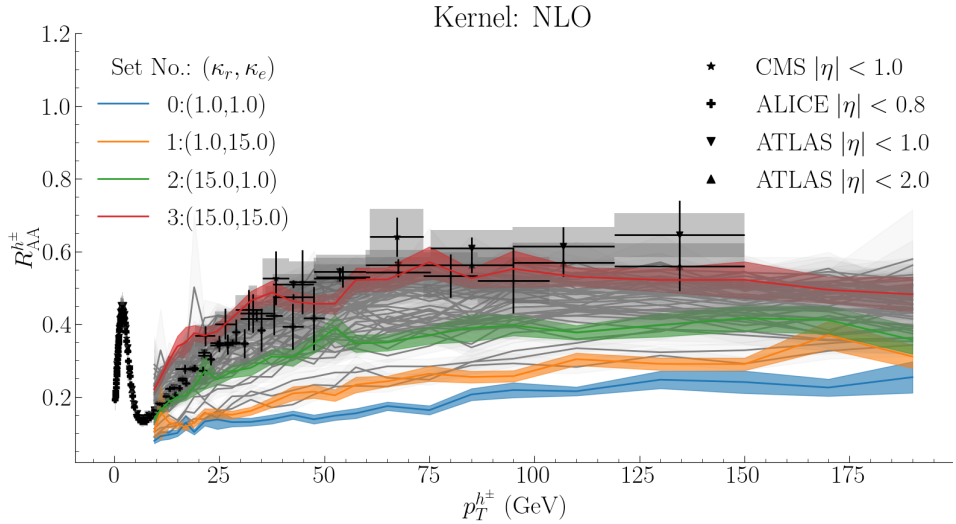

(b) $R_{AA}^{h^\pm}$ initial runs, NLO set

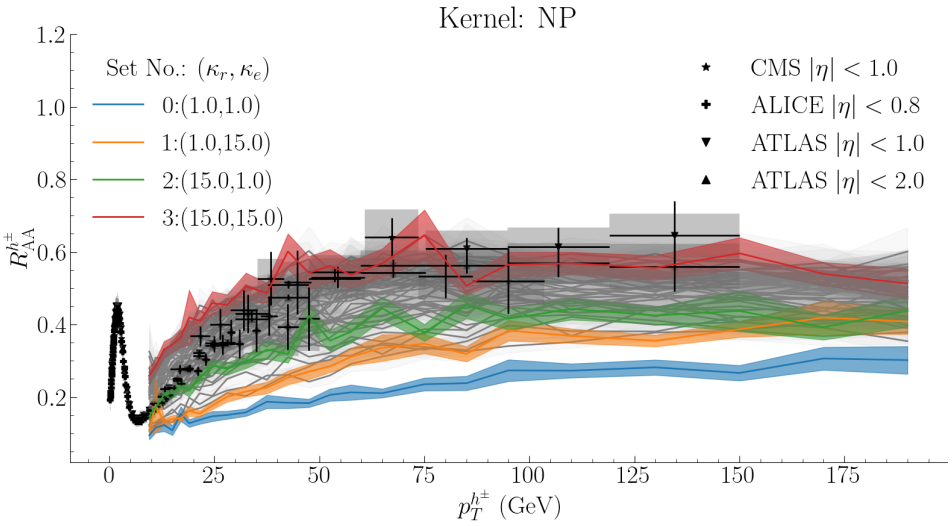

(c) $R_{AA}^{h^\pm}$ initial runs, NP set

Figure 5.12: Charged hadron nuclear modification factors from the sampled values of $\kappa_{r,e}$.

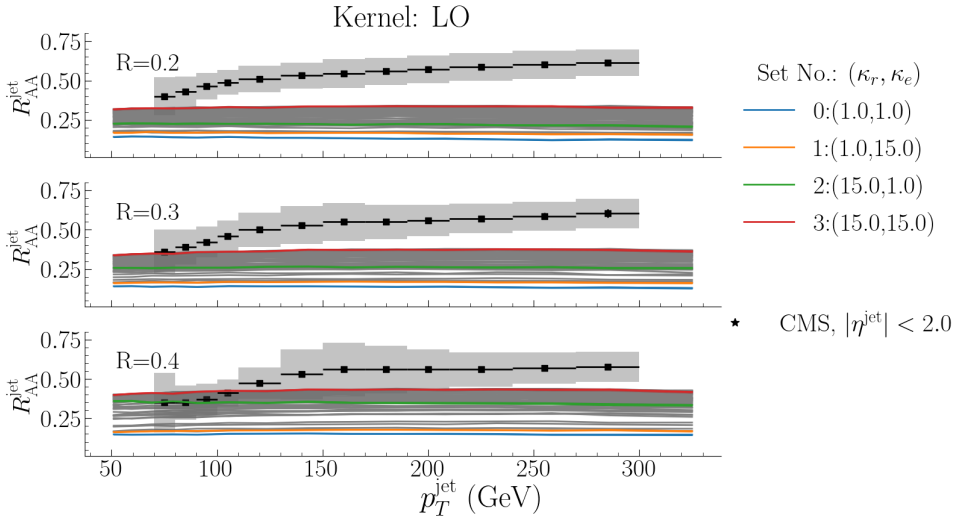

(a) R^{j}_{AA} initial runs, LO set

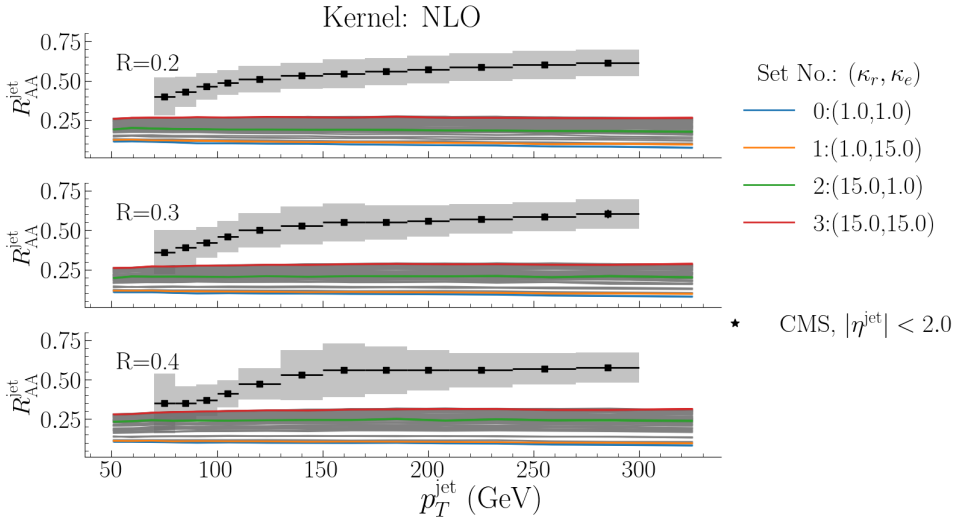

(b) R^{j}_{AA} initial runs, NLO set

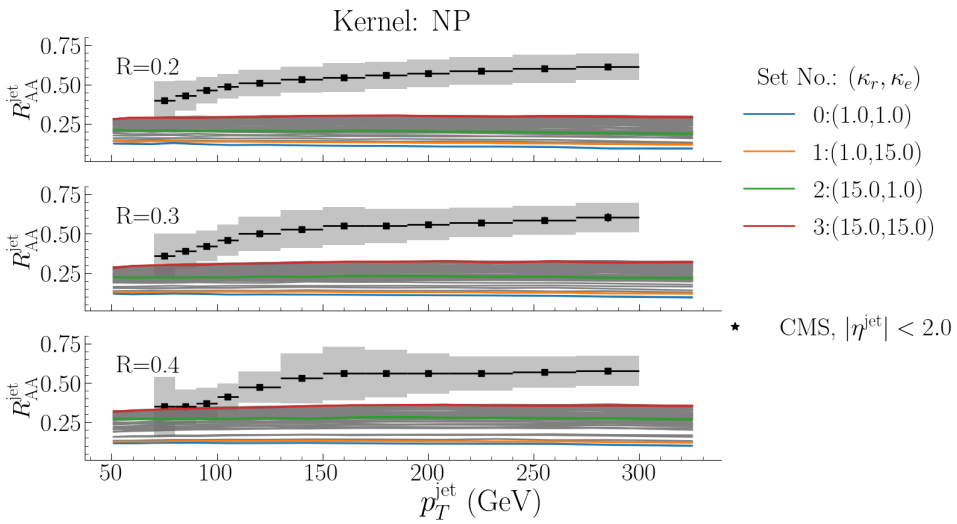

(c) R^{j}_{AA} initial runs, NP set

Figure 5.13: Inclusive jet nuclear modification factors from the sampled values of $\kappa_{r,e}$.

where R is the cone radius used to cluster the hadrons into jets in the anti-k_T algorithm. Figure 5.13 shows the jet nuclear modification factor calculations from the same simulations. While the degeneracy observed in charged hadron R_{AA} is broken when jets are included, the over-quenching issue is observed even more dramatically here. All $\kappa_{r,e}$ sets miss the jet R_{AA} data by nearly a factor of two. This is a setback in the single-stage view of jet energy loss in HIC and an important topic which we will come back to in Section 5.4. For now, we consider other jet observables, such as jet shape, an observable that deals with the internal substructure of jets and is defined as

$$\rho\left(r, R_0\right) \equiv \frac{N_{\text{norm}}}{N_{\text{jet}}} \sum_{\text{jets}} \sum_{r \in [r_{\min}, r_{\max})}^{r_{\max} < R_0} \frac{p_T^{\text{trk}}}{p_T^{\text{jet}}} \tag{5.19}$$

where the sums run over all jets with a cone radius of $R = R_0$. The variable r is the radial distance of the charged hadron track from the jet axis in the plane transverse to it and is given by

$$r = \sqrt{\left(\phi_{\text{trk}} - \phi_{\text{jet}}\right)^2 + \left(\eta_{\text{trk}} - \eta_{\text{jet}}\right)^2}. \tag{5.20}$$

The jet shape analog to jet nuclear modification factor is the jet shape ratio, which for a given jet cone radius $R = R_0$, is defined as

$$R_\rho\left(r, R_0\right) = \frac{\rho_{AA}\left(r, R_0\right)}{\rho_{pp}\left(r, R_0\right)} \tag{5.21}$$

where $\rho_{AA}(r)$ and $\rho_{pp}(r)$ are the `A-A` and `p-p` jet shape functions computed via Equation 5.19. This quantity measures the effect of jet-medium interactions on the shape of the jet as a function of the radial distance from the jet axis in the $\eta - \phi$ plane.

Figure 5.14 gives the jet shape ratio calculated using Equation 5.21 for the parameter runs of Figure 5.11. While the simulations miss the jet nuclear modification factor, indicating that they are significantly over-quenching the jet spectra, the shape of the jets coming out of the simulations is remarkably close to the data. It seems that the charged hadron R_{AA} and jet shape ratio are resilient to over-quenching. Or, put differently, while the populations of charged hadrons and jets shown in Figs. 5.12,5.13,5.14 are wrong, MARTINI-modified jets will look as they should. Thus, the observables used for the fit are the charged hadron nuclear modification factor and jet shape.

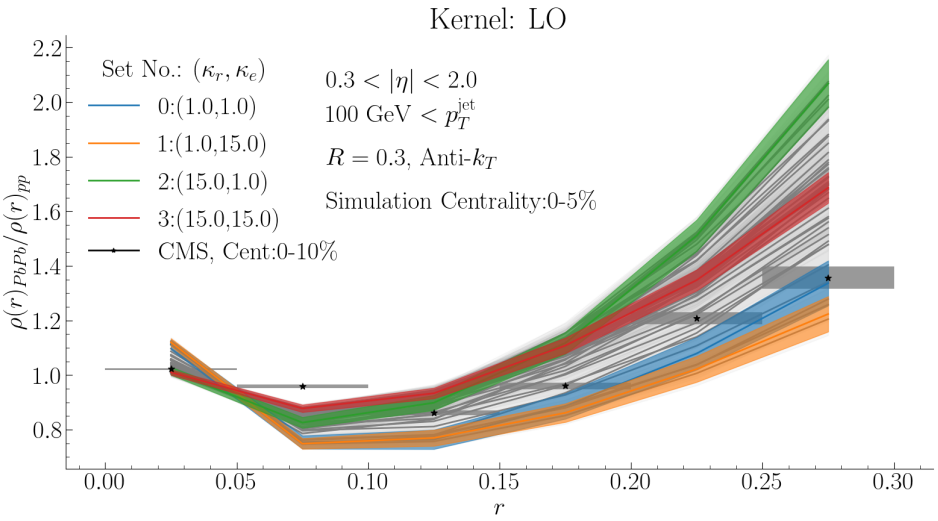

(a) Jet shape ratio initial runs, LO set

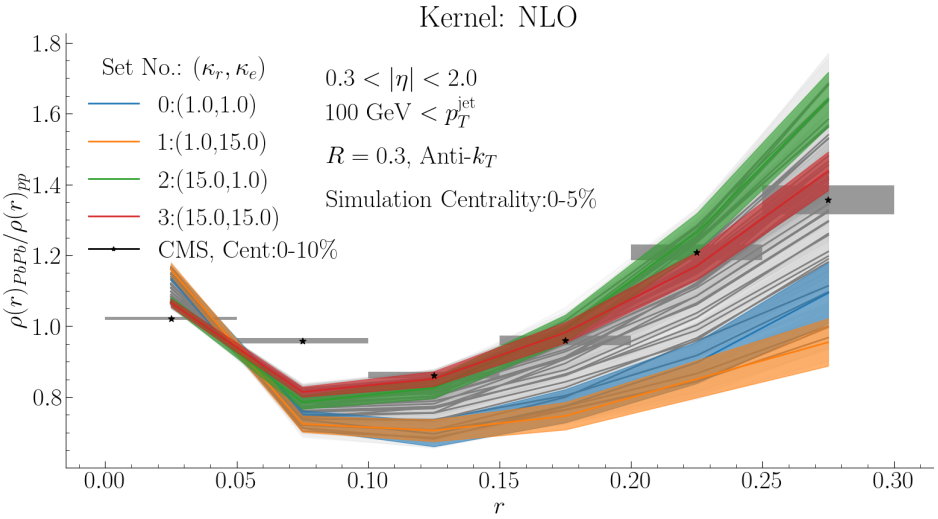

(b) Jet shape ratio initial runs, NLO set

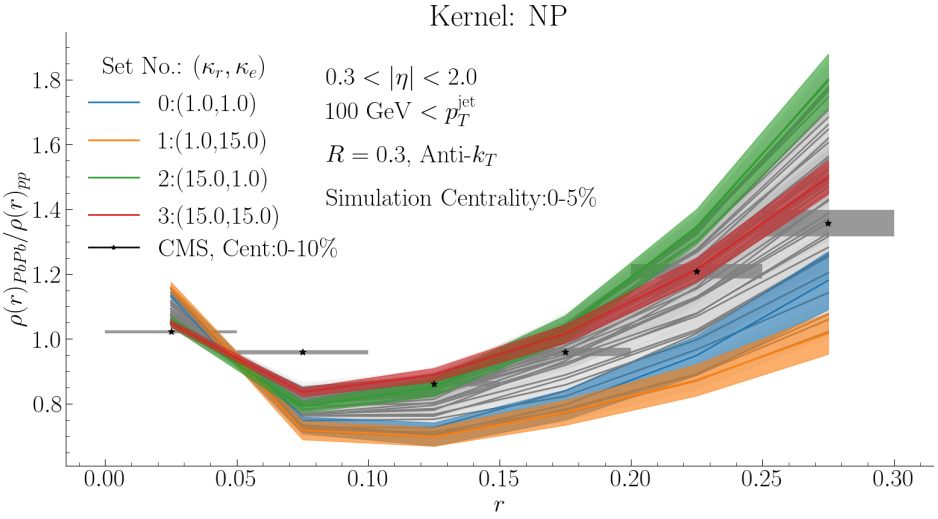

(c) Jet shape ratio initial runs, NP set

Figure 5.14: Jet shape ratios from the sampled values of $\kappa_{r,e}$.

5.3.2 *Fit Procedure*

For the fit target, the same χ^2 function of Equation 5.16 is considered. For each (κ_r, κ_e) set, χ^2 is calculated using charged hadron R_{AA} data from the CMS, ALICE and ATLAS Collaborations for 0-5% centrality class of `Pb-Pb` collisions at 2.76 ATeV, as well as jet shape ratio for the 0-10% centrality class of the same system from the CMS Collaboration. We are particularly interested in the potential degeneracy in the model and how sensitive its performance is to the parameter space. Thus, we utilize Gaussian Process Regression (GPR) [181] for the fit.

5.3.2.1 *Gaussian Process Regression: brief overview*

Why Gaussian Process Regression? The aim is to arrive at optimal or close to optimal parameters in the running of the strong coupling of MARTINI with *optimal* defined by the performance of MARTINI simulations in reproducing the target observables. There exists a function, $f(\kappa_r, \kappa_e)$, underneath our calculations, and it is this function that we want to optimize in order to get our fit results. Typically one would go about this process by assuming a shape or functional form for f and fit the free parameters of this functional form. From there, it is a simple matter of taking derivatives. This can be called a *restriction* bias approach where we restrict the space of functions that can fit our data [181]. However, we do not know what this function is, nor its dependence on the parameters. The two parameters are simply values that multiply the scale at which α_s is evaluated and thus enter the simulations in a highly non-linear way. Furthermore, there is no physics input or direction that could guide us here toward a specific functional form. On the other hand, we can also come at this problem in a *preference* bias way [181]. In this case, we do not restrict ourselves to only a specific class of functions but instead, consider all possible functions that can describe our data. This is done by using Gaussian process regression (GPR). A Gaussian process can be thought of as the generalization of a Gaussian distribution that seeks to describe functions instead of trying to describe scalars or vectors. Thus a GP is, in effect, a Gaussian prior placed on the target function. Each sampling of the GP results in a random function [11]. In this way, the interpolation is done in function space, and we are not specifically attached to a given modelling choice, making life

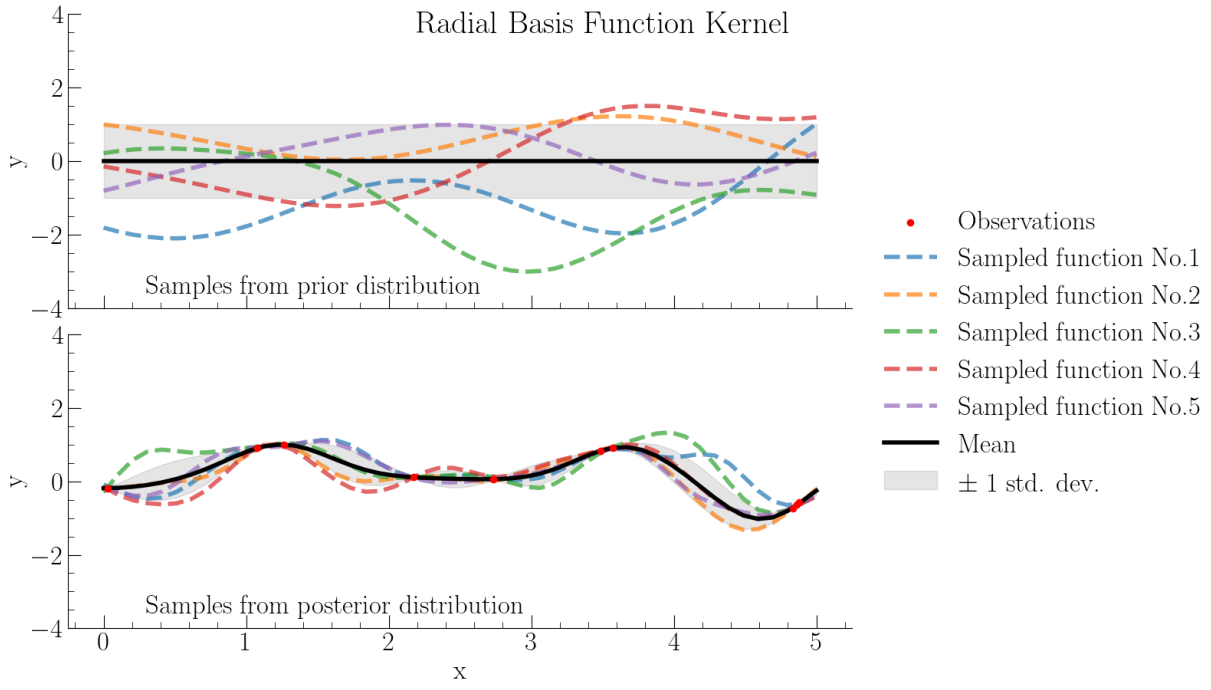

Figure 5.15: Example of sampling from a Gaussian process before (top) and after (bottom) training on observed data.

so much simpler. In esssense, we are *emulating* the model – which is MARTINI energy loss – very efficiently. This also gives the second –and very practical– reason to use GPR: computational expense. Each model evaluation entails a full simulation of 0-5% centrality `Pb-Pb` collisions at 2.76 ATeV. In practical terms, each evaluation takes approximately 1 core-year[10]. In a typical fitting exercise, the model would need to be evaluated hundreds, if not thousands, of times. The computational expense and time-cost of fitting a model like MARTINI can very quickly get out of control. Gaussian process regression is therefore an extremely efficient and simple way to learn more about the model and its parameter space.

A Gaussian Process (GP) is specified [181] by a mean and a kernel function

$$\begin{aligned} m(x) &= E[f(x)] \\ k(x,x') &= E[f(x) - m(x)(f(x') - m(x'))]. \end{aligned} \tag{5.22}$$

10 A core-year is defined as the amount of computation done by one CPU if it was to be in constant use for 1 year.

where $f(x)$ is the process or target function we wish to study. The kernel function, $k(x, x')$, describes the covariance of any two points. An example of a kernel is the radial basis function or RBF

$$\mathrm{RBF}(x, x'; l) = \exp\left(-\frac{d(x, x')^2}{2l^2}\right) \tag{5.23}$$

where l is the length scale, a *hyperparameter*. In a GPR, the hyperparameter(s) of the kernel are learned from the data. The learning is done by maximizing the log-marginal-likelihood (LML). Once the kernel's hyperparameters are learned, we can then use our GPR to predict the value of the target function at a new position. Figure 5.15 shows an example of this for the RBF kernel. In the top panel, we have an example of an untrained GPR, and each sample of the GPR results in a function normally distributed around 0 with a standard deviation of 1. Ten artificial data points were used in the bottom panel to train the GPR. Now each sampling from the GPR is conditioned to give functions normally distributed around the target function and pass through (or close to) the trained points. Notice that the uncertainty grows between the points where there is no data.

5.3.2.2 *Procedure*

The goal is to train a GPR on the computed values of χ^2. The compound kernel used in the regression step is

$$k(x, x') = \mathrm{Matern}(x, x'; \nu, l) + \mathrm{RBF}(x, x'; l) \tag{5.24}$$

In the above, $\mathrm{RBF}(x, x'; l)$ is the Radial Basis Function kernel, a stationary kernel defined in Equation 5.23 and the Matérn kernel, which is a generalization of the RBF kernel and is given by

$$k(x, x'; \nu, l) = \frac{1}{\Gamma(\nu)2^{\nu-1}}\left(\frac{\sqrt{2\nu}}{l}d(x, x')\right)^{\nu} K_\nu\left(\frac{\sqrt{2\nu}}{l}d(x, x')\right) \tag{5.25}$$

where K_ν is the modified Bessel function. The parameter ν controls the smoothness of the function and as $\nu \to \infty$, a Matérn kernel approaches the RBF kernel.

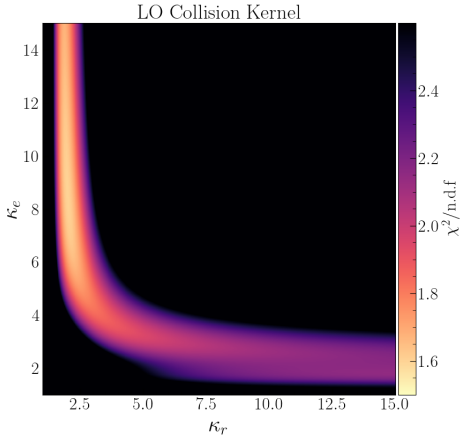

(a) (κ_r, κ_e) space, LO rate

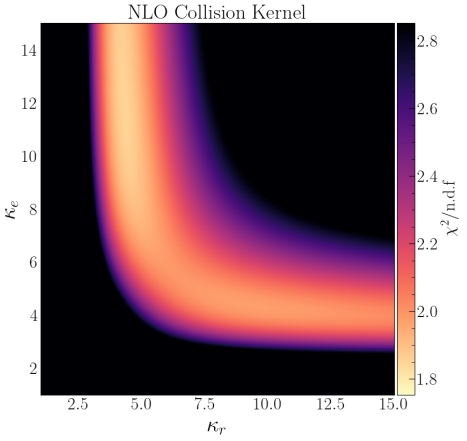

(b) (κ_r, κ_e) space, NLO rate

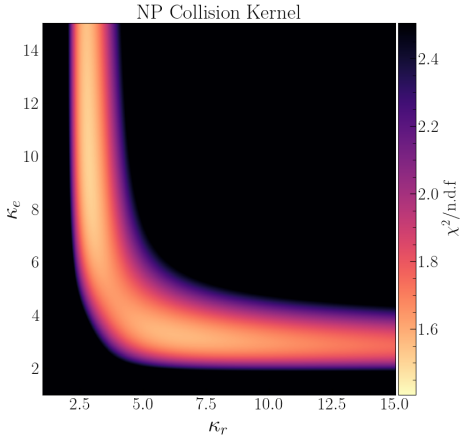

(c) (κ_r, κ_e) space, NP rate

Figure 5.16: Heat map of the LO, NLO and NP (κ_r, κ_e) generated using Guassian Process Regression of the calculated χ^2 of each κ pair.

For the choice of a kernel, it was found, through trial and error, that the composite kernels

$$\begin{aligned} k_{LO}(\mathbf{x}, \mathbf{x}') &= \text{Matern}(\mathbf{x}, \mathbf{x}'; \nu = 3/2, l = 1) + \text{RBF}(\mathbf{x}, \mathbf{x}'; \mathbf{l} = (0.001, 0.001)) \\ k_{NLO}(\mathbf{x}, \mathbf{x}') &= \text{Matern}(\mathbf{x}, \mathbf{x}'; \nu = 5/2, l = 1) + \text{RBF}(\mathbf{x}, \mathbf{x}'; \mathbf{l} = (0.001, 0.001)) \\ k_{NP}(\mathbf{x}, \mathbf{x}') &= \text{Matern}(\mathbf{x}, \mathbf{x}'; \nu = 5/2, l = 1) + \text{RBF}(\mathbf{x}, \mathbf{x}'; \mathbf{l} = (0.001, 0.001)) \end{aligned} \tag{5.26}$$

yield the best results when judged visually. We use $\mathbf{x} \equiv \vec{\kappa}^{-1} = \left(\kappa_r^{-1}, \kappa_e^{-1}\right)$ as the argument in the above kernels due to observations of significant nonlinearity in the calculated values of the χ^2. This modification made it easier for the GPR to train on the data. From here, 2000 iterations were made where 3 data points would be randomly

RATE SET	κ_r	κ_e
LO	2.0	8.6
NLO	4.4	11.6
NP	2.8	9.8

Table 5.4: Fit results of (κ_r, κ_e) for the different rate sets using Gaussian process regression.

chosen and set aside as test points at each step while the GPR was trained on the other 47. After the training, the mean-squared-error of the trained model versus the test points

$$\text{MSE} = \frac{1}{3}\sum_{i=1}^{3}(\mathcal{GP}(\mathbf{x}_i) - y_i)^2 \tag{5.27}$$

is calculated. The model with the lowest MSE is then chosen as the best performing. The result of the calculation is shown in Figure 5.16. The fit results, or the optimal (κ_r, κ_e) set, is found by evaluating the GPR over the entire plane and finding the set that is the minimum of the function. This is equivalent to evaluating

$$\kappa_r, \kappa_e = \mathrm{argmin}_i(\mathcal{GP}(\mathbf{x}_i)) \tag{5.28}$$

where i runs over the (κ_r, κ_e) pairs for which the GPR is evaluated.

The structure observed in the heatmaps of Figure 5.16 shows the significant level of degeneracy in the parameters of the running coupling in MARTINI. It is clear that with the current implementation of MARTINI in a single-stage simulation, similar amounts of energy loss can be observed for a range of different values of the parameters. The strength of the coupling can be thought of as a measure of the strength of specific channel, elastic or inelastic energy loss. In essence, it indicates that in a simulation where radiative channels are weak but elastic channels are strong, we can have nearly the same amount of energy loss as one which has strong radiative channels but weak elastic ones. At this stage, it is an open question whether the observed degeneracy is a property of MARTINI as a physical model or is due to the way it is being employed, in a single-stage energy loss calculation.

Table 5.4 shows the resulting κ_r and κ_e valeus from the procedure above. The ordering of the different κ values follows the discussion of the rates in a static medium

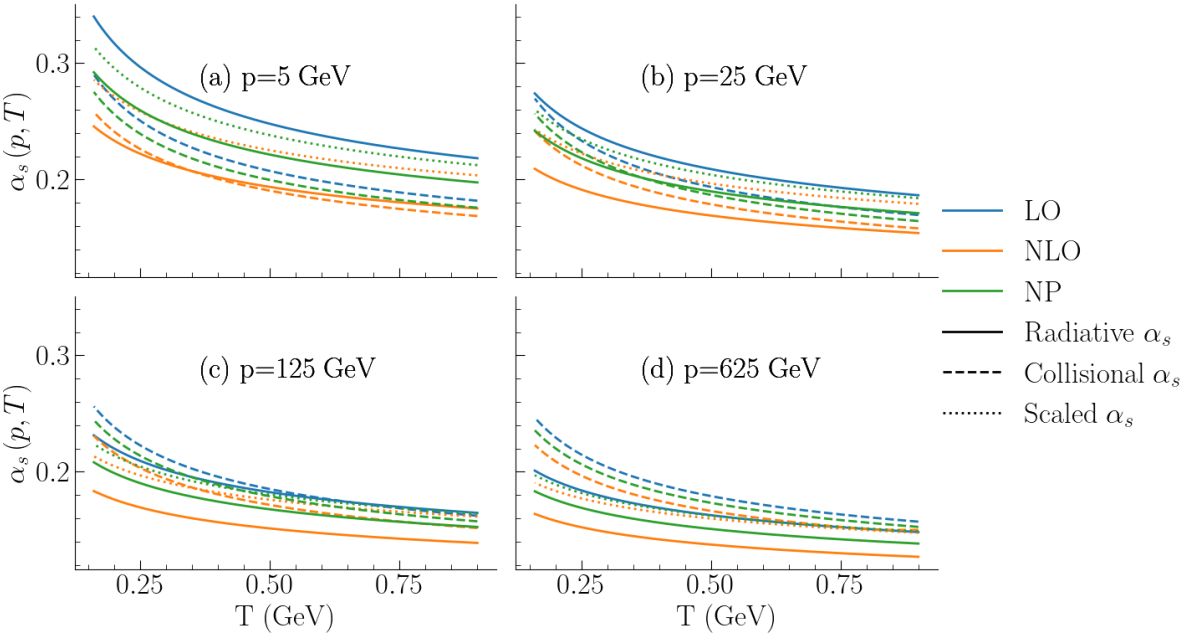

Figure 5.17: Plot of the temperature and momentum dependence of $\alpha_{s,rad.}$ and $\alpha_{s,elas.}$ for the three rate sets using the optimized running parameters of Table 5.4. The solid and dashed lines are the radiative and elastic coupling constants. The dotted lines are the radiative α_s of NLO and NP, scaled according to Equation 5.7.

(Section 5.1) and the fixed coupling in a dynamic medium (Section 5.2). This is seen more clearly in Figure 5.17 where the running coupling is plotted. Since we saw in Section 5.1 that the NLO and NP rates are above the LO rate, even after scaling, it is not surprising to see that tuned to the same data, the strong coupling of the NLO and NP are systematically below the LO result. If at the same coupling, the NLO and NP rates quench more, then for the same amount of quenching, their α_s should be smaller. The figure also includes *scaled* curves where the radiative α_s curves of NLO and NP sets are scaled by Equation 5.7. The scaled results match the LO curve at high temperature and momentum, with the biggest difference between the dotted and the solid lines observed for $p = 5$ GeV for all plotted temperatures.

A short note on the choice of the compound kernel is in order. Another compound kernel with equal performance was found to be

$$k(\mathbf{x}, \mathbf{x}') = \mathrm{RBF}(\mathbf{x}, \mathbf{x}'; \mathbf{l} = (0.001, 0.001)) + \mathrm{WhiteKernel}(\mathbf{x}, \mathbf{x}')$$

where the Matérn kernel was completely dropped in favour of a white kernel which models random noise and is defined as

$$\text{WhiteKernel}(\mathbf{x}, \mathbf{x}'; \lambda) = \lambda \delta(\mathbf{x} - \mathbf{x}'). \tag{5.29}$$

In the above, λ is the parameter of the white kernel, denoting the noise level at each point.

The ability of the GPR to give equivalent performance[11] using the Matérn-less kernel indicates that one can simply assume the smoothness of the underlying function and use a White Kernel to account for the statistical noise. Furthermore, the important feature of the kernel, which is also seen clearly in the heatmaps of Figure 5.16 is the anisotropy in the parameter space. This is an expected feature. Equal changes in κ_r and κ_e are not the same, given the relative difference in the strengths of the total rates of the elastic and inelastic energy loss channels. Therefore a separate length scale should be used for each parameter. All the results in the rest of this chapter, were generated from fits which used Equation 5.26.

5.3.3 *Fit Results*

With the parameters of the running coupling tuned separately for each rate set, we can consider a multi-probe study. Figure 5.18 shows the charged hadron R_{AA} calculation compared to experimental data using the parameters of Table 5.4 in the running coupling of the simulation. Since this data was used in the fit, the good performance of the model is to be expected. However, the agreement between the curves themselves is excellent and perhaps indicative that even with running coupling, the differences between the LO, NLO and NP rate sets can be absorbed into the coupling.

Performance of the simulations using the new running couplings are also shown against the other observable used in the fit, the jet shape ratio, in Figure 5.19. There is a clear ordering here, and unlike the charged hadron R_{AA} where the three simulation results stacked neatly on each other, the jet shape still shows some differences between them. This is a remnant of the difference at rate level in Figure 5.2 where after scaling the rates, the ordering of NP $>$ NLP $>$ LO was observed, particularly

11 With the exception of the NLO kernel, which performed better when Matérn was used.

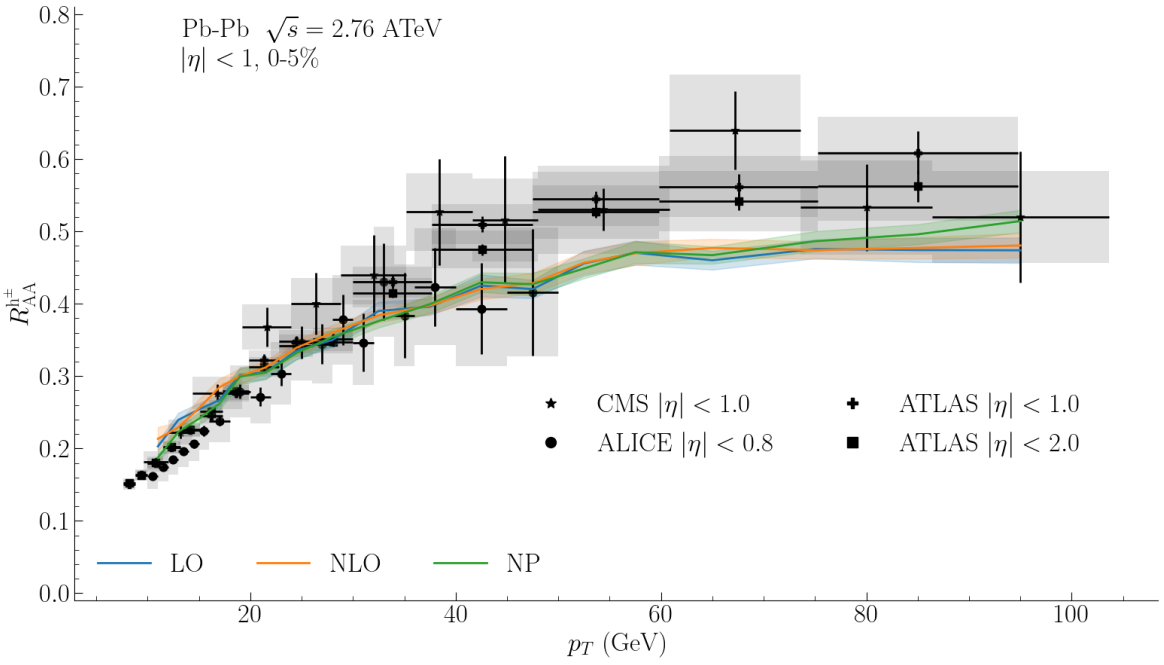

Figure 5.18: Charged hadron nuclear modification factor for 0-5% centrality of Pb-Pb collisions at $\sqrt{s} = 2.76$ ATeV. The figures show the simulation results using a running coupling for the LO, NLO and NP rate sets.

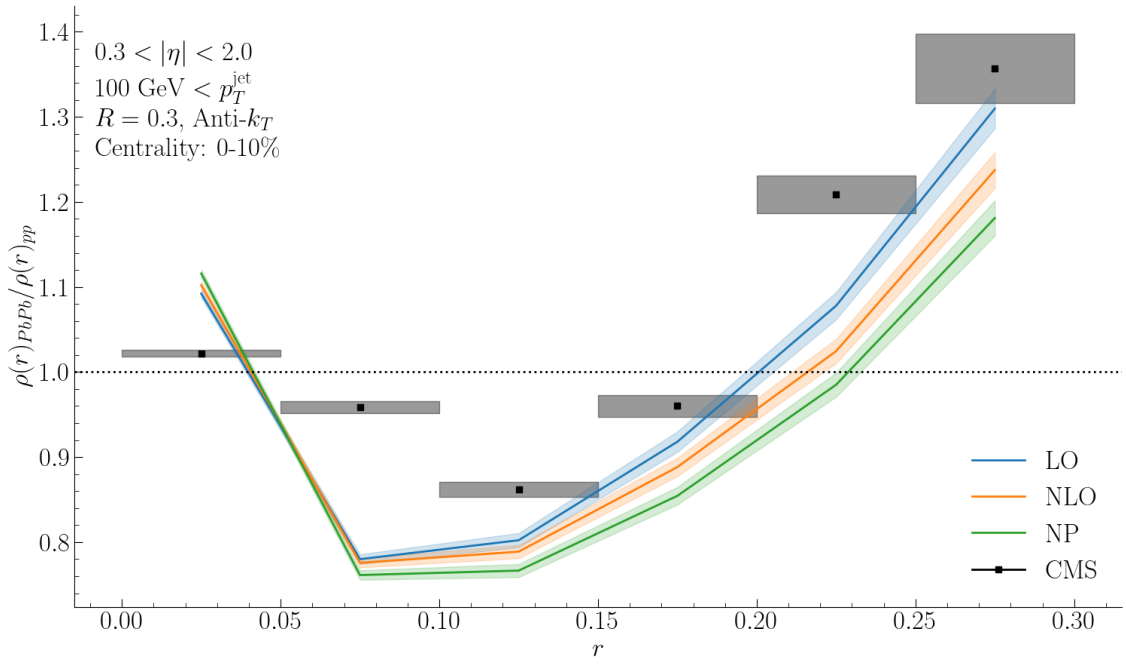

Figure 5.19: Jet shape ratio of inclusive jets clustered using the anti-k_T algorithm for $R = 0.3$. Charged hadron tracks passing the cut $p_T^{h^\pm} > 1$ GeV are used in constructing the observable. Data from the CMS Collaboration [182].

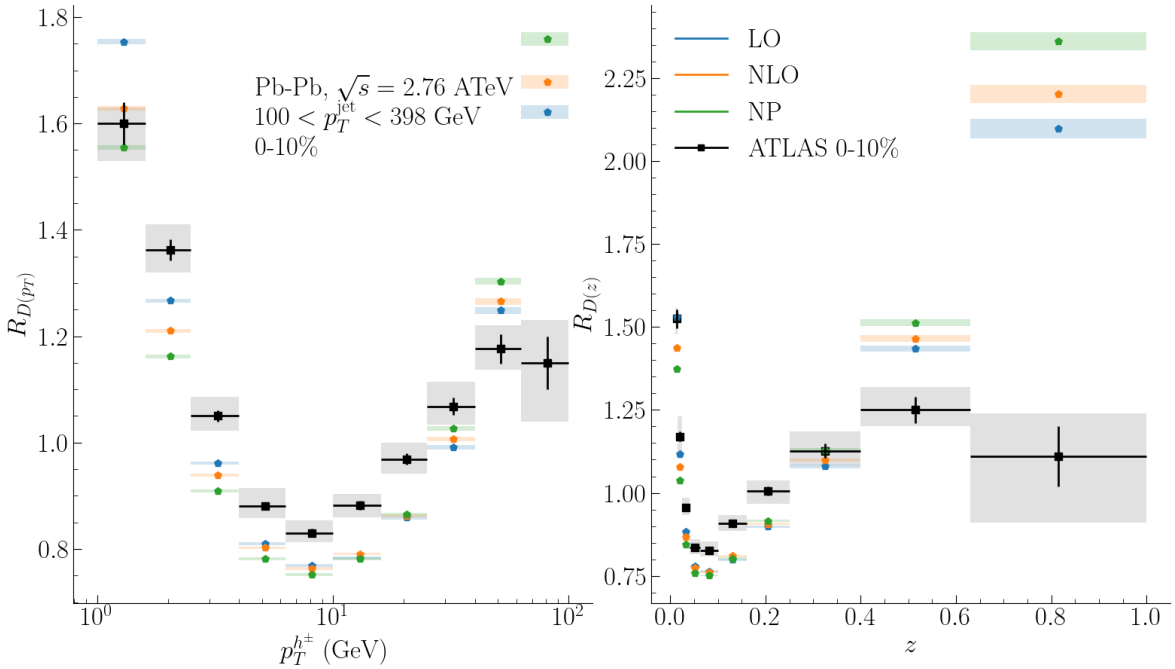

Figure 5.20: Jet fragmentation function ratios of inclusive jets clustered using the anti-k_T algorithm for $R = 0.4$. No cuts were placed on the charged hadrons. Data from the ATLAS Collaboration [183].

for smaller values of the radiated parton energy. Thus in jet shape, partons radiating according to the NP rates are radiating more soft gluons than the other two rate sets. Elastic scatterings then push these soft gluons out of the jet cone, hence the observed ordering of the simulations. It should be noted that all three rate sets capture the general features of the data. The first observable not used in the fit process are jet fragmentation function (FF) ratios presented in Figure 5.20. Fragmentation functions are defined in two ways, first as a function of the transverse momentum of the charged hadrons within the jet

$$D(p_T) = \frac{1}{N_{\text{jet}}} \sum_{\text{jets}} \sum_{p_{T,\text{trk}} \in [p_T^{\min}, p_T^{\max})} \frac{1}{p_T^{\max} - p_T^{\min}} \tag{5.30}$$

and then as a function of the momentum fraction of the charged hadron along the jet axis, z[12]

$$z \equiv \frac{\mathbf{p}_{\text{jet}} \cdot \mathbf{p}_{\text{trk}}}{\mathbf{p}_{\text{jet}} \cdot \mathbf{p}_{\text{jet}}}$$
$$D(z) = \frac{1}{N_{\text{jet}}} \sum_{\text{jets}} \sum_{z \in [z_{\min}, z_{\max})} \frac{1}{z_{\max} - z_{\min}}. \tag{5.31}$$

12 The variable z in this chapter corresponds to the x variable in Chapter 4.

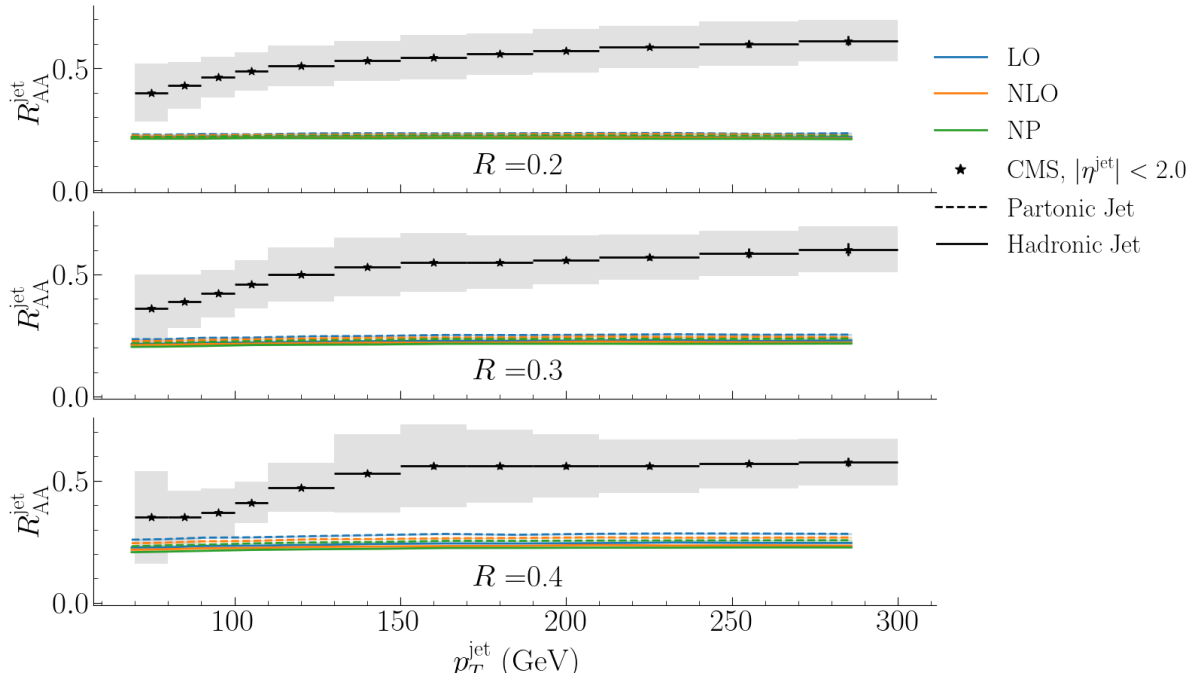

Figure 5.21: Inclusive jet nuclear modification factor for Pb-Pb collisions at 2.76 ATeV and 0-5% centrality. The jets are clustered for three different cone radii. The solid lines denote jets clustered from hadrons, while the dashed lines are jets clustered from partons before hadronization. Data from the CMS Collaboration [184].

The FF ratio, defined analogously to nuclear modification factors of charged hadrons and jets, is given by the ratio

$$R_{D(z)} = \frac{D_{AA}(z)}{D_{pp}(z)}, \quad R_{D(p_T)} = \frac{D_{AA}(p_T)}{D_{pp}(p_T)} . \tag{5.32}$$

In the above, the fragmentation functions $D_{pp,AA}(p_T)$ and $D_{pp,AA}(z)$ are given by Equation 5.30 and Equation 5.31, respectively.

Overall agreement with the fragmentation function ratio data (from the ATLAS Collaboration) is very good for small z or $p_T^{h^\pm}$. All three rate sets, however, miss the behaviour of the primary charged hadrons ($p_T^{h^\pm} \geqslant 80$ GeV or $z > 0.6$). A systematic trend is observed between the three rate sets in their relative ordering. For values of $p_T^{h^\pm} < 20$ GeV or $z < 0.2$, the ordering in the FF ratios are $R_{D(p_T)}[\text{LO}] < R_{D(p_T)}[\text{NLO}] < R_{D(p_T)}[\text{NP}]$ and it is reversed as we get to more energetic charged hadrons travelling in the direction of the jet ($p_T^{h^\pm} > 20$ GeV or $z > 0.2$).

Figure 5.21 shows the inclusive jet R_{AA} calculation using the new running parameters, both at a hadronic and *partonic* level. Partonic jets are clustered from partons, using the same kinematic cuts as the hadronic jets, before hadronization. Much like

Figure 5.13, the fitted runs also miss the data. This, taken together with the other two jet-related observables, jet shape ratio and jet FF ratio, indicates that while the MARTINI energy loss model within a single-stage simulation can be made to fit charged hadron R_{AA} and jet shape ratio in a sophisticated fit, it simply cannot do so with the *correct* population of jets. The strong quenching that results from using MARTINI energy loss from the very beginning of the evolution means that the most energetic partons coming from the initial hard scattering will efficiently fill the lower energy modes, and the whole population cascades down. The lower p_T part of this cascade can be made to fit the data for charged hadron R_{AA}. The jet substructure observables are scaled quantities measuring the shape of a typical jet in a given kinematic range. Thus they are not overly dependent on a good agreement between the jet R_{AA} calculation and data and except for a few bins in jet FF ratio, the theory curves can match the data even though it is completely missing the actual jet R_{AA}.

5.3.4 *Jet-Medium photons*

The objects of study so far in this chapter have been charged hadrons and jets. The main goal in the studies of strongly interacting probes, like those mentioned, is that they are related to the evolving hard parton distribution. However, two complicating factors make gluon bremsstrahlung calculations difficult. First, while we may wish to learn about the energy loss mechanisms and evolution at a parton-level, experimental observables are measured at the hadron level. Due to the effects of confinement, partons are dressed as hadrons, and in theory calculations, hadronization models need to be used. Second, the radiated gluon can also interact with the medium and will receive modifications from it. This is where photons come in. Photons are not charged under QCD and therefore do not experience confinement. Furthermore, due to their large mean free path relative to the size of the medium, they are extremely unlikely to interact with the QGP surrounding them at the moment of emission. This means the jet-medium photon spectrum is proportional to the evolving hard $q/\bar{q}$ spectrum.

In this section, to compare to experimental data, the prompt and jet-medium photon spectra are scaled by the average number of binary collisions. This value has been previously calculated using the Monte Carlo Glauber model in Ref. [37][13].

The aim is to calculate the *direct* photon spectrum. Photon production occurs at all stages of the evolution. By far, the largest source of photons from a heavy ion collision is *decay* photons which result from electromagnetic decays of mesons[14]. Direct photons emanate directly from the collision or the resulting evolution of QGP. Given the experimental difficulty of disentangling the photons by source, the typical technique of extracting the direct photons is statistically subtracting the decay photons from the measured inclusive spectrum.

Direct photons consist of

A. pre-equilibrium photons, emanating from the initial stage of evolution

B. thermal photons from the expanding QGP medium and the hadronic gas

C. prompt photons, created in hard scatterings of the nucleons and the resulting parton shower

D. jet-medium photons, resulting from interactions of hard partons with the plasma.

The first two channels, thermal and pre-equilibrium photons, are dominant for (relatively) small values of the photon transverse momentum, given the mechanism behind their production and the relevant scale: the local temperature. Prompt photons, on the other hand, are produced during the hard collision event and the parton shower that follows. These can be produced at much higher transverse momenta and may be used in measurements of the gluon content of nuclei. For the prompt photon contribution, we use the spectra generated by PYTHIA simulations of `Pb-Pb` collisions, using the same tune and PDFs as those used for the generation of the rest of the event. The spectrum is then scaled by a numerical factor (k-factor) to match the central value of the data at the highest available p_T bin. This factor was determined to be 0.736. Thermal and pre-equilibrium photons are taken from Ref. [55], as stated previously.

13 Specifically, table 9 of that reference.

14 Particularly π^0 and η-meson.

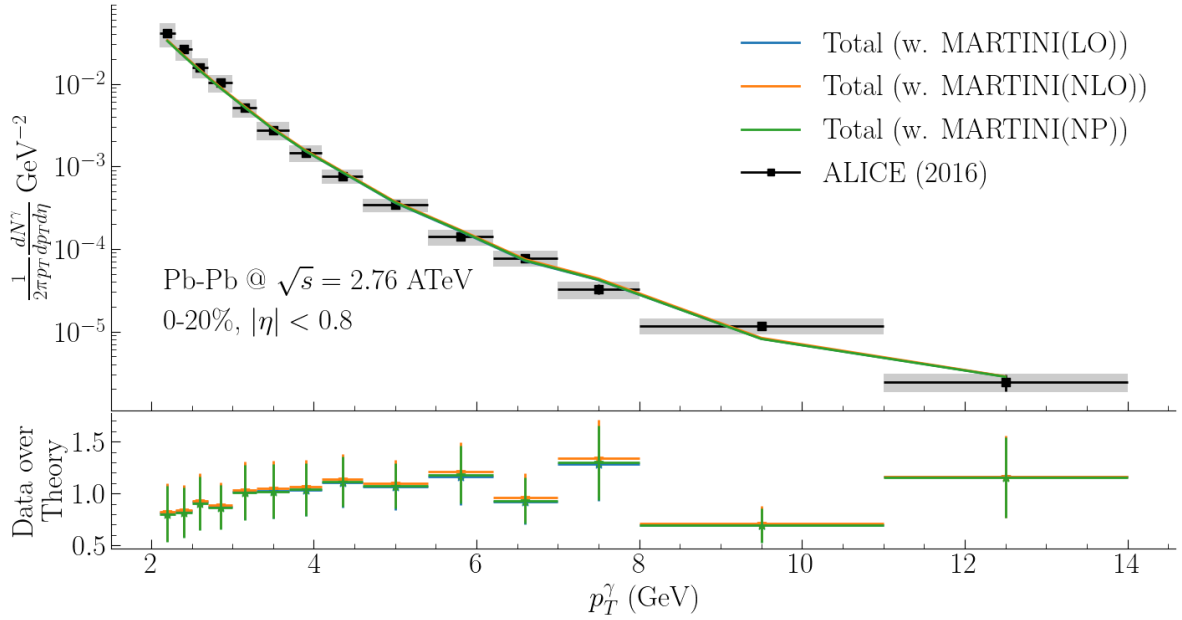

Figure 5.22: Total photon yield at midrapidity of Pb-Pb collisions at 2.76 ATeV for 0-20% centrality. The yields include thermal, pre-equilibrium and prompt photons, as well as jet-medium photons computed using the different collision kernels in the rates. Data from the ALICE Collaboration [185].

The resulting direct photon spectrum, including jet-medium photons produced by the three independent simulations of the new rate sets, also point toward an over-quenching conclusion, as can be seen in Figure 5.22. The range of photon p_T that is plotted against data from the ALICE Collaboration is relatively low, and while the NLO results are peaking above the LO and NP points (most visible in the bottom panel of the figure where the ratio to the data is taken), the total yields including jet-medium photons are very close to each other. Given that for each curve, all photon channels other than jet-medium are identical, we can conclude that the yield of jet-medium photons is very close for LO, NLO and NP results.

The ratio of jet-medium photon yield to the total, as presented in Figure 5.23, clearly demonstrates the point. The difference in the jet-medium yield from the different rate sets is at a few percent level. The conclusion from this exercise, as it stands, is that the differences between the rate sets, evaluated with different collision kernels, can be mostly absorbed in the running of the coupling. However, the considerable energy loss experienced by the partons in the simulations has significantly softened the spectra of quarks and anti-quarks and eliminated any potential signal. Whether

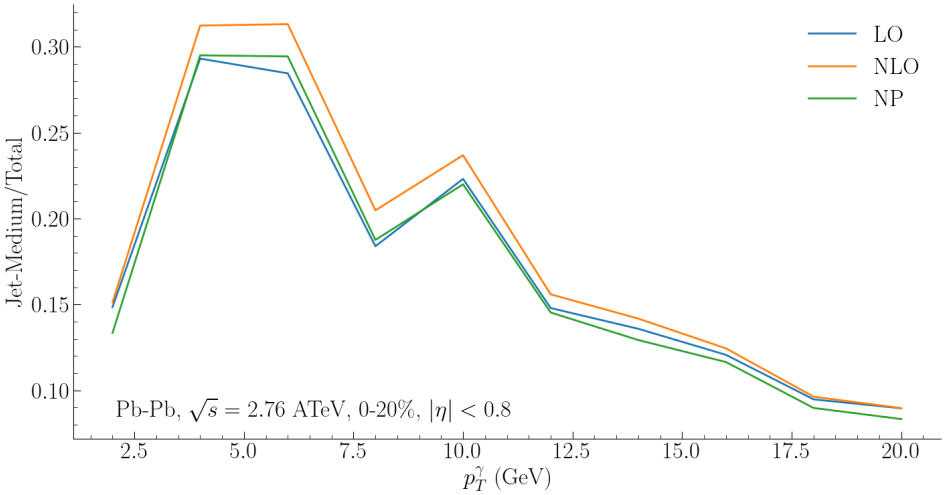

Figure 5.23: ratio of jet-medium photons calculated using the new kernels for each rate set over the associated total photon yield. Plotted for `Pb-Pb` collisions at 2.76 ATeV and 0-5% centrality.

the long evolution time in MARTINI is allowing for a partial thermalization of the soft partons around the jet would require a more detailed study. Jet-medium photons considered here are at low enough p_T where they should be sensitive to the difference in the rates, as observed in Figure 5.2.

It is difficult to make a stronger statement at this moment, given the observed inability of the single-stage energy loss simulations in simultaneously capturing charged hadron and jet R_{AA} within the same simulation. The cause and possible solution to this issue is discussed in the next section.

5.4 SHOWER FORMATION TIME

In Section 5.3, it was observed that MARTINI in a single-stage simulation, cannot capture the nuclear modification factor of jets. Jet-medium photons and, consequently, the total direct photon yield were also insensitive to using the different rate sets. This is despite their almost direct proportionality to evolving hard fermion distribution and intermediate to low p_T window in which we computed them. This is the region where one would expect significant differences between the rates (see Figure 5.2). This observation stands in stark contrast to our independent and complementary study of MARTINI in multi-stage simulations of Chapter 6 where jet R_{AA} for different jet cone

radii and at different centralities was easily reproduced. The major difference between the two models is their single vs. multi-stage nature[15].

This observed difference between single and multi-stage simulations is due to the unphysical way the single-stage simulation generates the parton shower. The parton shower is generated in a vacuum and instantaneously. Thus at the start time of the hydrodynamic evolution, MARTINI begins to evolve a full parton shower which includes both soft and hard partons. In the multi-stage simulations of Chapter 6, as we will see, MATTER contains spacetime information for the evolving virtual partons. Thus, many shower particles are emitted later in the evolution when the temperatures and interaction rates are lower or are emitted outside of the fireball altogether. This section seeks to demonstrate that it is indeed the lack of shower formation time that is primarily responsible for the over-quenching observed in the single-stage simulations. This has previously been shown in Refs. [141, 186, 187] though all were mostly focused on the study of the charged hadron yield and did not consider the effect of a long parton shower time on jets or jet substructure. Other novel aspects of the work presented here are the usage of MARTINI as the energy loss model as well as using state-of-the-art simulations of the soft sector.

The idea is tested by comparing the LO rates within both single-stage and the multi-stage model of Chapter 6 using the following shorthand for the (κ_r, κ_e) factors used in each simulation

$$k_0 = (1.5, 4.5)\,, \quad k_1 = (2.0, 8.6)\ . \tag{5.33}$$

where k_0 is the value of the parameters of the running coupling as used in the simulations of Chapter 6. Figure 5.24 shows a comparison of four different simulations, three using the composite model of the previous chapter and one evolving with the single-stage model, shown in Figure 5.18. The two new JETSCAPE runs for this figure are

A. final state shower provided by MATTER (including energy loss), MARTINI uses the k_1 parameter set

15 The simulation of the soft sector is also different between the two methods. However, jet energy-loss is not particularly sensitive to the details of the modelling of the thermal background. This is, in particular, true for the types of observables considered here: event-averaged spectra and jet-substructure

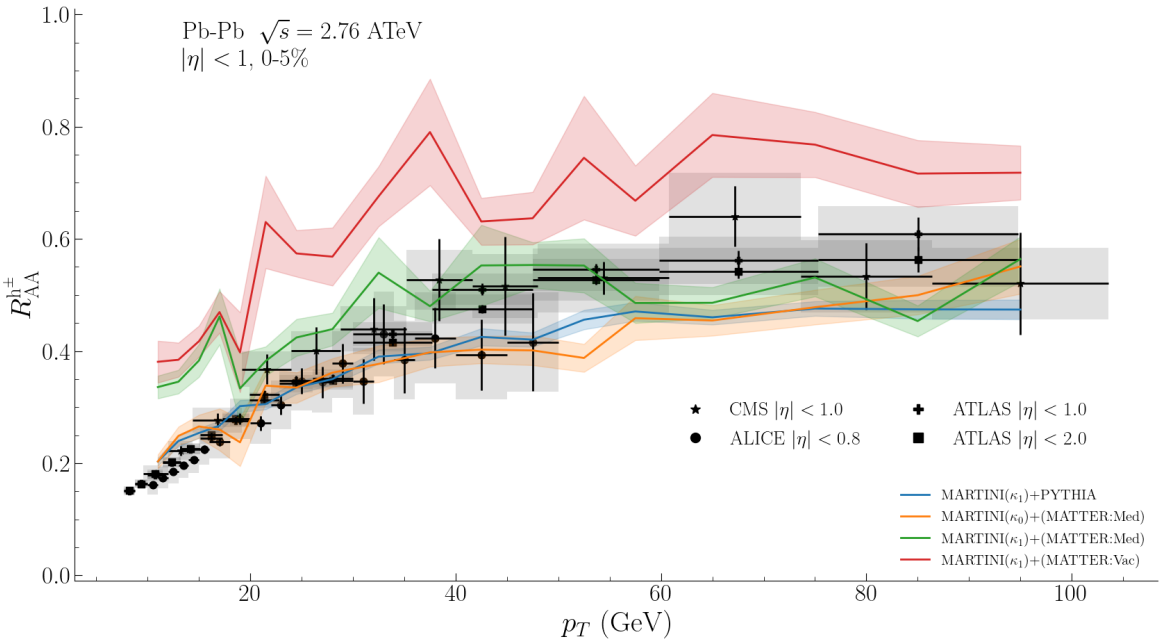

Figure 5.24: Comparison charged hadron R_{AA} for MARTINI energy loss with and without a time-dependent parton shower as well as high virtuality energy loss. The collision system is `Pb-Pb` at 2.76 ATeV, 0-5% centrality. The blue line here corresponds to Figure 5.18. The orange line corresponds to the multi-stage MARTINI simulation in Figure 6.7. For the simulation where MATTER is used in vacuum mode (red line), the $\hat{q}$ parameter in Equation 4.45 is set to zero.

b. final state shower provided by MATTER (no energy loss), MARTINI uses the k_1 parameter set.

The resulting charged hadron R_{AA} from the single-stage (in blue) and multi-stage energy loss simulations (in orange), are nearly identical to each other. Both these workflows were fitted to the charged hadron R_{AA} data which is shown in the figure. As such, their agreement with the data is not surprising, though given the significant differences in all other aspects of evolution, this is quite remarkable. The two other simulations, as described above, test the effect of a time-dependent (or time-delayed) final state shower with and without energy loss. First, running the multi-stage of Chapter 6 but using the newly fitted parameter set, k_1, one can see that the high p_T part of the charged hadron nuclear modification factor is mostly unperturbed. The lower p_T part, however, is less quenched. This is due to the role of MARTINI in the multi-stage model as a low-virtuality stage. Low p_T charged hadrons are more likely to originate from partons which undergo low-virtuality evolution. Furthermore, the

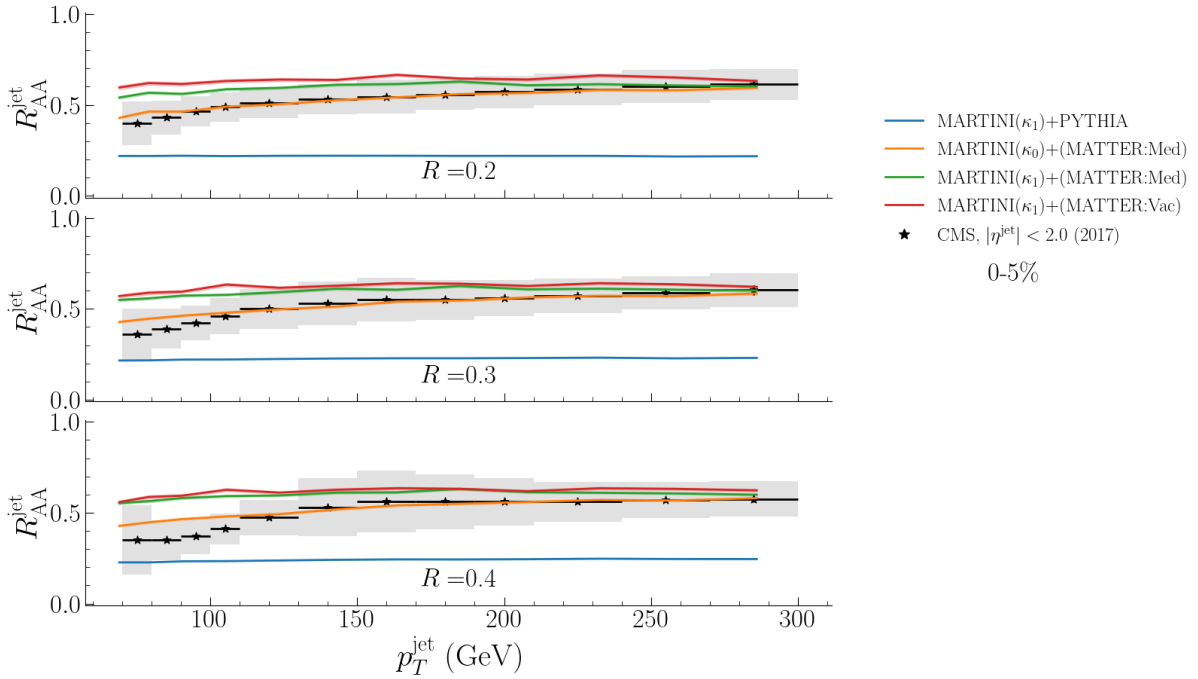

Figure 5.25: Comparison of inclusive jet R_{AA} for MARTINI energy loss with and without a time-dependent parton shower as well as high virtuality energy loss. Same setup as Figure 5.24. Data from the CMS Collaboration [184].

parameter values in k_1, which govern the running coupling, are larger relative to k_0, resulting in a smaller α_s, leading to less quenching relative to simulations using k_0 parameters in MARTINI. The effect of jet energy loss during the parton shower can be studied by turning off the energy loss part of MATTER which couples the evolving virtual partons to the medium. By setting $\hat{q}$ to zero in Equation 4.45, the MATTER shower in the medium becomes a PYTHIA final state shower but with spacetime information. The result is the red curve in Figure 5.24. There, a portion of the shower either never experiences energy loss or only does so for a short period. As such, the charged hadron R_{AA} is larger, indicating less quenching.

The effect described above is even starker for the nuclear modification of inclusive jets, shown in Figure 5.25. First, even though the single-stage run with new parameters k_1 matched the results of the composite model when considering charged hadron R_{AA}, they are very clearly separated when considering jet R_{AA}. Regardless of the parameter set used, the three runs which include MATTER are significantly above the single-stage model. In particular, the effect of medium energy loss in jet R_{AA} is small (difference between the green and red lines), and the dominant effect is the delay in

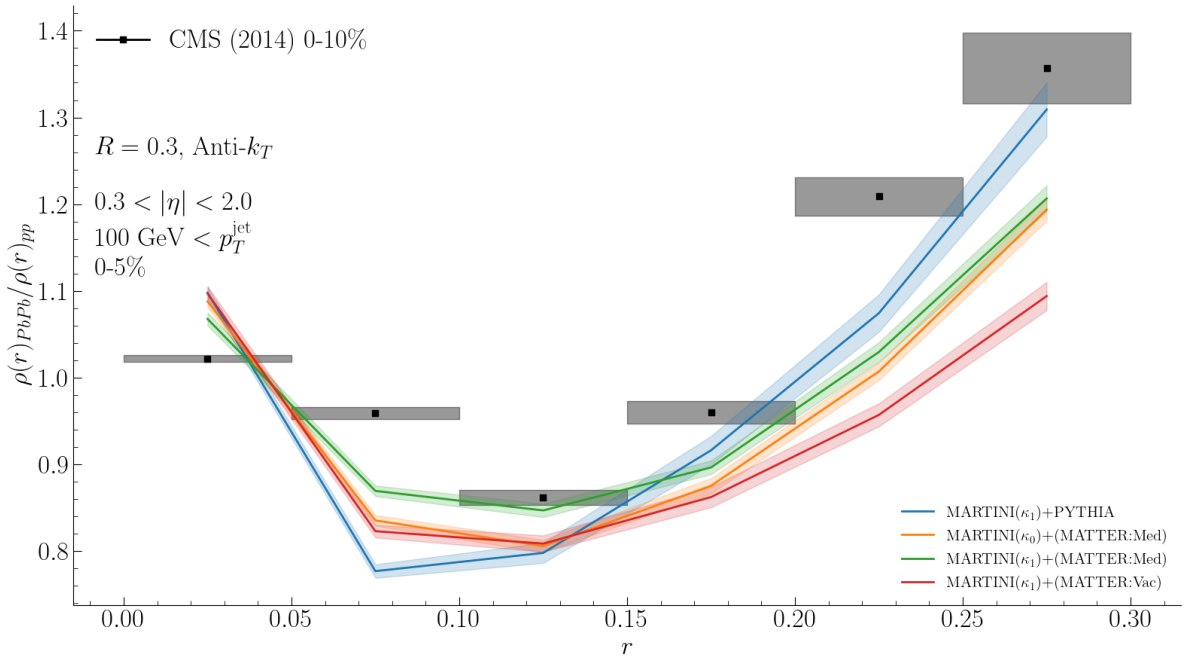

Figure 5.26: effect of a time-dependent final state shower on jet shape ratio for jets clustered using the anti-k_T algorithm for radius $R = 0.3$ with a $p_T > 1$ GeV cut placed on the charged hadron transverse momentum at clustering level. The theory curves are calculated for 0-5% centrality class while the data is for 0-10% centrality. The setup is identical to Figure 5.24. Data from the CMS Collaboration [182].

the full development of the parton shower that is generated due to spacetime information incorporated by MATTER.

The inclusion of an initial stage of energy loss also modifies the two jet observables studied here. For the jet shape ratio, given in Figure 5.26, the last bin, the multi-stage framework with in-vacuum shower (MATTER:Vac or $\hat{q} = 0$) sees a reduction of nearly 30% when contrasted with the single-stage MARTINI simulation, using the same running α_s parameters (k_1). When MARTINI takes over the evolution at later times, there is less quenching and less elastic scattering with the medium. Thus the leading hadron loses less energy, and the partons around the jet are not likely to receive kicks that push them out of the jet cone, bringing the jet shape closer to that of the p-p case. The jet fragmentation function ratios, given in Figure 5.27, also show the modification by the suppression relative to the MARTINI-only run for the largest p_T or z bin. Unlike the jet shape ratio, jet FF ratios are not absolutely normalized. As

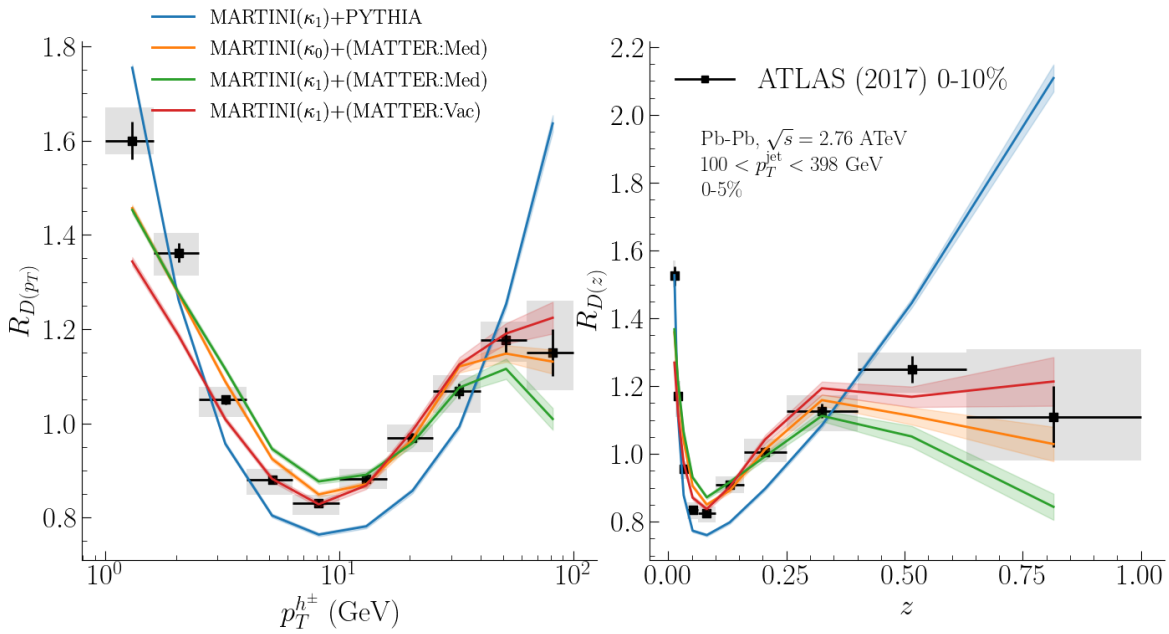

Figure 5.27: effect of a time-dependent final state shower on jet fragmentation function ratio for jets clustered using the anti-k_T algorithm for radius $R = 0.4$. The theory curves are calculated for 0-5% centrality class while the data is for 0-10% centrality. The setup is identical to Figure 5.24. Data from the CMS Collaboration [182].

such, they are more sensitive than the jet shape ratio to the jet population and if it is indeed captured correctly by the simulation.

A solution to this over-quenching problem is incorporating a formation time into the PYTHIA parton shower. In Ref. [187], the PYTHIA shower was modified by the assignment of a formation time using Equation 4.24. There, jet R_{AA} reconstructed at the partonic level achieved a better performance against the data than the case where an instantaneous parton shower seeded the energy loss mechanism[16]. The formation time is introduced by tracking the history of partons coming out of the hard interaction and calculating the total formation time

$$\tau_{\text{form.,p}} = \sum_i \tau_{\text{form.,i}} \tag{5.34}$$

where p denotes a final state parton and the sum over i runs over all the branchings in the parton's history. This is, in effect, poor man's MATTER. Ref. [186] used a MATTER+LBT model and showed the importance of high-viruality energy loss stage and

16 Similar work was done in Ref. [188–190] for LBT energy loss model for LHC energies. The partonis resulting from the jet evolution where not hadronized and jet spectra were reconstructed at a partonic level. No jet-substructre observables were used in those calculations.

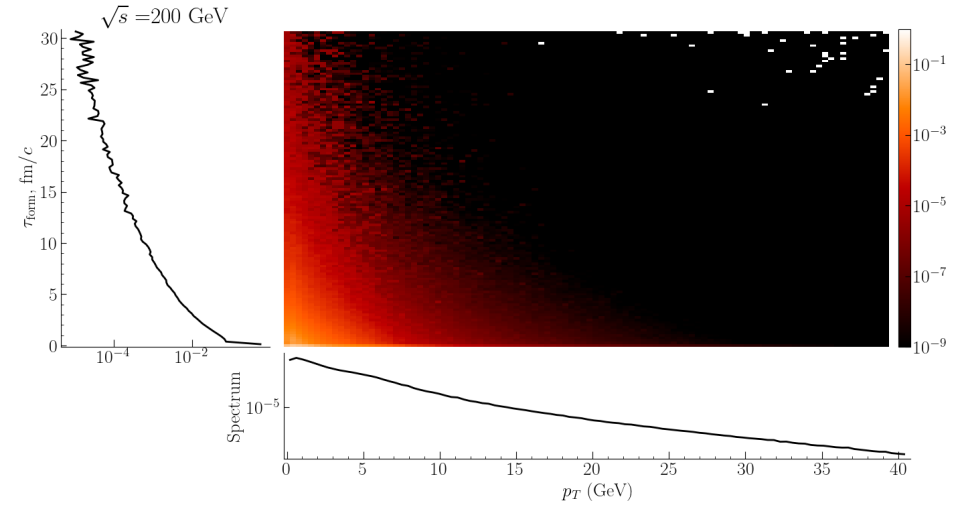

(a) p-pcollisions at 200 GeV

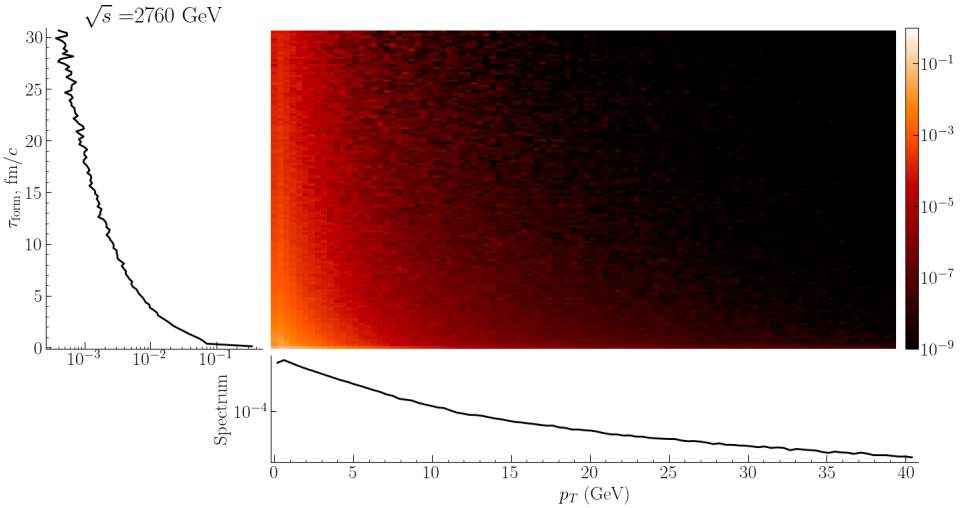

(b) p-pcollisions at 2.76 TeV

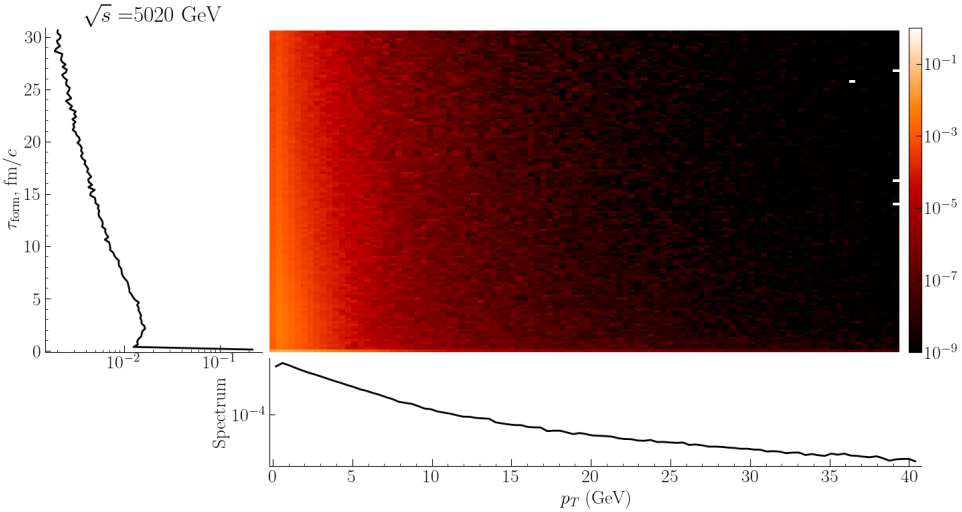

(c) p-pcollisions at 5.02 TeV

Figure 5.28: Formation time of partons in simulations of p-pcollisions at 0.2, 2.76 and 5.02 TeV.

shower formation time for Pb-Pb collisions at 2.76 ATeV while Ref. [187] achieved similar results by using this shower formation time in a PYTHIA+LBT simulation applied to Au-Au collisions at 200 AGeV.

The form of $\tau_{\text{form.},i}$ is given by Equation 4.24. This was implemented for the case of p-p collisions at 0.2, 2.76 and 5.02 TeV, resulting in Figure 5.28. The heat map should be almost entirely black if the zero shower formation time was a good approximation. Instead, however, we can observe significant structure throughout the space. Furthermore, the shape of the heatmap for collisions at 200 GeV is visibly different from those at the LHC energies. This is due to increased phase space for jet production. It is clear that at the partonic level if this is implemented for a Pb-Pb collision at the same energy, some partons may never experience an interaction with the thermal medium (formation time larger than the lifetime of the plasma). Many of these shower particles may encounter the medium at some finite time, where the medium is at lower temperatures and thus experience a lower energy loss rate. Based on the figures, this is particularly true for low and intermediate p_T partons, which have a higher production rate than the very high p_T partons. The delay in the interactions of the parton shower with the medium would then mean significantly less elastic scatterings with the medium and less radiation and thus recovery of the energy of the original hard parton at jet clustering level.

5.5 CONCLUSION

This chapter presented the first study of the new, higher-order collision kernels in a static and evolving QGP. The simulations were performed with both fixed and running coupling constants. In the static QGP, it was observed that while the rate sets evaluated with the new collision kernels are quite different from the LO set and result in a very different parton population, these differences could be absorbed into a rescaling of the strong coupling. This observation was also made for simulations of jet quenching in an evolving QGP with fixed coupling. The Guassian process regression fit is the first systematic study of the running coupling parameters of the MARTINI framework.

During the fitting process it was found that the quenching is too strong in a single-stage energy loss simulation. This meant that the model could not simultaneously describe charged hadron and jet R_{AA}. The cause of the over-quenching was found to be the *instantaneous development* approximation for the parton shower. Previously, in jet energy loss calculations, it was assumed that all partons in the shower would rapidly lose all their virtuality before QGP formation. A major finding of this study is to show that this is not the case. The importance of a time-delayed parton shower and high virtuality energy loss has been demonstrated to be extremely significant. Without a time-dependent parton shower, it is not possible to capture jet and charged hadron nuclear modification factors within the same simulation setup. In a single-stage approximation, all shower partons lose energy via elastic and radiative processes, from the very first moment they enter the QGP all the way to freezeout. Many of these partons have low or intermediate momenta which are crucial for jet reconstruction. They are also partons which are modified the most by energy loss to QGP. After hadronization and clustering stage in these simulations, the resuling jets are missing significant energy, due to the removal of these softer partons (and their resulting hadrons) from the jet cone.

The only currently existing model which incorporates the physics of the initial, high-virtuality energy loss is MATTER. Our work shows the importance of incorporating MATTER (or at least a MATTER-like approach in delaying the parton shower) and therefore crucial need to move toward multi-stage simulations of jet energy loss. This is the first time this effect has been demonstrated with MARTINI. It is also the first time that jets and their substructre have been used as sensitive probes of the multi-stage nature of parton energy loss in an evolving QGP.

The inability to capture jet and charged hadron R_{AA} limits our capacity to make more definitive conclusions about the new rates. However, it is clear that after rescaling the α_s or retuning the running coupling parameters, the spectra of charged hadron and jets alone are not significantly modified by using the new collision kernels. On the other hand, jet substructure observables are much more sensitive and have promise in helping to study these kernels further. Photon spectra were found to be too affected by the large amount of energy loss resulting from the long evolution time and could not distinguish between the rates.

By delaying the energy loss, photon-producing channels such as conversion and bremsstrahlung are not activated until later in the evolution when temperatures are lower. As such, the spectrum of the jet-medium photons will be harder than what has been presented in Figure 5.22 where the parton shower was taken to occur at $\tau = 0^+$ fm/c. The shorter evolution time would mean that the signal of the difference between the rate sets would potentially not get pushed to lower and lower p_T^γ, where thermal sources are expected to dominate the jet-medium signal significantly. Thus, including the shower formation time would allow jet-medium photons to study the effect of the higher-order collision kernels at a *partonic* level with potentially more discriminatory power.

The setup and execution of the fitting process presented here is the first application of Gaussian process regression to fit the parameters of MARTINI. Beyond the physics modification of a formation time for the parton shower, a natural next step for the study is to perform a full Bayesian study of all parameters of MARTINI, including those which were not included in the fit here.

6

COMPARATIVE ANALYSIS OF CUJET AND MARTINI

Chapter 4 introduced energy loss of energetic partons in equilibrium (or close to equilibrium) QGP medium. Particular emphasis was placed on two models of radiative energy loss, MARTINI and CUJET. In this chapter, these models are embedded within a larger, multi-stage [1] framework of jet evolution inside a plasma. We previously saw that CUJET and MARTINI are very different at a rate level: they have a different view of the radiative energy loss of jets and the medium within which they travel. We aim to see how these models compare, using a state-of-the-art integrated approach, against the data and, more interestingly, against each other. The question is whether the data can tell us anything about energy loss mechanisms, and if so, how much information can we extract?

This work is the first modern comparative study of these models and focuses on a multi-probe analysis. The most recent comparative study of various energy loss models was set in the context of a static QGP brick [191]. The emphasis was a comparison of theoretical assumptions behind the derivation of each model and then examining their effects on evolving parton distributions in a fixed temperature, static QGP medium. Later, an effort was made by the JET Collaboration [97] to compile the results of jet quenching calculations of these models and to extract the effective value of the jet quenching transport coefficient, $\hat{q}$. The limiting factor in that analysis was how different calculations were not only different in their modelling of the jet energy loss mechanism but also in their modelling of jet production, hydrodynamic evolution, and hadronization. The JETSCAPE Collaboration was grown out of, and in response to, this effort.

The *Jet energy loss Tomography with a Statistically and Computationally Advanced Program Envelope* or JETSCAPE [192], is a framework for a comprehensive simulation of the evolution of a jet through a heavy ion collision event. It allows for composite mod-

1 Multi-stage here means that the energy loss of hard partons is broken into evolution stages based on a given parameter, virtuality in this case, and each stage is governed by a different model.

elling of jet evolution from the initial hard scattering that produces the hard partons to the pre-equilibrium stage, hydrodynamic evolution and finally, particlization and fragmentation. The JETSCAPE emphasis on a modular approach to simulation of jets and their interactions allows its use as either a *model factory* where jet energy loss is treated as a multi-stage process or as a laboratory for systematic and comparative studies of different jet energy loss models. It provides a unified framework of jet simulation, which allows us to faithfully compare two different models of the same stage of a heavy ion collision- jet energy loss models, hadronization models or any other topic of interest- while keeping all other aspects of the evolution identical. It is this aspect of JETSCAPE that we leverage in this chapter.

This chapter presents the first results of our multi-probe and multi-stage comparative study of CUJET and MARTINI within a JETSCAPE framework and workflow. These results use modified and novel Monte Carlo implementation of CUJET and include

A. first realistic calculation of jets with CUJET,

B. first realistic calculation of jet-medium photons with CUJET,

C. first multi-stage study of CUJET and MARTINI,

D. and first controlled, comparative of CUJET and MARTINI in a multi-stage, multi-probe simulation.

For simulation results, this chapter will focus on `Pb-Pb` collisions at the LHC for the centre of mass energy of $\sqrt{s} = 2.76$ ATeV and centrality classes up to 50%. For the results of `Pb-Pb` collisions at $\sqrt{s} = 5.02$ ATeV and `Au-Au` collisions at RHIC for $\sqrt{s} = 200$ AGeV see Section B.2. Note that radiative rates used by MARTINI in this chapter are evaluated using the LO collision kernel. The soft sector of these simulations is modelled using the T-V approach. In this chapter, we do not use the IP-GLASMA model of initial conditions or (3+1)D modelling of the hydrodynamic evolution. The choice not to use the state-of-the-art might strike the reader as strange. However, it should be noted that due to the scale separation of the hard jets from the soft medium, observables under consideration in this chapter are not particularly sensitive to the details of the modelling of the soft sector. Furthermore, the current modelling of the initial state, as provided by IP-GLASMA is computationally expensive, making it unsuited

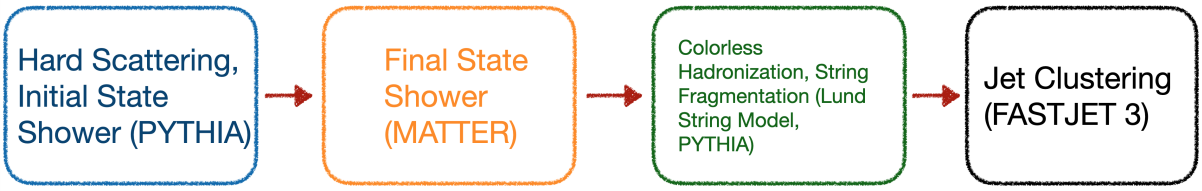

Figure 6.1: The JETSCAPE workflow of proton-proton simulations in this chapter. The red arrows denote the flow of information, which in this case is the evolving particle list.

for large-scale, event-by-event simulations. In its place, we used the T-V approach to modelling the soft sector, as it provides identical performance in most integrated observables of the soft sector compared to the IPG-M model and is significantly less computationally expensive.

6.1 MULTI-STAGE SIMULATION OF JET ENERGY LOSS IN JETSCAPE

In this section we first present a brief discussion of the flow of information in `p-p` and `A-A` multi-stage simulations, as well as the modelling choices made regarding the values of various parameters. The results of the simulations are presented immediately after.

6.1.1 *Proton-proton simulations: the baseline*

Figure 6.1 presents the flow of information in `p-p` collisions with simulations using the JETSCAPE framework. The parameters of the various models are fixed using the fit results of Ref. [143]. The hard scattering events which produce the energetic partons, along with their associated initial state shower and multiparton interactions, are modelled by PYTHIA 8.243 [167] using `NNPDF2.3 LO` parton distribution functions [193–195] [2]. The last stage of the parton shower, the final state radiation, is handled by MATTER [140–142], which evolves the partons down to the cutoff scale $Q_0 = 1$ GeV, below which perturbative QCD is no longer valid.

After the parton shower has fully developed, non-perturbative effects of hadronization and fragmentation set in. The default hadronization mechanism in this workflow

2 The PYTHIA tune is set to the default Monash-2013 tune [196].

is the `colourless` hadronization mechanism. This hadronization method is a variant of the famous Lund String Model and is consistent with it [143]. In short, the hadronization scheme assigns the colour tags of all partons by minimizing their distance in the η-ϕ plane via

$$r = \sqrt{\Delta\eta^2 + \Delta\phi^2} \tag{6.1}$$

where $\Delta\eta$ and $\Delta\phi$ are the differences in the pseudorapidities and the azimuthal angles of the quark and anti-quark, respectively. After the q-$\bar{q}$ pairs, which form the two ends of the colour strings, are identified, the gluon list is traversed, and gluons are assigned to a given string according to their average distance (measure provided by Equation 6.1) to the two ends of it. After all colour tags have been assigned, the event is checked for colour neutrality and passed to PYTHIA for string fragmentation via the Lund string model. As before, PYTHIA is also tasked with decaying unstable hadrons, defined as any hadron with a mean lifetime less than or equal to $\tau = 10$ mm/c. The jet clustering is then done after hadrons have formed and the unstable ones have decayed. Much like Chapter 5, here we use the anti-k_T algorithm for jet clustering.

6.1.2 *Simulation results for p-p collisions at $\sqrt{s} = 2.76$ TeV*

The jet clustering step concludes the simulation of `p-p` collisions and at this stage, various spectra or other observables of interest can be constructed. This section presents the calculations of the hadronic observables for `p-p` collisions at $\sqrt{s} = 2.76$ TeV. Similar calculations for $\sqrt{s} = 200$ GeV and 5.02 TeV are presented in Section A.1. It should be noted that all the results presented below are computed within the same simulation, using the same event record and the same simulation parameters.

The first observable to consider is the invariant differential charged hadron yield, produced at midrapidity

$$\begin{aligned} E\frac{d^3N^{h^\pm}}{dp^3}(p_T) &= \frac{1}{\sigma^{NN}_{Inel.}} E\frac{d^3\sigma^{h^\pm}}{dp^3}(p_T) \\ &= \frac{1}{\sigma^{NN}_{Inel.}} \frac{1}{2\pi p_T} \frac{d\sigma^{h^\pm}}{dp_T\, d\eta}(p_T) \end{aligned} \tag{6.2}$$

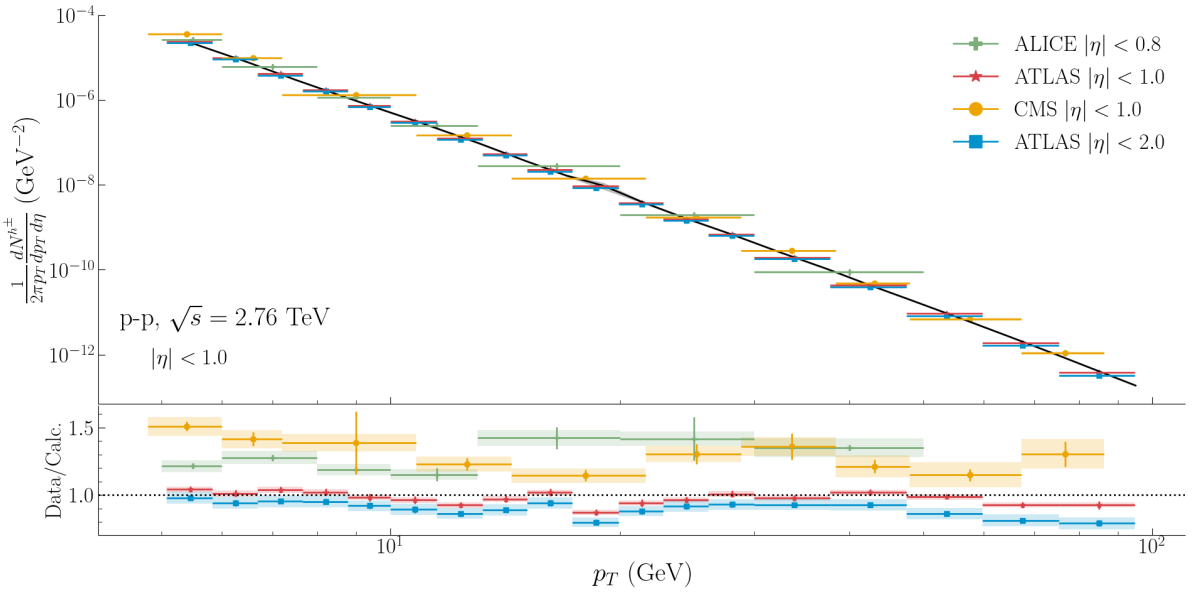

Figure 6.2: Invariant differential yield of inclusive charged hadrons at midrapidity ($|\eta_{h^\pm}| < 1.0$) compared to measurements from ALICE [175], ATLAS [176] and CMS [177] Collaborations. The lower panel shows the ratio of experimental data over the theoretical calculations, where error bars and shaded boxes denote the statistical and systematic experimental uncertainties, respectively.

where $\sigma_{\text{inel.}}^{\text{NN}}$ is the nucleon-nucleon inelastic cross section. The values used in this thesis are given in Table 5.1.

Figure 6.2 compares the theoretical simulation of inclusive charged hadrons vs measurements from experimental collaborations at the LHC. There is overall good agreement between theory and experiment, with most data points being within 20% of the theoretical calculation. We can conclude that the charged hadron yield simulation results provide a good baseline for the heavy ion calculation.

The next step beyond the inclusive charged hadron spectrum is to look at jet observables. These include inclusive jet spectra for jets of different cone-size radii and jet-substructure measurements. The differential jet cross section is calculated by clustering final state hadrons into jets using the same definition of a jet as the experimental collaborations. These are inclusive jets, as no cuts are placed on the clustered hadrons, and both stable charged and neutral hadrons are used in the analysis. Figure 6.3 compares the theoretical calculation to the experimental measurements of ALICE, ATLAS and CMS Collaborations and for three different jet cone radii at midrapidity. Once

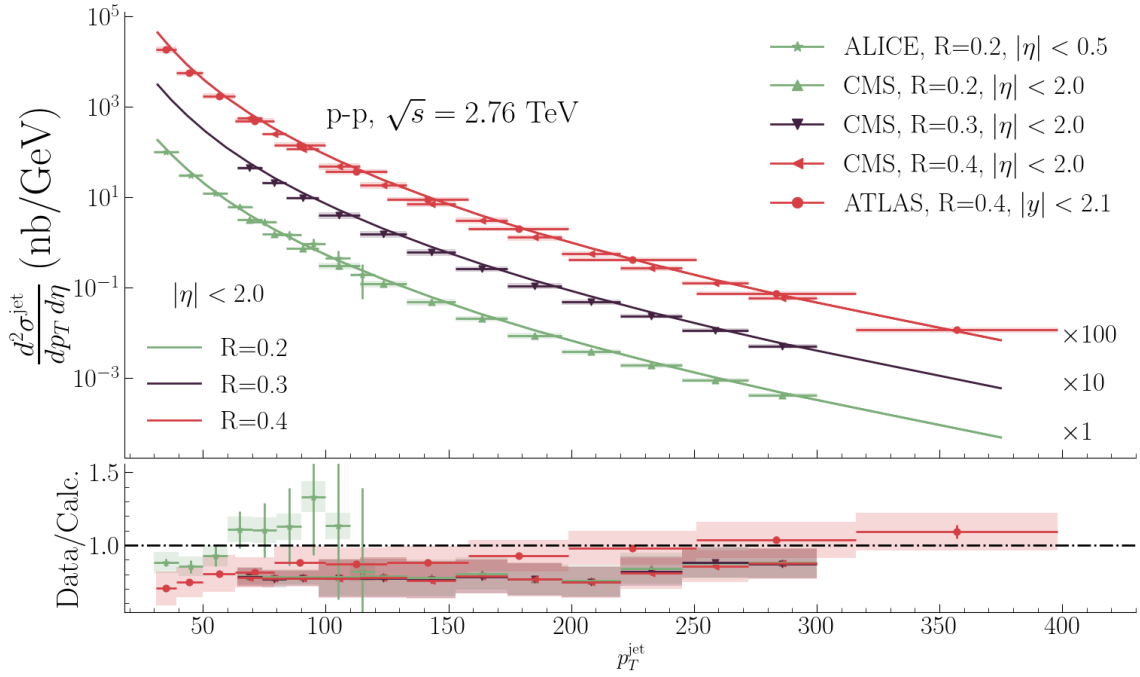

Figure 6.3: Differential cross section of jets for jet cone radii of R = 0.2 (Green), R = 0.3 (Purple) and R = 0.4 (Red) at midrapidity, clustered using the anti-k_T algorithm. The theory curve and associated experimental data are colour-coded. The R = 0.3 and 0.4 results are multiplied by an arbitrary number for clarity. Calculations are compared to data from ALICE [197], ATLAS [198] and CMS [184] Collaborations. The bottom panel shows the ratio of experiments to the theory simulation results, with error bars and shaded boxes denoting the statistical and systematic uncertainties of the experimental data, respectively.

again, the agreement between theory and experiment is quite good, with most data points falling within 20% of the theory results.

Finally, the next two observables deal with the internal substructure of jets. These are jet shape and jet-charged hadron fragmentation functions (referred to as *fragmentation functions* from here on).

Figure 6.4 presents the results of the normalized jet shape (Equation 5.19) calculations in p-p collisions. The results are mostly within 20-25% of the experimental data, and the agreement between the theory and experiment is satisfactory[3]. The final ob-

3 Jet shape as an observable is sensitive to $\mathcal{O}(\alpha_s^3)$ effects [199]. Thus for potential improvements in agreement between theory and data, one should consider higher-order matrix elements in the hard event generation or higher-order evaluation of the DGLAP splitting functions. These effects are far beyond what this thesis considers.

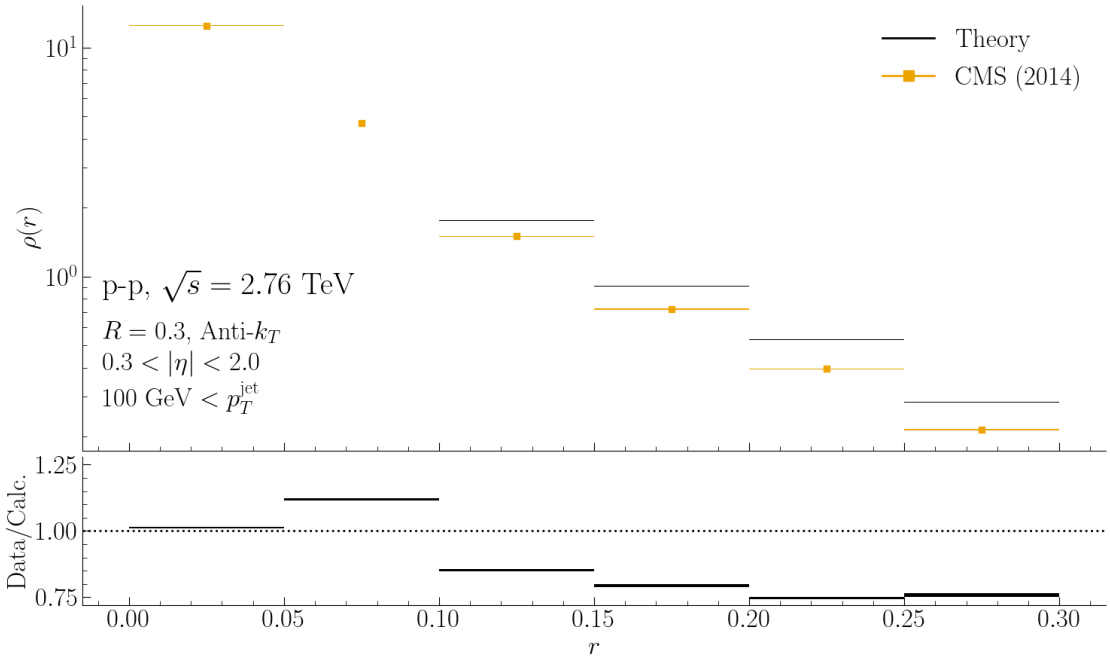

Figure 6.4: Jet shape calculations from p-p simulations using the JETSCAPE workflow. Jets are clustered using the anti-k_T algorithm for $R = 0.3$ for rapidity window $0.3 < |\eta| < 2.0$ and jets with $p_T^{\text{jet}} > 100$ GeV are chosen. A transverse momentum cut of $p_T^{\text{trk}} > 1$ GeV is applied to charged hadron tracks when clustering the jets. Horizontal black lines give the theoretical calculations, while experimental data are denoted by horizontal orange lines and in both cases, the thickness of the line is proportional to the uncertainty. The bottom panel shows the ratio of experimental to theoretical calculation. The thickness of the lines corresponds to the systematic and statistical uncertainties for experimental and theoretical results, respectively. The calculations are compared to data from the CMS Collaboration [182].

servable here is the fragmentation function of charged hadrons in the jet, defined in Equation 5.30 and Equation 5.31.

Figure 6.5 shows the calculation of jet fragmentation function against experimental data from the ATLAS Collaboration. The chosen jet population for the analysis are inclusive jets at midrapidity with transverse momentum in the $[100, 398)$ GeV range. The agreement between theory and experiment is very good, with all data points within 15% of the theory calculation, indicating that this is a solid baseline for studies of heavy ion simulations. A final note regarding the complementary nature of the jet substructure observables discussed here is in order. While jet shape measures the distribution of charged hadrons as a function of their radial distance from the jet axis,

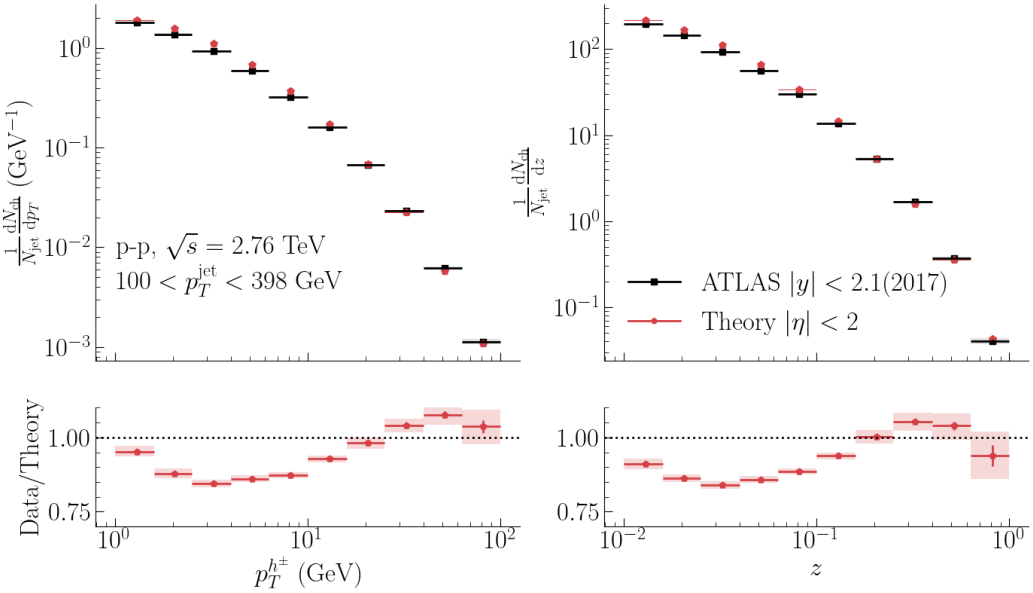

Figure 6.5: Comparison of the simulated jet fragmentation function (Red) to data from the ATLAS Collaboration [183] (Black). Chosen jets for the analysis are at midrapidity ($|\eta_{\text{jet}}| < 2.0$) and have transverse momentum between $100 < p_T^{\text{jet}} < 398$ GeV. No cuts are placed on the hadrons, neither at analysis nor at the jet-clustering level. The bottom panel shows the ratio of the experimental data to the theoretical calculation.

jet fragmentation functions look at the momentum of the charged hadrons along the jet axis. As such, these two observables can be used in conjunction with each other to study and compare the radiative and elastic energy loss mechanisms of different models.

6.1.3 *Heavy ion simulations: the workflow*

The multi-stage model for simulating jets and their energy loss in a heavy-ion collision is presented in Figure 6.6. The major difference between the `p-p` and `A-A` simulations, unsurprisingly, is the inclusion of the QGP medium and its effect on the subsequent evolution and energy loss of hard partons. Due to the presence of the medium, the MATTER final state shower is modified as described in Section 4.5.2 and the partons with low virtuality (assumed to be on the mass shell) are allowed energy

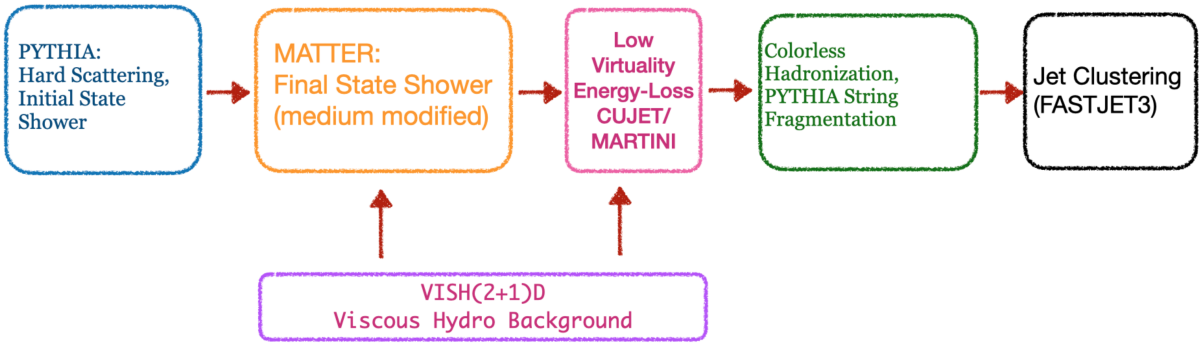

Figure 6.6: The JETSCAPE multi-stage workflow for simulating jet evolution through a QGP medium. The system goes through two extra stages, as compared to a p-p collision (Figure 6.1), for jet energy loss at high and low virtuality. The arrows from the hydrodynamic background denote the input of hydro information, namely local temperature and flow velocity, into the energy loss models.

loss via radiative or elastic scattering processes as provided by CUJET or MARTINI. As input, the energy loss models require local medium temperature and flow velocity from the hydrodynamic medium. The hydro medium histories used in this chapter are simulated using the T-V approach, as described in Chapter 3.

In this model, a hard collision event in a A-A goes through the following stages of evolution. The hard event generation is performed by PYTHIA with nuclear modifications to the PDFs as provided by LO EPS09 [174] parametrization. For the initial $\tau \leqslant 0.6$ fm/c of evolution (in the fluid rest frame), partons evolve as if in a vacuum and have vacuum-like splittings as described in Section 4.5.1. At $\tau = 0.6$ fm/c, the evolving partons begin to *see* the medium that is formed around them, and their shower receives modifications from their medium interactions. This was described in Section 4.5.2, where elastic scatterings with the medium and the transverse momentum broadening effects due to them were incorporated into the parton shower. Specifically, the strong coupling in this stage is held fixed at $\alpha_{s,\text{MATTER}} = 0.23$. If a parton leaves the medium and is still virtual, a condition defined as having virtuality $Q > Q_0 = 2$ GeV [200], it will proceed to continue branching in vacuum. If, on the other hand, the parton reaches the virtuality cutoff and remains in the QGP medium, it is considered an on-shell particle, and its further evolution is governed by the low virtuality model, either CUJET or MARTINI. This switching is done on a parton-by-parton basis. Partons then evolve in the QGP and experience scatterings with the

medium constituents until they either escape the medium, a condition defined as the local temperature falling below $T_c = 160$ MeV or if their momentum in the rest frame of the plasma is less than the momentum cut $p_{cut} = 2$ GeV[4].

After all partons are frozen out of evolution, the event is processed for hadronization and jet clustering, using the same techniques as in the p-p collision as described earlier in this chapter. The same recoil-hole prescription as described in Section 5.2.1 is implemented here as well. At this stage, the simulation and clustering are done, and the event is analyzed by constructing the observables of interest.

6.2 MULTI-PROBE STUDY OF CUJET AND MARTINI

In the previous section, the simulation details for both p-p and A-A collisions were discussed and the results of the p-p baseline for $\sqrt{s} = 2.76$ TeV were presented. All non-CUJET and non-MARTINI parameters of the workflow, as stated before, are fixed by JETSCAPE Collaboration fits to p-p [143] and Pb-Pb collisions [200].

The remaining parameters that need to be fixed are those governing the running of the strong coupling in CUJET ($\alpha_{s,max}$) and MARTINI (κ_r, κ_e). These are fitted to Pb-Pb collision data at $\sqrt{s} = 2.76$ ATeV and 0-5% centrality class. The reasons for the choice of this system are twofold

A. large collision energy and availability of high-p_T observables, which allow for more confident usage of pQCD techniques,

B. existence of photon data as well as hadronic and jet data which enables a multi-probe analysis.

After the parameters are fitted to the data, they are fixed for the rest of this chapter and the associated results presented in Appendix B. Table 6.1 presents the parameters used in our simulations.

4 The temperature cutoff is motivated by the desire to avoid the hadronic gas phase which sets in at $T_{sw.} = 151$ MeV. The momentum cut ensures that the energy loss models used here, MARTINI and CUJET are applied to energetic partons and stay within or close to their domain of applicability.

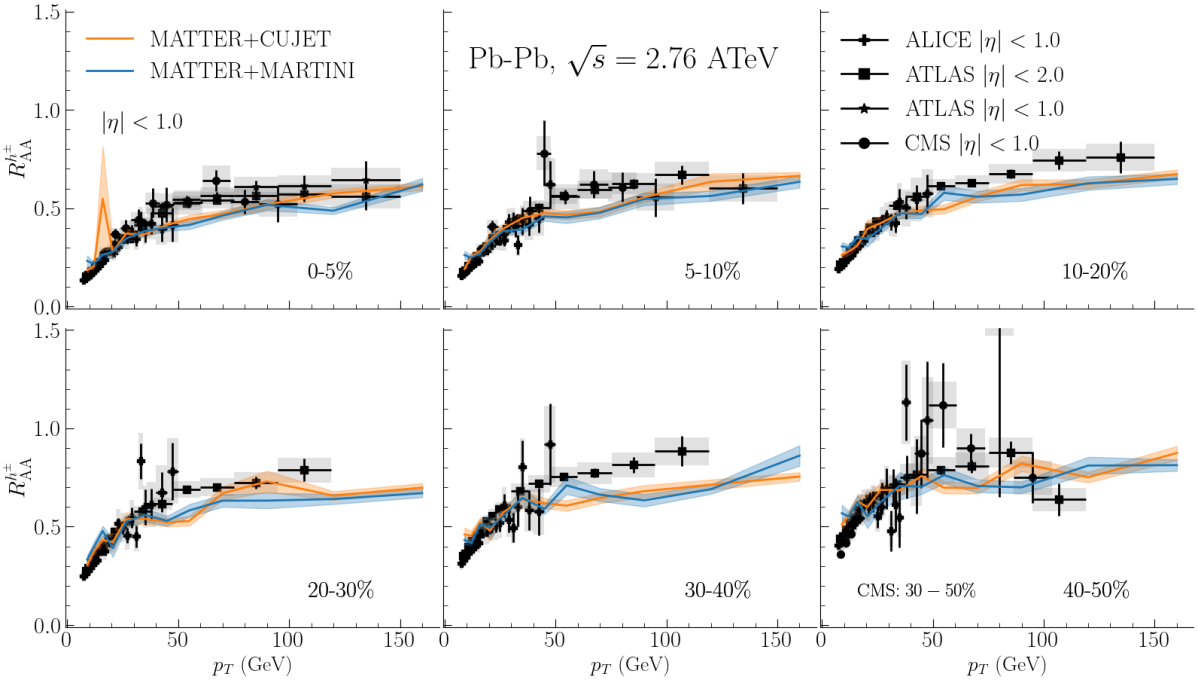

Figure 6.7: Comparison of charged hadron R_{AA} calculation with experimental data from ALICE [175], ATLAS [176] and CMS [177] Collaborations. The collision system is `Pb-Pb` at $\sqrt{s} = 2.76$ ATeV, and the 0-5% centrality class (upper leftmost subfigure) was used in the fitting of the running coupling parameters in CUJET and MARTINI. The spectra are constructed for midrapidity ($|\eta| < 1.0$). The denominator in the R_{AA} calculation is provided by Figure 6.2.

6.2.1 *Hadronic observables in `Pb-Pb` collisions at $\sqrt{s} = 2.76$ ATeV*

Figure 6.7 shows the charged hadron nuclear modification factor (R_{AA}) fit and calculation results for six centrality classes, using parameters if Table 6.1, going as high as 40-50% class, compared to experimental data from ALICE, ATLAS and CMS Collaboration results[5]. There is a great agreement between the theory simulation results and the experiment.

The two composite models, one with CUJET and the other MARTINI, are nearly indistinguishable from each other. This is in large part due to the fact that this observable was used as the fit target for both models. Another reason is the nature of charged hadron R_{AA}: it is an inclusive observable that encompasses both the leading and all subleading charged hadrons. As such, any possible sensitivity to the usage

5 See Section B.1 for comparative runs with and without low-virtuality energy loss

MODEL	PARAMETER	VALUE	NOTE
Both	N_c	3	Number of colours
	Λ_{QCD}	0.2 GeV	Eqs. (4.41), (4.19)
	p_{cut}	2.0 GeV	Energy loss cut
	T_{sw}	160 MeV	Decoupling temperature
	$\alpha_{s,conv.}$	0.3	Fixed coupling for conv. γ
MARTINI	N_f	3	Number of flavours
	$\alpha_{s,0}$	0.3	Eq. (4.41)
	κ_r	1.5	Eq. (4.39)
	κ_e	4.5	Eq. (4.39)
CUJET	N_f	2.5	Number of flavours
	α_{max}	0.68	Eq. (4.19)

Table 6.1: Parameter list of CUJET and MARTINI, including the running parameters ((κ_r, κ_e) for MARTINI and $\alpha_{s,max}$ for CUJET) which are fitted to charged hadron nuclear modification factor.

of different models for a given stage of jet quenching is likely to be lost. A more discriminatory observable is jet R_{AA}.

Figure 6.9 shows the jet R_{AA} results in four centrality classes for three jet cone radii, compared against data from the CMS Collaboration. There is great agreement between the two models and the data, as well as between the two models themselves. The relatively large experimental uncertainty makes any definite statement on the data preference for one model or another difficult. However, it is clear that the two models are moving with respect to each other as one moves from the most central towards more peripheral centrality classes (left to right movement in Fig. 6.9). This behaviour is more pronounced when the cone radius for jet reconstruction is increased from $R = 0.2$ to $R = 0.4$ (moving down a column in Fig. 6.9). The effect of going to higher centrality classes is to shrink the medium and lower evolution time. This corresponds to less time for the low virtuality shower to quench the jets.

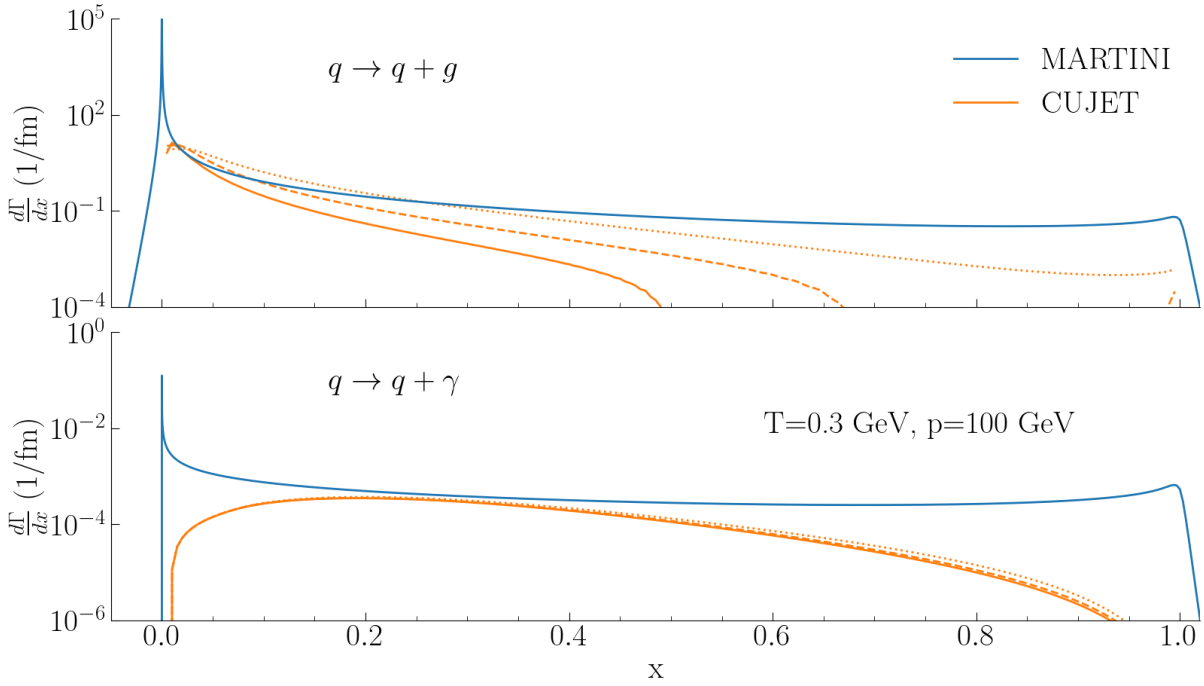

Figure 6.8: Comparing the differential radiative rates of CUJET and MARTINI for an energetic up quark of $p = 100$ GeV at the representative temperature of $T = 0.3$ GeV, as a function of the momentum fraction of the radiated particle. MARTINI framework allows for energy gain from the medium ($x < 0$ region). The effect of traversed length in CUJET is more pronounced for gluon emission than photon emission. The dips in the CUJET curves are the result of the LPM phase, see Equation 4.16.

The movement to larger cone radii within the same centrality class, however, is sensitive to the details of jet energy loss. Increasing the jet-cone radius has the effect of including more hadronic activity previously in the jet's periphery. These hadrons originate from (mostly) radiated gluons which were then kicked away from the parent parton due to elastic scatterings with the QGP medium. To further study this effect, one can form the ratio of jet R_{AA} for different cone radii to $R = 0.2$ jet R_{AA} as a reference in Figure 6.10. The general pattern is the same for simulations including either model: as jet p_T increases, the effect of going to larger cone sizes decreases. This is related to the composite nature of these models. The high virtuality part of jet evolution in the medium is handled by MATTER and therefore the jets with lower transverse momenta are more likely to be sensitive to the low virtuality part of energy loss. CUJET jet R_{AA} rises to nearly 40% for lower transverse momentum jets as jet cone radius increases, while for MARTINI this increase is less than 10%. This is due

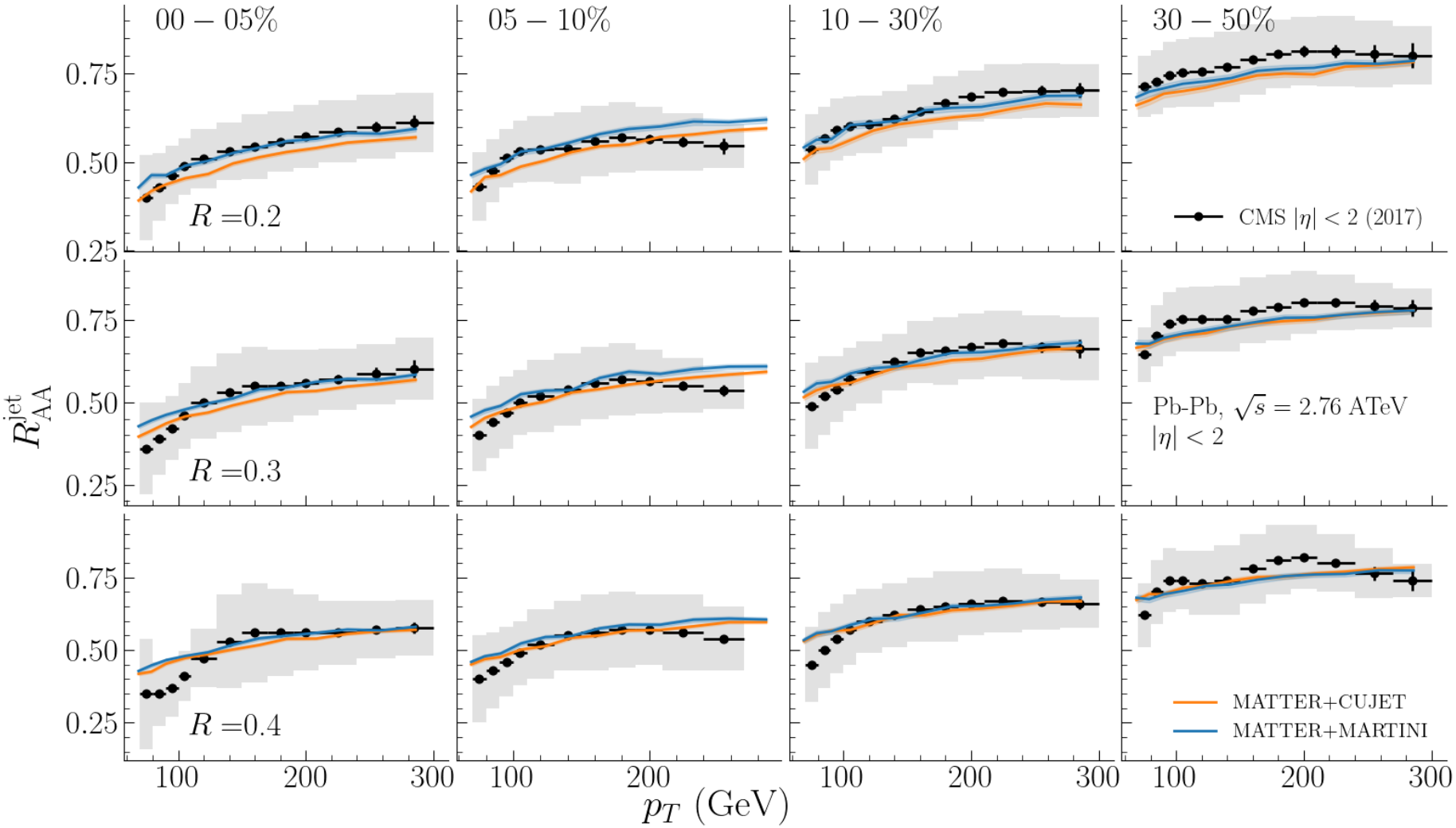

Figure 6.9: Simulation results for nuclear modification factor of jets at three jet cone radii $R \in [0.2, 0.3, 0.4]$ (rows) and four centrality classes (columns). Data from the CMS Collaboration [184]. The p-p baseline used is provided by Figure 6.3.

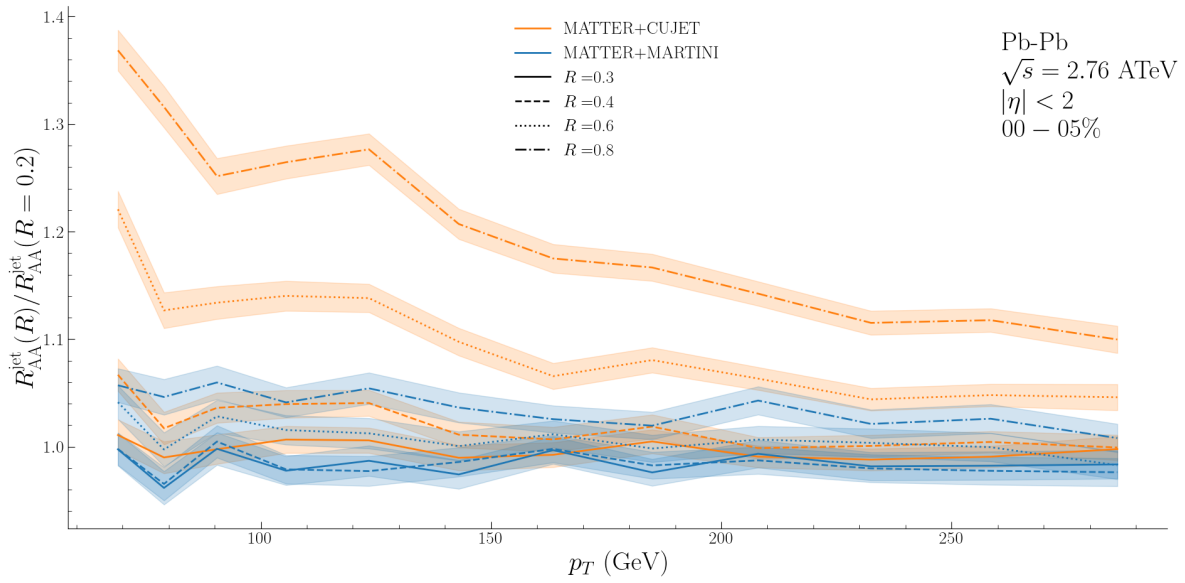

Figure 6.10: The ratio of the nuclear modification factor of (inclusive) jets of different cone radius to those with $R = 0.2$. Increasing the jet cone radius boosts the jet R_{AA} relative to jets with smaller cone radii. The effect is more pronounced for simulations including CUJET.

to the difference in radiative rates for DGLV and AMY, as seen in Figure 6.8. A parton evolving according to AMY rates is more likely to radiate a large number of soft gluons relative to a parton of the same energy evolving according to CUJET. At the level of implementation, both MARTINI and CUJET take the radiated gluon to be perfectly collinear to the parent parton. A soft gluon is much more effectively deflected by elastic processes than a harder gluon, resulting in a halo of soft gluon at larger and larger radii away from the parent parton. This indicates the sensitivity of jet R_{AA} as a function of jet cone radius, to the elastic scattering processes of jet energy loss and leads to the pattern observed in Figure 6.10. To further corroborate this observation, we consider substructure observables. Beginning with the jet shape ratio given in Equation 5.21.

The result of the jet shape ratio calculation in Figure 6.11 complements the observations made above. Both models compare favourably with the data, with both being able to recreate the depletion of the charged hadrons for $r < 0.1$ and the enhancement for $r > 0.2$. Comparing the models with each other, we see nearly identical results close to the jet axis followed by a divergence between the two for $r > 0.1$ where jet shape ratios, as computed by CUJET are systematically above MARTINI. The last

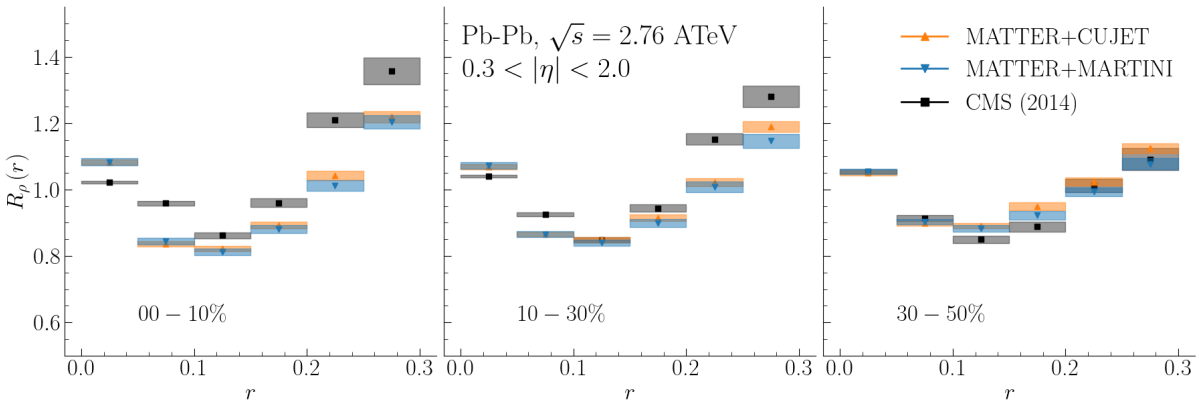

Figure 6.11: Comparison of jet shape ratio as calculated using CUJET and MARTINI versus experimental measurements in three centrality classes. Jets are clustered using the anti-k_T algorithm with $R = 0.3$ from inclusive hadrons in the rapidity window $0.3 < |\eta| < 2.0$. A cut of $p_T^j > 100$ GeV is placed on the transverse momentum of the jets. Jets are clustered from inclusive neutral hadrons as well as charged hadron tracks passing the condition $p_{trk} > 1$ GeV. The p-p the denominator, is given in Figure 6.4. Data from the CMS Collaboration [182].

jet observable remaining to discuss here is the jet fragmentation function ratios of Equation 5.32. Analogously to the jet shape ratio, jet fragmentation function ratios also demonstrate systematic differences between the two models arising from this interplay of radiative and elastic energy loss channels.

Figure 6.12 shows the theoretical jet fragmentation function ratios calculated using CUJET or MARTINI vs data from the ATLAS Collaboration for three centrality classes. The two models have a more pronounced difference in this case, particularly where the charged hadron transverse momentum (or the momentum fraction) is small. As observed in the jet-shape ratio, CUJET simulation results are systematically above those of MARTINI. Furthermore, for jet fragmentation function ratios, we can see that close to and along the jet axis, MARTINI is slightly above CUJET in all centrality classes. Specifically, in the bottom row of Figure 6.12, $R_D^{CUJET}(z < 0.1) > R_D^{MARTINI}(z < 0.1)$ while $R_D^{CUJET}(0.1 < z < 0.4) < R_D^{MARTINI}(0.1 < z < 0.4)$. While the difference for small values of the momentum fraction is due to the interplay of a large number of soft radiation and elastic scatterings, for intermediate values of z, one can observe the influence of the radiative rates. Comparing Figure 6.12 to the rates in Figure 6.8, shows that CUJET rates are mostly subdominant to MARTINI rates in this range of momentum

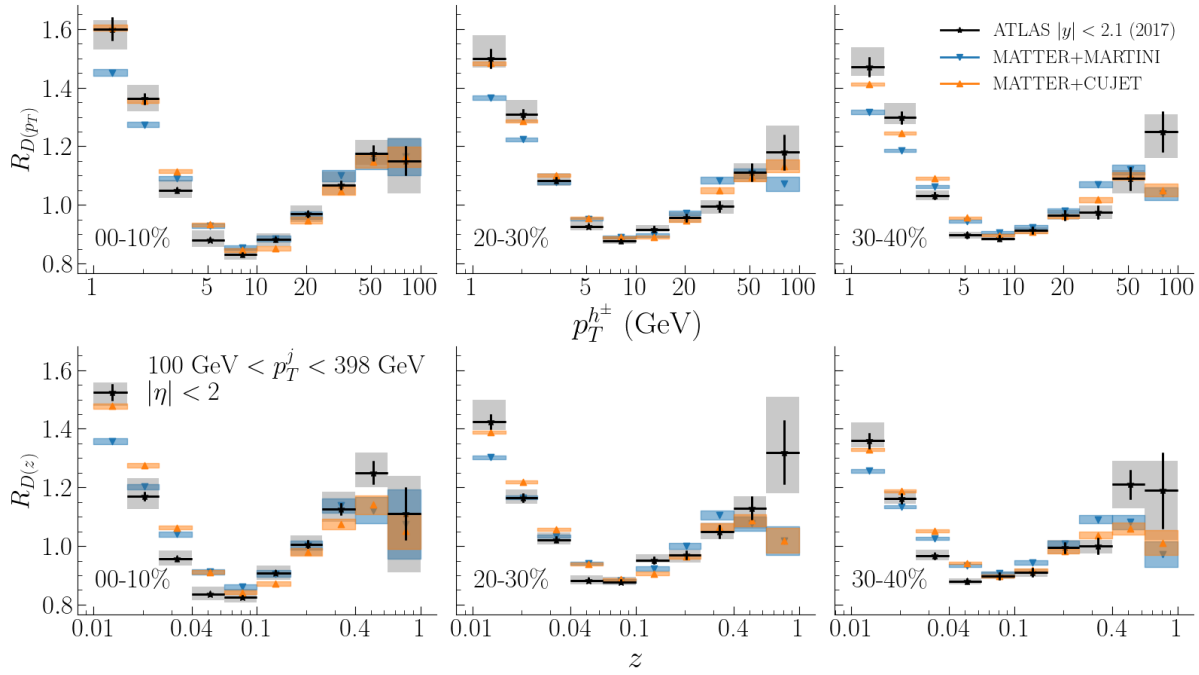

Figure 6.12: Comparison of jet fragmentation function ratios in three centrality classes (0-10%, 20-30% and 30-40%, columns) from CUJET and MARTINI simulations as a function of charged hadron transverse momentum (top row) and charged hadron momentum fraction (bottom). Inclusive jets are clustered at midrapidity ($|\eta| < 2.0$) using the anti-k_T algorithm with cone radius $R = 0.4$. Fragmentation functions of clustered jets passing the transverse momentum cut $100 < p_T^{jet} < 398$ GeV are then computed. The p-p baseline is given by Figure 6.5. Data from the ATLAS Collaboration [183].

fractions. For a jet with momentum $p = 100$ GeV, this means MARTINI curves in jet fragmentation function ratios are expected to be above CUJET the calculation for $10 \leqslant p_T^{h\pm} \leqslant 40$ GeV. This is observed in the top row of Figure 6.12 and given the relatively large energies involved, elastic scattering channels are not as relevant as for the $z < 0.07$ range. An important note to remember, of course, is that these are approximate ranges given the composite nature of the model with MATTER handling the high virtuality stage of jet energy loss.

Our analysis indicates that once fitted to the most central charged hadron R_{AA} data, two very different energy loss models, CUJET and MARTINI, are nearly indistinguishable for all other centralities. However, charged hadron nuclear modification factor is also a forgiving observable due to its integrated nature. Jets and jet substructure measurements, then, show remnants of the differences between the treatment of

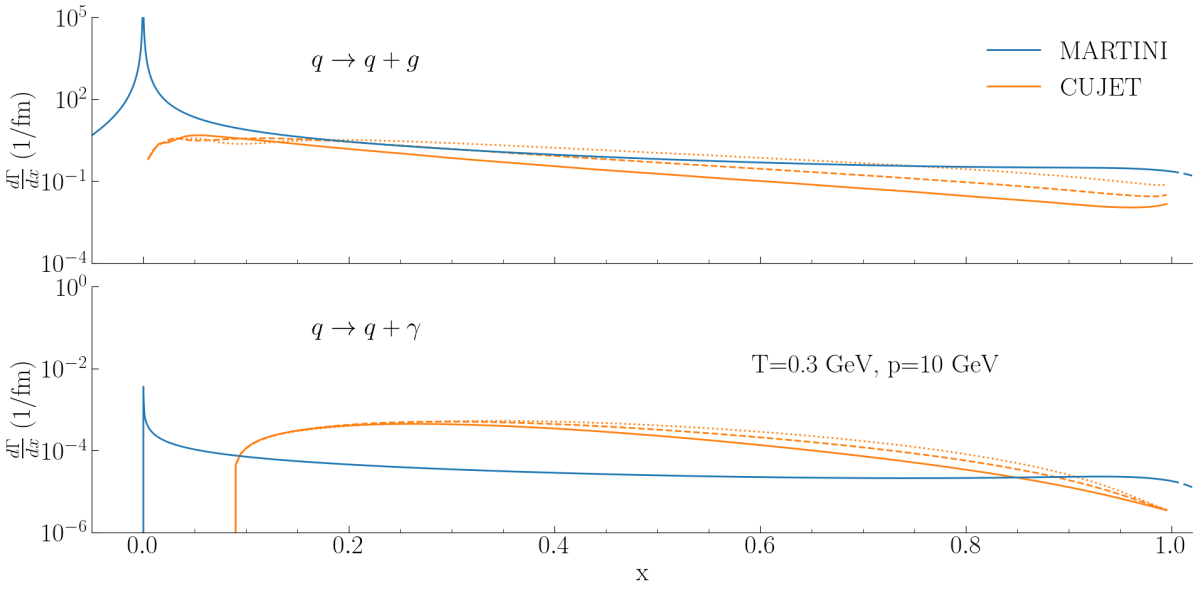

Figure 6.13: Same as Figure 6.8 but for a parton of momentum p = 10 GeV.

bremsstrahlung between CUJET and MARTINI. In particular, fragmentation function ratios of jets show systematic differences in how the models populate and distribute the charged hadrons along the jet axis.

6.2.2 *Jet-medium photons*

We previously introduced jet-medium photons as probes of the theory in Section 5.3.4. Here we perform a similar analysis, using the results of jet-medium photon calculations from `Pb-Pb` collisions at 2.76 ATeV, as well as `Pb-Pb` at 5.02 ATeV and `Au-Au` at 200 AGeV. The simulations of these systems are performed using the same physical settings as those shown earlier in this chapter. This was a conscious choice as we want to analyze the two energy loss models and their effects on the evolving hard partons. Re-fitting the running coupling parameters for each collision system may mask the differences between the models. Finally, the number of binary collisions is once again taken from Ref. [37][6].

The total direct photon spectrum, based on the discussion of Section 5.3.4 is constructed out of a sum of thermal, pre-equilibrium, jet-medium and prompt photons. The expectation is that for $p_T \leqslant 4$ GeV, thermal and pre-equilibrium photons are

6 Specifically, tables 9, 10 and 20 of that reference.

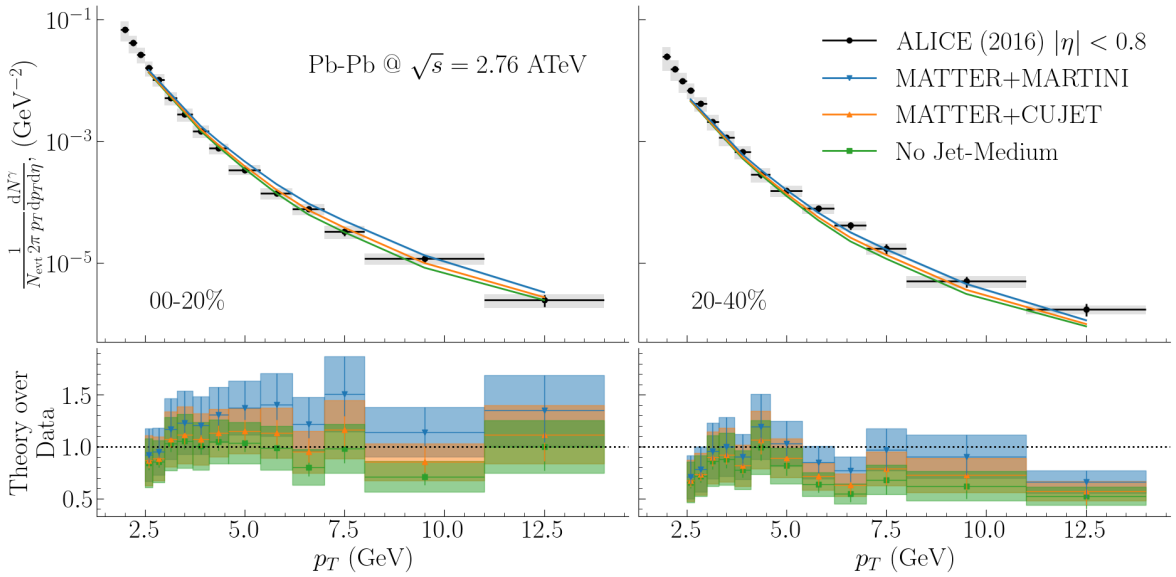

Figure 6.14: Direct photon spectra from Pb-Pb collisions at 2.76 ATeV collisions for two centralities compared against data from the ALICE Collaboration [185]. The photons are at midrapidity ($|\eta| < 0.8$). The three spectra are (a) direct photons without jet-medium contribution (green), (b) direct photons with jet-medium computed using MARTINI (blue) and (c) direct photons with jet-medium computed using CUJET. The prompt photon contribution (in all three spectra) is scaled by a k-factor (0.736). The lower panel shows the ratio of the theoretical calculation to data. See text for details.

the principle photon emission channels while $p_T \geqslant 20$ GeV would be dominated by prompt photons. The effect of the inclusion of jet-medium photons is studied by constructing the direct photon spectrum in three ways

A. spectrum 1: no jet-medium: sum of thermal, pre-equilibrium and prompt photons,

B. spectrum 2: MATTER + MARTINI: spectrum 1 + jet-medium photons given by MARTINI,

C. spectrum 3: MATTER + CUJET : spectrum 1 + jet-medium photons given by CUJET.

The same k-factor prescription of Section 5.3.4, where the spectrum is matched to the central value of the largest p_T bin of the data, is also used here.

Figure 6.14 shows the result of constructing the total direct photon using the three methods described above, present along with the photon data from the ALICE Col-

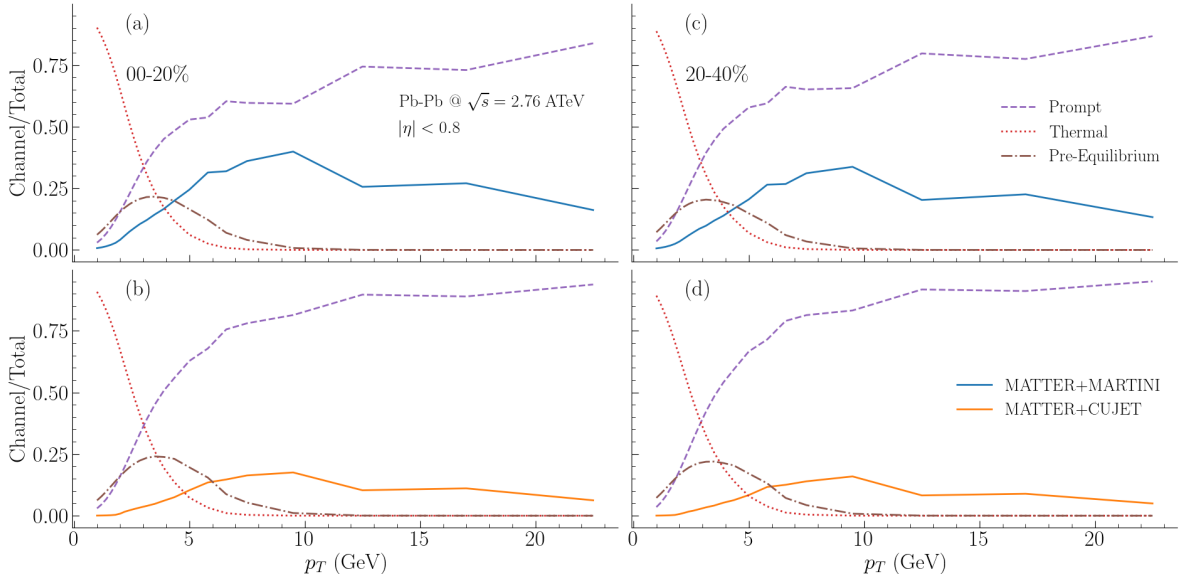

Figure 6.15: Breakdown of different photon production channels for Pb-Pb collisions at 2.76 ATeV. The ratios of figures (a) and (c) are calculated with jet-medium calculations from MARTINI for 0-20% and 20-40% centralities respectively. Figures (b) and (d) show the same using CUJET jet-medium photons. In all figures, the solid line is the ratio of the jet-medium photon spectrum over the total theory spectrum.

laboration. The prompt photon spectrum is set to $k_{fac.} = 0.736$) and used for both centrality classes.

The effect of the inclusion of jet-medium photons, using either CUJET or MARTINI energy loss models, is to bring the theory curve into better agreement with the data in the intermediate transverse momentum range, $p_T \in [4, 10]$ GeV. The effect is visible in the upper panels of Figure 6.14 when comparing spectra and the lower panels, where the ratio of the theoretical calculations to data is presented. The spectrum of direct photons, including jet-medium photons from MARTINI is clearly above that of CUJET for both centrality classes. This can be due to two related effects. First, the AMY photon radiation rates in MARTINI are larger than the equivalent LO-DGLV rates in CUJET. This is due to the difference between the rates for small x (see Figure 6.13 and Figure 6.8 for exampe). Thus a quark or anti-quark evolved with MARTINI would yield more bremsstrahlung photons. Second, MARTINI generates more energy loss via gluon emission. As such, a hard fermion spectrum is softened more when evolved with MARTINI, resulting in a larger population of relatively softer fermions, which are even more efficient at radiating photons in our p_T range of interest.

We can study the p_T dependence of the different photon production channels by forming the ratios of each channel to the total theoretical yield for each centrality

$$\frac{E\, dN^{ch}/d^3p}{\sum_i E\, dN^i/d^3p}. \tag{6.3}$$

Figure 6.15 shows the result of this exercise. The overall p_T behaviour at low and high values of photon transverse momentum is as previously expected. Thermal photons dominate for lower p_T, while prompt photons become increasingly more important as we go to higher photon transverse momentum. Both jet energy loss models expect a significant contribution for jet-medium photons for $p_T > 4$ GeV, with the most important contribution window being at $p_T \in [4, 10]$ GeV. The jet-medium contribution, when computed using MARTINI is approximately 40% of the total photon yield in this p_T window and remains large ($\approx 20\%$) even for transverse momentum of 20 GeV. CUJET, on the other hand, provides a jet-medium yield that has half the relative importance of MARTINI. There is only a slight decrease for jet-medium photons from both models when comparing the two centrality classes, and overall, the relative importance of the different photon channels remains unchanged in different centralities.

To study the effect of the initial hard parton distribution, we can consider `Au-Au` collisions at 0.2 ATeV.

The effect of using jet-medium photons to construct the total direct photon yield is shown in Figure 6.16. The prompt photon in this calculation is modified in the same way as in Figure 6.14, with a $k = 1.12$ factor multiplying the prompt spectrum as provided by a PYTHIA simulation in order to match the highest p_T bin of the data. We see that the introduction of jet-medium photons from either energy loss model improves the agreement of the direct photon spectrum with the data. While the MARTINI results are again clearly above those of CUJET, the jump from CUJET to MARTINI is not as pronounced as it was for `Pb-Pb` collisions at 2.76 ATeV.

We can look into the composition of the direct photon spectrum as a function of the photon transverse momentum in `Au-Au` collisions in Figure 6.17. There, we can see why the jump due to the inclusion of jet-medium photons is less significant than for the case of `Pb-Pb` at $\sqrt{s} = 2.76$ ATeV. The share of the direct photon spectrum from jet-medium photons is, again, larger for MARTINI than CUJET. However, unlike in Figure 6.15, the maximum contribution of MARTINI is approximately 25% and falls off

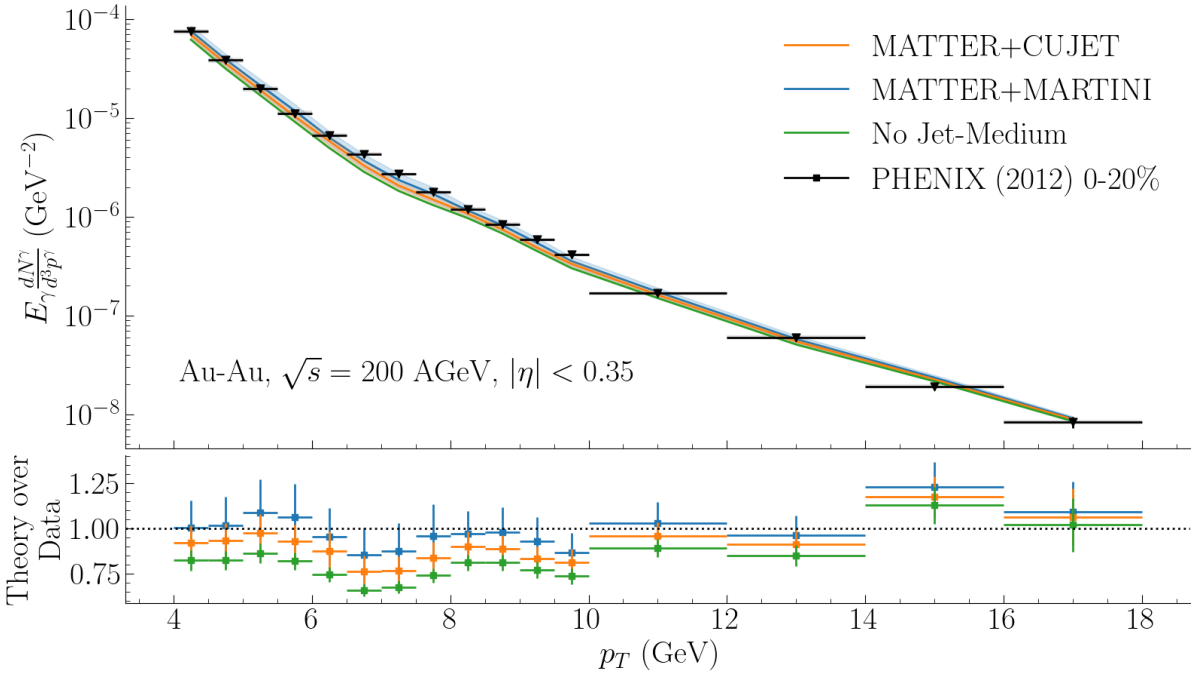

Figure 6.16: Direct photon spectrum in Au-Au collisions at 0-20% centrality and $\sqrt{s} = 200$ AGeV at midrapidity ($|\eta| < 0.35$). Same k-factor prescription ($k = 1.12$) and colour scheme as Figure 6.14. The bottom panels present the ratios of the theoretical calculation to the experimental observations. Data from the PHENIX Collaboration [201].

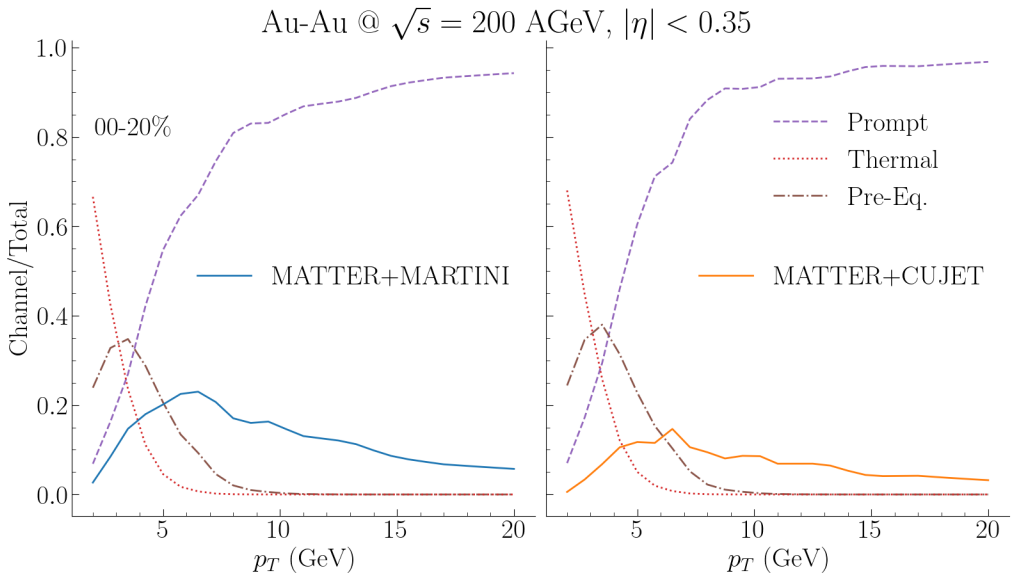

Figure 6.17: Channel-by-channel breakdown of the contribution of different photon production channels to the total direct photon spectrum in Au-Au collisions at 200 AGeV, at 0-20% centrality.

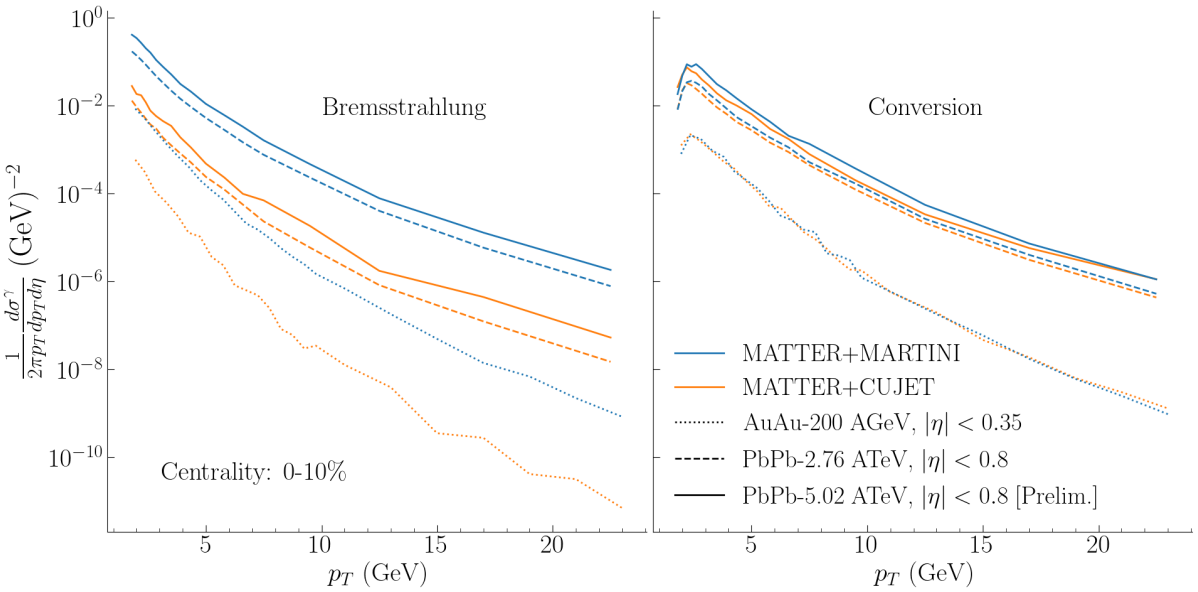

Figure 6.18: Comparison of the jet-medium photon channels via their invariant differential cross section for the three collision systems under study in this thesis, at 0-10% centrality class and at midrapidity ($|\eta| < 0.35$ for Au-Au, $|\eta| < 0.8$ for the Pb-Pb systems).

faster with increasing transverse momentum than the previous system. The difference in the contributions is, then, indicative of the importance of the jet population. The yield of the jet-medium photon channels is related to their own rates and those of the other inelastic and elastic rates. Thus, a low rate of photon bremsstrahlung or conversion can be mitigated if the other jet energy loss channels efficiently fill the underlying $q/\bar{q}$ population.

Figure 6.18 shows the invariant differential cross-section of the two jet-medium photon channels. The bremsstrahlung and conversion photon spectra are shown for the 0-10% centrality class of three collision systems: Pb-Pb at $\sqrt{s} = 2.76$ and 5.02 ATeV and Au-Au at 200 AGeV[7]. The large difference in the photon bremsstrahlung rates is evident on the left-hand side of this figure, where the bremsstrahlung photons from CUJET are subdominant to the MARTINI generated spectrum. The conversion channels are much closer to each other though differences can still be observed between the two models, and again, MARTINI shows a higher yield of jet-conversion photons. Given that the implementation of the conversion channel is identical for both models, down to the fixed value of α_s, we can conclude that the differences in that channel are

7 The hadronic results for Pb-Pb at 5.02 ATeV and Au-Au at 200 AGeV are shown in Section B.2

$\sqrt{s}$ (GeV)	BREM. RATIO	CONV. RATIO
Au-Au @ 200	52.7	1.03
Pb-Pb @ 2760	25.4	1.26
Pb-Pb @ 5020	22.9	1.40

Table 6.2: Average ratio of the MARTINI differential cross section to the CUJET differential cross section of the two jet-medium photon channels. Data corresponding to the curves of Figure 6.18.

entirely due to the underlying evolving $q/\bar{q}$ distribution. This means that MARTINI is better at populating the quark distribution, $f_{q/\bar{q}}(p_T)$, for intermediate and lower values of quark/anti-quark transverse momentum, which in itself is an indication of the ability of MARTINI in effectively quenching the initial distribution. This difference is not large, and if one was to compare gluon emission or conversion channels, it could be easily lost to hadronization effects during the full simulation stage, but it is here, in the photon spectrum.

Both conversion and bremsstrahlung channels show a different p_T dependence when comparing the Pb-Pb results to Au-Au, due to the effect of the initial jet distribution. At LHC energies, the jet population is larger, and the intermediate/lower momentum region of parton jets is seeded by the more energetic partons. MARTINI due to the relatively flat shape of its rate over a large range of the radiated partons momentum ratio x (see Figure 6.8 or Figure 6.13, for example), is able to create quarks or anti-quarks at lower momenta who then are more likely to radiate photons at even lower energies. Furthermore, MARTINI possesses more fermion-producing channels than CUJET, with the most important of them being the gluon branching process $g \to q + \bar{q}$.

MARTINI also radiates many more soft gluons than CUJET. This can be seen, as an example, in Figure 6.19 where two quarks of 20 GeV initial momentum are evolved for some time in a fixed temperature $T = 300$ MeV QGP brick and reach a final momentum of 12 GeV. We can see that the quark, as evolved by MARTINI has many more radiated gluons and that they are, in general, softer than the gluon emissions from a quark that is evolved by CUJET. In a realistic simulation, given the composite nature of

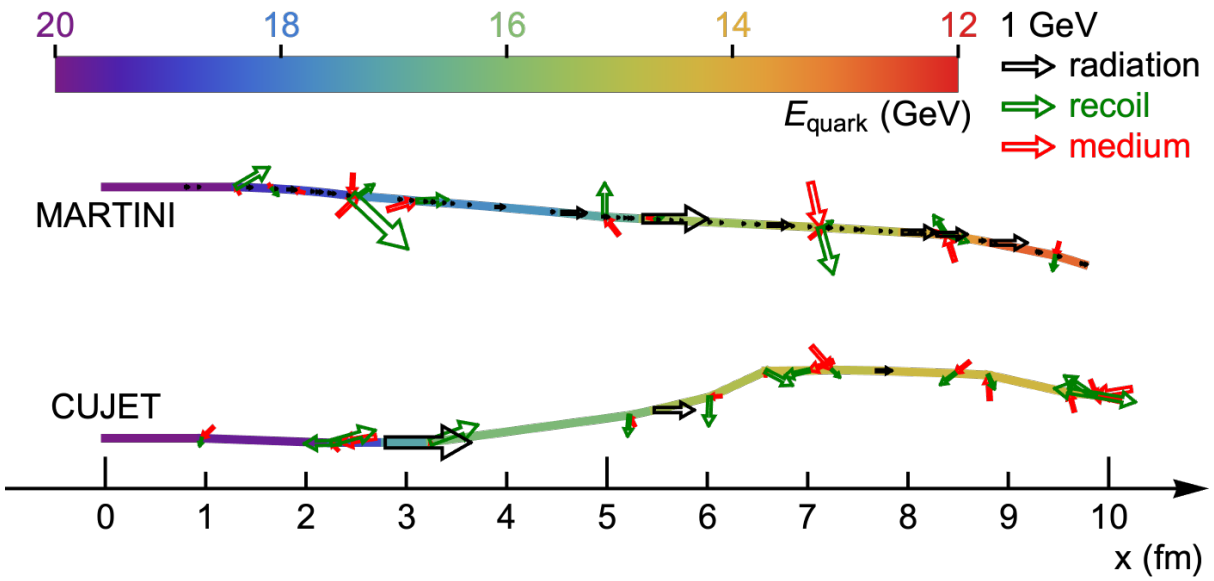

Figure 6.19: Evolution history of two hard quarks with initial momentum of 20 GeV and final momentum of 12 GeV. The horizontal and vertical position of the colour tube denotes the relative momentum direction of the parton with regard to its initial momentum. The upper and lower tubes are evolution histories according to MARTINI and CUJET, respectively. The colour of the tube corresponds to the energy of the quark. The black, green, and red arrows stand for the momentum vectors of the radiated gluon, recoil partons and incoming medium particles, respectively. Figure created by Dr. Shuzhe Shi.

our models, many of these gluons are likely to have been radiated in the middle of the evolution. In such a situation, considering the information in Figure 4.10, the gluon branching channel can make a non-trivial contribution since its rate at $T = 200$ MeV, is comparable to that of gluon emission from a gluon, particularly for $0.2 \leqslant x \leqslant 0.5$. For RHIC energies, the initial jet population is much smaller, and the lifetime of the medium is shorter. Therefore, the efficiency of the energy loss model at populating the $q/\bar{q}$ distribution becomes even more significant since the initial jet distribution for `Au-Au` at 200 AGeV is cut off at $\sqrt{s}/2 = 100$ GeV, whereas for the LHC energies, the initial distribution (though falling as a power law) can go as high as an order of magnitude above this value. Table 6.2 shows the result of taking the average ratio of the MARTINI jet-medium photons to the CUJET jet-medium photons in the three systems. Since the conversion rates are identical, the difference in the conversion channel is entirely due to the underlying fermion population, which can go from 3% at 200

AGeV collisions of Au-Au to 40% for Pb-Pb collisions at 5.02 ATeV. Given the direct proportionality of conversion photon spectrum to the $q/\bar{q}$ spectrum and after integrating over the spacetime history of jet evolution through the plasma, a MARTINI simulation is likely to have 40% more fermions in $[4, 25]$ GeV transverse momentum window than a CUJET simulation. The differences in bremsstrahlung ratios further demonstrate the point made in the above discussion on the effect of the initial jet population and its interplay with the energy loss rates. The two LHC energies result in roughly the same ratio for MARTINI to CUJET bremsstrahlung, while the Au-Au collisions at a much lower center of mass energy show a much larger difference between the two models.

6.2.3 *Direct photon scaling*

An interesting way of looking at direct photons is via the study of the dependence of their yield on system size. One can ask about the scaling relation of the direct photon yield with system size and consider how the scaling changes by changing the kinematic cuts on the photons. By using the charged hadron multiplicity at midrapidity as a proxy for system size, the PHENIX Collaboration [202] found the following scaling relation between the direct photon and charged hadron multiplicities

$$\frac{dN^{\gamma}}{dy} = A\left(\frac{dN^{h^{\pm}}}{dy}\right)^{\alpha}, \tag{6.4}$$

where $\alpha = 1.25$. When computing the photon multiplicity, we have to integrate over the differential yield,

$$\frac{dN^{\gamma}}{d\eta} = \int_{p_T^{cut}}^{\infty} p_T\, dp_T \frac{dN^{\gamma}}{p_T\, dp_T\, d\eta}. \tag{6.5}$$

Considering the above equation along with the information in Figure 6.17 and Figure 6.15, we find that we can probe the scaling properties of different photon production channels by varying the lower bound on the momentum integral.

For the charged hadron multiplicity, only the charged hadrons from the soft sector are considered. For each system and centrality class, these are provided in Table 6.3 This is an approximation it takes the dominant source of charged hadron production to be through the hadronization and fragmentation of the QGP, with jets and

SYSTEM	CENTRALITY	$dN^{h^{\pm}}/d\eta$
AuAu-200 AGeV	0-10%	424.35
AuAu-200 AGeV	10-20%	291.65
PbPb-2.76 ATeV	0- 05%	2302.0
PbPb-2.76 ATeV	05-10%	1893.59
PbPb-2.76 ATeV	10-20%	1436.59
PbPb-2.76 ATeV	20-30%	968.85
PbPb-2.76 ATeV	30-40%	633.65
PbPb-2.76 ATeV	40-50%	519.23
PbPb-5.02 ATeV	0-10%	2660.08
PbPb-5.02 ATeV	10-20%	1813.17
PbPb-5.02 ATeV	30-50%	647.93

Table 6.3: Charged hadron multiplicity at midrapidity from the hydrodynamic simulation of the QGP background used in this chapter.

jet-related contributions seen as merely a small correction. While this is a reasonable approximation, it ignores the coupling of the jets to the soft background via their energy loss. Recent concurrent simulations [20] where deposited or subtracted energy by the jet is treated as a source term for the hydrodynamic simulation have shown that particularly at low p_T, the jet modifications to the soft sector are significant and should be accounted for. For now and in this work, the original assumption of the independence of the jet energy loss simulation from the hydrodynamic one is maintained.

From Figure 6.20 it is clear that increasing the p_T^{cut}, has a major effect. As the lower bound increases, a smaller proportion of the soft sources (thermal and pre-equilibrium photons) contributes to direct photon multiplicity. Given that these are by far the dominant sources of photon production, by yield, the overall photon yield collapses by nearly two orders of magnitude.

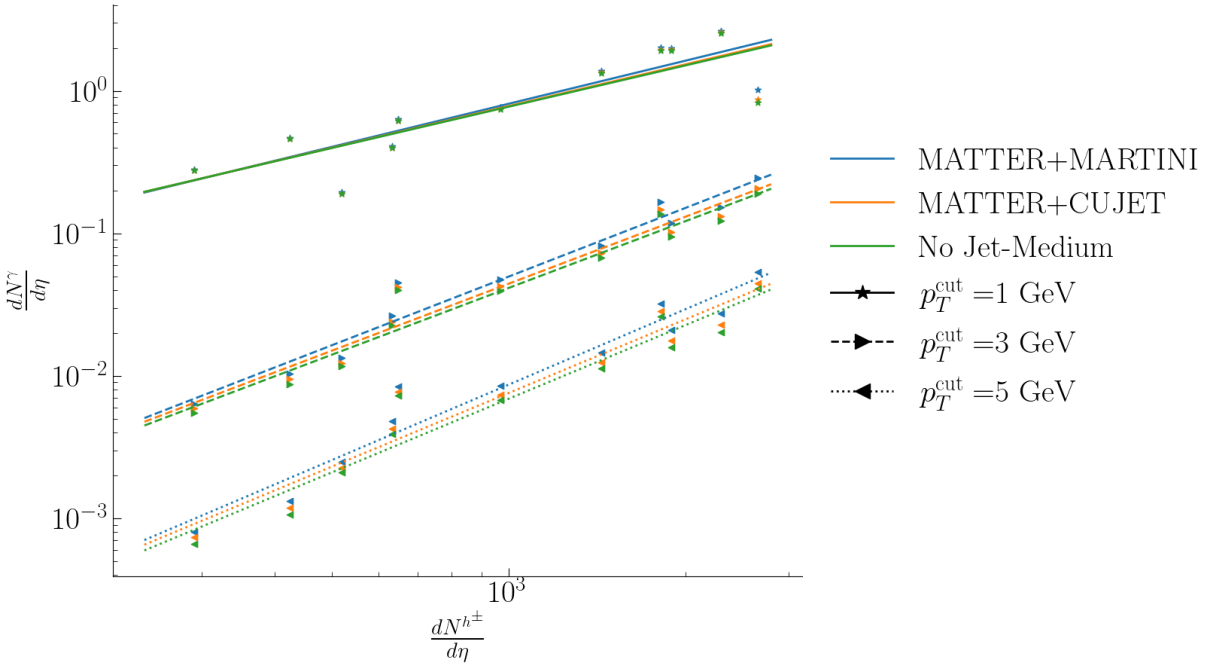

Figure 6.20: Photon multiplicity versus charged hadron multiplicity (data from Table 6.3) at midrapidity. The markers denoted as star, left triangles, and right triangles correspond to the numerical integration of the spectra using the three values of $p_T^{cut} = 1, 3$ and 5 GeV, respectively (or going from top to middle to bottom of the figure). The solid, dashed and dotted lines are the fits of these results to Equation 6.4. Direct photon spectrum from the MARTINI governed jet energy loss simulations is clearly distinct from that of CUJET, which itself is very close to the case with no jet-medium photons. See text for details.

p_T^{cut} (GeV)	α		
	MATTER+MARTINI	MATTER+CUJET	NO JET-MED.
1.00	1.00	0.97	0.96
3.00	1.60	1.56	1.56
5.00	1.76	1.72	1.72

Table 6.4: Numerical values of the scaling factor, α from Equation 6.4 for the three sets of the momentum cut in Figure 6.20. The effect of increasing the momentum cut is an increase in this scaling factor.

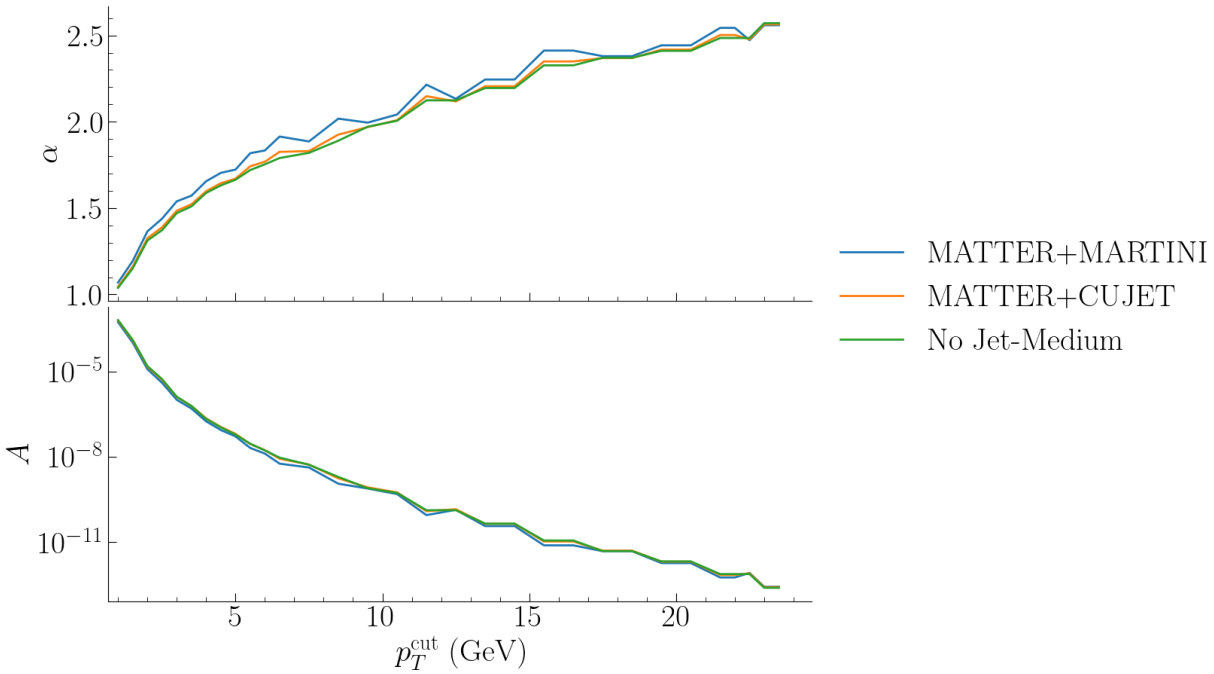

Figure 6.21: Plot of the scaling power α and the coefficient A (for completeness) as a function of the p_T^{cut}. The curves converge as this momentum cut increases beyond the region of significance of the jet-medium sources.

Consequently, the scaling factor α increases as the curves become more and more steep. One can then use the relationship between direct photon multiplicity and hadron multiplicity to map the importance of the contribution of jet-medium photon sources. Table 6.4 shows the values for α associated with the fits in the figure.

The full fit results for more values of p_T^{cut} are presented in Figure 6.21. Initially, as the momentum cut is relatively low, the three direct photon curves do not show much difference from each other. This agrees with the results previously shown in Figure 6.15 and Figure 6.17. As the p_T^{cut} increases, the contribution of thermal and pre-equilibrium photons is cut away, and the weight of the prompt and jet-medium sources increases. In this case, since the system as governed by the MATTER+MARTINI composite model produced more jet-medium photons than MATTER+CUJET, the net effect is the separation of the two when α is shown against p_T^{cut}. Further increases in p_T^{cut} will eventually reach the region where jet-medium photons, even from MARTINI, start to lose their significance, and this translates to a convergence of the MARTINI curve with the CUJET as well as the case with no jet-medium photons. Other theoretical cal-

culations of direct photons have reached similar conclusions regarding the transverse momentum dependence of the scaling power α [55, 203]. As mentioned before, the PHENIX Collaboration found the power $\alpha = 1.25$ independent of the p_T^{cut}. This is in significant tension with our calculations here. The source of this disagreement is unknown and further study is necessary to illuminate this issue.

Another reason to study the scaling properties of direct photons as a function of kinematic cuts is with an eye toward experimental observations. Measurements of jet medium photons are a significant experimental challenge. Currently, typical photon measurements at the LHC and RHIC generally fall into one of three categories

A. isolated prompt photons for high-p_T measurements where a cone is defined around the photon, and only those where the hadronic activity around them is below a cutoff are accepted,

B. inclusive direct photons measurements for intermediate p_T values, as we saw previously in this chapter,

C. inclusive direct photons for $p_T < 4$ GeV, where thermal photon sources are expected to dominate.

Recently, the PHENIX Collaboration [204] reported their non-prompt, direct photon measurements as the yield of direct photons with the binary collision-scaled measurement of `p-p` prompt photons subtracted. This photon sample called the *non-prompt direct photons* currently has large error bars though similar measurements in the LHC experimental facilities may not have the same problem. As for the experimental studies of jet-medium photons and the general behaviour of the different photon sources, direct photon scaling measurements are currently the only viable option for the transverse momentum regions of interest here.

6.3 SUMMARY

This chapter presented the first Monte Carlo implementation of a modified CUJET jet energy loss model, which allowed, for the first time, calculations of jets, jet substructure and jet-medium photons using the LO opacity expansion of DGLV. Another first

and novel calculation is that of jet-medium photons using MARTINI, another model of jet energy loss. Both models were used in a multi-probe comparative analysis using a multi-stage simulation of jet energy loss with the JETSCAPE framework. The work presented in this chapter is the first controlled and comparative study of CUJET and MARTINI using a realistic simulation setting.

It is known that, at the rate level, the two models are quite dissimilar and make very different assumptions regarding the nature of the QGP medium, as seen by the hard parton. On the other hand, the models offer good agreement with the data when used in a multi-stage Monte Carlo simulation. However, the agreement between the models themselves depends on the observable. The charged hadron nuclear modification factor, used to tune the parameters of the models, was found to be the least discriminatory. In contrast, jet and jet substructure observables showed systematic differences in the hadronic structure of jets. They maintained a *memory* of the partonic structure of the event. Our results indicated that measurements of jet nuclear modification factor with different cone radii are very sensitive to the details of the hard partons interaction with the medium and the interplay of the bremsstrahlung and elastic scattering channels. In particular, MARTINI and CUJET predict very different behaviours for the ratios of jet R_{AA} at different cone radii, due to the difference in the emission rate of softer gluons between the two models.

While jet spectra and jet substructure observables are useful probes in studies of the medium as well as tools to analyze different energy loss models, their usage is limited by the confining effects of QCD. In this work, we used jet-medium photons as a complementary probe. The mean free path of photos is significantly larger than the size of the QGP medium, and therefore, they receive no modifications from final state interactions. They are also not affected by the non-perturbative effects of hadronization. We showed that these photons are directly related to the evolving hard fermion distribution, and their yield is very sensitive to the details of the energy loss model. Though it is not currently possible to measure jet-medium photons exclusively, we demonstrated the potential of using both the direct photon yield and its scaling properties to indirectly probe the contribution of the jet-medium photons to the direct photon spectrum. The scaling calculations are in significant tension with the reported

experimental results of the PHENIX Collaboration and indicate the need for further study.

On the project's future outlook, several avenues of improvement were alluded to in the text. A first step would be to use the same elastic scattering model in both CUJET and MARTINI and therefore narrow the source of the observed differences to the radiative channels only. Another extension of the comparative study concerns the quark-producing channels. CUJET does not currently include processes that result in a final state quark beyond the gluon bremsstrahlung channel, $q \to q + g$. MARTINI, on the other hand, allows for more fermion production channels. An example would be implementing the $q \to g$ and $g \to q$ channels for CUJET while going beyond the collinear approximation for both channels and their equivalent photon-producing process. Gluon branching to $q + \bar{q}$ is also missing in CUJET. At relatively lower temperatures, we saw in Figure 4.10 that the gluon to fermion branching channel can, in some situations, compete with the gluon branching channel. Thus its inclusion in CUJET would enable us to simulate and compare the two models against more exotic and interesting observables. An example would be a study of jet charge in `A-A` vs `p-p` collisions.

There are other avenues of potential improvements though they get progressively more computationally intensive and physically complicated. These include, for example, concurrent simulation of jet energy loss and hydrodynamic modelling of QGP or using more suitable hadronization models in the intermediate to low p_T region.

Part III

CONCLUSION AND OUTLOOK

7

CONCLUSIONS AND OUTLOOK

Jet energy loss of hard partons in QGP is an important signal of the creation of the strongly interacting medium. Produced at the moment of hard collision, jets also traverse the medium during its evolution and receive modifications. Thus more than a signal of existence, they can also be used as probes of the QGP medium. In this work, the aim was to use jet energy loss not just as a probe of the medium but as a probe of our models. To that end, two independent and complimentary comparative analyses of jet energy loss were performed.

The first study presented a multi-probe analysis of the effect of the new, higher-order collision kernels using a single-stage simulation of jet energy loss using MARTINI. The new kernels were studied by generating radiative rates using these kernels and then embedding the rates in a static QGP brick and a realistically expanding plasma. A state-of-the-art IPG-M approach provided the modelling of the expanding plasma. The new rates differed significantly from those with the LO kernel, even when scaled according to their asymptotic behaviour. The QGP brick simulations showed that much of the difference between the evolving parton distribution could be absorbed by rescaling the strong coupling. When performing a realistic simulation using a fixed α_s, a similar behaviour was found: different rates would result in very different charged hadron R_{AA} when evaluated with the same α_s and the results would collapse on top of each other when the strong couplings were fitted to the data. Interestingly, these simulations exhibited a similar scaling for the value of their coupling as those observed at a rate level.

To thoroughly study the new rates, the first major fit for the running coupling parameters of MARTINI was undertaken. The simulation of the new rates resulted in the unexpected observation that a MARTINI single-stage jet energy loss calculations cannot simultaneously reproduce the experimentally-observed nuclear modification factors of charged hadron and jets within the same simulation. Previous work in

the literature had shown the effect of the high-virtuality energy loss (Ref. [186]) for charged hadron R_{AA}. Other studies [188–190] have utilized the formation-time procedure described in Chapter 5 for jet calculations, though only using the partonic information and no jet-substructre observables. A recent publication also studied a time-delayed parton shower and its effect on partonic jet R_{AA}. Results in this thesis are the first study of this kind for MARTINI and the first to use jet and jet substructre observables. This is a significant finding, and one that seriously challenges the assumption that shower partons lose all their virtuality before they ever encounter the QGP. The significant and unsurmountable over-quenching observed in single-stage MARTINI simulations, regardless of how weak the strong coupling was, points clearly towards a multi-stage view of jet energy loss. By comparing the single-stage and multi-stage studies performed in this thesis, it was found that the inclusion of MATTER as a model of high-virtuality energy loss is absolutely essential in simultaneous description of charged hadron and jet R_{AA}. The aspect of MATTER that most contributed to this effect, was found to be the time dependence that it introduces to the development of the parton shower.

Despite the over-quenching issue the parameter fit proceeded, using charged hadron $R_{AA}$and jet shape ratio as the fit target data. The parameter space of the elastic and radiative coupling constants was sampled using Sobol sampling. Gaussian process regression was used as a general-purpose tool to get the fit results. This itself is a novel contribution and constitutes the first, signficant and comprehensive parameter-tunning effort done for MARTINI. While the performance of the three rate sets was nearly identical for charged hadron R_{AA}, it was found that the jet shape, fragmentation function and jet R_{AA} results demonstrated slight differences between the rates that survived after the fitting procedure. Given the significant energy loss, the jet-medium photon spectra were also insensitive to including new collision kernels. This similarity of the jet-medium photon spectrum may indicate a partial thermalization of the low-p_T part of the evolving hard parton spectrum. Whether this effect would survive the introduction of a shower formation time is an open question and left for future work.

The second study is a new multi-probe, multi-stage analysis of two jet energy loss models, CUJET and MARTINI. The theory behind the models and their different as-

sumptions about the medium and energy loss process was presented in Chapter 4. Previous comparative studies of these models had been in a simple, static QGP held a fixed temperature. Chapter 6 presents a novel and original contribution to comparative studies of jet quenching where two models of interest were embedded in a multi-stage composite model of jet evolution. Using the JETSCAPE framework as a model factory, it became possible to perform the first systematic, multi-probe and multi-stage comparison of a CUJET and MARTINI. This study also required the modification of CUJET, to a Monte Carlo generator and the inclusion of an entirely new energy loss channel, photon bremsstrahlung.

The results of the multi-stage simulations were presented in Chapter 6 where the calculations of jets and jet substructure from CUJET as well as the first realistic simulation of jet medium photons from either CUJET or MARTINI were shown. After a simple tuning with the data, the models produced very similar results for two traditional observables, the nuclear modification factor of charged hadrons and jets. Jets, owing to their inherently 3D structure, are sensitive to the delicate interplay between radiative and elastic scattering channels. The differences become more apparent when ratios of the jet nuclear modification factors are taken at different jet cone radii, thus creating an observable sensitive to the soft gluon bremsstrahlung from the incoming partons. The ratio of jet R_{AA} shows clearly the interplay of the radiative and elastic channels, where the many soft gluons produced by MARTINI are pushed out of the jet cone and recovered as jet cone radius is expanded. A similar effect also exists for CUJET but due to the difference in the bremsstrahlung rates, a hard parton evolving according to CUJET radiates fewer such soft gluons. Therefore, expanding the cone radius of the jet clustering algorithm will eventually capture all the stranded hadrons resulting from the fragmentation of the radiated gluons, and the energy recovery converges much faster than MARTINI.

The jet substructure observables considered in this thesis, jet shape ratio and jet fragmentation function, also show that jets constructed after evolution by either MARTINI or CUJET look fairly similar to each other, particularly for intermediate annuli around the jet axis. However, important and systematic differences can be observed towards the periphery of the jets. The overall conclusion is the same: MARTINI emits a larger number of soft particles than CUJET. The net effect is not immediately clear

in the spectra of strongly interacting particles, and one needs to consider differential ones.

Jet-medium photons help to paint a more detailed picture. Like the gluon emission channel, photon bremsstrahlung rates in the two models are very different. However, unlike hadronic and jet observables, this leads to significantly different behaviour between the two approaches in the jet medium photon yield. While in MARTINI bremsstrahlung photons are the main source of jet medium photons, in CUJET they are but an afterthought. The photon bremsstrahlung channel indicates the need to go beyond LO in the opacity expansion. Within the jet-medium photon channels, jet conversion photons show the differences between the two models at a partonic level as they relate to the evolving hard fermion spectrum. Depending on the collision system considered, MARTINI can see as much as 40% more hard fermions in the intermediate p_T region, relative to CUJET. This indicates a strong need for further study and improvements on the model by going beyond a collinear conversion approximation.

The comparative studies performed in this work and the discussions above, naturally point towards points of improvement where one can go beyond the analysis presented. Many of these points have been hinted at or stated throughout the text. They are summarized here.

For comparisons of CUJET and MARTINI, a natural step is to make the elastic scattering energy loss channel identical. This allows for more concrete and clear conclusions from comparing clustered jets and jet substructures, as the only point of difference would be the radiative rates. Another issue is the hadronization framework. While colourless hadronization can reproduce observed hadron and jet results at high-p_T and midrapidity, it is known that recombination [205] is the dominant hadronization mechanism for intermediate and low transverse momenta. Using a new hadronization mechanism requires a full new fit of the parameters of the models in the multi-stage framework. Furthermore, hadronization models, including recombination, are still in the early stages of development and present their own unique modelling challenges.

The ability of jet medium photon channels to shed light on the evolving hard parton distribution has been demonstrated. Many other energy loss models have been proposed and compared in multi-stage simulations like the one done here, but they

have yet to consider jet medium photons. This should become a standard part of the analysis and comparison process. Given the uncertainties and ambiguities of rescattering after emission and final hadronization that gluons experience, the clean photon signal can help by giving access to the number of evolving quarks and anti-quarks. This thesis showed that the theoretical calculations of direct photon scaling have a clear momentum dependence. Experimental measurements of such an observable can allow for indirect measurements of jet-medium photons. However, existing measurement by the PHENIX Collaboration is currently in tension with the theoretical expectation, and the causes of the tension need to be clarified. A possible avenue to probe the cause of the discrepancy is to allow for concurrent simulations of the soft sector and jet energy loss, where rather than a passive medium response (the hole and recoil parton formulation), one allows for a hydrodynamic response to the jet propagation. Recent studies [20] of HIC in this vein indicate significant modifications to the hydrodynamic evolution history, which may have meaningful consequences for jet quenching.

The continuation of the kernel study in MARTINI requires a mechanism of delaying the parton shower. Implementing a formation time for the parton shower can enable the MARTINI framework to reproduce jet and charged hadron R_{AA} within the same simulation. The fit of the new MARTINI would then allow for a more precise determination of the differences in jet energy loss calculations using the new collision kernels. This requires an overhaul of the hadronization mechanism of MARTINI and thus a new fit of the MARTINI workflow for `p-p` baseline as well as the `A-A` side. Preliminary work along these lines is in progress and is currently showing great promise.

The Gaussian process regression method applied to perform a fit of the MARTINI parameters also points toward another possible avenue of future work for MARTINI. Using GPR, one can construct emulators of the model, which can efficiently mimic the extremely costly MARTINI simulations. They can be used in the context of a large scale Bayesian parameter estimation of MARTINI, to study the dependence of energy loss on critical temperature (where jets decouple from the medium), various momentum cuts and start time of energy loss (the time where jets see a hydrodynamic medium) among others.

An important note on the simulations is to remind the reader of the nature of the simulation software. Throughout the thesis, the hard scattering event has been generated by PYTHIA which uses LO matrix elements for the hard event. For the p-p baselines, most theory calculations shown here were within $20-25\%$ of the data. This is acceptable performance levels, but there is potential for improvement by using event generators such as POWHEG, previously mentioned in Chapter 2. By generating the hard scattering at NLO accuracy, one can potentially improve the performance of the p-p baseline against all observables. However, the complicating factor is the implementation of such a prescription for A-A as well as the p-p collisions. This task is expected to be challenging at both theoretical and implementation levels.

Finally, as mentioned in the text, the assumption of the independece or scale separation of the hard sector simulations and soft sector modelling has recently come under scrutiny. In Ref. [20] it was shown that the hydrodynamic history is altered significantly when the modifications from including low-p_T partons from hard scatterings are considered. Our work here also points toward the potential need for concurrent simulations of jet energy loss and hydrodynamic evolution. This can be seen in the prominence of jet-medium spectra at lower p_T, almost approaching the thermal photon domain, as well as the importance of an accurate accounting of the soft hadrons generated via the jet energy loss mechanisms. Naively, a concurrent simulation means a smaller amount of soft hadrons, relative to the current simulations, would come out of the hydrodynamic stage, which in turn means that the medium history through which jets travel may not last as long, or be as hot. This affects the jet quenching stage in non-trivial ways and thus further studies of concurrent simulations are needed to illucidate the effect on both soft and hard observables. The conclusion is the necessity to go toward this concurrent simulation, with the jet energy loss model and the hydro working in tandem. This will be a major computational effort but it is a much needed step in the direction of more realistic simulations of the QGP and a logical next step for either of the studies discussed in this work.

I conclude by referring to what a famous theorist said to disagree respectfully: One can learn much from colliding watches. We should collide even more of them!

Part IV

APPENDIX

A

PROTON-PROTON BASELINES

This appendix presents all the proton-proton collision baselines used to generate the various nuclear modification factor figures shown in the thesis.

A.1 ADDITIONAL p-p RESULTS FOR MULTI-STAGE MODELS

The following gives the p-p baseline simulations used in the JETSCAPE simulations of Appendix B.

A.2 p-p SIMULATIONS FOR SINGLE STAGE SIMULATIONS

The figures presented here are the proton-proton baselines used in Chapter 5 for the Pb-Pb collision results at 2.76 ATeV. The p-p results are computed using the MARTINI in the single-stage setup for jet analysis. This is simply a PYTHIA simulation with some bookkeeping and flow control done by MARTINI. The parton distribution functions and tunes are identical to those used in the A-A simulations of Chapter 5.

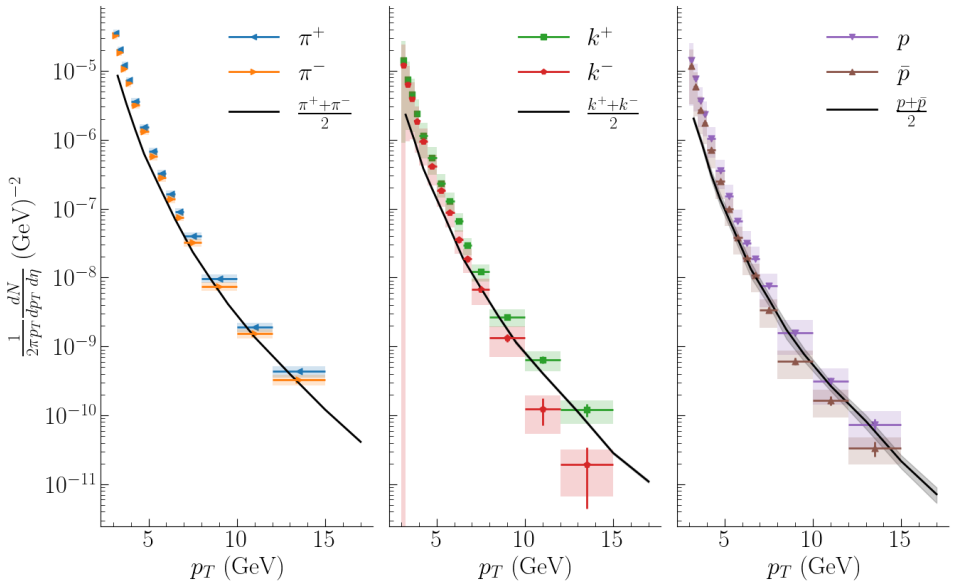

Figure A.1: Invariant spectra at midrapidity ($|\eta| < 0.5$) of charged pions, charged kaons, protons and anti-protons. The data are identified spectra of h^+ and h^- for a given hadron type h while the black lines are the average theoretical spectrum of the same. Theory curves are computed using the p-p JETSCAPE workflow. Data from STAR Collaboration [206].

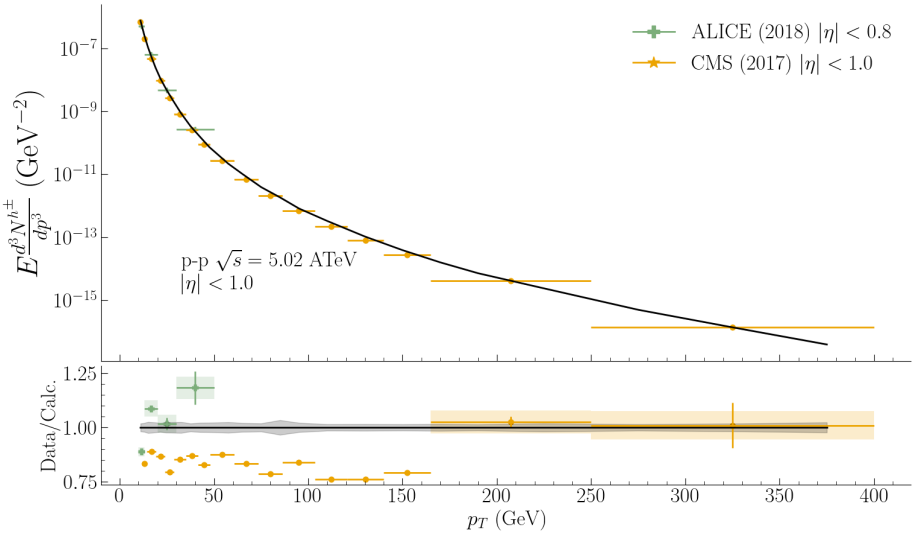

Figure A.2: Invariant charged hadron spectrum at midrapidity ($|\eta| < 1.0$) calculated using the p-p JETSCAPE workflow. Data from the CMS [207] and ALICE [208] Collaborations.

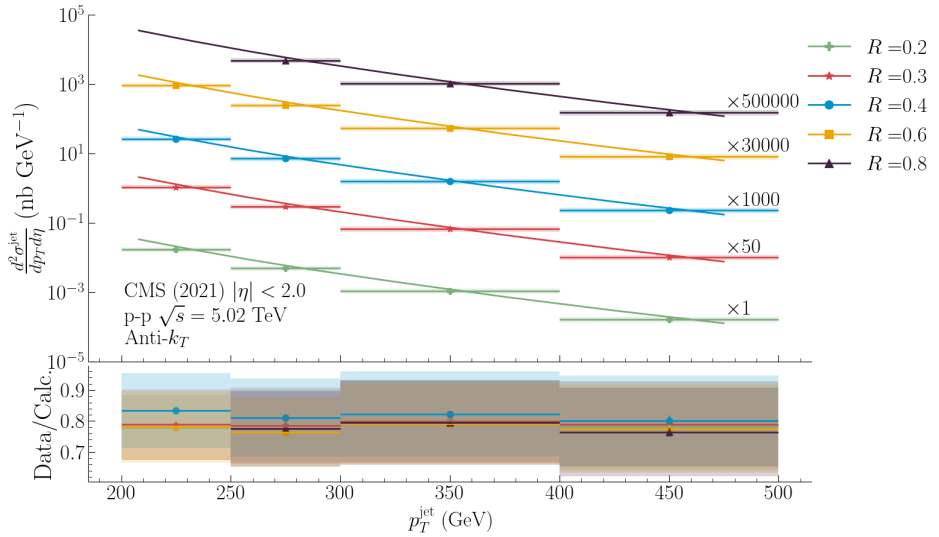

Figure A.3: Diffenetial yield of inclusive jets, clustered at different jet cone radii and at for the rapidity window $|\eta| < 2.0$. The data is from the CMS Collaboration [209].

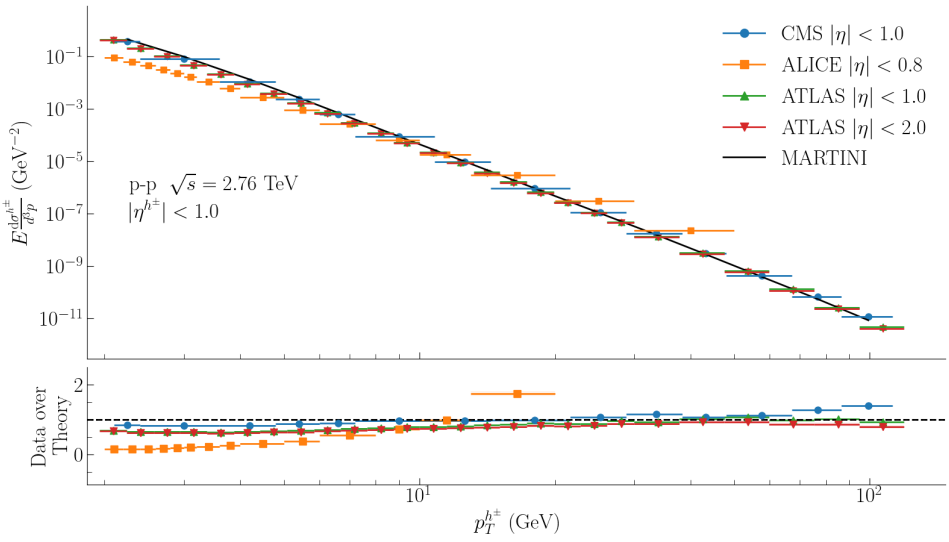

Figure A.4: Invariant different cross section of charged hadrons from p-p collisions at 2.76 TeV calculated with MARTINI embedded in the single-stage worflow. Compared to data from ALICE [175], ATLAS [176] and CMS [177] Collaborations.

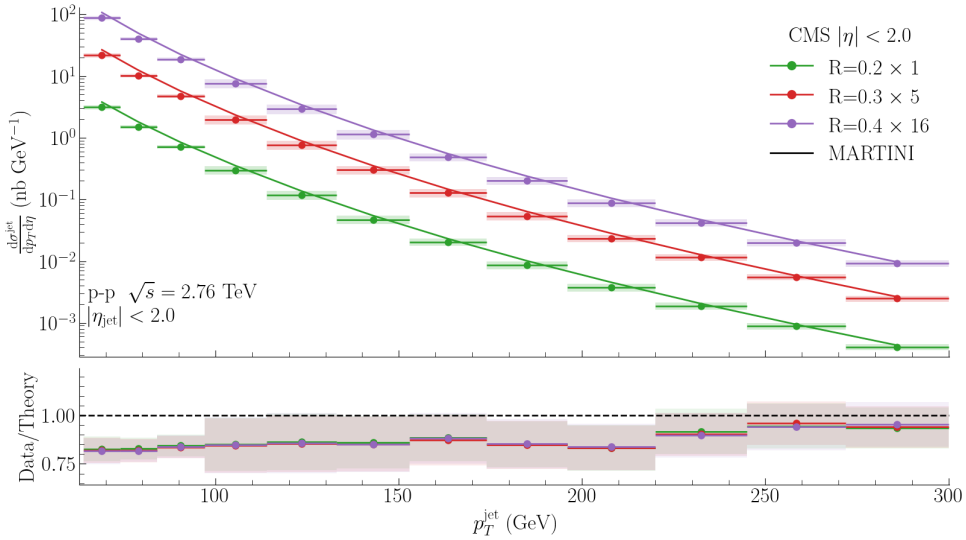

Figure A.5: Differential cross-section of inclusive jets clustered with three jet cone radii $R = [0.2, 0.3, 0.4]$ and clustered with the anti-k_T algorithm at midrapidity ($|\eta| < 2.0$). Theory curves (solid lines) are computed using MARTINI and run in a single-stage mode for proton-proton collisions. Compared to data from the CMS Collaboration [184].

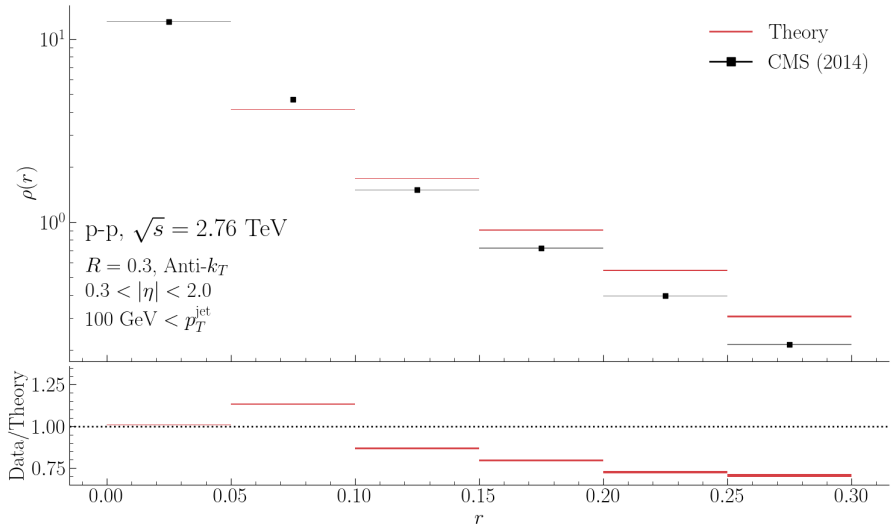

Figure A.6: Jet shape observable for jets of $R = 0.3$ and in $0.3 < |\eta| < 2.0$ in p-p collisions at 2.76 TeV. Jets are clustered with a $p_T > 1$ GeV cut on charged tracks at reconstruction. The calculation uses MARTINI in a single-stage setup. Data from the CMS Collaboration [182].

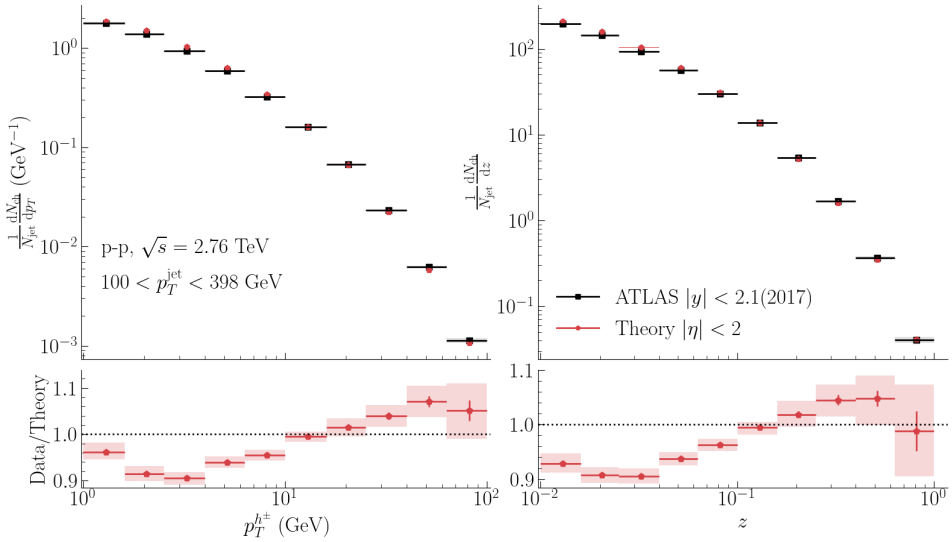

Figure A.7: Jet fragmentation function for jets of $R = 0.4$ and $100 < p_T^{\text{jet}} < 398$ GeV and at midrapidity ($|\eta| < 2.0$). The collision system is p-p at 2.76 TeV. Theory results are computed using MARTINI in the single-stage workflow.

B

JETSCAPE SUPPLEMENTARY RESULTS

This appendix provides the supplementary results for the multi-stage studies of Chapter 6. These are results of the 0-5% centrality `Pb-Pb` runs at $\sqrt{s} = 2.76$ ATeV where we study the effect of and the need for low-virtuality energy-loss by comparing simulations with and without the low-virtuality models, CUJET and MARTINI.

Results are also shown for `Pb-Pb` runs at 5.02 ATeV and `Au-Au` at 200 AGeV. These runs were made with the same parameter set as those of `Pb-Pb` at 2.76 ATeV. They are presented here to allow for a multi-system study of the two low-virtuality models, CUJET and MARTINI. However, the agreement with the data is not as good as the system for which the composite models were fitted, `Pb-Pb` at 2.76 ATeV.

B.1 ISOLATING LOW-VIRUALITY EFFECTS

The effect of the high-virtuality energy loss model, MATTER is to delay the energy loss of the parton shower. In the initial stage of the jet energy loss simulation, high p_T and high virtuality partons are evolved with MATTER only. In terms of energy loss, high p_T partons are lose energy to the medium, via the medium modification of the DGLAP splitting function in Equation 4.44. In Figure B.1 shows that for large charged hadron transverse momenta, a MATTER controlled energy loss alone is enough to recreate the high-p_T behaviour of the charged hadron R_{AA}. On the other hand, the intermediate to lower p_T charged hadron are less and less affected. This is not surprising: radiative and elastic rates, for both CUJET and MARTINI, are rather high for intermediate energy partons. In a MATTER only run, these partons are radiated from higher virtuality parton and have some residual virtuality themselves, which is quickly radiated away. After which, they are effectively decoupled from the medium. Ref. [186] shows similar work for with MATTER+LBT (Linear Boltzmann Transport). We can then consider the jet nuclear modification factor as a function of the jet cone radius. Figure B.2 shows

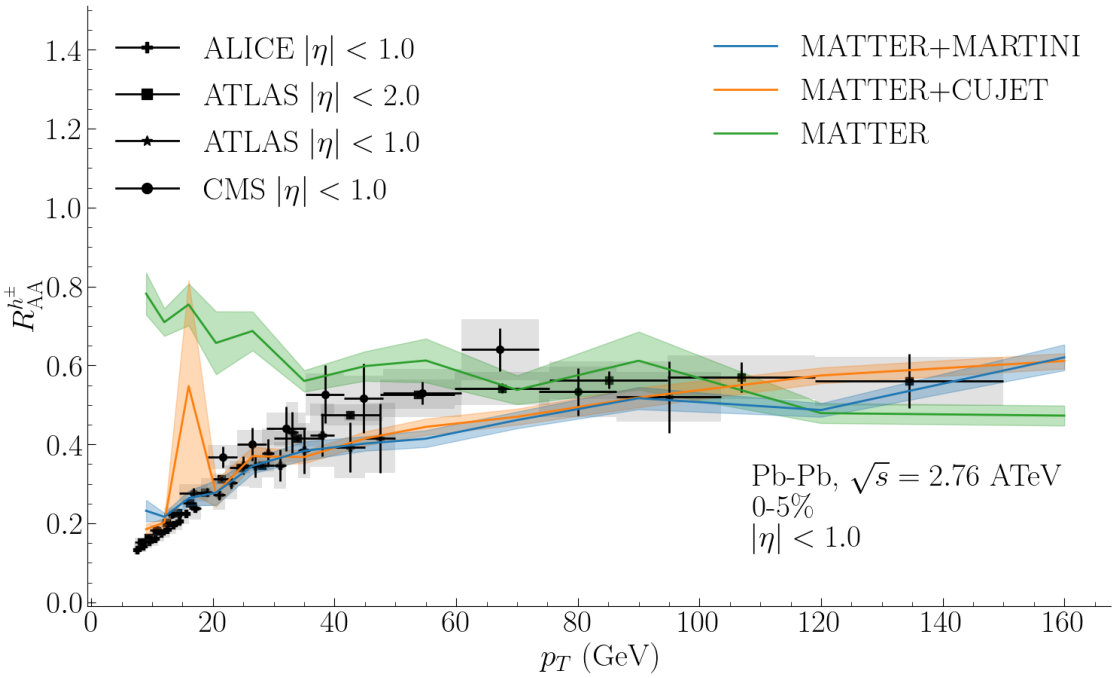

Figure B.1: Comparison of charged hadron nuclear modification factor for jet energy loss simulations, with and without low virtuality energy loss in Pb-Pb collisions at 2.76 ATeV at 0-5% centrality class.

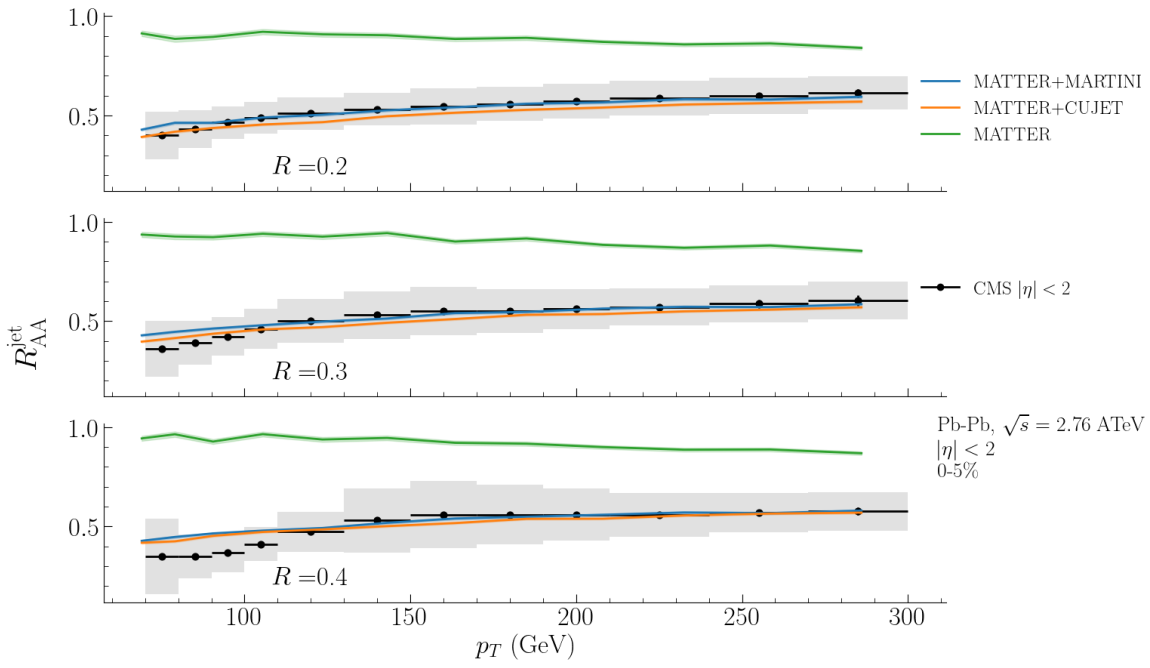

Figure B.2: Comparison of inclusive jet nuclear modification factor, with three different jet cone radii for jet energy loss simulations, with and without low virtuality energy loss in Pb-Pb collisions at 2.76 ATeV, 0-5% centrality.

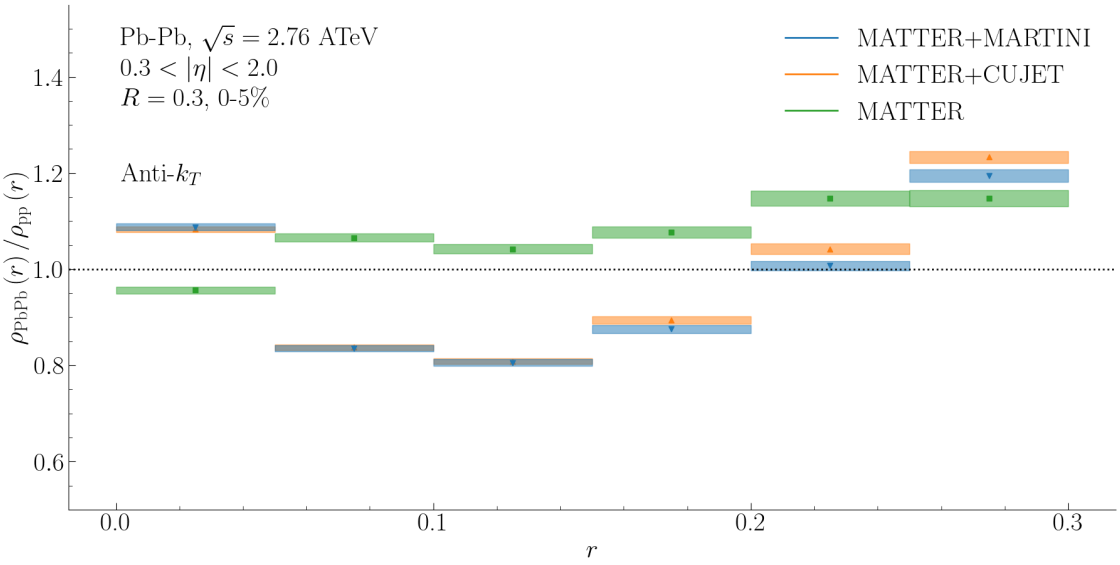

Figure B.3: Comparison of jet shape ratio, with and without low virtuality energy loss for jets of R = 0.3 and $0.3 < |\eta| < 2.0$. There is a transverse momentum cut of $p_T > 1$ GeV on the charged hadron tracks that go into the jet clustering step. The collision system is Pb-Pb collisions at 2.76 ATeV, 0-5% centrality.

the same type of calculation, with and without low-virtuality energy loss, as provided by CUJET or MARTINI. The downward trend in the MATTER-only runs, as we look at higher and higher jet p_T, shows the effect of MATTER on high-virtuality partons coming out of the initial hard scattering. On the other hand, jets with lower p_T are mostly unaffected by the evolution, as expected. The jet shape ratio comparison of Figure B.3 shows that deviations from a p-p baseline are very minor, except for the leading hadron and those along outer regions of the jet, both of which are modified by the parton shower. The figure shows that in order to arrive at the dip and rise that is seen in the data (see Figure 6.11), the inclusion of a low-virtuality model is crucial. Indeed, this observable, in its form in Equation 5.21 and Equation 5.19, is not particularly sensitive to the high virtuality part of evolution loss. We can see this by comparing Figure B.3 and Figure 5.19, the latter of which does not have such an evolution stage. Finally, jet fragmentation function ratios of Figure B.4 shows the same information as the jet shape ratios (if we flip the x-axis, the shapes are basically the same as Figure B.3). The effect of having no low-virtuality energy loss is the disappearance of the intermediate z (or p_T) dip from the jet FF ratio. This observable,

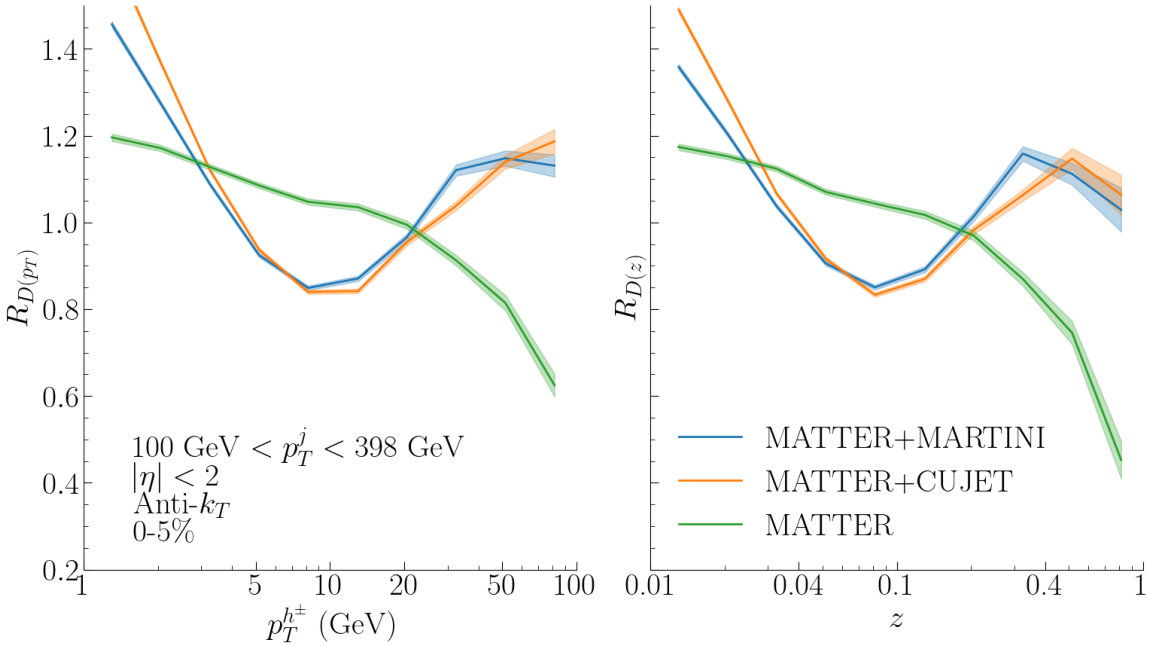

Figure B.4: Comparison of jet fragmentation function ratios, for inclusive jets with R = 0.4 and $|\eta| < 2.0$. The collision system is Pb-Pb collisions at 2.76 ATeV, 0-5% centrality.

unlike jet shape ratio, is more sensitive to the initial stages of the parton evolution, as evidenced both by Figure B.4 and Figure 5.27.

B.2 ADDITIONAL SIMULATION RESULTS FOR JETSCAPE IN a-a

In this section, additional results are presented from the simulations comparing MARTINI and CUJET in a JETSCAPE composite model. These are specifically for Au-Au at 200 AGeV and Pb-Pb at 5.02 ATeV collisions, whose data were not part of the fit of our multi-stage model. All results presented here were generated using the exact same parameters as those presented in Chapter 6. Figure B.5 and Figure B.6 present the charged hadron and inclusive jet nuclear modification ratios computed for Pb-Pb collisions at 5.02 ATeV and compared to experimental data from CMS and ATLAS Collaborations. The general message of Chapter 6, the indistinguishability of the two models, is reinforced in these figures. However, the parameter set used in the simulation is generating too much energy loss. This can be noticed for charged hadron R_{AA} of Figure B.5 at high p_T. For jet R_{AA}, this effect is most noticeable for theoretical calculation of the 30-50% centrality class which matches the ATLAS data of 30-40%

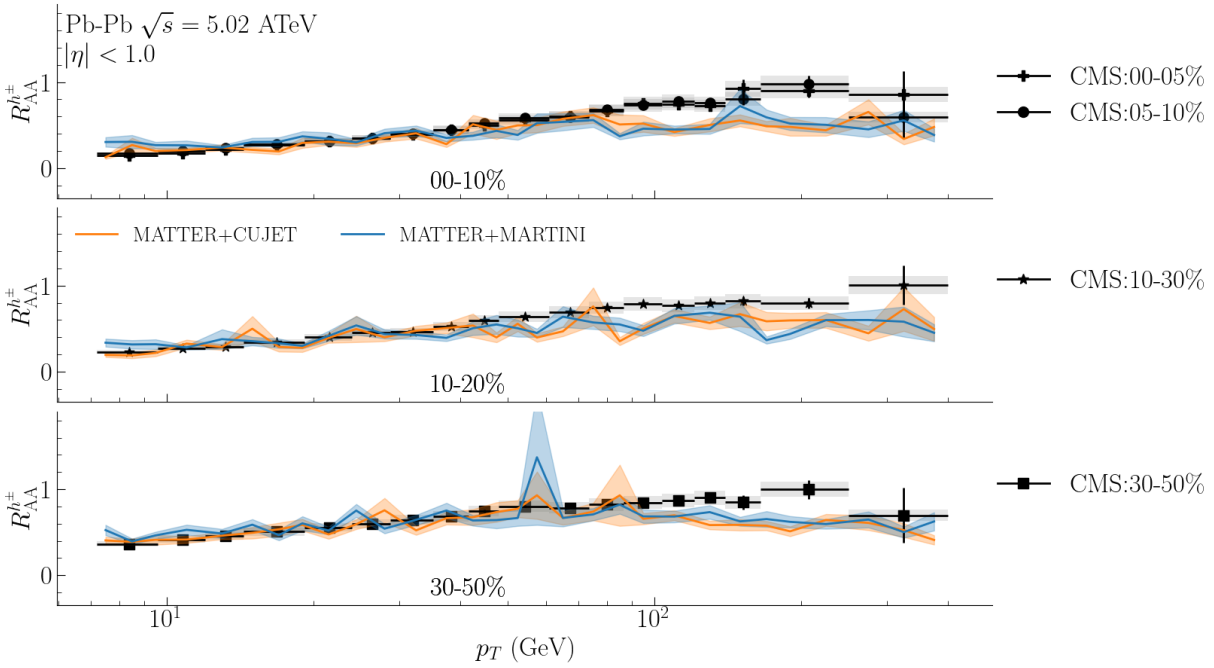

Figure B.5: Comparison of CUJET and MARTINI using charged hadron nuclear modification factor in Pb-Pb collisions at 5.02 ATeV, at three centrality classes. Theory calculations are compared to data from the CMS Collaboration [207].

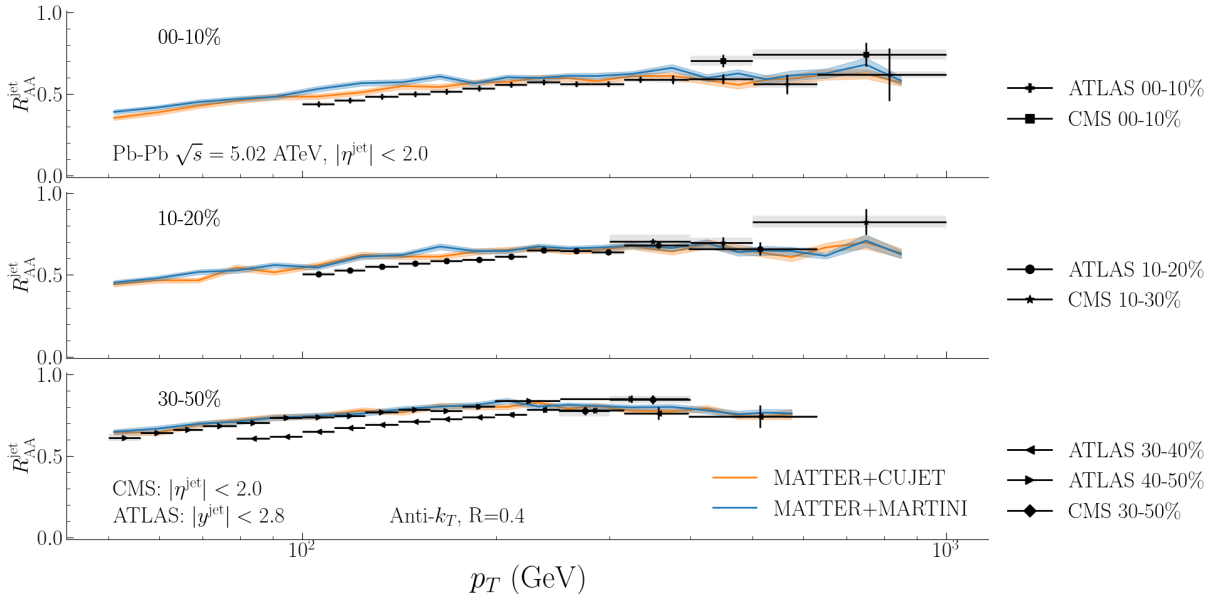

Figure B.6: Comparison of CUJET and MARTINI using inclusive jet nuclear modification factor for Pb-Pb collisions at 5.02 ATeV. Jets are clustered using the anti-k_T algorithm for a jet cone radius of $R = 0.4$ and at midrapidity ($|\eta| < 2.0$). Compared to experimental data from CMS [209] and ATLAS [210] Collaborations.

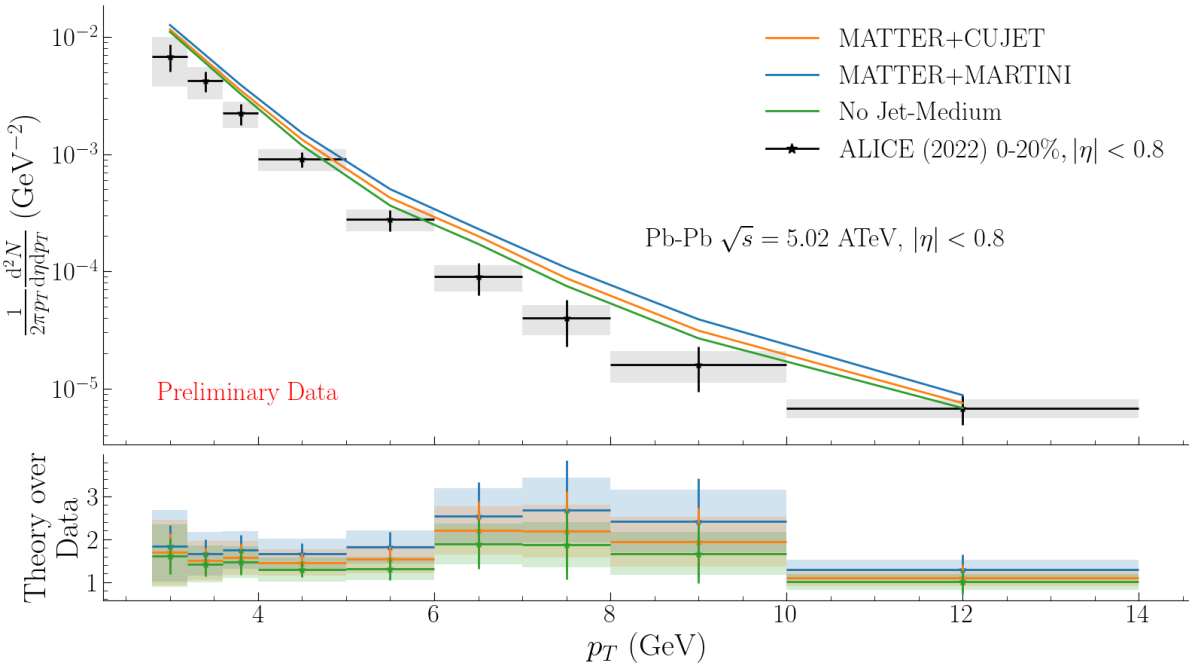

Figure B.7: Comparison of CUJET and MARTINIusing direct photon spectrum of Pb-Pb collisions at 5.02 ATeV, at 0-20% centrality. Preliminary data from the ALICE Collaboration [212].

centrality at lower p_T and 40-50% at higher p_T, while it should be located *between* the two. This observation confirms and tracks with recent work by the JETSCAPE Collaboration [144, 172] where it was found that the formulation of MATTER as provided in Section 4.5 results in too much energy loss for high virtuality partons at 5.02 ATeV collisions. The reason for this is coherence effects [211]. A high-virtuality parton resolves the very short-distance structure of the medium and thus sees a much more dilute medium than a lower virtuality parton. This effect can be accounted for by introducing a virtuality-dependent modulation function [144, 172]

$$f(Q^2) = \begin{cases} \frac{1+10\ln^2 Q_{sw}^2+100\ln^4 Q_{sw}^2}{1+10\ln^2 Q^2+100\ln^4 Q^2} & \text{if } Q^2 > Q_{sw}^2 \\ 1 & \text{if } Q^2 \leqslant Q_{sw}^2 \end{cases} \tag{B.1}$$

where $Q_{sw} = 2$ GeV is the same switching value for determining whether a parton has low or high virtuality (and consequently whether MATTER or a low-virtuality model should be responsible for its evolution). This modulation function is introduced to Equation 4.45 and has the net effect of reducing energy loss in the high virtuality stage. For completeness, the direct photon calculations for Pb-Pb at 5.02 ATeV are

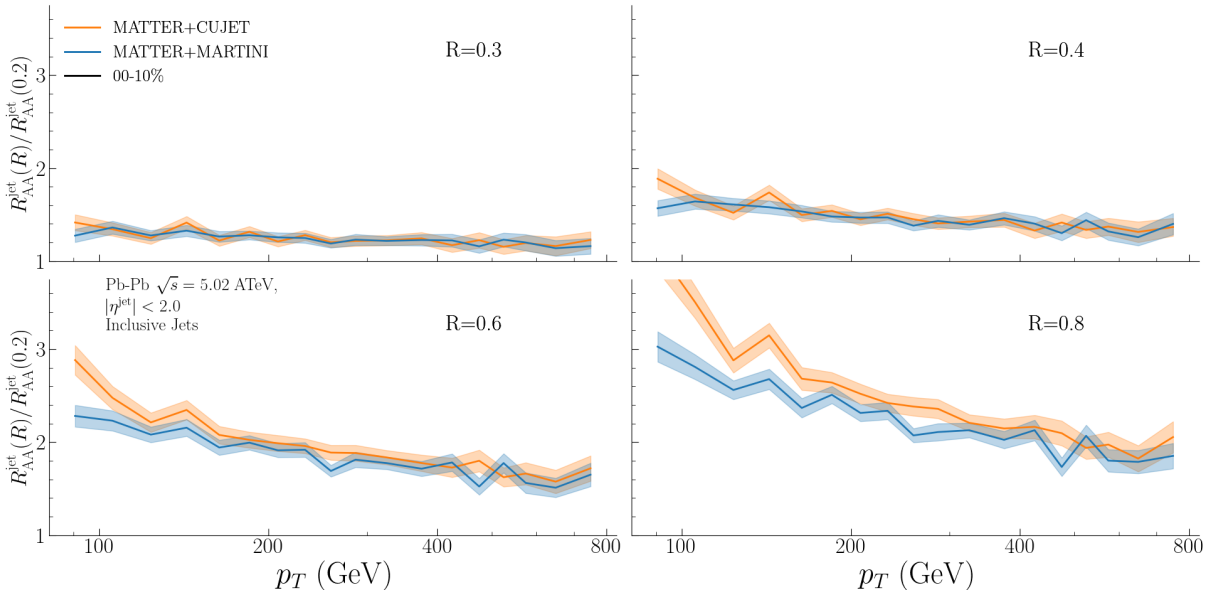

Figure B.8: Ratio of inclusive jet R_{AA} calculated for Pb-Pb collisions at 5.02 ATeV. The ratios are taken for jets clustered at midrapidity ($|\eta| < 2.0$) and for different cone radii to the baseline given by $R = 0.2$.

presented in Figure B.7. The prompt photons are scaled using the same procedure as in Chapter 6, where the prompt spectrum was scaled to match the highest p_T bin of the data, with a k-factor of 0.95. The prompt photon spectrum is overshooting the data, and the addition of other channels (jet-medium, thermal and pre-equilibrium) is, therefore, theoretical curves significantly above the data points. The cause of this behaviour lies in how the prompt photon spectrum is computed: using a PYTHIA parton shower. The prompt photon spectrum is then constructed out of the photons coming from the hard scattering process and photons that are generated during the parton shower. The latter is the dominant contribution, particularly for low and intermediate p_T. However, a parton shower calculation like this assumes that the virtual parton distribution underneath is well approximated by a p-p-like shower. Thus the shower part of the prompt photon contribution should be calculated in a MATTER-like framework. This is currently limited by statistics. Figure B.8 shows the ratio of the nuclear modification factor of inclusive jets clustered using the anti-k_T algorithm with $R \in [0.3, 0.4, 0.6, 0.8]$ cone radii to those clustered with $R = 0.2$. The rapidity window is identical for all is the same $|\eta| < 2.0$. As the cone size radius is increased, the hadrons at the periphery of the jet are brought in, increasing the total reconstructed energy. This effect then shows itself in an increase in the R_{AA} ratio relative to $R = 0.2$. For

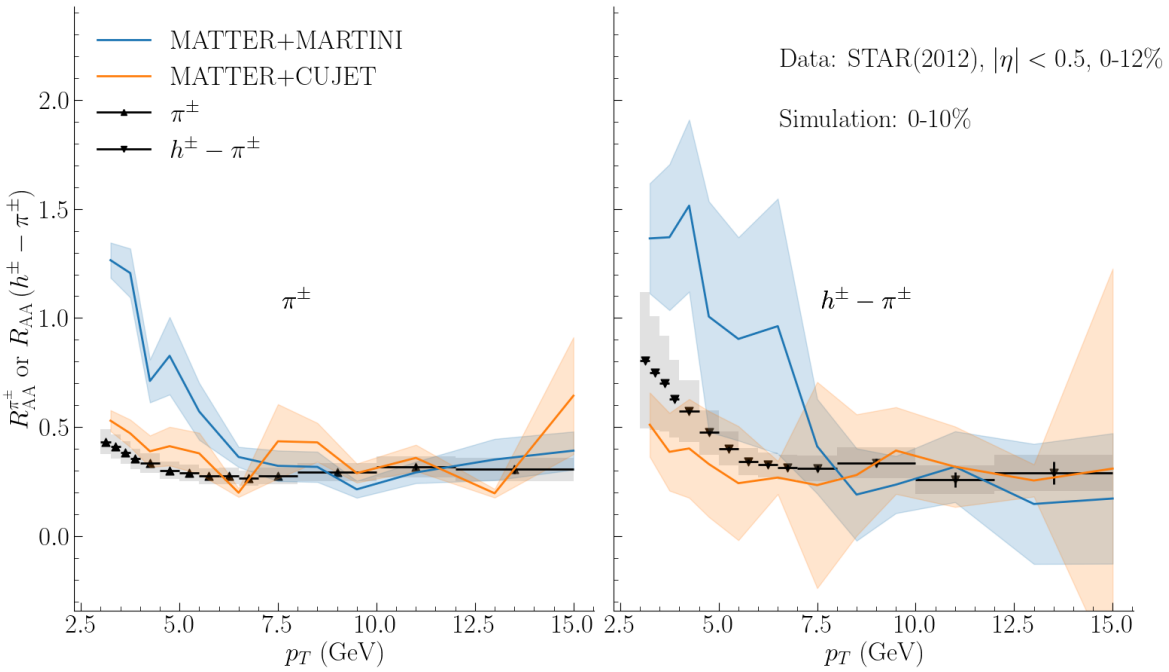

Figure B.9: Comparison of CUJET and MARTINI using nuclear modification factor of charged pions, kaons and protons, compared to data from the STAR Collaboration [213]. The subplots on the left-hand side show the nuclear modification of charged pions, while the figure on the right is the nuclear modification factor of charged kaons and protons. The latter is constructed by subtracting the charged pion yield from the total charged hadron yield of the heavy ion collision. The system under study is Au-Au collisions at 200 AGeV. The data and theory calculations are at midrapidity, $|\eta| < 0.5$. The centrality of the data is 0-12% while the theory calculations are at 0-10%.

high jet-p_T, the two models give very similar results since this is the region where MATTER is becoming more and more important. However, going from R(0.3)/R(0.2) ratio to R(0.8)/R(0.2) and focusing on the low p_T part of the figure, we can see that the CUJET and MARTINI curves are diverging. This shows the same behaviour as in Figure 6.10. Figure B.9 shows the charged hadron R_{AA} the calculation for Au-Au collisions at 200 AGeV for 0-10% centrality, compared to STAR Collaboration data (for a similar centrality class, 0-12%). The calculations include charged pion R_{AA} and the combined $k^{\pm} + p^{\pm}$ R_{AA}. The latter is constructed by subtracting the charged pion spectrum from the total charged hadron spectrum, as is done by the STAR Collaboration [213]. The figure is at a much lower p_T range than all other hadronic or jet figures in this thesis, and it is known that in this region, the dominant mode of hadronization

is *recombination*, which I do not use here. However, while the absolute agreement with the data given this fact is not reliable, we can still see the effect of the difference in the radiative rates from MARTINI and CUJET in the clear divergence of the two at low p_T with MARTINI on top. Identified hadronic final state or identified hadron R_{AA} can be a great signal for probing the fermionic/baryonic content of events and individual jets, and this figure illustrates the need for further improvements in the hadronization models provided in the JETSCAPE framework and the necessity of a concurrent simulation with hydro and energy loss working in tandem. This large number of *almost* or *mostly* thermal partons can significantly alter the hydrodynamic simulation history and distort the isothermal surfaces from which hadronic spectra are produced using the Cooper-Frye technique.

OPEN SOURCE SOFTWARE

The scientific computational packages used to generate the results of this work have been cited throughout the text. In addition, a number of other programs were used during the course of the research and those are cited here.

A. MATPLOTLIB [214]

B. SCIPY [215]

C. NUMPY [216]

D. SCIKIT-LEARN [217]

E. H5PY [218]

F. PANDAS [219, 220]

Final Version as of September 13, 2023 (`classicthesis` version 6.0).

BIBLIOGRAPHY

[1] R.D. Field. *Applications Of Perturbative QCD*. Ed. by D. Pines. Perseus Books, 1995. ISBN: 0-201-483620-9.

[2] R. L. Workman et al. "Review of Particle Physics." In: *PTEP* 2022 (2022), p. 083C01. DOI: 10.1093/ptep/ptac097.

[3] Mark Thomson. *Modern particle physics*. Cambridge University Press, 2013.

[4] Matthew D. Schwartz. *Quantum Field Theory and the Standard Model*. Cambridge University Press, Mar. 2014. ISBN: 978-1-107-03473-0, 978-1-107-03473-0.

[5] M. Arslandok et al. *Hot QCD White Paper*. 2023. arXiv: 2303.17254 [nucl-ex].

[6] A. Bazavov et al. "Equation of state in $(2+1)$-flavor QCD." In: *Physical Review D* 90.9 (2014). DOI: 10.1103/physrevd.90.094503. URL: https://doi.org/10.1103%2Fphysrevd.90.094503.

[7] Asakawa Masayuki and Yazaki Koichi. "Chiral restoration at finite density and temperature." In: *Nuclear Physics A* 504.4 (1989), pp. 668–684. ISSN: 0375-9474. DOI: https://doi.org/10.1016/0375-9474(89)90002-X. URL: https://www.sciencedirect.com/science/article/pii/037594748990002X.

[8] A. Bazavov et al. "Chiral crossover in QCD at zero and non-zero chemical potentials." In: *Physics Letters B* 795 (2019), pp. 15–21. ISSN: 0370-2693. DOI: https://doi.org/10.1016/j.physletb.2019.05.013. URL: https://www.sciencedirect.com/science/article/pii/S0370269319303223.

[9] R. Bellwied et al. "The QCD phase diagram from analytic continuation." In: *Physics Letters B* 751 (2015), pp. 559–564. ISSN: 0370-2693. DOI: https://doi.org/10.1016/j.physletb.2015.11.011. URL: https://www.sciencedirect.com/science/article/pii/S0370269315008588.

[10] K. Aamodt et al. "Higher harmonic anisotropic flow measurements of charged particles in Pb-Pb collisions at $\sqrt{s_{NN}}$=2.76 TeV." In: *Phys. Rev. Lett.* 107 (2011), p. 032301. DOI: 10.1103/PhysRevLett.107.032301. arXiv: 1105.3865 [nucl-ex].

[11] Matthew Heffernan. "Quantification of the Quark-Gluon Plasma with statistical learning." PhD thesis. McGill U., Apr. 2023.

[12] Jean-Yves Ollitrault. "Anisotropy as a signature of transverse collective flow." In: *Phys. Rev. D* 46 (1992), pp. 229–245. DOI: 10.1103/PhysRevD.46.229.

[13] J. Pumplin, D. R. Stump, J. Huston, H. L. Lai, Pavel M. Nadolsky, and W. K. Tung. "New generation of parton distributions with uncertainties from global QCD analysis." In: *JHEP* 07 (2002), p. 012. DOI: 10.1088/1126-6708/2002/07/012. arXiv: hep-ph/0201195.

[14] Andy Buckley, James Ferrando, Stephen Lloyd, Karl Nordström, Ben Page, Martin Rüfenacht, Marek Schönherr, and Graeme Watt. "LHAPDF6: parton density access in the LHC precision era." In: *Eur. Phys. J. C* 75 (2015), p. 132. DOI: 10.1140/epjc/s10052-015-3318-8. arXiv: 1412.7420 [hep-ph].

[15] Zoltan Nagy and Davison E. Soper. "Ordering variable for parton showers." In: *JHEP* 06 (2014), p. 178. DOI: 10.1007/JHEP06(2014)178. arXiv: 1401.6366 [hep-ph].

[16] Christian Bierlich et al. "A comprehensive guide to the physics and usage of PYTHIA 8.3." In: (Mar. 2022). DOI: 10.21468/SciPostPhysCodeb.8. arXiv: 2203.11601 [hep-ph].

[17] Yasuki Tachibana and Tetsufumi Hirano. "Hydrodynamic excitation by jets in the expanding QGP." In: *Nucl. Part. Phys. Proc.* 276-278 (2016). Ed. by Charles Gale et al., pp. 173–176. DOI: 10.1016/j.nuclphysbps.2016.05.037.

[18] Michito Okai, Koji Kawaguchi, Yasuki Tachibana, and Tetsufumi Hirano. "New approach to initializing hydrodynamic fields and mini-jet propagation in quark-gluon fluids." In: *Phys. Rev. C* 95.5 (2017), p. 054914. DOI: 10.1103/PhysRevC.95.054914. arXiv: 1702.07541 [nucl-th].

[19] Yasuki Tachibana. "Medium response to jet-induced excitation: theory overview." In: *Nucl. Phys. A* 982 (2019). Ed. by Federico Antinori, Andrea Dainese, Paolo Giubellino, Vincenzo Greco, Maria Paola Lombardo, and Enrico Scomparin, pp. 156–162. DOI: 10.1016/j.nuclphysa.2018.10.074.

[20] Daniel Pablos, Mayank Singh, Sangyong Jeon, and Charles Gale. "Minijet quenching in a concurrent jet+hydro evolution and the nonequilibrium quark-gluon plasma." In: *Phys. Rev. C* 106.3 (2022), p. 034901. DOI: 10.1103/PhysRevC.106.034901. arXiv: 2202.03414 [nucl-th].

[21] Jonah E. Bernhard. "Bayesian parameter estimation for relativistic heavy-ion collisions." PhD thesis. Duke U., Apr. 2018. arXiv: 1804.06469 [nucl-th].

[22] Jonah E. Bernhard, J. Scott Moreland, and Steffen A. Bass. "Bayesian estimation of the specific shear and bulk viscosity of quark–gluon plasma." In: *Nature Phys.* 15.11 (2019), pp. 1113–1117. DOI: 10.1038/s41567-019-0611-8.

[23] Matthew R. Heffernan, Charles Gale, Sangyong Jeon, and Jean-François Paquet. "Bayesian quantification of strongly-interacting matter with color glass condensate initial conditions." In: (Feb. 2023). arXiv: 2302.09478 [nucl-th].

[24] Michael L. Miller, Klaus Reygers, Stephen J. Sanders, and Peter Steinberg. "Glauber modeling in high energy nuclear collisions." In: *Ann. Rev. Nucl. Part. Sci.* 57 (2007), pp. 205–243. DOI: 10.1146/annurev.nucl.57.090506.123020. arXiv: nucl-ex/0701025.

[25] J. Scott Moreland, Jonah E. Bernhard, and Steffen A. Bass. "Alternative ansatz to wounded nucleon and binary collision scaling in high-energy nuclear collisions." In: *Phys. Rev. C* 92.1 (2015), p. 011901. DOI: 10.1103/PhysRevC.92.011901. arXiv: 1412.4708 [nucl-th].

[26] Zi-Wei Lin, Che Ming Ko, Bao-An Li, Bin Zhang, and Subrata Pal. "A Multi-phase transport model for relativistic heavy ion collisions." In: *Phys. Rev. C* 72 (2005), p. 064901. DOI: 10.1103/PhysRevC.72.064901. arXiv: nucl-th/0411110.

[27] Bjoern Schenke, Prithwish Tribedy, and Raju Venugopalan. "Fluctuating Glasma initial conditions and flow in heavy ion collisions." In: *Phys. Rev. Lett.* 108 (2012), p. 252301. DOI: 10.1103/PhysRevLett.108.252301. arXiv: 1202.6646 [nucl-th].

[28] H. Niemi, K. J. Eskola, and R. Paatelainen. "Event-by-event fluctuations in a perturbative QCD + saturation + hydrodynamics model: Determining QCD matter shear viscosity in ultrarelativistic heavy-ion collisions." In: *Phys. Rev. C*

93.2 (2016), p. 024907. DOI: 10.1103/PhysRevC.93.024907. arXiv: 1505.02677 [hep-ph].

[29] B. Alver, M. Baker, C. Loizides, and P. Steinberg. "The PHOBOS Glauber Monte Carlo." In: (May 2008). arXiv: 0805.4411 [nucl-ex].

[30] C. Loizides, J. Nagle, and P. Steinberg. "Improved version of the PHOBOS Glauber Monte Carlo." In: *SoftwareX* 1-2 (2015), pp. 13–18. DOI: 10.1016/j.softx.2015.05.001. arXiv: 1408.2549 [nucl-ex].

[31] A. Bialas, M. Bleszynski, and W. Czyz. "Multiplicity Distributions in Nucleus-Nucleus Collisions at High-Energies." In: *Nucl. Phys. B* 111 (1976), pp. 461–476. DOI: 10.1016/0550-3213(76)90329-1.

[32] Roy J. Glauber. "Quantum Optics and Heavy Ion Physics." In: *Nucl. Phys. A* 774 (2006). Ed. by T. Csorgo, P. Levai, G. David, and G. Papp, pp. 3–13. DOI: 10.1016/j.nuclphysa.2006.06.009. arXiv: nucl-th/0604021.

[33] Roger D. Woods and David S. Saxon. "Diffuse Surface Optical Model for Nucleon-Nuclei Scattering." In: *Phys. Rev.* 95 (2 1954), pp. 577–578. DOI: 10.1103/PhysRev.95.577. URL: https://link.aps.org/doi/10.1103/PhysRev.95.577.

[34] Giuliano Giacalone, Jiangyong Jia, and Chunjian Zhang. "Impact of Nuclear Deformation on Relativistic Heavy-Ion Collisions: Assessing Consistency in Nuclear Physics across Energy Scales." In: *Phys. Rev. Lett.* 127.24 (2021), p. 242301. DOI: 10.1103/PhysRevLett.127.242301. arXiv: 2105.01638 [nucl-th].

[35] H. De Vries, C. W. De Jager, and C. De Vries. "Nuclear charge and magnetization density distribution parameters from elastic electron scattering." In: *Atom. Data Nucl. Data Tabl.* 36 (1987), pp. 495–536. DOI: 10.1016/0092-640X(87)90013-1.

[36] D. Adhikari et al. "Accurate Determination of the Neutron Skin Thickness of ^{208}Pb through Parity-Violation in Electron Scattering." In: *Phys. Rev. Lett.* 126.17 (2021), p. 172502. DOI: 10.1103/PhysRevLett.126.172502. arXiv: 2102.10767 [nucl-ex].

[37] Constantin Loizides, Jason Kamin, and David d'Enterria. "Improved Monte Carlo Glauber predictions at present and future nuclear colliders." In: *Phys. Rev. C* 97.5 (2018). [Erratum: Phys.Rev.C 99, 019901 (2019)], p. 054910. DOI: 10.1103/PhysRevC.97.054910. arXiv: 1710.07098 [nucl-ex].

[38] David d'Enterria and Constantin Loizides. "Progress in the Glauber Model at Collider Energies." In: *Ann. Rev. Nucl. Part. Sci.* 71 (2021), pp. 315–344. DOI: 10.1146/annurev-nucl-102419-060007. arXiv: 2011.14909 [hep-ph].

[39] Betty Abelev et al. "Centrality determination of Pb-Pb collisions at $\sqrt{s_{NN}}$ = 2.76 TeV with ALICE." In: *Phys. Rev. C* 88.4 (2013), p. 044909. DOI: 10.1103/PhysRevC.88.044909. arXiv: 1301.4361 [nucl-ex].

[40] E. Abbas et al. "Performance of the ALICE VZERO system." In: *JINST* 8 (2013), P10016. DOI: 10.1088/1748-0221/8/10/P10016. arXiv: 1306.3130 [nucl-ex].

[41] Scott McDonald, Chun Shen, Francois Fillion-Gourdeau, Sangyong Jeon, and Charles Gale. "Hydrodynamic predictions for Pb+Pb collisions at 5.02 TeV." In: *Phys. Rev. C* 95.6 (2017), p. 064913. DOI: 10.1103/PhysRevC.95.064913. arXiv: 1609.02958 [hep-ph].

[42] Scott McDonald. "The initial State of heavy ion collisions in the IP-glasma framework." PhD thesis. McGill U., 2017.

[43] Francois Gelis, Edmond Iancu, Jamal Jalilian-Marian, and Raju Venugopalan. "The Color Glass Condensate." In: *Ann. Rev. Nucl. Part. Sci.* 60 (2010), pp. 463–489. DOI: 10.1146/annurev.nucl.010909.083629. arXiv: 1002.0333 [hep-ph].

[44] Ernst Sichtermann. "Gluon Saturation and EIC." In: *Nuclear Physics A* 956 (2016). The XXV International Conference on Ultrarelativistic Nucleus-Nucleus Collisions: Quark Matter 2015, pp. 233–239. ISSN: 0375-9474. DOI: https://doi.org/10.1016/j.nuclphysa.2016.03.009. URL: https://www.sciencedirect.com/science/article/pii/S0375947416001779.

[45] Scott McDonald. "Towards fully 3-dimensional simulations of heavy ion collisions in the IP-Glasma initial state framework." PhD thesis. McGill U., 2020.

[46] Scott McDonald, Sangyong Jeon, and Charles Gale. "The 3+1D initialization and evolution of the Glasma." In: (June 2023). arXiv: 2306.04896 [hep-ph].

[47] Henri Kowalski and Derek Teaney. "An Impact parameter dipole saturation model." In: *Phys. Rev. D* 68 (2003), p. 114005. DOI: 10.1103/PhysRevD.68.114005. arXiv: hep-ph/0304189.

[48] Jonah E. Bernhard, J. Scott Moreland, Steffen A. Bass, Jia Liu, and Ulrich Heinz. "Applying Bayesian parameter estimation to relativistic heavy-ion collisions: simultaneous characterization of the initial state and quark-gluon plasma medium." In: *Phys. Rev. C* 94.2 (2016), p. 024907. DOI: 10.1103/PhysRevC.94.024907. arXiv: 1605.03954 [nucl-th].

[49] D. Everett et al. "Phenomenological constraints on the transport properties of QCD matter with data-driven model averaging." In: *Phys. Rev. Lett.* 126.24 (2021), p. 242301. DOI: 10.1103/PhysRevLett.126.242301. arXiv: 2010.03928 [hep-ph].

[50] D. Everett et al. "Multisystem Bayesian constraints on the transport coefficients of QCD matter." In: *Phys. Rev. C* 103.5 (2021), p. 054904. DOI: 10.1103/PhysRevC.103.054904. arXiv: 2011.01430 [hep-ph].

[51] Govert Nijs, Wilke van der Schee, Umut Gürsoy, and Raimond Snellings. "Bayesian analysis of heavy ion collisions with the heavy ion computational framework Trajectum." In: *Phys. Rev. C* 103.5 (2021), p. 054909. DOI: 10.1103/PhysRevC.103.054909. arXiv: 2010.15134 [nucl-th].

[52] Aleksi Kurkela, Aleksas Mazeliauskas, Jean-François Paquet, Sören Schlichting, and Derek Teaney. "Matching the Nonequilibrium Initial Stage of Heavy Ion Collisions to Hydrodynamics with QCD Kinetic Theory." In: *Phys. Rev. Lett.* 122.12 (2019), p. 122302. DOI: 10.1103/PhysRevLett.122.122302. arXiv: 1805.01604 [hep-ph].

[53] Wojciech Broniowski, Wojciech Florkowski, Mikolaj Chojnacki, and Adam Kisiel. "Free-streaming approximation in early dynamics of relativistic heavy-ion collisions." In: *Phys. Rev. C* 80 (2009), p. 034902. DOI: 10.1103/PhysRevC.80.034902. arXiv: 0812.3393 [nucl-th].

[54] Jia Liu, Chun Shen, and Ulrich Heinz. "Pre-equilibrium evolution effects on heavy-ion collision observables." In: *Phys. Rev. C* 91.6 (2015). [Erratum: Phys.Rev.C

92, 049904 (2015)], p. 064906. DOI: 10.1103/PhysRevC.91.064906. arXiv: 1504.02160 [nucl-th].

[55] Charles Gale, Jean-François Paquet, Björn Schenke, and Chun Shen. "Multi-messenger heavy-ion collision physics." In: *Phys. Rev. C* 105.1 (2022), p. 014909. DOI: 10.1103/PhysRevC.105.014909. arXiv: 2106.11216 [nucl-th].

[56] Edmond Iancu and Raju Venugopalan. "The Color glass condensate and high-energy scattering in QCD." In: *Quark-gluon plasma 4*. Ed. by Rudolph C. Hwa and Xin-Nian Wang. Mar. 2003, pp. 249–3363. DOI: 10.1142/9789812795533_0005. arXiv: hep-ph/0303204.

[57] Aleksi Kurkela, Aleksas Mazeliauskas, Jean-François Paquet, Sören Schlichting, and Derek Teaney. "Effective kinetic description of event-by-event pre-equilibrium dynamics in high-energy heavy-ion collisions." In: *Phys. Rev. C* 99.3 (2019), p. 034910. DOI: 10.1103/PhysRevC.99.034910. arXiv: 1805.00961 [hep-ph].

[58] Liam Keegan, Aleksi Kurkela, Aleksas Mazeliauskas, and Derek Teaney. "Initial conditions for hydrodynamics from weakly coupled pre-equilibrium evolution." In: *JHEP* 08 (2016), p. 171. DOI: 10.1007/JHEP08(2016)171. arXiv: 1605.04287 [hep-ph].

[59] Aleksi Kurkela and Aleksas Mazeliauskas. "Chemical Equilibration in Hadronic Collisions." In: *Phys. Rev. Lett.* 122 (2019), p. 142301. DOI: 10.1103/PhysRevLett.122.142301. arXiv: 1811.03040 [hep-ph].

[60] Mayank Singh. "Characterizing the quark gluon plasma using soft thermal fluctuations and hard parton interactions." PhD thesis. McGill U., 2021.

[61] Huichao Song and Ulrich W. Heinz. "Causal viscous hydrodynamics in 2+1 dimensions for relativistic heavy-ion collisions." In: *Phys. Rev. C* 77 (2008), p. 064901. DOI: 10.1103/PhysRevC.77.064901. arXiv: 0712.3715 [nucl-th].

[62] William A. Hiscock and Lee Lindblom. "Generic instabilities in first-order dissipative relativistic fluid theories." In: *Phys. Rev. D* 31 (4 1985), pp. 725–733. DOI: 10.1103/PhysRevD.31.725. URL: https://link.aps.org/doi/10.1103/PhysRevD.31.725.

[63] Christopher Plumberg, Dekrayat Almaalol, Travis Dore, Jorge Noronha, and Jacquelyn Noronha-Hostler. "Causality violations in realistic simulations of heavy-ion collisions." In: *Phys. Rev. C* 105.6 (2022), p. L061901. DOI: 10.1103/PhysRevC.105.L061901. arXiv: 2103.15889 [nucl-th].

[64] Ingo Müller. "Zum paradoxon der wärmeleitungstheorie." In: *Zeitschrift für Physik* 198.4 (1967), pp. 329–344.

[65] W. Israel and J.M. Stewart. "Transient relativistic thermodynamics and kinetic theory." In: *Annals of Physics* 118.2 (1979), pp. 341–372. ISSN: 0003-4916. DOI: https://doi.org/10.1016/0003-4916(79)90130-1. URL: https://www.sciencedirect.com/science/article/pii/0003491679901301.

[66] G. S. Denicol, T. Koide, and D. H. Rischke. "Dissipative relativistic fluid dynamics: a new way to derive the equations of motion from kinetic theory." In: *Phys. Rev. Lett.* 105 (2010), p. 162501. DOI: 10.1103/PhysRevLett.105.162501. arXiv: 1004.5013 [nucl-th].

[67] G. S. Denicol, H. Niemi, E. Molnar, and D. H. Rischke. "Derivation of transient relativistic fluid dynamics from the Boltzmann equation." In: *Phys. Rev. D* 85 (2012). [Erratum: Phys.Rev.D 91, 039902 (2015)], p. 114047. DOI: 10.1103/PhysRevD.85.114047. arXiv: 1202.4551 [nucl-th].

[68] G. S. Denicol, S. Jeon, and C. Gale. "Transport Coefficients of Bulk Viscous Pressure in the 14-moment approximation." In: *Phys. Rev. C* 90.2 (2014), p. 024912. DOI: 10.1103/PhysRevC.90.024912. arXiv: 1403.0962 [nucl-th].

[69] Bjoern Schenke, Sangyong Jeon, and Charles Gale. "(3+1)D hydrodynamic simulation of relativistic heavy-ion collisions." In: *Phys. Rev. C* 82 (2010), p. 014903. DOI: 10.1103/PhysRevC.82.014903. arXiv: 1004.1408 [hep-ph].

[70] Chun Shen, Zhi Qiu, Huichao Song, Jonah Bernhard, Steffen Bass, and Ulrich Heinz. "The iEBE-VISHNU code package for relativistic heavy-ion collisions." In: *Comput. Phys. Commun.* 199 (2016), pp. 61–85. DOI: 10.1016/j.cpc.2015.08.039. arXiv: 1409.8164 [nucl-th].

[71] Paul Romatschke and Ulrike Romatschke. "Viscosity Information from Relativistic Nuclear Collisions: How Perfect is the Fluid Observed at RHIC?" In:

Phys. Rev. Lett. 99 (2007), p. 172301. DOI: 10.1103/PhysRevLett.99.172301. arXiv: 0706.1522 [nucl-th].

[72] Huichao Song and Ulrich W. Heinz. "Multiplicity scaling in ideal and viscous hydrodynamics." In: *Phys. Rev. C* 78 (2008), p. 024902. DOI: 10.1103/PhysRevC.78.024902. arXiv: 0805.1756 [nucl-th].

[73] G. S. Denicol, T. Kodama, T. Koide, and Ph. Mota. "Effect of bulk viscosity on Elliptic Flow near QCD phase transition." In: *Phys. Rev. C* 80 (2009), p. 064901. DOI: 10.1103/PhysRevC.80.064901. arXiv: 0903.3595 [hep-ph].

[74] Frithjof Karsch, Dmitri Kharzeev, and Kirill Tuchin. "Universal properties of bulk viscosity near the QCD phase transition." In: *Phys. Lett. B* 663 (2008), pp. 217–221. DOI: 10.1016/j.physletb.2008.01.080. arXiv: 0711.0914 [hep-ph].

[75] Jacquelyn Noronha-Hostler, Jorge Noronha, and Carsten Greiner. "Transport Coefficients of Hadronic Matter near T(c)." In: *Phys. Rev. Lett.* 103 (2009), p. 172302. DOI: 10.1103/PhysRevLett.103.172302. arXiv: 0811.1571 [nucl-th].

[76] Fred Cooper and Graham Frye. "Single-particle distribution in the hydrodynamic and statistical thermodynamic models of multiparticle production." In: *Phys. Rev. D* 10 (1 1974), pp. 186–189. DOI: 10.1103/PhysRevD.10.186. URL: https://link.aps.org/doi/10.1103/PhysRevD.10.186.

[77] Sydney Chapman and Thomas George Cowling. *The mathematical theory of non-uniform gases: an account of the kinetic theory of viscosity, thermal conduction and diffusion in gases*. Cambridge university press, 1990.

[78] Harold Grad. "On the kinetic theory of rarefied gases." In: *Communications on Pure and Applied Mathematics* 2.4 (1949), pp. 331–407. DOI: https://doi.org/10.1002/cpa.3160020403. eprint: https://onlinelibrary.wiley.com/doi/pdf/10.1002/cpa.3160020403. URL: https://onlinelibrary.wiley.com/doi/abs/10.1002/cpa.3160020403.

[79] S. A. Bass et al. "Microscopic models for ultrarelativistic heavy ion collisions." In: *Prog. Part. Nucl. Phys.* 41 (1998), pp. 255–369. DOI: 10.1016/S0146-6410(98)00058-1. arXiv: nucl-th/9803035.

[80] M. Bleicher et al. "Relativistic hadron hadron collisions in the ultrarelativistic quantum molecular dynamics model." In: *J. Phys. G* 25 (1999), pp. 1859–1896. DOI: 10.1088/0954-3899/25/9/308. arXiv: hep-ph/9909407.

[81] J. D. Bjorken. "Energy Loss of Energetic Partons in Quark - Gluon Plasma: Possible Extinction of High p(t) Jets in Hadron - Hadron Collisions." In: (Aug. 1982).

[82] Markus H. Thoma and Miklos Gyulassy. "Quark Damping and Energy Loss in the High Temperature QCD." In: *Nucl. Phys. B* 351 (1991), pp. 491–506. DOI: 10.1016/S0550-3213(05)80031-8.

[83] Munshi G. Mustafa and Markus H. Thoma. "Quenching of hadron spectra due to the collisional energy loss of partons in the quark gluon plasma." In: *Acta Phys. Hung. A* 22 (2005), pp. 93–102. DOI: 10.1556/APH.22.2005.1-2.10. arXiv: hep-ph/0311168.

[84] Abhee K. Dutt-Mazumder, Jan-e Alam, Pradip Roy, and Bikash Sinha. "Stopping power of hot QCD plasma." In: *Phys. Rev. D* 71 (2005), p. 094016. DOI: 10.1103/PhysRevD.71.094016. arXiv: hep-ph/0411015.

[85] Munshi G. Mustafa. "Energy loss of charm quarks in the quark-gluon plasma: Collisional versus radiative." In: *Phys. Rev. C* 72 (2005), p. 014905. DOI: 10.1103/PhysRevC.72.014905. arXiv: hep-ph/0412402.

[86] A. Adil, M. Gyulassy, W. A. Horowitz, and S. Wicks. "Collisional Energy Loss of Non Asymptotic Jets in a QGP." In: *Phys. Rev. C* 75 (2007), p. 044906. DOI: 10.1103/PhysRevC.75.044906. arXiv: nucl-th/0606010.

[87] Simon Wicks and Miklos Gyulassy. "Improving a radiative plus collisional energy loss model for application to RHIC and LHC." In: *J. Phys. G* 34 (2007). Ed. by Yu-Gang Ma, Zhi-Yuan Zhu, En-Ke Wang, Xu Cai, Huan-Zhong Huang, and Xin-Nian Wang, S989–S993. DOI: 10.1088/0954-3899/34/8/S141. arXiv: nucl-th/0701088.

[88] Thorsten Renk. "The Phenomenology of Elastic Energy Loss." In: *Phys. Rev. C* 76 (2007), p. 064905. DOI: 10.1103/PhysRevC.76.064905. arXiv: 0708.4319 [hep-ph].

[89] Bjoern Schenke, Charles Gale, and Guang-You Qin. "The Evolving distribution of hard partons traversing a hot strongly interacting plasma." In: *Phys. Rev. C* 79 (2009), p. 054908. DOI: 10.1103/PhysRevC.79.054908. arXiv: 0901.3498 [hep-ph].

[90] R. Baier, Yuri L. Dokshitzer, Alfred H. Mueller, S. Peigne, and D. Schiff. "Radiative energy loss of high-energy quarks and gluons in a finite volume quark - gluon plasma." In: *Nucl. Phys. B* 483 (1997), pp. 291–320. DOI: 10.1016/S0550-3213(96)00553-6. arXiv: hep-ph/9607355.

[91] R. Baier, Yuri L. Dokshitzer, Alfred H. Mueller, S. Peigne, and D. Schiff. "Radiative energy loss and p(T) broadening of high-energy partons in nuclei." In: *Nucl. Phys. B* 484 (1997), pp. 265–282. DOI: 10.1016/S0550-3213(96)00581-0. arXiv: hep-ph/9608322.

[92] B. G. Zakharov. "Fully quantum treatment of the Landau-Pomeranchuk-Migdal effect in QED and QCD." In: *JETP Lett.* 63 (1996), pp. 952–957. DOI: 10.1134/1.567126. arXiv: hep-ph/9607440.

[93] Urs Achim Wiedemann. "Jet quenching versus jet enhancement: A Quantitative study of the BDMPS-Z gluon radiation spectrum." In: *Nucl. Phys. A* 690 (2001), pp. 731–751. DOI: 10.1016/S0375-9474(01)00362-1. arXiv: hep-ph/0008241.

[94] Urs Achim Wiedemann. "Gluon radiation off hard quarks in a nuclear environment: Opacity expansion." In: *Nucl. Phys. B* 588 (2000), pp. 303–344. DOI: 10.1016/S0550-3213(00)00457-0. arXiv: hep-ph/0005129.

[95] Xiao-feng Guo and Xin-Nian Wang. "Multiple scattering, parton energy loss and modified fragmentation functions in deeply inelastic e A scattering." In: *Phys. Rev. Lett.* 85 (2000), pp. 3591–3594. DOI: 10.1103/PhysRevLett.85.3591. arXiv: hep-ph/0005044.

[96] Xin-Nian Wang and Xiao-feng Guo. "Multiple parton scattering in nuclei: Parton energy loss." In: *Nucl. Phys. A* 696 (2001), pp. 788–832. DOI: 10.1016/S0375-9474(01)01130-7. arXiv: hep-ph/0102230.

[97] Karen M. Burke et al. "Extracting the jet transport coefficient from jet quenching in high-energy heavy-ion collisions." In: *Phys. Rev. C* 90.1 (2014), p. 014909. DOI: 10.1103/PhysRevC.90.014909. arXiv: 1312.5003 [nucl-th].

[98] Margaret E. Carrington, Alina Czajka, and Stanislaw Mrowczynski. "Jet quenching in glasma." In: *Phys. Lett. B* 834 (2022), p. 137464. DOI: 10.1016/j.physletb.2022.137464. arXiv: 2112.06812 [hep-ph].

[99] M. B. Kislinger and P. D. Morley. "Collective Phenomena in Gauge Theories. 1. The Plasmon Effect for Yang-Mills Fields." In: *Phys. Rev. D* 13 (1976), p. 2765. DOI: 10.1103/PhysRevD.13.2765.

[100] Robert D. Pisarski. "How to Compute Scattering Amplitudes in Hot Gauge Theories." In: *Physica A* 158 (1989), pp. 246–250. DOI: 10.1016/0378-4371(89)90525-6.

[101] Eric Braaten and Robert D. Pisarski. "Soft Amplitudes in Hot Gauge Theories: A General Analysis." In: *Nucl. Phys. B* 337 (1990), pp. 569–634. DOI: 10.1016/0550-3213(90)90508-B.

[102] Eric Braaten and Robert D. Pisarski. "Resummation and Gauge Invariance of the Gluon Damping Rate in Hot QCD." In: *Phys. Rev. Lett.* 64 (1990), p. 1338. DOI: 10.1103/PhysRevLett.64.1338.

[103] Eric Braaten and Robert D. Pisarski. "Simple effective Lagrangian for hard thermal loops." In: *Phys. Rev. D* 45.6 (1992), R1827. DOI: 10.1103/PhysRevD.45.R1827.

[104] J. Frenkel and J. C. Taylor. "High Temperature Limit of Thermal QCD." In: *Nucl. Phys. B* 334 (1990), pp. 199–216. DOI: 10.1016/0550-3213(90)90661-V.

[105] J. Frenkel and J. C. Taylor. "Hard thermal QCD, forward scattering and effective actions." In: *Nucl. Phys. B* 374 (1992), pp. 156–168. DOI: 10.1016/0550-3213(92)90480-Y.

[106] J. C. Taylor and S. M. H. Wong. "The Effective Action of Hard Thermal Loops in QCD." In: *Nucl. Phys. B* 346 (1990), pp. 115–128. DOI: 10.1016/0550-3213(90)90240-E.

[107] Chanwook Park, Sangyong Jeon, and Charles Gale. "Jet modification with medium recoil in quark-gluon plasma." In: *Nucl. Phys. A* 982 (2019), pp. 643–646. DOI: 10.1016/j.nuclphysa.2018.10.057. arXiv: 1807.06550 [nucl-th].

[108] Eric Braaten and Markus H. Thoma. "Energy loss of a heavy fermion in a hot plasma." In: *Phys. Rev. D* 44 (1991), pp. 1298–1310. DOI: 10.1103/PhysRevD.44.1298.

[109] Eric Braaten and Markus H. Thoma. "Energy loss of a heavy quark in the quark - gluon plasma." In: *Phys. Rev. D* 44.9 (1991), R2625. DOI: 10.1103/PhysRevD.44.R2625.

[110] Miklos Gyulassy and Xin-nian Wang. "Multiple collisions and induced gluon Bremsstrahlung in QCD." In: *Nucl. Phys. B* 420 (1994), pp. 583–614. DOI: 10.1016/0550-3213(94)90079-5. arXiv: nucl-th/9306003.

[111] Miklos Gyulassy, Peter Levai, and Ivan Vitev. "Jet quenching in thin quark gluon plasmas. 1. Formalism." In: *Nucl. Phys. B* 571 (2000), pp. 197–233. DOI: 10.1016/S0550-3213(99)00713-0. arXiv: hep-ph/9907461.

[112] M. Gyulassy, P. Levai, and I. Vitev. "Reaction operator approach to nonAbelian energy loss." In: *Nucl. Phys. B* 594 (2001), pp. 371–419. DOI: 10.1016/S0550-3213(00)00652-0. arXiv: nucl-th/0006010.

[113] M. Gyulassy, P. Levai, and I. Vitev. "NonAbelian energy loss at finite opacity." In: *Phys. Rev. Lett.* 85 (2000), pp. 5535–5538. DOI: 10.1103/PhysRevLett.85.5535. arXiv: nucl-th/0005032.

[114] M. Gyulassy, I. Vitev, and X. N. Wang. "High p(T) azimuthal asymmetry in noncentral A+A at RHIC." In: *Phys. Rev. Lett.* 86 (2001), pp. 2537–2540. DOI: 10.1103/PhysRevLett.86.2537. arXiv: nucl-th/0012092.

[115] Bojana Blagojevic, Magdalena Djordjevic, and Marko Djordjevic. "Calculating hard probe radiative energy loss beyond the soft-gluon approximation: Examining the approximation validity." In: *Phys. Rev. C* 99.2 (2019), p. 024901. DOI: 10.1103/PhysRevC.99.024901. arXiv: 1804.07593 [nucl-th].

[116] Magdalena Djordjevic and Miklos Gyulassy. "The Ter-Mikayelian effect on QCD radiative energy loss." In: *Phys. Rev. C* 68 (2003), p. 034914. DOI: 10.1103/PhysRevC.68.034914. arXiv: nucl-th/0305062.

[117] Magdalena Djordjevic and Miklos Gyulassy. "Heavy quark radiative energy loss in QCD matter." In: *Nucl. Phys. A* 733 (2004), pp. 265–298. DOI: 10.1016/j.nuclphysa.2003.12.020. arXiv: nucl-th/0310076.

[118] Magdalena Djordjevic and Ulrich Heinz. "Radiative heavy quark energy loss in a dynamical QCD medium." In: *Phys. Rev. C* 77 (2008), p. 024905. DOI: 10.1103/PhysRevC.77.024905. arXiv: 0705.3439 [nucl-th].

[119] Magdalena Djordjevic and Ulrich W. Heinz. "Radiative energy loss in a finite dynamical QCD medium." In: *Phys. Rev. Lett.* 101 (2008), p. 022302. DOI: 10.1103/PhysRevLett.101.022302. arXiv: 0802.1230 [nucl-th].

[120] Jiechen Xu, Alessandro Buzzatti, and Miklos Gyulassy. "Azimuthal jet flavor tomography with CUJET2.0 of nuclear collisions at RHIC and LHC." In: *JHEP* 08 (2014), p. 063. DOI: 10.1007/JHEP08(2014)063. arXiv: 1402.2956 [hep-ph].

[121] L. D. Landau and I. Pomeranchuk. "Limits of applicability of the theory of bremsstrahlung electrons and pair production at high-energies." In: *Dokl. Akad. Nauk Ser. Fiz.* 92 (1953), pp. 535–536.

[122] L. D. Landau and I. Pomeranchuk. "Electron cascade process at very high-energies." In: *Dokl. Akad. Nauk Ser. Fiz.* 92 (1953), pp. 735–738.

[123] A. B. Migdal. "Bremsstrahlung and pair production in condensed media at high-energies." In: *Phys. Rev.* 103 (1956), pp. 1811–1820. DOI: 10.1103/PhysRev.103.1811.

[124] Pasi Huovinen and Pter Petreczky. "QCD Equation of State and Hadron Resonance Gas." In: *Nucl. Phys. A* 837 (2010), pp. 26–53. DOI: 10.1016/j.nuclphysa.2010.02.015. arXiv: 0912.2541 [hep-ph].

[125] Han-zhong Zhang, Zhong-bo Kang, Ben-Wei Zhang, and Enke Wang. "Photon Radiation and Dilepton Production Induced by Rescattering in Strong Interacting Medium." In: *Eur. Phys. J. C* 67 (2010), pp. 445–454. DOI: 10.1140/epjc/s10052-010-1330-6. arXiv: hep-ph/0609159.

[126] Bjoern Schenke, Charles Gale, and Sangyong Jeon. "MARTINI: An Event generator for relativistic heavy-ion collisions." In: *Phys. Rev. C* 80 (2009), p. 054913. DOI: 10.1103/PhysRevC.80.054913. arXiv: 0909.2037 [hep-ph].

[127] Peter Brockway Arnold, Guy D. Moore, and Laurence G. Yaffe. "Photon emission from ultrarelativistic plasmas." In: *JHEP* 11 (2001), p. 057. DOI: 10.1088/1126-6708/2001/11/057. arXiv: hep-ph/0109064.

[128] Peter Brockway Arnold, Guy D. Moore, and Laurence G. Yaffe. "Photon emission from quark gluon plasma: Complete leading order results." In: *JHEP* 12 (2001), p. 009. DOI: 10.1088/1126-6708/2001/12/009. arXiv: hep-ph/0111107.

[129] Peter Brockway Arnold, Guy D. Moore, and Laurence G. Yaffe. "Photon and gluon emission in relativistic plasmas." In: *JHEP* 06 (2002), p. 030. DOI: 10.1088/1126-6708/2002/06/030. arXiv: hep-ph/0204343.

[130] Sangyong Jeon and Guy D. Moore. "Energy loss of leading partons in a thermal QCD medium." In: *Phys. Rev. C* 71 (2005), p. 034901. DOI: 10.1103/PhysRevC.71.034901. arXiv: hep-ph/0309332.

[131] P. Aurenche, F. Gelis, R. Kobes, and H. Zaraket. "Bremsstrahlung and photon production in thermal QCD." In: *Phys. Rev. D* 58 (1998), p. 085003. DOI: 10.1103/PhysRevD.58.085003. arXiv: hep-ph/9804224.

[132] Azfar Adil and Ivan Vitev. "Collisional dissociation of heavy mesons in dense QCD matter." In: *Phys. Lett. B* 649 (2007), pp. 139–146. DOI: 10.1016/j.physletb.2007.03.050. arXiv: hep-ph/0611109.

[133] J. I. Kapusta and Charles Gale. *Finite-temperature field theory: Principles and applications*. Cambridge Monographs on Mathematical Physics. Cambridge University Press, 2011. ISBN: 978-0-521-17322-3, 978-0-521-82082-0, 978-0-511-22280-1. DOI: 10.1017/CBO9780511535130.

[134] Peter Brockway Arnold and Wei Xiao. "High-energy jet quenching in weakly-coupled quark-gluon plasmas." In: *Phys. Rev. D* 78 (2008), p. 125008. DOI: 10.1103/PhysRevD.78.125008. arXiv: 0810.1026 [hep-ph].

[135] Rainer J. Fries, Berndt Muller, and Dinesh K. Srivastava. "High-energy photons from passage of jets through quark gluon plasma." In: *Phys. Rev. Lett.* 90 (2003), p. 132301. DOI: 10.1103/PhysRevLett.90.132301. arXiv: nucl-th/0208001.

[136] R. Baier, H. Nakkagawa, A. Niegawa, and K. Redlich. "Production rate of hard thermal photons and screening of quark mass singularity." In: *Z. Phys. C* 53 (1992), pp. 433–438. DOI: 10.1007/BF01625902.

[137] Joseph I. Kapusta, P. Lichard, and D. Seibert. "High-energy photons from quark - gluon plasma versus hot hadronic gas." In: *Phys. Rev. D* 44 (1991). [Erratum: Phys.Rev.D 47, 4171 (1993)], pp. 2774–2788. DOI: 10.1103/PhysRevD.47.4171.

[138] GuangYou Qin. "Penetrating probes in relativistic heavy ion collisions." PhD thesis. McGill University, 2008.

[139] Chanwook Park. "Jet modification in strongly-coupled quark-gluon plasma." PhD thesis. McGill U., 2021.

[140] Abhijit Majumder. "Incorporating Space-Time Within Medium-Modified Jet Event Generators." In: *Phys. Rev. C* 88 (2013), p. 014909. DOI: 10.1103/PhysRevC.88.014909. arXiv: 1301.5323 [nucl-th].

[141] A. Majumder and J. Putschke. "Mass depletion: a new parameter for quantitative jet modification." In: *Phys. Rev. C* 93.5 (2016), p. 054909. DOI: 10.1103/PhysRevC.93.054909. arXiv: 1408.3403 [nucl-th].

[142] Shanshan Cao and Abhijit Majumder. "Nuclear modification of leading hadrons and jets within a virtuality ordered parton shower." In: *Phys. Rev. C* 101.2 (2020), p. 024903. DOI: 10.1103/PhysRevC.101.024903. arXiv: 1712.10055 [nucl-th].

[143] A. Kumar et al. "JETSCAPE framework: p + p results." In: *Phys. Rev. C* 102.5 (2020), p. 054906. DOI: 10.1103/PhysRevC.102.054906. arXiv: 1910.05481 [nucl-th].

[144] A. Kumar et al. "Inclusive jet and hadron suppression in a multistage approach." In: *Phys. Rev. C* 107.3 (2023), p. 034911. DOI: 10.1103/PhysRevC.107.034911. arXiv: 2204.01163 [hep-ph].

[145] Raktim Abir, Gagan Deep Kaur, and Abhijit Majumder. "Multiple scattering of heavy-quarks in dense matter and the parametric prominence of drag." In: *Phys. Rev. D* 90.11 (2014), p. 114026. DOI: 10.1103/PhysRevD.90.114026. arXiv: 1407.1864 [nucl-th].

[146] Raktim Abir and Abhijit Majumder. "Drag-induced radiative energy loss from semihard heavy quarks." In: *Phys. Rev. C* 94.5 (2016), p. 054902. DOI: 10.1103/PhysRevC.94.054902. arXiv: 1506.08648 [nucl-th].

[147] Shanshan Cao, Abhijit Majumder, Guang-You Qin, and Chun Shen. "Drag Induced Radiation and Multi-Stage Effects in Heavy-Flavor Energy Loss." In: *Phys. Lett. B* 793 (2019), pp. 433–439. DOI: 10.1016/j.physletb.2019.05.020. arXiv: 1711.09053 [nucl-th].

[148] Yayun He, Tan Luo, Xin-Nian Wang, and Yan Zhu. "Linear Boltzmann Transport for Jet Propagation in the Quark-Gluon Plasma: Elastic Processes and Medium Recoil." In: *Phys. Rev. C* 91 (2015). [Erratum: Phys.Rev.C 97, 019902 (2018)], p. 054908. DOI: 10.1103/PhysRevC.91.054908. arXiv: 1503.03313 [nucl-th].

[149] Simon Caron-Huot. "O(g) plasma effects in jet quenching." In: *Phys. Rev. D* 79 (2009), p. 065039. DOI: 10.1103/PhysRevD.79.065039. arXiv: 0811.1603 [hep-ph].

[150] Guy D. Moore and Niels Schlusser. "Transverse momentum broadening from the lattice." In: *Phys. Rev. D* 101.1 (2020). [Erratum: Phys.Rev.D 101, 059903 (2020)], p. 014505. DOI: 10.1103/PhysRevD.101.014505. arXiv: 1911.13127 [hep-lat].

[151] Eric Braaten and Agustin Nieto. "On the convergence of perturbative QCD at high temperature." In: *Phys. Rev. Lett.* 76 (1996), pp. 1417–1420. DOI: 10.1103/PhysRevLett.76.1417. arXiv: hep-ph/9508406.

[152] Mikko Laine and Aleksi Vuorinen. *Basics of Thermal Field Theory*. Vol. 925. Springer, 2016. DOI: 10.1007/978-3-319-31933-9. arXiv: 1701.01554 [hep-ph].

[153] Jorge Casalderrey-Solana and Derek Teaney. "Transverse Momentum Broadening of a Fast Quark in a N=4 Yang Mills Plasma." In: *JHEP* 04 (2007), p. 039. DOI: 10.1088/1126-6708/2007/04/039. arXiv: hep-th/0701123.

[154] Andrei D. Linde. "Infrared Problem in Thermodynamics of the Yang-Mills Gas." In: *Phys. Lett. B* 96 (1980), pp. 289–292. DOI: 10.1016/0370-2693(80)90769-8.

[155] Jacopo Ghiglieri, Juhee Hong, Aleksi Kurkela, Egang Lu, Guy D. Moore, and Derek Teaney. "Next-to-leading order thermal photon production in a weakly coupled quark-gluon plasma." In: *JHEP* 05 (2013), p. 010. DOI: 10.1007/JHEP05(2013)010. arXiv: 1302.5970 [hep-ph].

[156] Jacopo Ghiglieri, Guy D. Moore, and Derek Teaney. "Jet-Medium Interactions at NLO in a Weakly-Coupled Quark-Gluon Plasma." In: *JHEP* 03 (2016), p. 095. DOI: 10.1007/JHEP03(2016)095. arXiv: 1509.07773 [hep-ph].

[157] Tianyu Dai, Jean-François Paquet, Derek Teaney, and Steffen A. Bass. "Parton energy loss in a hard-soft factorized approach." In: *Phys. Rev. C* 105.3 (2022), p. 034905. DOI: 10.1103/PhysRevC.105.034905. arXiv: 2012.03441 [hep-ph].

[158] Guy D. Moore, Soeren Schlichting, Niels Schlusser, and Ismail Soudi. "Non-perturbative determination of collisional broadening and medium induced radiation in QCD plasmas." In: *JHEP* 10 (2021), p. 059. DOI: 10.1007/JHEP10(2021)059. arXiv: 2105.01679 [hep-ph].

[159] Marco Panero, Kari Rummukainen, and Andreas Schäfer. "Lattice Study of the Jet Quenching Parameter." In: *Phys. Rev. Lett.* 112.16 (2014), p. 162001. DOI: 10.1103/PhysRevLett.112.162001. arXiv: 1307.5850 [hep-ph].

[160] Michela D'Onofrio, Aleksi Kurkela, and Guy D. Moore. "Renormalization of Null Wilson Lines in EQCD." In: *JHEP* 03 (2014), p. 125. DOI: 10.1007/JHEP03(2014)125. arXiv: 1401.7951 [hep-lat].

[161] Guy D. Moore and Niels Schlusser. "Full O(a) improvement in electrostatic QCD." In: *Phys. Rev. D* 100.3 (2019), p. 034510. DOI: 10.1103/PhysRevD.100.034510. arXiv: 1905.09708 [hep-lat].

[162] Soeren Schlichting and Ismail Soudi. "Splitting rates in QCD plasmas from a nonperturbative determination of the momentum broadening kernel C(q⊥)." In: *Phys. Rev. D* 105.7 (2022), p. 076002. DOI: 10.1103/PhysRevD.105.076002. arXiv: 2111.13731 [hep-ph].

[163] Gerhard A. Schuler and Torbjorn Sjostrand. "Hadronic diffractive cross-sections and the rise of the total cross-section." In: *Phys. Rev. D* 49 (1994), pp. 2257–2267. DOI: 10.1103/PhysRevD.49.2257.

[164] Gerhard A. Schuler and Torbjorn Sjostrand. "A Scenario for high-energy gamma gamma interactions." In: *Z. Phys. C* 73 (1997), pp. 677–688. DOI: 10.1007/s002880050359. arXiv: hep-ph/9605240.

[165] Jaroslav Adam et al. "Results on total and elastic cross sections in proton–proton collisions at $\sqrt{s}$ = 200 GeV." In: *Phys. Lett. B* 808 (2020), p. 135663. DOI: 10.1016/j.physletb.2020.135663. arXiv: 2003.12136 [hep-ex].

[166] Betty Abelev et al. "Measurement of inelastic, single- and double-diffraction cross sections in proton–proton collisions at the LHC with ALICE." In: *Eur. Phys. J. C* 73.6 (2013), p. 2456. DOI: 10.1140/epjc/s10052-013-2456-0. arXiv: 1208.4968 [hep-ex].

[167] Torbjörn Sjöstrand, Stefan Ask, Jesper R. Christiansen, Richard Corke, Nishita Desai, Philip Ilten, Stephen Mrenna, Stefan Prestel, Christine O. Rasmussen, and Peter Z. Skands. "An introduction to PYTHIA 8.2." In: *Comput. Phys. Commun.* 191 (2015), pp. 159–177. DOI: 10.1016/j.cpc.2015.01.024. arXiv: 1410.3012 [hep-ph].

[168] Matteo Cacciari, Gavin P. Salam, and Gregory Soyez. "The anti-k_t jet clustering algorithm." In: *JHEP* 04 (2008), p. 063. DOI: 10.1088/1126-6708/2008/04/063. arXiv: 0802.1189 [hep-ph].

[169] Matteo Cacciari and Gavin P. Salam. "Dispelling the N^3 myth for the k_t jet-finder." In: *Phys. Lett. B* 641 (2006), pp. 57–61. DOI: 10.1016/j.physletb.2006.08.037. arXiv: hep-ph/0512210.

[170] Matteo Cacciari, Gavin P. Salam, and Gregory Soyez. "FastJet User Manual." In: *Eur. Phys. J. C* 72 (2012), p. 1896. DOI: 10.1140/epjc/s10052-012-1896-2. arXiv: 1111.6097 [hep-ph].

[171] Gavin P. Salam. "Towards Jetography." In: *Eur. Phys. J. C* 67 (2010), pp. 637–686. DOI: 10.1140/epjc/s10052-010-1314-6. arXiv: 0906.1833 [hep-ph].

[172] Y. Tachibana et al. "Hard Jet Substructure in a Multi-stage Approach." In: (Jan. 2023). arXiv: 2301.02485 [hep-ph].

[173] Vardan Khachatryan et al. "Event generator tunes obtained from underlying event and multiparton scattering measurements." In: *Eur. Phys. J. C* 76.3 (2016), p. 155. DOI: 10.1140/epjc/s10052-016-3988-x. arXiv: 1512.00815 [hep-ex].

[174] K. J. Eskola, H. Paukkunen, and C. A. Salgado. "EPS09: A New Generation of NLO and LO Nuclear Parton Distribution Functions." In: *JHEP* 04 (2009), p. 065. DOI: 10.1088/1126-6708/2009/04/065. arXiv: 0902.4154 [hep-ph].

[175] Betty Abelev et al. "Centrality Dependence of Charged Particle Production at Large Transverse Momentum in Pb–Pb Collisions at $\sqrt{s_{NN}} = 2.76$ TeV." In: *Phys. Lett. B* 720 (2013), pp. 52–62. DOI: 10.1016/j.physletb.2013.01.051. arXiv: 1208.2711 [hep-ex].

[176] Georges Aad et al. "Measurement of charged-particle spectra in Pb+Pb collisions at $\sqrt{s_{NN}} = 2.76$ TeV with the ATLAS detector at the LHC." In: *JHEP* 09 (2015), p. 050. DOI: 10.1007/JHEP09(2015)050. arXiv: 1504.04337 [hep-ex].

[177] Serguei Chatrchyan et al. "Study of high-pT charged particle suppression in PbPb compared to pp collisions at $\sqrt{s_{NN}} = 2.76$ TeV." In: *Eur. Phys. J. C* 72 (2012), p. 1945. DOI: 10.1140/epjc/s10052-012-1945-x. arXiv: 1202.2554 [nucl-ex].

[178] IM Sobol and YL Levitan. *The production of points uniformly distributed in a multidimensional*. Tech. rep. Technical Report Preprint 40, Institute of Applied Mathematics, USSR Academy . . ., 1976.

[179] I.M. Sobol. "Uniformly distributed sequences with an additional uniform property." In: *USSR Computational Mathematics and Mathematical Physics* 16.5 (1976), pp. 236–242. ISSN: 0041-5553. DOI: https://doi.org/10.1016/0041-5553(76)90154-3. URL: https://www.sciencedirect.com/science/article/pii/0041555376901543.

[180] I.A. Antonov and V.M. Saleev. "An economic method of computing LPτ-sequences." In: *USSR Computational Mathematics and Mathematical Physics* 19.1 (1979), pp. 252–256. ISSN: 0041-5553. DOI: https://doi.org/10.1016/0041-5553(79)90085-5. URL: https://www.sciencedirect.com/science/article/pii/0041555379900855.

[181] C.E. Rasmussen and C.K.I. Williams. *Gaussian Processes for Machine Learning*. Adaptive Computation and Machine Learning series. MIT Press, 2005. ISBN: 9780262182539. URL: https://books.google.ca/books?id=Tr34DwAAQBAJ.

[182] Serguei Chatrchyan et al. "Modification of Jet Shapes in PbPb Collisions at $\sqrt{s_{NN}} = 2.76$ TeV." In: *Phys. Lett. B* 730 (2014), pp. 243–263. DOI: 10.1016/j.physletb.2014.01.042. arXiv: 1310.0878 [nucl-ex].

[183] Morad Aaboud et al. "Measurement of jet fragmentation in Pb+Pb and pp collisions at $\sqrt{s_{NN}} = 2.76$ TeV with the ATLAS detector at the LHC." In: *Eur. Phys. J. C* 77.6 (2017), p. 379. DOI: 10.1140/epjc/s10052-017-4915-5. arXiv: 1702.00674 [hep-ex].

[184] Vardan Khachatryan et al. "Measurement of inclusive jet cross sections in pp and PbPb collisions at $\sqrt{s_{NN}} = 2.76$ TeV." In: *Phys. Rev. C* 96.1 (2017), p. 015202. DOI: 10.1103/PhysRevC.96.015202. arXiv: 1609.05383 [nucl-ex].

[185] Jaroslav Adam et al. "Direct photon production in Pb-Pb collisions at $\sqrt{s_{NN}} = 2.76$ TeV." In: *Phys. Lett. B* 754 (2016), pp. 235–248. DOI: 10.1016/j.physletb.2016.01.020. arXiv: 1509.07324 [nucl-ex].

[186] Shanshan Cao, Chathuranga Sirimanna, and Abhijit Majumder. "The medium modification of high-virtuality partons." In: (Jan. 2021). arXiv: 2101.03681 [hep-ph].

[187] Mengxue Zhang, Yang He, Shanshan Cao, and Li Yi. "Effects of the formation time of parton shower on jet quenching in heavy-ion collisions*." In: *Chin. Phys. C* 47.2 (2023), p. 024106. DOI: 10.1088/1674-1137/aca4c1. arXiv: 2208.13331 [nucl-th].

[188] Yayun He, Shanshan Cao, Wei Chen, Tan Luo, Long-Gang Pang, and Xin-Nian Wang. "Interplaying mechanisms behind single inclusive jet suppression in heavy-ion collisions." In: *Phys. Rev. C* 99.5 (2019), p. 054911. DOI: 10.1103/PhysRevC.99.054911. arXiv: 1809.02525 [nucl-th].

[189] Wenbin Zhao, Weiyao Ke, Wei Chen, Tan Luo, and Xin-Nian Wang. "From Hydrodynamics to Jet Quenching, Coalescence, and Hadron Cascade: A Coupled Approach to Solving the RAA⊗v2 Puzzle." In: *Phys. Rev. Lett.* 128.2 (2022), p. 022302. DOI: 10.1103/PhysRevLett.128.022302. arXiv: 2103.14657 [hep-ph].

[190] Yayun He, Wei Chen, Tan Luo, Shanshan Cao, Long-Gang Pang, and Xin-Nian Wang. "Event-by-event jet anisotropy and hard-soft tomography of the quark-gluon plasma." In: *Phys. Rev. C* 106.4 (2022), p. 044904. DOI: 10.1103/PhysRevC.106.044904. arXiv: 2201.08408 [hep-ph].

[191] Nestor Armesto et al. "Comparison of Jet Quenching Formalisms for a Quark-Gluon Plasma 'Brick'." In: *Phys. Rev. C* 86 (2012), p. 064904. DOI: 10.1103/PhysRevC.86.064904. arXiv: 1106.1106 [hep-ph].

[192] J. H. Putschke et al. "The JETSCAPE framework." In: (Mar. 2019). arXiv: 1903.07706 [nucl-th].

[193] Richard D. Ball, Valerio Bertone, Stefano Carrazza, Luigi Del Debbio, Stefano Forte, Alberto Guffanti, Nathan P. Hartland, and Juan Rojo. "Parton distributions with QED corrections." In: *Nucl. Phys. B* 877 (2013), pp. 290–320. DOI: 10.1016/j.nuclphysb.2013.10.010. arXiv: 1308.0598 [hep-ph].

[194] Stefano Carrazza. "Towards the determination of the photon parton distribution function constrained by LHC data." In: *PoS* DIS2013 (2013). Ed. by E. Kajfasz, p. 279. DOI: 10.22323/1.191.0279. arXiv: 1307.1131 [hep-ph].

[195] Stefano Carrazza. "Towards an unbiased determination of parton distributions with QED corrections." In: *48th Rencontres de Moriond on QCD and High Energy Interactions*. 2013, pp. 357–360. arXiv: 1305.4179 [hep-ph].

[196] Peter Skands, Stefano Carrazza, and Juan Rojo. "Tuning PYTHIA 8.1: the Monash 2013 Tune." In: *Eur. Phys. J. C* 74.8 (2014), p. 3024. DOI: 10.1140/epjc/s10052-014-3024-y. arXiv: 1404.5630 [hep-ph].

[197] Jaroslav Adam et al. "Measurement of jet suppression in central Pb-Pb collisions at $\sqrt{s_{NN}} = 2.76$ TeV." In: *Phys. Lett. B* 746 (2015), pp. 1–14. DOI: 10.1016/j.physletb.2015.04.039. arXiv: 1502.01689 [nucl-ex].

[198] Georges Aad et al. "Measurements of the Nuclear Modification Factor for Jets in Pb+Pb Collisions at $\sqrt{s_{NN}} = 2.76$ TeV with the ATLAS Detector." In: *Phys. Rev. Lett.* 114.7 (2015), p. 072302. DOI: 10.1103/PhysRevLett.114.072302. arXiv: 1411.2357 [hep-ex].

[199] Stephen D. Ellis, Zoltan Kunszt, and Davison E. Soper. "Jets at hadron colliders at order $\alpha - s^{3:}$ A Look inside." In: *Phys. Rev. Lett.* 69 (1992), pp. 3615–3618. DOI: 10.1103/PhysRevLett.69.3615. arXiv: hep-ph/9208249.

[200] Amit Kumar et al. "Jet quenching in a multi-stage Monte Carlo approach." In: *Nucl. Phys. A* 1005 (2021). Ed. by Feng Liu, Enke Wang, Xin-Nian Wang, Nu Xu, and Ben-Wei Zhang, p. 122009. DOI: 10.1016/j.nuclphysa.2020.122009. arXiv: 2002.07124 [nucl-th].

[201] S. Afanasiev et al. "Measurement of Direct Photons in Au+Au Collisions at $\sqrt{s_{NN}} = 200$ GeV." In: *Phys. Rev. Lett.* 109 (2012), p. 152302. DOI: 10.1103/PhysRevLett.109.152302. arXiv: 1205.5759 [nucl-ex].

[202] Axel Drees. "PHENIX Measurements of Beam Energy Dependence of Direct Photon Emission." In: *PoS* HardProbes2018 (2019). Ed. by David d'Enterria, Andreas Morsch, and Philippe Crochet, p. 176. DOI: 10.22323/1.345.0176.

[203] Charles Gale. Private Communications.

[204] U. A. Acharya et al. "Nonprompt direct-photon production in Au+Au collisions at $\sqrt{s_{NN}} = 200$ GeV." In: (Mar. 2022). arXiv: 2203.17187 [nucl-ex].

[205] R. J. Fries, Berndt Muller, C. Nonaka, and S. A. Bass. "Hadronization in heavy ion collisions: Recombination and fragmentation of partons." In: *Phys. Rev. Lett.* 90 (2003), p. 202303. DOI: 10.1103/PhysRevLett.90.202303. arXiv: nucl-th/0301087.

[206] G. Agakishiev et al. "Identified hadron compositions in p+p and Au+Au collisions at high transverse momenta at $\sqrt{s_{NN}} = 200$ GeV." In: *Phys. Rev. Lett.* 108 (2012), p. 072302. DOI: 10.1103/PhysRevLett.108.072302. arXiv: 1110.0579 [nucl-ex].

[207] Vardan Khachatryan et al. "Charged-particle nuclear modification factors in PbPb and pPb collisions at $\sqrt{s_{NN}} = 5.02$ TeV." In: *JHEP* 04 (2017), p. 039. DOI: 10.1007/JHEP04(2017)039. arXiv: 1611.01664 [nucl-ex].

[208] S. Acharya et al. "Transverse momentum spectra and nuclear modification factors of charged particles in pp, p-Pb and Pb-Pb collisions at the LHC." In: *JHEP* 11 (2018), p. 013. DOI: 10.1007/JHEP11(2018)013. arXiv: 1802.09145 [nucl-ex].

[209] Albert M Sirunyan et al. "First measurement of large area jet transverse momentum spectra in heavy-ion collisions." In: *JHEP* 05 (2021), p. 284. DOI: 10.1007/JHEP05(2021)284. arXiv: 2102.13080 [hep-ex].

[210] Morad Aaboud et al. "Measurement of the nuclear modification factor for inclusive jets in Pb+Pb collisions at $\sqrt{s_{NN}} = 5.02$ TeV with the ATLAS detector." In: *Phys. Lett. B* 790 (2019), pp. 108–128. DOI: 10.1016/j.physletb.2018.10.076. arXiv: 1805.05635 [nucl-ex].

[211] Amit Kumar, Abhijit Majumder, and Chun Shen. "Energy and scale dependence of $\hat{q}$ and the "JET puzzle"." In: *Phys. Rev. C* 101.3 (2020), p. 034908. DOI: 10.1103/PhysRevC.101.034908. arXiv: 1909.03178 [nucl-th].

[212] Meike Charlotte Danisch. "Measurement of neutral mesons and direct photons in Pb-Pb collisions at $\sqrt{s_{NN}} = 5.02$ TeV with ALICE at the LHC." Presented 12 Jan 2022. 2021. URL: https://cds.cern.ch/record/2800150.

[213] J. Adams et al. "Transverse momentum and collision energy dependence of high p(T) hadron suppression in Au+Au collisions at ultrarelativistic energies." In: *Phys. Rev. Lett.* 91 (2003), p. 172302. DOI: 10.1103/PhysRevLett.91.172302. arXiv: nucl-ex/0305015.

[214] J. D. Hunter. "Matplotlib: A 2D graphics environment." In: *Computing in Science & Engineering* 9.3 (2007), pp. 90–95. DOI: 10.1109/MCSE.2007.55.

[215] Pauli Virtanen et al. "SciPy 1.0: Fundamental Algorithms for Scientific Computing in Python." In: *Nature Methods* 17 (2020), pp. 261–272. DOI: 10.1038/s41592-019-0686-2.

[216] Charles R. Harris et al. "Array programming with NumPy." In: *Nature* 585.7825 (Sept. 2020), pp. 357–362. DOI: 10.1038/s41586-020-2649-2. URL: https://doi.org/10.1038/s41586-020-2649-2.

[217] F. Pedregosa et al. "Scikit-learn: Machine Learning in Python." In: *Journal of Machine Learning Research* 12 (2011), pp. 2825–2830.

[218] Andrew Collette. *Python and HDF5: unlocking scientific data*. " O'Reilly Media, Inc.", 2013.

[219] The pandas development team. *pandas-dev/pandas: Pandas*. Version latest. Feb. 2020. DOI: 10.5281/zenodo.3509134. URL: https://doi.org/10.5281/zenodo.3509134.

[220] Wes McKinney. "Data Structures for Statistical Computing in Python." In: *Proceedings of the 9th Python in Science Conference*. Ed. by Stéfan van der Walt and Jarrod Millman. 2010, pp. 56 –61. DOI: 10.25080/Majora-92bf1922-00a.

COLOPHON

This document was typeset using the typographical look-and-feel `classicthesis` developed by André Miede. The style was inspired by Robert Bringhurst's seminal book on typography "*The Elements of Typographic Style*". `classicthesis` is available for both LaTeX and LyX:

https://bitbucket.org/amiede/classicthesis/

Final Version as of September 13, 2023 (`classicthesis` version 6.0).